Microchip Lasers

A Thesis submitted to the

University of St. Andrews

in Application for the

Degree of Doctor of Philosophy

by

Richard Conroy

March 1998

Declarations

I, Richard Conroy, hereby certify that this thesis, which is approximately 77000 words in length, has been written by me, that it is a record of work carried out by me and that it has not been submitted in any previous application for a higher degree. I was admitted as a research student in October 1994 and as a candidate for the degree of Doctor of Philosophy; the higher study for which this is a record was carried out in University of St. Andrews between 1994 and 1998.

In submitting this thesis to the University of St. Andrews I understand that I am giving permission for it to be made available for use in accordance with the regulations of the University Library for the time being in force, subject to any copyright vested in the work not being affected thereby. I also understand that the title and abstract will be published, and that a copy of the work may be made and supplied to any *bona fide* library or research worker.

Richard Conroy 28 August, 2008

I hereby certify that the candidate has fulfilled the conditions of the Resolutions and Regulations appropriate for the degree of Doctor of Philosophy in the University of St. Andrews and that the candidate is qualified to submit this thesis in application for that degree.

Dr Bruce Sinclair 28 August, 2008

Acknowledgements

'Not everything in black & white makes sense' - Guinness Advert

This thesis has only been made possible by the contributions and support of a large number of people. I am especially indebted to Bruce for his support, guidance and enthusiasm over the last four years.

I had great pleasure working with Neil and Dave over the first two years of this work, both teaching me a lot, some of which is perhaps better not knowing! More recently Alan and Graham have taken the group in new directions, including underwater, and I have thoroughly enjoyed the experience of working with them. Much of the content of this thesis has been aided by these four, and on a day-to-day basis they provided an excellent group in which to work, and I owe them a big vote of thanks.

Over the years we also saw a number of other people come and go from the group, mainly honours degree project students. James, Tanya, Liese and Alex all provided a welcome diversion and made a significant contribution to the work recorded here and I am very grateful to them for their enthusiasm and hard work.

My refuge of Regs was a great place to adjust back to normality. A large number of people, especially Kate and Ian, helped in showing there was more to life than an office with no windows and kept me (reasonably?) sane during the last four years.

Finally, I am indebted to my family for supporting and encouraging me through the last eight years, and perhaps, who knows, I may be able to get a 'proper' job now!

Abstract

This thesis is concerned with the characterisation of sub-millimetre sized solid-state lasers. These 'microchip' lasers are examined in two forms; one as monolithic devices where the dielectric mirrors forming the laser cavity are directly deposited onto two near parallel faces of the laser gain crystal, and the second where the microchip gain material is used in combination with a nonlinear crystal to form a composite device.

A range of neodymium doped crystals, operating continuous wave and in gain-switched mode at 1064nm, are compared as potential microchip laser gain materials, including Nd:YVO_4, Nd:YOS, Nd:SFAP and Nd:SVAP. With the exception of Nd:SVAP, slope efficiencies exceeding 40% and thresholds of less than 100mW were measured for all these lasers. A comparison of the 1064nm and 1342nm transitions in Nd:YVO_4 is also carried out showing similar performance for both transitions.

The formation of the cavity within these monolithic lasers is described in detail, in particular for the thermal and gain guiding effects in Nd:YVO_4. Both analytical and numerical modelling of these effects are compared with experimental measurement of the cavity formation.

When used in conjunction with a saturable absorber, these sub-millimetre sized lasers can be used to produce short, high intensity pulses. This is demonstrated using Cr:YAG as a saturable absorber for Nd:YVO_4 at 1064nm to produce pulses as short as 1.38ns and peak powers of up to 1kW, and V:YAG to Q-switch Nd:YVO_4 at 1342nm to produce pulses with durations as short as 9.5ns and peak powers up to 360W.

Active control for generating pulses is also demonstrated using a novel range of deflective Q-switches. These low cost, low loss, compact devices produced pulses of up to 12kW peak power and pulses durations of less than 1.1ns on demand.

The continuous wave, intracavity frequency doubling of the three main Nd^{3+} transitions, to give red, green and blue light is described. Up to 220mW of green light, with an efficiency approaching 40%, 33mW of blue light and 10mW of single-frequency red light were produced.

Glossary of Acronyms

Crystals

Laser Crystals

LNP ($LiNdP_4O_{12}$) - lithium neodymium tetraphosphate

Nd:LSB ($Nd:LaSc_3(BO_3)_4$) - lanthanum scandoborate doped with triply ionised neodymium

Nd:SFAP ($Nd:Sr_5(PO_4)_3F$) - strontium fluorophosphate doped with triply ionised neodymium

Nd:SVAP ($Nd:Sr_5(VO_4)_3F$) - strontium fluorovanadate doped with triply ionised neodymium

Nd:YAG ($Nd:YAl_2O_3$) - yttrium aluminium garnet doped with triply ionised neodymium

Nd:YLF - yttrium lithium fluoride doped with triply ionised neodymium

Nd:YOS ($Nd:Y_2SiO_5$) - yttrium orthosilicate doped with triply ionised neodymium

$Nd:YVO_4$ - yttrium orthovanadate doped with triply ionised neodymium

Nonlinear Crystals

BBO (BaB_2O_4) - beta-barium borate

$KNbO_3$ - potassium niobate

KTP ($KTiOPO_4$) - potassium titanyl phosphate

LBO (LiB_3O_5) - lithium triborate

$LiNbO_3$ - lithium niobate

$LiTaO_3$ - lithium tantalate

PPLN - periodically-poled lithium niobate

Laser Characterisation

AR - anti-reflecting

CCD - charge coupled device

CPM - critical phase matching

CW - continuous wave

DPSSL - diode-pumped solid-state laser

DRO - doubly resonant oscillator

ESA - excited state absorption

FWHM - full width, half maximum

GSA - ground state absorption

HR - highly reflecting

MISER - monolithic isolated single-mode end-pumped ring

MOCVD - metal-organic chemical vapour deposition

MOPA - master oscillator power amplifier

MQW - multiple quantum well

NCPM - non-critical phase matching

OPA - optical parametric amplifier

OPD - optical path difference

OPO - optical parametric oscillator

OSA - optical spectrum analyser

Q-Switching - 'quality' switching alters the ratio of the energy stored to the loss of a laser cavity. Can be either passive or active

QPD - quadrupole deflector

QPM - quasi phase-matching

( )%R - reflectivity of a dielectric coating

SEL - surface emitting laser

SESAM - semiconductor saturable absorbing mirror

SHG - second harmonic generation

SLM - single longitudinal mode

SQW-SCH - single quantum well, separate confinement heterostructure structure

( )%T - transmission of a dielectric coating

TEM_{00} - transverse electro-magnetic mode with no dark regions in both the vertical and horizontal planes. This is a diffraction limited transverse mode with a single intensity lobe

TIR - total internal reflection

VCSEL - vertical surface cavity emitting laser

Table of Contents

Chapter 1 - Overview of Diode-Pumped Solid-State Lasers (DPSSLs)

1.1 Introduction

Lasers are already impacting in many areas of our lives, often without our knowledge of their use. This is a virtue of their compactness and ease of use and the advantages they offer over more traditional technologies. This thesis is an investigation of a particular class of lasers, 'microchip' lasers, which are formed from sub-millimetre sized monolithic crystals. This class of laser is of particular interest in the areas where a solid-state laser is desirable over a semiconductor laser diodes, such as in generating visible light, short high intensity pulses or in good quality beams.

The first chapter of this thesis is a review of the technologies that have contributed to the development of these microchip lasers to set the context for the work described in the succeeding chapters. This review looks at both the historical development of both suitable solid-state gain materials for these lasers and the laser diode pump sources used and indicates some of the potential directions in which this field may go in the near future due to recent research.

The second and third chapters examine the operating characteristics of a range of different gain materials prepared as monolithic microchip lasers and how the laser cavity is formed within the material. These chapters provide an important background in the understanding of what makes a good microchip laser and how they can be modelled to maximise their performance. The operating limitations of these lasers are also investigated.

The fourth and fifth chapters investigate how the microchip concept can be extended to form a composite device by including a nonlinear element. In the case of chapter four this nonlinear element is in the form of a saturable absorber or electro-optic crystal which can be used to generate short, high intensity pulses through passive and active Q-switching respectively. In chapter five non-centrosymmetric crystals are used in combination with the gain materials to give frequency conversion, in particular frequency doubling, to generate red, green and blue light.

1.1.1 Background

In 1996 more than 17,000 peer-reviewed papers were published in scientific journals on the development and applications of lasers, with a sustained annual rise of 7-10% [1]. In the same year, the estimated world-wide sales of the laser industry exceeded $2.8 billion, with a healthy 18% expansion of the market forecast for 1997 [2].

Host	Active Element	Laser Name	Example
Inorganic			
Crystal	Paramagnetic Ion	Paramagnetic Ion	Nd:YAG
Crystal	-	Stoichometric	NdP_5O_{14}
Crystal	Electron/Hole Vacancy	Colour Centre	KCl:Li F_A (II)
Crystal	Chemical Impurity	Impurity Centre	$KCl:O^-_2$
Glass	Paramagnetic Ion	Glass	Er:Glass
Glass	Organic Dye	Glass Dye	Rhodamine 6G in Glass matrix
Organic			
Liquid Crystal	Organic Dye	Liquid Crystal	Rhodamine 6G in CBOA
Polymer	Organic Dye	Polymer Dye	Rhodamine 6G in polyurethane
Crystal	Organic Dye	Organic Molecule	Anthracene in Fluorene
Glass	Organic Dye	Solid Solution	Coronen in Methyl-Cyclohexane
Semiconductors			
Crystal	Ion	Extrinsic	GaAs:Te
Crystal	-	Intrinsic	CdS, ZnS
Crystal	p-n Junction	Diode	GaAs/AlGaAs

Table 1 – Range of solid-state laser materials and processes [after 3]

Solid-state lasers cover a wide variety of laser types as shown Table 1. More than 60% of the laser market now arises from semiconductor laser diodes, with solid-state lasers replacing gas lasers as the second largest field. This is a reflection of the doubling of research papers related to solid-state lasers in the first five years of this decade, compared to a constant number relating to more mature gas laser technology.

The increased availability of cheaper, higher power laser diodes and the advantages they offer as pump sources over more conventional lamp pumping has had a knock on effect in the development and marketing of diode-pumped solid state lasers (DPSSLs) in particular. The DPSSLs field is now one of the fastest growing in terms of research and development.

This chapter begins with an historical review of the important technological breakthroughs that have made miniature diode-pumped solid-state lasers possible. Then it proceeds to give a brief overview of solid-state laser gain materials to explain the background of the work contained in this thesis.

1.2 Historical Development of DPSSLs

To understand the development of diode-pumped solid-state lasers, and microchip lasers in particular, it is important to consider the technological requirements and historical problems that have affected progress towards miniature DPSSLs. This section will review the development of the basic laser ideas along the two major paths of laser diode development and suitable doped crystalline laser materials.

1.2.1 Realisation of The Laser

In 1916 Einstein published his own new and simple proof of Planck's law and through his use of statistical mechanics introduced the concept of stimulated emission [4]. Experimental observation of stimulated emission was nearly made in the 1930's by Ladenburg through his work on negative dispersion [5], but it was nearly 20 years before Weber gave the first demonstration of stimulated emission based on a microwave transition [6].

Work began almost immediately on the development of an optical analogue with Schawlow and Townes laying most of the ground work, but they were beaten to the first experimental demonstration by Maiman who, in 1960, showed a flash-lamp pumped ruby laser operating at 694nm [7]. Shortly after the first gas laser was realised [8], followed by an explosion of interest that created the many different types of laser available today.

1.2.2 Development of Laser Diodes as Pump Sources

Watanabe and Nishizawa were the first to propose that light could be generated from the recombination of hole-electron pairs at a p-n junction in 1957, suggesting the possibility of stimulated emission in a semiconductor [9]. However, difficulty with the preparation and quality of such semiconductor junctions lead to a five year wait before the first experimental demonstration of laser action in a p-n junction of GaAs cooled to 77K with liquid nitrogen [10]. In order to see line narrowing from stimulated emission, a large threshold current density of 10^4-10^5Acm^{-2} was required, limiting these early laser diodes to pulsed operation due to thermal constraints.

The operation of these homojunctions was fundamentally limited in two respects. The first problem arose because the charge carriers could recombine over the entire area of the junction, which meant high currents were required to get a sufficient current density to give stimulated emission, as opposed to spontaneous emission. Secondly, much of the light generated in the active plane was diffracted into the strongly absorbing p and n regions surrounding the active region, further increasing the threshold current, and limiting these devices to pulsed operation [11].

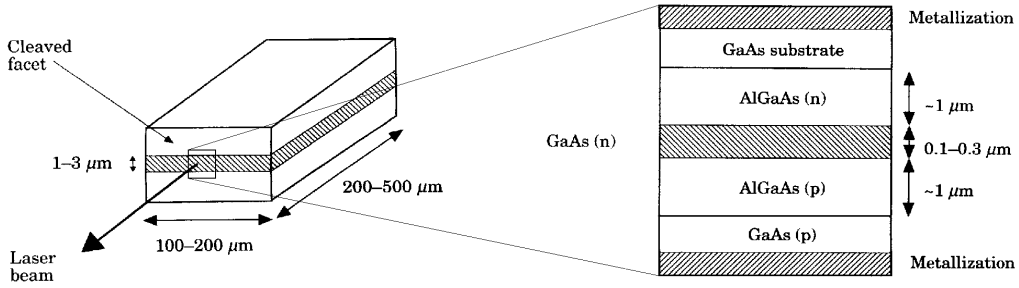

Figure 1 - Double heterostructure laser diode [after 12**]**

In 1963 the idea of a heterojunction was proposed by Kroemer to address the second of these limitations [13]. Again, material problems meant that six years elapsed before the first experimental demonstration of a heterojunction laser diode, formed between p-AlGaAs and n-GaAs [14]. A refinement of this idea lead to the development of the now common ‘double heterostructures’, shown in Figure 1, formed by a sandwich of the active region of p-GaAs and n-GaAs surrounded by layers p-AlGaAs and n-AlGaAs. Double heterostructures offer more efficient, CW operation at room temperature [15] and have three main advantages over homostructures:

1. The refractive index of the GaAs is slightly higher than the surrounding AlGaAs (n(GaAs)-n(Ga(1-x)Al(x)As)=0.62x), forming an optical waveguide, and improving the confinement of the light produced in the active region. In addition to the natural refractive index guiding, gain guiding provides further confinement of the lasing mode
2. The band gap of GaAs (~1.3eV) is significantly smaller than AlGaAs (1.3-2.2eV), confining the injected holes and electrons to the active layer. This gives an increased carrier density and correspondingly higher gain in the active layers, decreasing the current threshold required for lasing action
3. The different band gap energies also reduce the amount of laser light absorbed by the surrounding AlGaAs layers, improving performance.

A subsequent refinement to the double heterostructure in the 1980's was the idea of 'quantum wells'. Quantum wells address the first limitation of homostructures in providing a means of charge confinement into 2D potential energy wells, decreasing the current required to reach threshold further. There are two main ways in which quantum wells are implemented in modern diode lasers, 'multiple quantum wells' and 'single quantum well, separate confinement structures'.

Typically, multiple quantum wells (MQW) are fabricated by growing alternate thin (~5-20nm) layers of GaAs and AlGaAs in the active region to form miniature heterojunctions as shown in Figure 2. Charge confinement by proton implantation, is then introduced to give many separate emitting regions.

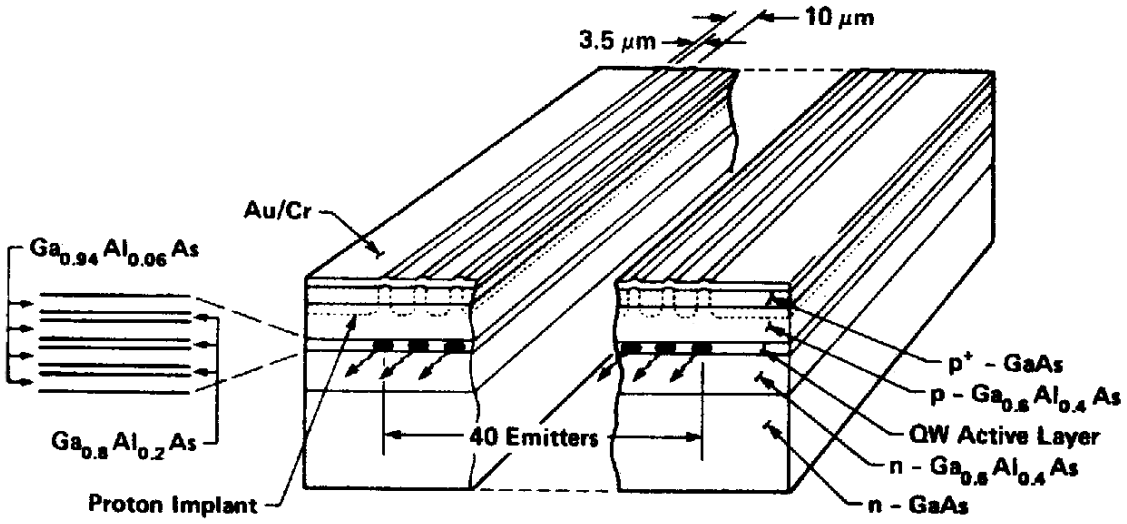

Figure 2 - Schematic of multiple quantum well laser array [after 16]

The alternative approach is to use a single quantum well, separate confinement heterostructure structure (SQW-SCH. In this case the charge is confined using proton implantation into the p-GaAs layer. In addition there is a single p-GaAlAs active layer surrounded by layers of higher refractive index to give further confinement.

SQW-SCH diodes have a longer optimal length than MQW structures because of their poorer overlap between the optical mode and active region. However this can be an advantage with high power devices because of the reduced thermal resistance of a larger device.

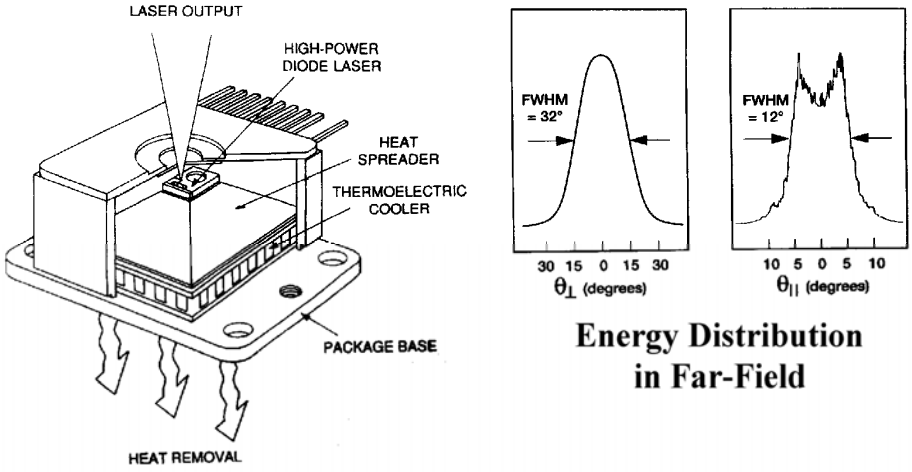

Figure 3 - Schematic of SDL-2300 Series – Up to 4W, high brightness CW GaAlAs laser diodes

A modern array, MQW, high-brightness AlGaAs laser diode is shown in Figure 3. The electrical-to-optical efficiency of this device is approximately 30% with a threshold current density of ~100Acm^{-2} [17]. CW output powers of up to 4W are possible from such devices, with a multi-transverse mode output polarised (20:1) perpendicular to the junction. The emitter size varies from 50-500x1μm for output powers of 0.5-4W respectively. Figure 3b) shows the typical intensity profiles parallel and perpendicular to the junction. The bandwidth of these laser diode is generally around 2.5nm FWHM, giving a coherence length of approximately 0.1mm. Devices from this family were used in the subsequent chapters of this thesis as the pump sources for our microchip lasers.

1.2.3 Modern Laser Diode Development

Much of the work on laser diodes until the mid-80's concentrated on the refinement of material growth and the diode structure. In the last decade the emphasis has shifted towards new cavity geometries, higher powers, higher brightness and single mode outputs.

1.2.3.1 Single Mode Operation and Scaling to Higher Powers

Most modern laser diodes are constructed by the growth of layers of semiconductor material onto wafer substrates using metal-organic chemical vapour deposition (MOCVD). The wafers undergo processing by photolithography and proton implantation, followed by die processing in the form of metallisation, cleaving, dicing and mirror coating to form the diode structure. A single wafer can be diced into several thousand laser diodes making the process highly cost effective and ideal for mass production.

The general operating characteristics of these lasers, multi-transverse and multi-longitudinal mode, are sufficient for many applications. However if single mode operation is required, a number of recently developed techniques can be used, some of which are now described.

By fabrication of quantum wells of the appropriate width, single frequency output is possible, as well as a dramatic increase in both the optical and electrical efficiency of these devices at room temperature [18]. However, this method is only possible in low power devices and requires tight control of the fabrication procedure.

For higher powers, the incorporation of either a distributed feedback (Bragg) reflector into the cavity of a normal laser diode, or the use of a grating as part of an external cavity, can also offer single frequency operation [17]. Scaling of these devices is primarily limited only by the semiconductor material properties and therefore they potentially offer the most exciting advance to higher power, single-frequency laser diode pump sources.

By the fabrication of miniature active regions it is possible to achieve single transverse modes as well. Active regions, of the order of 3x1μm, formed by quantum wells in a single double hetrojunction can offer CW powers of up to 150mW in a single transverse mode. By making an array of these stripes, CW powers of 1.2W are

possible from active regions of 100x1μm, though coupling between the stripes limits the density and number of stripes possible. Such an array gives a high brightness output, making them more useful as a pump source.

Recent work on the amplification of single mode laser diodes, in the form of master oscillator power amplifiers (MOPA), has lead to the possibility of higher powers (~1W) in a single frequency, diffraction limited beam [17] negating some of the disadvantages associated with high power laser diodes. As the technology behind this technique matures, further power scaling will be possible.

For scaling to higher powers, a bar structure is usually adopted to overcome thermal problems. Tens of 100-200x1μm stripes in parallel are grown on 1cm substrates and operated together to give tens of watts of CW output power [17]. Again thermal considerations determine the separation required between stripes; for CW devices this limits the packing density to 20%, but for quasi-CW devices this can rise to close to 100%.

By pulsing the diodes with a low duty cycle to overcome the thermal constraints, it is possible to get peak powers in excess of 5kW [17]. Many laser diodes can now be purchased with optional fibre pigtails, which can be bundled together to produce high average powers, in excess of 10W from a 380μm multi-mode fibre [17]. Fibres can additionally provide an element of beam shaping to give a circular output, though with a sacrifice on the polarisation of the output.

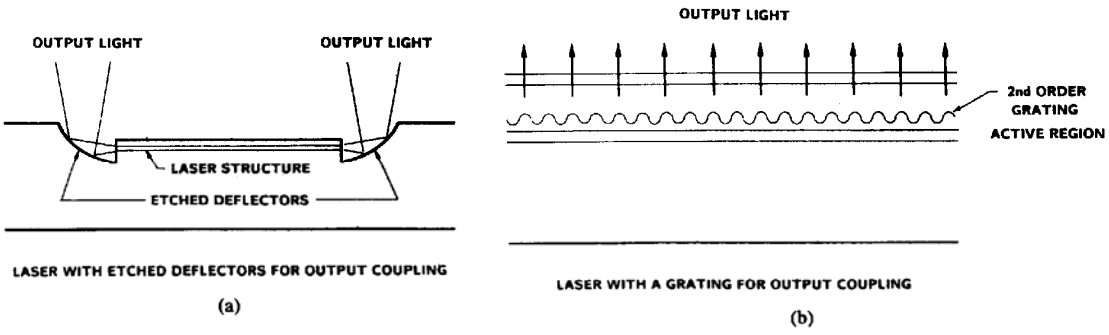

Figure 4- Surface Emitting Lasers [after 16]

As an alternative to edge-emitting structures, surface emitting diode geometries, as illustrated in Figure 4, have been developed for the telecommunications market. They can offer higher brightness and better beam quality in a monolithic device and

therefore can be more easily used with optical fibres than traditional edge-emitting diodes. There are two commonly used schemes employed to couple the light out perpendicular to the junction, the more basic of which uses curved reflectors at either end of the active area. A more novel approach is to deposit a periodic refractive index variation above the active region, as shown in Figure 4b), which acts as a grating, forcing the laser radiation out vertically.

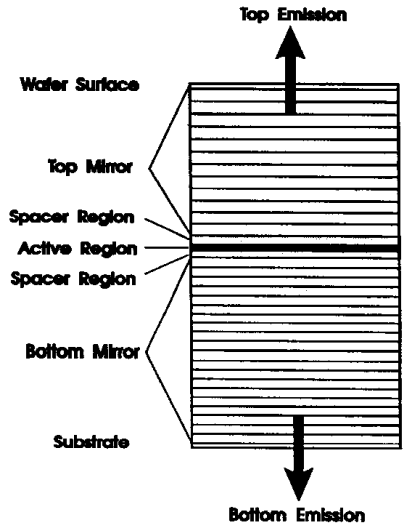

Figure 5 - Schematic of the Structure of a VCSEL

A more recent development in surface emitting lasers is vertical surface cavity emitting lasers (VCSELs). Typically a VSCEL has a sandwich structure with an active layer, InGaAs for example, surrounded by alternating layers of GaAs and AlGaAs as shown in Figure 5. The layers are then etched into stacks, typically several microns in diameter. The alternating layers of GaAs and AlGaAs act as Bragg reflectors, giving much higher reflectivity than normal diode facets. This leads to low threshold currents and slope efficiencies of >60%. Single transverse and longitudinal modes are readily achievable with CW output powers of up to 10mW from each stack [19].

1.2.3.2 Band-Gap Engineering of Laser Diodes

As well as single mode operation, interest in semiconductor lasers operating at many different wavelengths has increased over the last decade. The wavelength of a laser diode is determined by the band gap energy of the junction and can be altered by changing the composition of the host material or the junction temperature. Lasers diodes, such as the ones used in this thesis, operating between 770-900nm are

generally based on $Ga_{1-x}Al_xAs$, where the wavelength can be increased ~1nm by increasing the Al concentration by 1%. Similarly the peak emission wavelength changes by 0.3nm/^oC of the diode junction temperature.

$Ga_{1-x}Al_xAs$ diodes have come to prominence because their wavelength range can be made to match the 810nm absorption band of Nd^{3+} and a number of other commonly used transition metal ions. This and similar coincidences have helped to drive research into both diode and solid-state laser research. Table 2 summarises the main semiconductor materials used in laser diodes, the wavelength range over which they operate, and some of the ions which they can be used to excite.

There are two main limitations on the range of semiconductor materials that can be used in laser diodes. For efficient operation the band gap must be direct so the electron-hole recombination can occur without the assistance of other physical processes; this rules out silicon structures. The matching of lattice constants is the other important constraint. The doping and impurity concentrations determine the lattice mismatch with the underlying the crystalline substrate. Lattice mismatch leads to poor electric contact and stress and strain in the area around the junction causing structural failure. This second constraint can be addressed in a number of ways, both in the fabrication and design of the diode structure.

Material	Wavelength /nm	Excitable Ions
GaN/AlGaN	430-550	Pr^{3+}
ZnSSe	447-480	Pr^{3+}
ZnCdSe	490-525	Ti^{3+}, Sm^{2+}, Ho^{3+}
AlGaInP/AlGaAs	620-680	Cr^{3+}
GaInP/GaAs	670-686	Cr^{3+}
AlGaAs/GaAs	750-870	V^{2+}, Tm^{3+}, Ho^{3+}, Nd^{3+}, Er^{3+}
GaAs/GaAs	904	
InGaAs/GaAs	870-1100	Yb^{3+}, Er^{3+}, Cr^{4+}
InGaAsP/InP	1100-1650	Ce^{2+}, Dy^{2+}, Ni^{2+}, Er^{3+},Cr^{2+}
AlGaAsSb/InGaAsSb	2000-3000	
PbCdS	2700-4200	
PbSSe	4200-8000	
PbSnTe	5500-30000	
PbSnSe	8000-30000	

Table 2 - Major semiconductor laser materials

For 870-1100nm operation, strained-layer super lattice structures have been developed based on InGaAs, mainly for the pumping of erbium doped fibre amplifiers and telecommunications applications. To create a strained active layer a thin layer of material only a few nanometers thick, is grown between two different lattices to take the strain of the mismatch of the lattice without producing flaws. A strained layer allows a lattice mismatch of up to 1%, in contrast to the 0.1% for direct lattice matching [20]. Further development and refinement of this technique still needs to be made for the power levels of InGaAs diodes to match the power available from GaAlAs.

At shorter wavelengths, strained-layer AlGaInP diodes have been developed to operate in the 630-680nm region. These devices can match the broad absorption of Cr^{3+} around 670nm and have led to the development of new diode-pumped Cr^{3+} doped materials. Low power AlGaInP diodes have begun to replace HeNe lasers in many applications, for example in laser scanners, and offer the possibility of visible laser designation in the form of laser pointers and theodolites.

More recently, breakthroughs in production techniques have led to the development of wider band gap materials such as the III-V material GaN and the II-VI material ZnSe. Haase et al. [21] were the first to demonstrate a pulsed II-VI diode operating at 490nm using ZnSe in liquid nitrogen, followed by CW laser action shown later that year [22]. However, research has been hampered by lattice mismatching with the underlying GaAs or InP substrates. This has led to growth, lifetime problems and poor electrical contact.

Work on InGaN active layers has proved more successful and at present threshold currents are within an order of magnitude of AlGaAs diodes, with lifetimes of hundred of hours reported and operating at a variety of wavelengths from 430-550nm [23]. By either of these routes, within the next ten years we can expect to see green and blue laser diodes in the marketplace.

In conclusion, the next decade will bring higher power diodes with higher brightness over a wider range of wavelengths. This will increase the range and efficiency of solid-state lasers that can be diode-pumped.

1.2.4 Historical Development of Diode Pumped Solid-State Lasers

The quest for suitable sold-state gain materials for miniature diode-pumped solid-state lasers has happened in parallel to the development of laser diode pump sources. Many of the rapid advances in DPSSL technology came with the advancements in diode technology described in the previous section. However there has always been exploration for new materials and new cavity designs to exploit the virtues of diode pumping, some of which is explored in this section.

1.2.4.1 Early Diode Pumped Solid State Lasers

Pumping of paramagnetic ion solid-state lasers using diodes dates back to the early 1960's. However the poor performance of the available laser diodes meant that little attention was paid to them as a pump source for more than two decades in deference to cheaper, more efficient flash lamp pumping.

Newman [24] was the first to demonstrate excitation of the fluorescence of Nd^{3+} ions in $CaWO_4$ in 1963 using light emitting diodes (LEDs) as the pump source. Although cheaper than laser diodes, the efficiency of modern LEDs is still typically less than 20%, with low optical power densities and broad emission spectrums; therefore their use as pump sources for solid-state lasers is still limited.

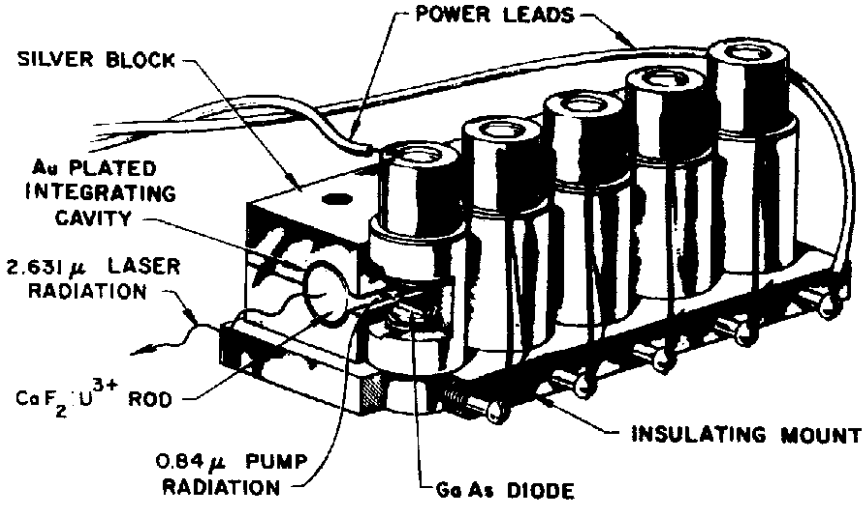

Figure 6 - Schematic of First DPSSL [after 25]

In 1964, shortly after the first demonstration of GaAs diodes lasers, Keyes and Quist were the first to demonstrate pumping of solid-state gain materials using the new diode lasers [25]. Their setup is illustrated in Figure 6. A set of five GaAs laser diodes was used to transversely pump a U:CaF_2 laser rod, giving laser operation at 2.61μm,

while cooled to liquid helium temperatures. This device gave respectable performance, with quasi-CW operation possible. Similar work followed by a number of other groups who showed lasing was possible in a number of other active ions, including Dy^{2+} [26].

1.2.4.2 Rare Earth Doped Materials, Fibres and Longitudinal Pumping

The rest of the 1960's and 1970's showed slow but steady progress in the development of diode-pumped lasers, mainly limited by the quality of laser diodes available [27].

Initial work concentrated on the development of rare-earth-ion doped laser hosts for diode pumping, because rare-earth ions have higher stimulated emission cross-sections that other ions, giving higher gain and lower thresholds. These properties were important for the pulsed, low power diodes available at the time. Nd^{3+} was soon identified as the most promising rare-earth ion because its absorption band around 810nm matched the wavelength of AlGaAs diodes, and its terminating laser level for 1.06μm was far above the ground level, making population inversion easier to achieve.

Nd:YAG was first demonstrated as a laser host in 1964 [28], and was diode-pumped in 1968 by Ross [29]. It has since become one of the most widely used solid-state laser materials because of its good all round performance [30]. A more thorough discussion of neodymium doped materials will be given later in this chapter.

Early work on DPSSLs used transverse pumping geometries, which were convenient when poor quality pump light or a number of different sources were being used. However, transverse pumping is generally inefficient because of the poor coupling between the pumped and lasing volumes.

The alternative, longitudinal or end-pumping was first demonstrated in 1973 giving much greater efficiency, but with only limited possibilities for power scaling [31,32]. However, as the brightness of diodes has increased, end-pumping has become a more attractive technique because of the good pump/laser mode overlap and ability to favour TEM_{00} operation.

Stone and Burrus took a more novel approach by doping fibres with rare-earth ions in 1974 [33]. Fibres overcome a number of problems associated with bulk solid-state lasers. A long, narrow, graded index fibre gives good overlap between the pump and lasing volumes, both of which are guided in the fibre. The long interaction length also allows the use of ions with low cross-sections and different pumping geometries to maximise the excitation of the ions. Therefore low thresholds and transitions with lower stimulated emission cross-sections are possible in fibre lasers [34].

There is now a wide range of fibre lasers available, exploiting many different effects in optical fibre from up-conversion to short pulse generation. In particular, a lot of effort has gone into the development of erbium-doped fibre amplifiers operating near 1.54μm [35] which corresponds to the low loss window in silica fibres for use in long distance telecommunications [36].

1.2.4.3 Improved Fabrication of Diodes and Crystals

The development of high-power, reliable semiconductor diode lasers in the 1980's enabled more rapid development of DPSSLs, to the point where the advantages of diode pumping exceeded those of flash lamp pumping. The longer operating life and compact size of these laser diodes, combined with their low unit costs has acted as a stimulus to manufacturers to develop commercial DPSSLs.

To complement the development of diode pump sources, work on host materials for lasing ions increased in the 1980's, leading to hosts which could sustain high doping concentrations without fluorescence quenching and give a broad, strong absorption band around 810nm. Crystal growing techniques also improved to give very low scattering losses and impurity concentrations. This was complemented by an improvement in the modelling and deposition of dielectric coatings. These advances led to the possibility of gain crystals less than a millimetre long, which could be coated on two near-parallel faces with dielectric coatings forming a monolithic device, and efficiently end-pumped with a laser diode - a 'microchip laser'.

1.2.4.4 Monolithic Solid State Lasers

The first laser demonstrated by Maiman in 1960 was also the first monolithic laser. The ruby crystal he used was coated with silvered mirrors deposited onto two near-parallel faces. This is the most basic form of laser cavity, but potentially the most interesting in a number of respects, as will be illustrated by this thesis.

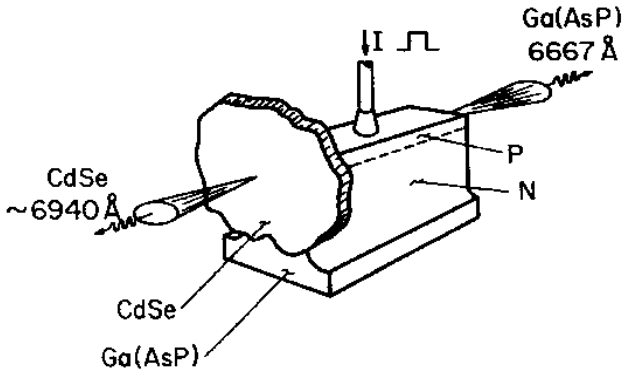

Figure 7 - Ultrathin Single-Mode CdSe Platelet DPSSL [after 37]

In 1966, the first monolithic semiconductor laser was demonstrated [37]. A CdSe platelet, two microns thick, was coated with dielectric coating on two near-parallel faces (Figure 7). This was end-pumped by a diode at 77K, and showed the possibility for monolithic devices to give efficient single frequency operation.

The first diode-pumped monolithic rare-earth ion doped laser, a Nd:YAG rod, was demonstrated in 1973 [38]. Later in the same year an end-pumped device showed the further promise of this design, giving low thresholds (6.2mW) and high slope efficiencies (~35%), though this was hampered by low power diodes [39]. CW lasing at 1047nm and 1317nm in a monolithic LNP crystal (Nd^{3+} active ions in stiochiometric crystal) at room temperature was demonstrated in 1979, indicating stiochiometric crystals have good absorption properties, useful in short cavities [40].

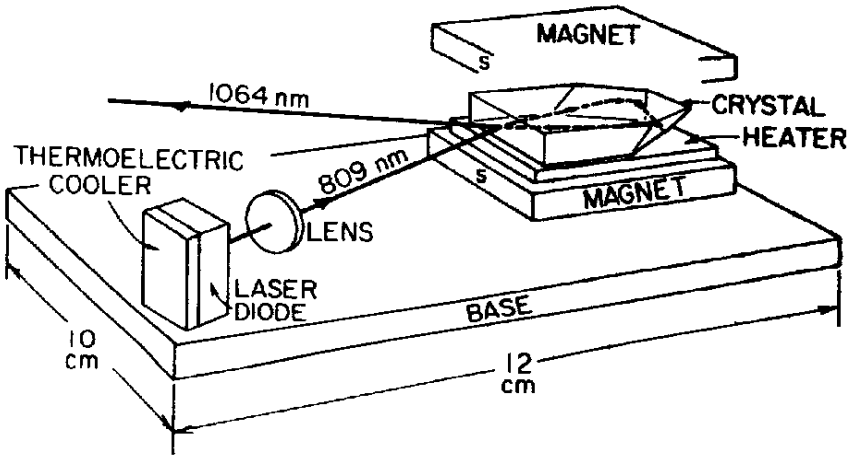

Figure 8 - Schematic of a MISER [after 27]

In 1985 a novel monolithic laser based on a unidirectional ring design was demonstrated and is illustrated above in Figure 8. A ring is formed by a highly reflecting front surface and total internal reflection on the faces opposite to establish a cavity. The cavity is non-planar and when a magnetic field is applied the rotation of the polarisation in one direction causes total internal reflection (TIR) to form the cavity, though no TIR is experienced in the opposite direction and therefore a uni-directional ring is formed. Kane and Byer patented this system as a MISER - 'Monolithic Isolated Single-mode End-pumped Ring'. These devices have produced single frequency powers of 25mW and linewidths of less than 3kHz with good stability [41], though the requirement for a high brightness pump source has limited the development of this geometry. However, this form of ring geometry is potentially useful for materials with low absorption cross-sections or for more unusual pumping geometries, although it will always be more difficult to operate than an on-axis system.

Mooradian was the first to coin the term ‘microchip laser’ for monolithic lasers less than a millimetre in length in 1989 [42]. These microchip lasers offered many new possibilities because of their very small cavity length and unusual geometry.

Much of the early work on microchip lasers came from two groups at the end of the 1980’s. Zayhowski et al. at MIT Lincoln Labs started using the 1064nm transition in Nd:YAG, demonstrating single frequency operation, gain-switching and frequency modulation of these devices [43,44,45].

Dixon et al. at Amoco Laser Company started working on their 'cube' laser based on the more unusual stiochiometric crystal LNP. They showed single mode operation at 1047nm and 1317nm, and intracavity frequency doubling using these cubes [46,47,48].

These groups and subsequent work have shown slope efficiencies approach the quantum limit from these microchip lasers, with low thresholds and the possibility of significant power in a single transverse and longitudinal mode. There will be further discussion of these devices in the next chapter of this thesis, in particular Nd:YVO_4 microchip lasers, the primary gain material used in this thesis.

1.2.4.5 Composite Microchip Lasers

A major breakthrough came with the idea of composite cavities, formed by contacting a non-linear crystal to the microchip gain material. The first demonstration of a composite green microchip, formed from a piece of Nd:YVO_4 and KTP, was in 1981 [49].Over 500mW CW of frequency doubled power at 532nm has subsequently been obtained from a microchip laser [50], with demonstrations of doubling of the other two main Nd^{3+} transitions, to give blue and red light [51]. Chapter five of this thesis will report on the work in St.Andrews on the development of these doubled devices to produce red, green and blue light.

By using an electro-optic crystal or saturable absorber in place of the KTP crystal, frequency and amplitude modulation can be achieved. With passive Q-switching, the second, third, fourth and fifth harmonics of the 1064nm transition have been produced from a microchip laser [52]. Actively Q-switched microchip lasers have produced sub-nanosecond pulses with peak powers exceeding 50kW [53,54,55,56,57]. Frequency modulation using both pump power modulation and the electro-optic crystal $LiNbO_3$, has also been demonstrated [58,59]. The fourth chapter of this thesis will look at the active and passive Q-switching of Nd:YVO_4 microchip lasers, and their ability to produce nanosecond pulses of multi-kilowatt peak power.

1.2.4.6 Other Microchip Devices

There has also been research into many other gain materials in many various cavity

configurations. Other Nd^{3+} hosts which have been demonstrated in a microchip format include: Nd:LMA [60], LNP [61], Nd:LSB [62], Nd:MgO:$LiNbO_3$ [63], NYAB [64], Nd:$GdLaVO_4$ [65], Nd:YOS Nd:SVAP Nd:SFAP [66], Nd:CWO and Nd:NGWO [67], all offering impressive performance and particular advantages over Nd:YAG.

Recently, other lasing ions have been demonstrated in a microchip format:

1. Yb:SFAP with low quantum defect heating (ratio of pump/signal photon energies) and long upper state lifetime, lasing at 1047nm and pumped at 899nm, with a slope efficiency of 78% [68]
2. Er,Yb:glass has been shown to operate with a single frequency of linewidth less than 1kHz and slope efficiency of 22% at 1530nm [69];
3. Ho,Tm:YAG operating in a single frequency at 2091nm, with optical bistability and dual polarisation modes [70,71,72];
4. Cr:LiSAF which could be tuned while lasing on a single frequency [73]
5. Tm:YVO_4 operating at 1940nm with slope efficiencies of 48% pumped at 799nm which coincides with a major absorption band of water [74,75,76]

As with diode lasers, new pumping geometries can further exploit the virtues of microchip lasers. With the development of surface emitting lasers (SELs), there has been an interest in developing arrays of lasers, particularly for telecommunications applications. Figure 9 shows a 2D array of surface emitting lasers, similar in design to Figure 4a, pumping a close-coupled Er:YSGG microchip in 48 separate elements. Output powers of several milliwatts were measured from each element, with each element having the possibility of being operated independently [77].

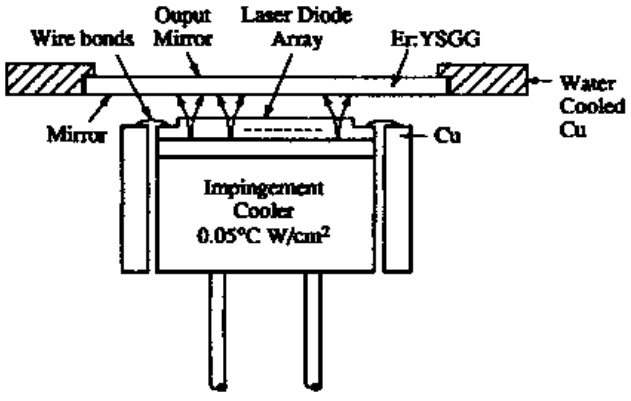

Figure 9 - Array Pumping of Er:YSGG by SEL [after 77]

As the output and wavelength range available from laser diodes improves in the future, we can expect to see microchip lasers operating closer to their maximum quantum efficiencies with lower thresholds, providing real commercial competition for diode lasers and larger DPSSL systems. There will be a sustained increase in the number of ions and hosts that can operate in a microchip format, as new diode technology becomes available allowing access to new ions.

1.3 Solid-State Laser Materials

The aim of the second part of this chapter is to give a broad overview of solid state laser materials and the active ions involved.

Active Ion	Example Material	Lasing Wavelengths (mm)	Pump Wavelengths (mm)	Ion Lifetime (ms)	Emission X-Section ($10^{-20}cm^{-2}$)	Absorption X-Section ($10^{-20}cm^{-2}$)
Ce^{3+}	Ce:YLF [78]	0.28-0.4			0.03	
Co^{2+}	Co:MgF_2 [79]	1.7- 2.6	1.3-1.4	37	1.1	0.36
Cr^{2+}	Cr:ZnSe [80]	1.8-3.0	1.6-1.9	4-13	75-188	
Cr^{3+}	Cr:LiSAF [81]	0.76-1.01	0.55-0.75	67	5	4.5
Cr^{4+}	Cr:Mg_2SiO_4 [82]	1.16-1.34	1.064	3	14.4	1-2cm^{-1}
Dy^{2+}	Dy:CaF_2 [83]	2.35	1.25, 1.62	40000-50000		
Er^{3+}	Er:YSGG [77]	0.5, 0.7, 0.85, 1.55, 1.77, 2.69-2.94	0.97,0.79	1300-2000	2.6	0.64 (Er:Yb)
Eu^{3+}	Eu:Y_2O_3 [84]	0.61-0.62	0.53	870		
Ho^{3+}	Ho:$LiYF_4$ [**81**]	0.55, 0.75, 0.98, 1.4, 1.5; 2.36, 2.9	0.48, 0.51,0.98	14300	1-2	0.9
Nd^{3+}	Nd:YAG [85]	0.9, 1.06, 1.3, 1.8	0.81, 0.78	240	33	7
Ni^{2+}	Ni:ZnSe [86]	2.5-2.8	1.1-1.35, 1.9-2.1	106	8	
Pr^{3+}	Pr:YLF [87]	0.53, 0.6, 0.64, 0.69, 0.72; 0.996	0.44, 0.47, 0.48, 0.59	9-45, 160	2-28	0.8-2.4
Sm^{2+}	Sm:CaF_2 [88]	0.7-0.77	0.4-0.45,0.6-0.65	1.4	40	300
Ti^{3+}	Ti:Al_2O_3 [89]	0.68-1.1	0.4-0.65	3.2	32	6
Tm^{3+}	Tm:YVO_4 [75]	0.45, 1.8- 2.0, 2.35	0.78-0.79	2500-2700	5.6	3.5 (5%)
U^{3+}	U:CaF_2 [90]	2.2-2.6	0.52-0.58, 1.12	140		
V^{2+}	V:MgF_2 [91]	1.12-1.26	0.83-0.91	2300	0.8	
Yb^{3+}	Yb:SFAP [92]	1.047	0.89-0.91	1260	7.3	8.6

Table 3 - Lasing Ion Properties

In particular we are interested in paramagnetic ions that show lasing through an electronic transition of a metal ion held in a solid matrix. In general to achieve stimulated emission the ion must possess a relatively long-lived (>1μs) excited state from which a radiative transfer occurs, to a short-lived (<100ns) terminating level.Table 3 details some of the active ions from which stimulated emission has been observed and some of the relevant parameters associated with the lasing transitions. The ions can be split into two broad groups:

1. **The rare-earth ions,** comprising the lanthanides (^{4}F electrons) and actinides (^{5}F electrons), have narrow transitions involving purely electronic F-F transitions. The outer, optically active electrons are shielded from the nucleus and the transition is not broadened by nucleon vibrational or rotational energy
2. **The transition metal ions** comprise members of the iron group (^{3}D electrons) which have broad D-F transitions because of phonon assisted decay. The outer electron shell is not shielded from the nucleus and therefore is dependent on its energy state, through phonon interaction

As can be seen from Table 3 lasing is possible over much of the visible and infrared spectrum, in both broadband tuning ranges and narrow lines, with varied pump absorption spectra. The lasing properties are quite different even for ions of the same element and vary as well according to the host matrix's properties. We will now consider the two main classes of ion, and Nd^{3+} in particular, followed by a brief overview of the classification of hosts.

1.3.1 Vibronic Laser Materials (Transition Metal Ions)

The transition metals: Ce^{3+}, Co^{2+}, Cr^{3+}, Ho^{3+}, Ni^{2+}, Sm^{2+}, Ti^{3+} and V^{2+}, are elements of the iron group of transition metals which exhibit broad band optical emission when excited. Johnson et al. [93] realised in 1963 that transitions of the ^{3}D electrons of these ions are broadened through phonon interactions, making the transition energy dependent on the vibronic energy state of the nucleus of the active ion as well as its electronic state. This broadening can also be observed in the absorption bands making these ions ideal for pumping with broad-band sources, as sensitisers for other ions [94] and as passive Q-switch elements [95].

Figure 10 illustrates the energy levels of five of these ions. Normally each of the ions

only has one suitable lasing transition. The broad absorption bands in the visible part of the spectrum for each ion can be seen at the top of the diagram, giving each its distinctive colour. The dotted line represents the upper limit of the phonon assisted terminating level for each ion, which normally is very close to the ground level. Therefore these ions are generally three-level systems, with the emission bandwidth decreasing and shifting to longer wavelengths as the gain crystal is heated. Therefore many of these gain crystals are operated well below room temperature in pulsed mode and pumped by flashlights because of the strong visible absorption. For example, flashlamp-pumped Ni:MgF_2 has a threshold of ~100J and wavelength centre of 1.62μm at 22K, has a threshold of 1800J and centre wavelength 1.8μm at 240K [96].

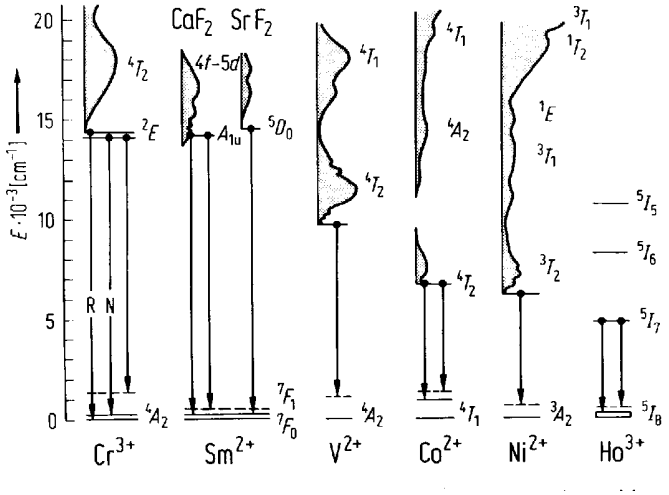

Figure 10 – Transition schemes of phonon-terminated lasers. The dashed lines indicate the position of phonon levels [after 97]

Non-radiative decay processes, which increase with temperature, limit the quantum efficiency of these ions further. For example, the broad upper-state energy levels are prone to excited state absorption because of their greater overlap with higher energy levels. This effect and others can greatly reduce the internal quantum efficiency of the lasing transition at higher temperatures [98].

The broadband emission is however very attractive and much effort has gone into developing suitable systems where these ions can be exploited while minimising the problems highlighted. Cr^{3+} and Ti^{3+} have been the most successful transition metal ions with Ti^{3+} reaching commercial importance through broadly tuneable Ti:sapphire lasers in the near-infrared. Cr^{3+} has come to prominence in more recent years through the development of high power AlGaInP diodes suitable for pumping Cr^{3+} around

670nm [99,100,101]. Cr^{4+} in the form of doped fosterite ($Cr:Mg_2SiO_4$) has helped spearhead this push for room temperature vibronic lasers because of its tuneability from 1130-1367nm when pumped by the 1064nm output of a Nd^{3+} laser and its good lasing performance [102].

The broad emission bandwidth and lower gain of these ions allows effective mode-locking of these lasers with pulses down to several femtoseconds in an all-solid-state design [103,104,105], leading to many interesting and novel applications.

More recently, diode-pumped vibronic microchip lasers have been demonstrated based on Cr:LiSAF [106]. Our own work in St.Andrews has shown these devices have very low thresholds with good output beam quality and emit over a wide wavelength range [107]. Their output power is generally limited by thermal considerations however, making them a niche market for miniature and pulsed laser systems.

With refinement of host materials to provide better thermal management and development of new cavity geometries, vibronic laser materials are set to make a large impact on DPSSL and microchip laser research. Miniature lasers with wide tuning ranges in the infrared and visible spectrum have many potential applications and will be the basis of much new laser research in the next decade.

1.3.2 Rare-Earth-Ion Doped Materials

In contrast, rare-earth ions have narrow transition bandwidths, with limited broadening. Nd^{3+} is the most common rare-earth ion used, though recently there is a resurgence of interest in the other ions, in particular Yb^{3+}, Er^{3+}, Ho^{3+} and Tm^{3+}.

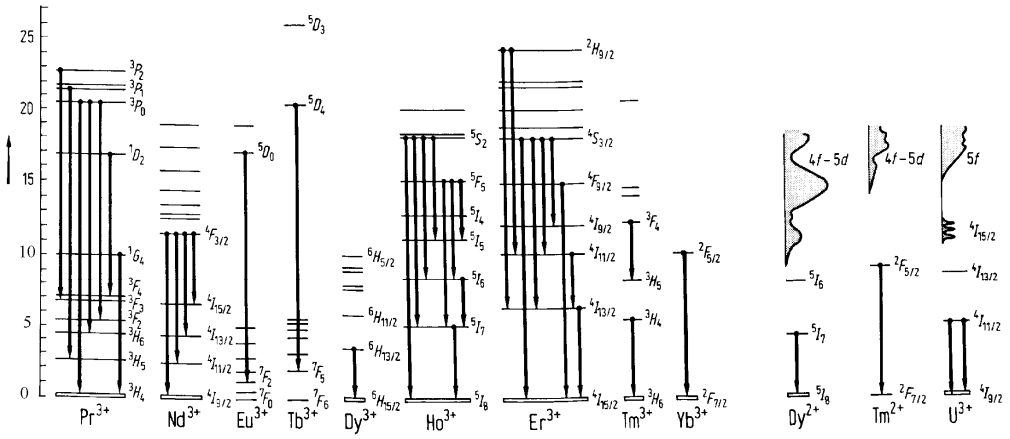

Figure 11 – Operation schemes of crystal lasers that emit on purely electronic transitions [after 97]

The electronic structure of some of the rare-earth ions is illustrated in Figure 11. Typically these ions have a number of photon decay routes from the upper state, providing different terminating conditions and the possibility of many different operating systems, some of which will be discussed later. The upper state lifetime is generally longer for these ions because of the narrower decay routes, though this also usually equates to the benefit of no excited state absorption. The effect of temperature also has much less of an impact and they can be operated under most conditions.

The narrow absorption bands make flashlamp pumping inefficient, however they can be ideal for laser diodes of the correct wavelength, giving efficiencies in excess of 60% [108]. Before the availability of good quality, cheap, high power diodes a lot of work went into broadening the emission and absorption bands of these ions to make them more suitable for the wider band pumping of flash lamps. One approach was to use the splitting of sub-levels of the terminating level in a suitable host to broaden the emission bandwidth of the transition, though this was difficult in practice for some ions.

Work has also gone into the development of disordered hosts, where the active ion occupies a number of different symmetry sites, which broadens the absorption and emission bands of the ion through the different dipole moments created by the different symmetries of the sites. Excitation-energy migration strongly connects the activator centres, giving efficient emission and absorption over a wide band [109].

Laser Ion	Transition	Sensitising Ions
Nd^{3+}	$^4F_{3/2} \rightarrow {}^4I_{11/2}$	Cr^{3+}, Ce^{3+}
Tb^{3+}	$^5D_4 \rightarrow {}^7F_5$	Gd^{3+}
Dy^{3+}	$^6H_{13/2} \rightarrow {}^6H_{15/2}$	Er^{3+}
Ho^{3+}	$^5I_7 \rightarrow {}^5I_8$	Cr^{3+}, Fe^{3+}, Tm^{3+}, Er^{3+}
	$^5S_2 \rightarrow {}^5I_8$	Yb^{3+}
Er^{3+}	$^4S_{3/2} \rightarrow {}^4I_{13/2}$	Ho^{3+}
	$^4I_{13/2} \rightarrow {}^4I_{15/2}$	Yb^{3+}
	$^4F_{9/2} \rightarrow {}^4I_{15/2}$	Yb^{3+}
Tm^{3+}	$^3F_4 \rightarrow {}^3H_5$	Cr^{3+}
	$^3H_4 \rightarrow {}^3H_6$	Cr^{3+}, Er^{3+}
Yb^{3+}	$^2F_{5/2} \rightarrow {}^2F_{7/2}$	Nd^{3+}, Cr^{3+}
Ni^{2+}	$^3T_2 \rightarrow {}^3A_2$	Mn^{2+}

Table 4 Sensitised Laser Crystals [after 97]

Co-doping with a sensitiser or donor ion is another alternative method of improving the efficiency of rare-earth doped laser hosts. Dexter [110] was the first to investigate this excitation-energy transfer and showed the most efficient transfer occurs when the emission spectrum is in resonance with the acceptor absorption spectrum. Many energy transfer schemes have been developed and some of the common ones are listed in Table 4.

The multiple decay routes of the rare-earth ions have led to two distinctive effects being observed, which are not possible in the vibronic laser materials:

1. **Cascade Systems:** Nd^{3+}, Dy^{2+}, Eu^{3+}, Pr^{3+}, Tb^{3+}, Tm^{3+}, U^{3+}, Yb^{3+} ions only have one metastable state. However Er^{3+} has five metastable states and Ho^{3+} has four, which can lead to cascade systems and multiple lasing transitions for a single pump transition. Cascade operation has been observed in Er^{3+}, Pr^{3+}, Er^{3+}:Tm^{3+}, Yb^{3+}:Tm^{3+}, Er^{3+}:Ho^{3+} and Tm^{3+}, allowing visible laser radiation through the up-conversion of infrared pump radiation [97].
2. **Self-Saturating Transitions:** this is where the terminating level has a longer lifetime than the metastable state and normally causes lasing to terminate. Co-doped ions can however act as de-activators allowing transitions which normally will not lase to lase. An alternative method is to artificially remove the population in the lower level by exciting it into a new level. These methods have

allowed a number of transitions, particularly in Er^{3+} and Tm^{3+}, to lase [97].

As can be seen the rare-earth ions have been explored in more detail than transition metal ions because their properties make laser design less stringent. Particular focus has been given to one of the rare-earth ions, the triply ionised neodymium ion, because of its attractive energy level structure and ease of doping.

1.3.2.1 Nd^{3+} Doped Materials

Trivalent neodymium was the first rare-earth ion to be used in a gain material, and has remained the most commonly used active ion found in solid state lasers. The intense luminescence and absorption of the narrow energy levels of Nd^{3+} along with a workable fluorescence lifetime have helped Nd^{3+} achieve its dominance.

The energy level structure of the Nd^{3+} ion is illustrated in Figure 12. It is traditionally pumped on either the 760nm or 810nm absorption bands though it can also be pumped in the green spectral region. The two main photon decay routes from the $^4F_{3/2}$ metastable level are the $^4F_{3/2} \rightarrow {}^4I_{11/2}$ transition (producing radiation at ~1.06μm) and the $^4F_{3/2} \rightarrow {}^4I_{13/2}$ transition (producing radiation at ~1.3μm). Both of these are four level systems, giving efficient CW operation on these transitions at 300K and above, without significant population in the lower lasing level causing reabsorption. The third transition $^4F_{3/2} \rightarrow {}^4I_{9/2}$ (producing radiation at ~0.9μm) is a quasi-four level system, with the lower lasing level close to the ground level, having a significant thermal population. The fourth transition is two orders of magnitude weaker, though has been shown to lase at 1.83μm [111].

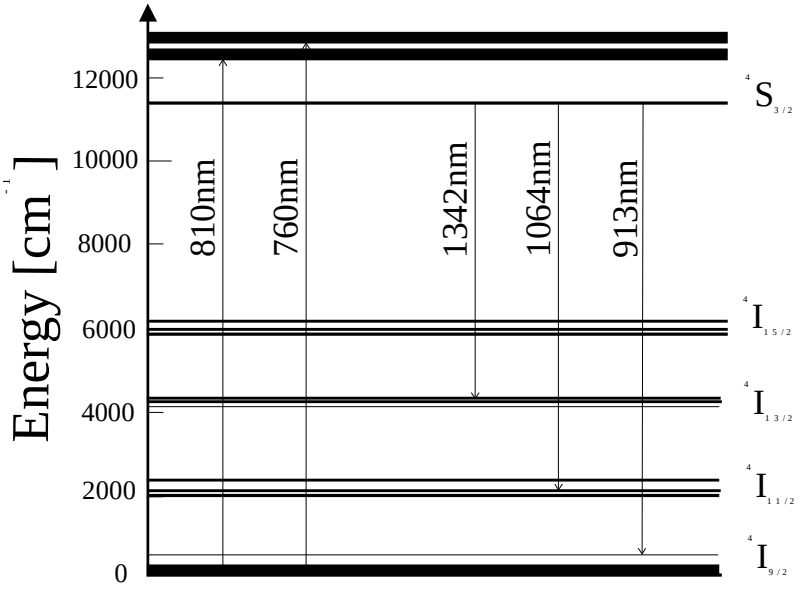

Figure 12 – Energy Levels of Nd^{3+} Ion

A wide range of pump sources have been used to excite the ion, from the more traditional laser diodes, Ti:sapphire laser and argon ion laser, to pyrotechnic sources, solar radiation and electron beams [109].

Table 5 details some of the commonly used crystalline Nd^{3+} hosts and their properties for lasing around 1064nm when pumped by an AlGaAs laser diode. Neodymium has been successfully doped into all the major types of hosts with respectably high concentrations and creditable lasing performance in all cases. Nd:YAG, as mentioned earlier, has good all round characteristics, although other hosts have particular properties which make them more suitable under specific circumstances. For example the broad and intense absorption band of Nd:YVO_4 at 810nm makes diode pumping easier than for Nd:YAG, however its short fluorescence lifetime and large stimulated emission cross-section provide a poorer Q-switched performance.

All of the materials in Table 5 have been shown to lase successfully in a microchip geometry. Further and more in-depth discussion of some of these materials will be given in the next chapter of this thesis, as we seek to compare their performance in a microchip environment.

Nd^{3+} Doped Crystal (Doping Concentration)	**Stimulated Absorption @~810nm $*10^{-19}cm^2$**	**Stimulated Emission (@~1064nm) $*10^{-19}cm^2$**	**Fluorescence Lifetime μs**	**Reference**
Oxides				
Nd:YAG (1.1%)	0.7	3.3	236	[112]
Nd:YOS (1%)	0.99	0.9	240	[113]
Nd:YVO_4 (1%)	2.7	12.2	98	[114]
Nd:$GdVO_4$ (1%)	5.1	7.6	90	[115]
Nd:MgO:$LiNbO_3$ (0.2%)	0.2 $^{cm-1}$	1.8	100	[116]
Nd:LMA (4%)	6.1 cm^{-1}	0.4	160	[117]
Nd:LSB (10%)	0.71	1.3	118	[118]
Fluorides				
Nd:SFAP (1%)	2.26	5.4	298	[119]
Nd:SVAP (1%)	1.8	5	215	[120]
Nd:YLF (1%)	32.1cm^{-1}	1.87	460	[121]

Stoichiometric				
NYAB	5.6 cm^{-1}	10.6	60	[122]
LNP	40 cm^{-1}	3.2	120	[123]

Table 5 Comparison of Common Nd^{3+} Doped Materials

Nd^{3+} lasers will continue to dominate the market because of the mature technology associated with them and because they offer the best lasing performance of any of the rare-earth ions, if wavelength is not a critical factor. Much of the work reported in this thesis is on Nd^{3+} doped materials because of its attractive features and undoubtedly it will remain at the centre of microchip laser work.

1.3.3 Classification of Host Matrices

The matrix in which the active ions are placed can significantly alter the characteristics of the ion. The crystal field into which the ion is placed causes this change and can be crucial to the operating characteristics of the laser. For example, an isotropic crystal has a symmetric field, producing an unpolarised output. Conversely, for anisotropic crystals the asymmetry in the crystal field polarises the ion and emission.

Each ion site in the matrix unit cell will experience a different field, and therefore different emission characteristics. This can be advantageous if you wish to produce a broadened output, but it will also increase non-radiative decay processes and decrease the intensity of the transition.

Solid-state hosts can be divided into three main crystalline types, plus non-crystalline glasses, each with differing characteristics:

1. **Oxides -** oxides are typically grown by the Czochralski method giving high optical purity and big crystals with good yields [124]. Oxides have good thermal and mechanical properties, though one of their major problems is fluorescence quenching which limits the doping concentrations that can be achieved.
2. **Fluorides -** Fluorides are usually grown using the Bridgman technique, which can introduce stress into the crystals, but which can contain the often volatile substances used in the preparation of these crystals [124]. Fluorides suffer less from fluorescence quenching than oxides, though their

thermal and mechanical properties are poorer. Interestingly these crystals usually have negative thermo-optical coefficients.

3. **Stoichiometric Crystals –** in self-activated, or stoichiometric, crystals the active ions are part of the crystal lattice giving much higher ion concentrations than for doping. For doped crystals with high doping concentrations, fluorescence quenching reduces the effective upper-state lifetime of laser ions [125], with the quenching dependent on the square of the concentration of doped ions. For stoichiometric crystals the quenching is linearly dependent on concentration, allowing concentrations up to two orders of magnitude higher [97]. These higher concentrations in turn lead to higher absorption coefficients and higher emission cross-sections and make these materials attractive as microchip gain materials. The first of this class of materials to be demonstrated was NdP_5O_{14} (NPP) which was first end-pumped by a pulsed dye laser [126], but later work with diode lasers showed a lasing threshold of 7mW [127]. LEDs have also been used to end-pump both NPP and LNP [128]. NYAB is an interesting stoichiometric crystal with non-linear properties that allow for self-frequency-doubling and frequency tuning [129]. Approximately ten stoichiometric laser crystals have been demonstrated to date and this number is gradually increasing [97]
4. **Glasses –** although glasses are not crystalline, they are commonly used as the host material for rare-earth ions. In bulk form, the ease of fabrication of doped glasses makes them attractive for high power lasers, where large-scale amplifiers are often required, although the lasing performance of the ion is generally weaker than for crystalline materials [130]. The other commonly used form of glass is fibre, again easily fabricated with the ability to dope it with many active ions. Fibre lasers can be attractive for a whole host of reasons because of the advantages of that particular geometry.

Doping of rare-earth ions into crystalline hosts can take advantage of other host characteristics. Self-frequency doubled lasers [131,132], frequency modulated [133] and amplitude modulated lasers [134] have all been demonstrated using the host crystal's properties. As an example, Er:Yb:$LiNbO_3$ is an attractive material because of

its good non-linear properties and the high doping concentrations of Er^{3+} possible, and its increased sensitisation with Yb^{3+}, makes diode pumping in a microchip format realisable [135,136]. Sequential two-photon absorption can also lead to the generation of green light from these devices using a 980nm diode pump [135].

With these advances in crystal technology, efficient laser diode pumping of many ions is now possible. Nd^{3+} and Yb^{3+} have been successfully pumped by AlGaAs diodes around 810nm and InGaAs diodes at 899nm respectively: Er^{3+} at 790, 980 and 1480nm, Pr^{3+} at 835nm, Tm^{3+} at 800nm and Ho^{3+} at 780nm.

Presently there are more than 280 crystalline hosts in which stimulated emission from rare-earth ions has been observed and this number is increasing by at least two every year [109].

1.4 The Future of DPSSLs

DPSSLs form only a small part of world-wide laser sales, some $53 million out of a total of $2.8 billion per annum. Nevertheless, they represent one of the fastest growing laser markets, with a projected increase in sales of 49% for the coming year [137]. They are beginning to replace lamp-pumped solid state lasers in the lucrative markets of material processing and medicine and to compete with ion gas lasers in the instrumentation, sensing, measuring and optical storage marketplaces.

Important in-roads have been made into a number of diode laser markets, such as telecommunications and optical storage, which account for more than 64% of all laser sales. The main barrier to faster sales and market dominance of DPSSLs is the price of laser diodes compared to flashlamps, though as demand increases this should change.

Diode-pumped solid-state lasers offer a number of key advantages over laser diodes and these help to determine their marketability and applications:

1. **Beam Quality** - The output beam of a DPSSL typically is a close approximation to a circular, diffraction limited, TEM_{00}, beam. In contrast laser diodes, especially higher power diodes, typically have a non-circular, high transverse mode output beam, dependent on the size of the emitting region.
2. **Linewidth** – The linewidth of a high power diode is typically several hundred

gigahertz, which is reduced to several megahertz for diodes designed for telecommunications applications by using distributed feedback. For solid-state lasers, linewidths of several hertz have been achieved by using active feedback and linewidths of tens of kilohertz are readily achievable in passive systems. These outputs, with narrow, stable linewidths can be used in heterodyne interferometers to determine the velocity and direction of liquid flow [138] and in ultrahigh sensitivity Doppler velocimeters and vibrometers [139,140]. The combination of short pulses and narrow line-width are ideal for time domain reflectometry which is used for fault finding in optical links [141].

3. **Output Stability** - The relatively good frequency and amplitude stability of laser diodes manifests itself in an even quieter output from a diode-pumped solid-state laser. For a microchip laser, amplitude noise is typically <1% of the signal, with a frequency stability of tens of megahertz over a minute [142], which makes it a strong contender for many meteorological, inspection and instrumentation applications. A novel application for the detection of ultrasound relies on the distortion of a microchip laser crystal, and hence its output, by an acoustic wave, giving high sensitivity [143].

4. **Peak Power** - Laser diodes are not suitable for high-peak power applications because the short recombination lifetime of holes and electrons (~1ns) prohibit efficient energy storage and the active regions have low damage thresholds (~$MWcm^{-2}$). In contrast the upper state lifetime of active ions can exceed several hundred microseconds making these systems useful for Q-switching and high-power pulsed applications. Indeed, solid-state lasers have produced pulses of less than 10 femtoseconds, and peak powers in excess of a terawatt, which have been used for many applications and in increasing the understanding of many reactions.

5. **Spectral Regions** - Solid-state lasers also offer the possibility of accessing regions of the electromagnetic spectrum where laser diodes or other lasers cannot be operated, in particular the green/blue/UV and the mid-infrared regions of the spectrum. Tm^{3+} doped DPSSLs, with their output around 2μm, have a number of applications from eye-safe laser ranging, to medical applications because the output can be tuned to strong water absorption bands [144]. The frequency

quadrupled output of a Nd:YAG microchip has been used to excite fluorescence in in-situ soil samples to determine concentrations of volatiles and other impurities for pollution monitoring. The combination of TEM_{00} modes operating at shorter wavelengths, for example in the case of frequency doubled microchip lasers, has led to the development of higher density optical storage systems [145,146].

To compete in the existing solid-state laser market, DPSSLs can offer a number of significant advantages over lamp pumped systems:

1. **Efficiency** – Efficiency of DPSSLs, from electrical to optical power, can exceed 15% [147]. These efficiencies can be an order of magnitude greater than those achieved in flashlamp-pumped and gas lasers, leading to other benefits such as the need for less electrical and thermal management and the minimising of deleterious thermal effects.
2. **Active Ions** – The range and efficiency of lasing materials, in particular for rare-earth ions, is enhanced for diode pumping because the pump wavelength can be matched to ionic absorption lines.
3. **Lifetime** - The lifetime of laser diodes can easily exceed 40,000 hours, making diode-pumped lasers more reliable and easier to maintain than rival laser systems [16]. A novel method for high volume production of microchip lasers has been developed by MIT to produce small DPSSLs at very low unit cost [42].
4. **Stability** – The amplitude and frequency stability of a DPSSL is typically a fraction of a percent because of the high stability of the diode pump lasers. In contrast flash lamps can be comparatively noisy, with fluctuations of around one percent. This also translates into the beam pointing instability.
5. **Compactness** – Matching the wavelength of the laser diode to the absorption band of the active ion and pumping in a longitudinal fashion, can lead to miniature systems, beyond the capability of flashlamp pumping. The lower thermal power and increased efficiency decreases the need for space and power consuming peripherals.

All of these advantages of DPSSLs over diode lasers and traditional flashlamp pumped solid-state lasers will help form a stable and increasing market for these devices and provide useful tools for further research.

To conclude this vision of the future of DPSSLs, the number and breadth of applications for DPSSLs and in particular microchip lasers is set to increase matched by an increase in the number of different materials and ions shown to operate as DPSSLs and microchip lasers. This thesis will explore some the advantages of microchip lasers outlined in this introduction, and the basic characteristics and limitations of these devices.

References:

[1] Results of B.I.D.S. search for 'lasers' (1996)

[2] S.G. Anderson, Laser Focus World, **33**, 72 (1997)

[3 A. Penzkofer, Opt. Quant. Elect., **19**, "Topics in Quantum Optics – Solid State Lasers" (1987)

[4] A. Einstein, Mitt. Phys. Ges., **16:18**, 47 (1916)

[5] R. Ladenburg, Rev. Mod. Phys., **5**, 243 (1933)

[6] J. Weber, Trans. IRE. Professional Group on Electron Devices, PGED-3, 1 (1953)

[7] T.H. Mainman, British Comm. & Elect., **7**, 674 (1960)

[8] A. Javan, W.R. Bennett and J. Herriott, Phys. Rev. Lett., **6**, 106 (1961)

[9] Y. Watanabe and W. Nishizawa, Japanese Patent no.273217: "Semiconductor Maser", (1957)

[10] R.N. Hall, G.E. Fenner, J.O. Kingsley, T.J. Soltys and R.O. Carlson, Phys. Rev. Lett., **9**, 366 (1962)

[11] O. Svelto, "Principles of Lasers", (3rd Ed.), Plenum Press, 351 (1989)

[12] P.M. Ripley, Lasers in Med. Sci., **11**, 71 (1996)

[13] H. Kroemer, Proc. IEEE, **51**, 1782 (1963)

[14] I. Hayashi and M.B. Panish, J. Appl. Phys., **41**, 150 (1970)

[15] I. Hayashi, M.B. Panish and P.W. Foy, Appl. Phys. Lett., **17**, 109 (1970)

[16] W. Streifer, D.R. Scifres, G.L. Haragel, D.F. Welch, J. Berger and M. Sakamoto, IEEE J. Quantum Electron., **24:10**, 883 (1988)

[17] SDL Product Catalog 1996/1997

[18] N. Holonyak, R.M. Kolbas and R.M. Dupuis, IEEE J. Quantum Elect., **16**, 170 (1980)

[19] K.D. Choquette and H.Q. Hou, Proc. IEEE, **85:11**, 1730 (1997)

[20] E.J. Lerner, Laser Focus World, **33:2**, 109 (1997)

[21] M.A. Haase, J. Qui, M. Depuydt and H. Vheng, Appl. Phys. Lett., **59:11**, 1272 (1991)

[22] H. Jeon, J. Ding, A.V. Nurmikko, H. Luo, N. Samarth and J. Furdyna, Appl. Phys. Lett., **59:11**, 1293 (1991)

[23] Photonics Spectra, **30:27** (1996)

[24] R. Newman, J. Appl. Phys., **34**, 437 (1963)

[25] R.J. Keyes and T.M. Quist, Appl. Phys. Lett., **4**, 50 (1964)

[26] S.A. Ochs, J.I. Pankove, Proc. IEEE, **56**, 196 (1968)

[27] T.Y. Fan and R.L. Byer, IEEE J. Quantum Elect., **24:6**, 895 (1988)

[28] J.E. Geusic, H.M. Marcos and J.G. van Uitert, Appl. Phys. Lett., **43**, 4603 (1964)

[29] M. Ross, Proc. IEEE, **56**, 196 (1968)

[30] D.W. Hughes and J.R.M. Barr, J. Phys. D: Appl. Phys., **25**, 563 (1992)

[31] D.A. Draegart, IEEE J. Quantum Electron., **9**, 1146 (1973)

[32] L.J. Rosencrantz, J. Appl. Phys. Lett., **43**, 4603 (1973)

[33] J. Stone and C.A. Burrus, Appl. Opt., **13**, 1256 (1974)

[34] C.A. Burrus, J. Stone and A.G. Dentai, Electron. Lett., **12**, 600 (1976)

[35] R.J. Mears, L. Reekie, I.M. Jauncey, S.B. Polle and D.N. Payne, Electron. Lett., **21**, 738 (1985)

[36] D.N. Payne, Fibre and Integrated Optics, **11**, 191-219 (1992)

[37] G.E. Stillman, M.D. Sirkis, J.A. Rossi, M.R. Johnson and N. Holonyak, Appl. Phys. Lett., **9:7**, 268 (1966)

[38] R.B. Chesler and D.A. Draegert, Appl. Phys. Lett., **23:5**, 235 (1973)

[39] D.A. Draegert, IEEE J. Quantum Electron., **9:12**, 1146 (1973)

[40] W.W. Kruhler, R.D. Plattner and W. Stetter, Appl. Phys., **20**, 329 (1979)

[41] T.J. Kane and R.L. Byer, Opt Lett, **10:2**, 65 (1985)

[42] J.J. Zayhowski, Lincoln Lab Journal, **3:3**, 427 (1990)

[43] J.J. Zayhowski, J. Ochoa and A. Mooradian, Opt. Lett., **14:23**, 1318 (1989)

[44] J.J. Zayhowski and A. Mooradian, Opt. Lett., **14:12**, 618 (1989)

[45] J.J. Zayhowski and A. Mooradian, Opt. Lett., **14:1**, 24 (1989)

[46] G.J. Dixon, L.S. Lingvay and R.H. Jarman, IEEE Phot. Tech. Lett., **1:5**, 97 (1989)

[47] G.J. Dixon, L.S. Lingvay and R.H. Jarman, Growth Characterisation and Applications of Laser Host and Nonlinear Crystals, **1104**, 107 (1989)

[48] G.J. Dixon and S.G. Grubb, OSA Tech. Digest Series: CLEO'90, Paper CPDP37-1 (1990)

[49] T. Sasaki, T. Kojima, A. Yokotani, O. Oguri and S. Nakai, Opt. Lett., **16:21**, 1665 (1991)

[50] V. Ostroumov and G. Huber, OSA Tech Digest Series: ECLEO'96, Paper CTuF1 (1996)

[51] D.G. Matthews, R.S. Conroy, B.D. Sinclair, N. MacKinnon, Opt. Lett., **21:3**, 198 (1996)

[52] J.J. Zayhowski, Opt. Lett., **21:8**, 588 (1996)

[53] J.J. Zayhowski,Opt Lett, **16:8**, 575 (1991)

[54] J.J. Zayhowski and C. Dill, Opt. Lett., **17:17**, 1201 (1992)

[55] J.J. Zayhowski and C. Dill, Opt. Lett., **19:18**, 1427 (1994)

[56] J.J. Zayhowski and C. Dill, Opt. Lett., **20:7**, 716 (1995)

[57] B. Braun, F.X. Kartner, G. Zhang, M. Moser and U. Keller, Opt. Lett., **22:6**, 381 (1997)

[58] J.J. Zayhowski and J.A. Keszenheimer, IEEE J. Quantum Electron., **28:4**, 1118 (1992)

[59] J.J. Zayhowski, P.A. Schulz, C. Dill and S.R. Henion, IEEE Photon. Tech. Lett., **5:10**, 1153 (1993)

[60] N. Mermilliod, B. Francois and C. Wyon, Appl. Phys. Lett., **59:27**, 3519 (1991)

[61] N. MacKinnon and B.D. Sinclair, Opt. Comm., **94:4**, 281 (1992)

[62] B. Beier, J.P. Meyn, R. Knappe, K.J. Boller, G. Huber and R. Wallenstein, Appl. Phys. B, **58:5**, 381 (1994)

[63] N. MacKinnon, C.J. Norrie and B.D. Sinclair, **11:3**, 519 (1994)

[64] T. Omatsu, Y. Kato, M. Shimosegawa, A. Hasegawa and I. Ogura, Opt. Comm., **118**, 3-4, 302 (1995)

[65] V.G. Ostroumov, G. Huber, A.I. Zagumennyi, Y.D. Zavartsev, P.A. Studenikin and I.A. Shcherbakov, Opt. Comm., **124**, 1-2, 63 (1996)

[66] D.G. Matthews, J.R. Boon, R.S. Conroy and B.D. Sinclair, J Mod. Opt. , **43:5**, 1079 (1996)

[67] N. Faure, C. Borel, M. Couchaud, G. Basset, R. Templier, C. Wyon, Appl. Phys. B, **63:6**, 593 (1996)

[68] M.R. Dickson, L.A.W. Gloster, N.W. Hopps and T.A. King, Opt. Comm., **132**, 275 (1996)

[69] P. Laporta, S. Taccheo, S. Longhi, O. Svelto and G. Sacchi, Opt. Lett., **18:15**, 1232 (1993)

[70] C.A. He and D.K. Killinger, Opt. Lett., **19:6**, 396 (1994)

[71] V.E. Hartwell, H. Nakajima and N. Djeu, Opt. Lett., **20:21**, 2210 (1995)

[72] M. Storm and W.W. Rohrbach, Appl. Opt., **28:23**, 4965 (1989)

[73] J.M. Sutherland, S. Ruan, R. Mellish, P.M.W. French, J.R. Taylor, Opt. Comm., **113**, 4-6, 458 (1995)

[74] H. Saito, S. Chaddha, R.S.F. Chang and N. Djeu, Opt. Lett., **17:3**, 189 (1992)

[75] C. Hauglie-Hanssen and N. Djeu, IEEE J. Quantum Electron., **30:2**, 275 (1994)

[76] J.J. Zayhowski, J. Harrison, C. Dill and J. Ochoa, Appl. Opt., **34:3**, 435 (1995)

[77] R. Waarts, D. Nam, S. Sanders, J. Harrison and B.J. Dinerman, Opt. Lett., **19:21**, 1738 (1994)

[78] D.J. Ehrlich, P.F. Moulton, R.M. Osgood, Opt. Lett., **4**, 184 (1979)

[79] D.M. Rines, P.F. Moulton, D. Welford and G.A. Rines, Opt. Lett., **19:9**, 628

(1994)

[80] R.H. Page, K.I. Schaffers, L.D. DeLoach, G.D. Wilke, F.D. Patel, J.B. Tassano, S.A. Payne, W.F. Krupke, K.T. Chen and A. Burger, IEEE J. Quantum Electron., **33:4**, 609 (1997)

[81] S.A. Payne, L.L. Chase, L.K. Smith, W.L. Kway and H.W. Newkirk, J. Appl. Phys., **66**, 1051 (1989)

[82] Data-sheet for Fosterite (Olivin), Uni-Export Instruments Ltd (1996)

[83] R.J. Pressley and J.P. Wittke, IEEE J. Quantum Electron., **3**, 116 (1967)

[84] N.C. Chang, J. Appl. Phys., **34**, 3500 (1963)

[85] J.K. Neeland and V. Evtuhov, Phys. Rev., **156:2**, 244 (1967)

[86] L.D. DeLoach, R.H. Page, G.D. Wilke, S.A. Payne and W.F. Krupke, IEEE J. Quantum Electron., **32:6**, 885 (1996)

[87] T. Sandrock, T. Danger, E. Heumann, G. Huber and B.H.T. Chai, Appl. Phys. B, **58:2**, 149 (1994)

[88] J.K. Lawson and S.A. Payne, J. Opt. Soc. Am. B, **8:7**, 1404 (1991)

[89] W.R. Rapoportand C.P. Khattak, Appl. Opt., **27**, 2677 (1988)

[90] J.P. Wittke, Z.J. Kiss, R.C. Duncan and J.J. McCormick, Proc. IEEE, **51**, 56 (1962)

[91] L.F. Johnson, H.J. Guggenheim and R.A. Thomas, Phys. Rev., **149**, 179 (1966)

[92] L.D. DeLoach, S.A. Payne, L.K. Smith, W.L. Kway and W.F. Krupke, J. Opt. Soc. Am. B, **11:2**, 269 (1994)

[93] L.F. Johnson, R.E. Dietz and H.J. Guggenheim, Phys. Rev. Lett., **11**, 318 (1963)

[94] M. Tempus, W. Luthy, H.P. Weber, V. Ostroumov, I.A. Shcherbakov, IEEE J. Quantum Electron., **30:11**, 2608 (1994)

[95] E. Munin, A.B. Villaverde, X.X. Zhang and M. Bass, Appl. Phys. Lett., **63:13**, 1739 (1993)

[96] L.F. Johnson, H.J. Guggenheim and R.A. Thomas, Phys. Rev., **149**, 179 (1966)

[97] A.A. Kaminskii, "Laser Crystals" (2^{nd} Ed), Springer-Verlag (1990)

[98] P.F. Moulton, IEEE J. Qunatum Electron., **18:8**, 1185 (1982)

[99] R. Scheps, IEEE Photon. Tech. Lett., **4:6**, 548 (1992)

[100] P.M.W. French, R. Mellish, J.R. Taylor, P.J. Delfyett and L.T. Florez, Opt. Lett., **18:22**, 1934 (1993)

[101] M.J.P. Dymott and A.I. Ferguson, Opt. Lett., **19:23**, 1988 (1994)

[102] T. Fujii, M. Nagano and K. Memoto, IEEE J. Quantum Electron., **32:8**, 1497 (1996)

[103] F. Falcoz, F. Balembois, P. Georges and B. Bruin, Opt. Lett., **20:18**, 1874 (1995)

[104] P.F. Curley, C. Spielmann, T. Brabec, F. Krausz, E. Wintner and A.J. Schmidt, Opt. Lett., **18:1**, 54 (1993)

[105] P.F. Moulton, IEEE J. Qunatum Electron., **18:8**, 1185 (1982)

[106] J.M. Sutherland, S. Ruan, R. Mellish, P.M.W. French, J.R. Taylor, Opt. Comm., **113**, 458 (1995)

[107] R. S. Conroy, D.G. Matthews and B.D. Sinclair, Private Communication

[108] M.R. Dickinson, L.A.W. Gloster, N.W. Hopps, T.A. King, Opt. Comm., **132**, 275 (1996)

[109] A.A. Kaminskii, Phys. Stat. Sol. (A), **148**, 9 (1995)

[110] D.L. Dexter, J. Chem. Phys., **21**, 836 (1953)

[111] T.S. Kubo and T.J. Kane, J. Quantum Electron., **28:4**, 1033 (1992)

[112] J.K. Neelnd, V. Evtuhov, Phys. Rev., **156:2**, 244 (1967)

[113] B. Comaskey, G.F. Albercht, S.P. Velsko and B.D. Moran, Appl. Opt., **33:27**, 6377 (1994)

[114] D. Tucker, J. Appl. Phys., **48:12**, 417 (1977)

[115] J.P. Meyn, T. Jensen and G. Huber, IEEE J. Quantum Electron., **30:4**, 913 (1994)

[116] T.Y. Fan, A. Cordova-Plaza, M.J. Digonnet, R.L. Byer and H.J. Shaw, J. Opt. Soc. Am. B, **3:1**, 140 (1986)

[117] N. Mermilliod, B. Francois and C.H. Wyon, Appl. Phys. Lett., **59:27**, 3519 (1991)

[118] J.P. Meyn, T. Jensen and G. Huber, IEEE J. Quantum Electron., **30:4**, 913 (1994)

[119] X.X. Zhang, P. Hong, G. Loutts, J. Lefaucheur, M. Bass and B.H.T. Chai, Appl. Phys. Lett., **64:24**, 3205 (1994)

[120] B.H.T. Chai, G. Loutts, J. Lefaucheur, X.X. Zhang, P. Hong and M. Bass, OSA Proc. on ASSL, **20**, 41 (1994)

[121] ITI Electro-Optics Data-Sheet (1996)

[122] T. Zhao, Z. Luo, Y. Huang, M. Qio and G. Chen, Opt. Comm., **109**, 115 (1994)

[123] W.W. Kruhler, R.D. Plattner and W. Stetter, Appl. Phys., **20**, 329 (1979)

[124] G. Huber, "Laser Sources and Applications", Proc. of 47th SUSSP, 141-162 (1996)

[125] H.G. Danielmeyer and M. Blatte, Appl. Phys., **1**, 269 (1973)

[126] H.P. Weber, T.C. Damen, H.G. Danielmeyer, B.C. Tofield, Appl. Phys. Lett., **22**, 534 (1973)

[127] S.R. Chinn, J.W. Pierce and H. Heckscher, IEEE J. Qunatum Electron., **11**, 747 (1975)

[128] M. Saruwatari and T. Kimura, IEEE J. Quantum Electron., **12**, 584 (1976)

[129] Y.F. Chen, S.C. Wang, C.F. Kao, T.M. Huang, IEEE Phot. Tech. Lett., **8:10**, 1313 (1996)

[130] W. Koechner, "Solid-State Laser Engineering" (3rd Ed.), Springer-Verlag (1992)

[131] L.F. Johnson and A.A. Ballman, J. Appl. Phys., **40**, 297 (1969)

[132] J.K. Yamamoto, A. Sugimoto and K. Yamagishi, Opt. Lett., **19:17**, 1311 (1994)

[133] N. MacKinnon, C.J. Norrie and B.D. Sinclair, J. Opt. Soc. Am. B, **11:3**, 519 (1994)

[134] A. Cordova-Plaza and M.J.F. Digonnet, J. Opt. Soc. Am. A, **2:13**, 44 (1985)

[135] J.J. Ju, T.Y. Kwon, S.I. Yun, M. Cha and H.J. Seo, Appl. Phys. Lett., **69:10**, 1358 (1996)

[136] L. Nunez, G. Lifante, F. Cusso, Appl. Phys. B, **62**, 485 (1996)

[137] S.G. Anderson, Laser Focus World, **33:1**, 72 (1997)

[138] J. Czarske and H. Muller, Electron. Lett., **30:12**, 970 (1994)

[139] K. Otsuka, Appl. Opt., **33:6**, 1111 (1994)

[140] J.W. Czarske and H. Mueller, Opt. Comm., **114**, 223 (1995)

[141] J.M. Senior, "Optical Fibre Communications" (2nd Ed), Prentice Hall International Series in Optoelectronics

[142] R.S. Conroy, D.G. Matthews, N. MacKinnon and B.D. Sinclair, OSA Tech. Digest ECLEO'96, Paper CFH1 (1996)

[143] A.R. Duggal, C.P. Yakymyshyn, D.F. Fobare and D.C. Hurley, Opt. Lett., **19:10**, 755 (1994)

[144] J.D. Kmetec, T.S. Kubo, T.J. Kane and C.J. Grund, Opt. Lett., **19:3**, 186 (1994)

[145] M. Oka and S. Kubota, Japanese J. Appl. Phys., **31**, 513 (1992)

[146] N. Eguchi and Y. Akiyama, Japanese J. Appl. Phys., **32**, 5307 (1993)

[147] R.A. Fields, M. Birnbaum and C.L. Fincher, OSA Tech. Digest CLEO'88, Paper PD3 (1988)

Chapter 2 - DIODE-PUMPING OF MONOLITHIC Nd^{3+} MICROCHIP LASERS

2.1 Introduction

This chapter examines and compares the diode-pumped performance of a number of materials doped with triply-ionised neodymium and coated with dielectric mirrors on two near parallel surfaces to form monolithic microchip lasers. The gain materials examined here have all previously been shown to be efficient gain materials for large frame lasers with a range of operating characteristics. Here we report the first operation of many of these gain materials as monolithic microchip lasers.

Neodymium ions are the most commonly used rare earth ions in solid-state laser materials because of their strong luminescence when pumped in the visible or near infrared. The 780nm and 810nm absorption bands are particularly attractive for pumping with AlGaAs laser diodes and can give efficient lasing operation from the transitions around 946, 1064 and 1320nm.

Monolithic lasers are the most basic form of laser and attractive for a number of reasons; primarily because there are no internal surfaces to provide additional loss and no cavity alignment problems. The simplicity of these devices can lead to low unit cost manufacturing, making them highly competitive with other laser technology.

The extremely short laser cavity length of a microchip laser (<1mm) provides a highly compact source of coherent and potentially single mode radiation. Thermal and gain effects, described in more detail in the next chapter, can define a single transverse mode. In addition, the large free spectral range of the cavity can lead only to only one cavity mode within the gain bandwidth, giving a single longitudinal mode output.

This chapter will begin with a review and characterisation of the range of gain materials to be examined: Nd:YVO_4, Nd:SFAP, Nd:YOS and Nd:SVAP. The CW lasing performance of these materials in the form of monolithic microchip lasers is then investigated and compared. Intensity modulation, in the form of gain switching, is considered as a method of generating short pulses from these lasers, and the chapter concludes by looking at their frequency tuning.

2.2 Material Characterisation

2.2.1 Introduction

As described in Chapter 1, the lasing properties of solid-state laser materials are derived primarily from the electronic structure of the active ion. The lattice into which these ions are placed has a secondary effect on the electronic structure, causing splitting, broadening and shifting of the energy levels.

We will begin this section by looking at the energy level structure of the Nd^{3+} ion and then move to consider how its structure can be modified when doped into a range of crystalline hosts. The development of the hosts used in this work will then be described, with an indication of their most attractive features.

2.2.1.1 Nd^{3+} Ion Properties

The most common lasing schemes for materials doped with triply ionised neodymium ions are shown in Figure 13. Nd^{3+} ions in the ground state can be excited by pump sources in the near-infrared, for example AlGaAs laser diodes, to either the $^4S_{7/2}$ (~760-780nm) or $^4S_{5/2}$ (~795-815nm) energy levels. Fast (~0.1ns), non-radiative decay then takes place from these levels to the metastable $^4S_{3/2}$ level. The lifetime of electrons in this metastable state varies according to host and doping density; however it is typically of the order of 30-500μs.

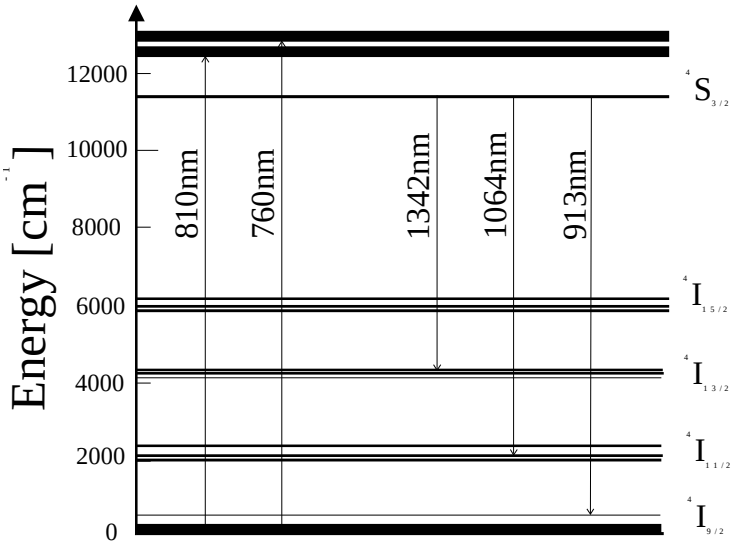

Figure 13 - Energy Levels of Nd^{3+} ion in Nd:YVO_4. The two most commonly used absorption bands are at 760nm and 810nm, with the three most prominent emission lines at 1342nm, 1064nm and 913nm.

Four radiative decays are possible from the $^4S_{3/2}$ level: giving fluorescence at approximately 940nm, 1064nm, 1342nm and 1820nm corresponding to terminating levels $^4I_{9/2}$, $^4I_{11/2}$, $^4I_{13/2}$ and $^4I_{15/2}$ respectively. There is then a further fast phonon relaxation from the terminating level back to the ground state, completing the cycle.

If thermal electrons do not heavily populate the terminating level, then stimulated emission is possible when pumping induces a population inversion. The narrow, intense absorption and emission lines of Nd^{3+} ions give rise to moderately large absorption and stimulated emission cross-sections, of the order of $1\text{-}10x10^{-19}cm^2$ in each case, promoting efficient lasing. In crystalline materials the fluorescence efficiency from the metastable state is typically greater than 99.5% [148]. This indicates that excited state absorption (ESA) from the $^4S_{3/2}$ level is not a significant problem in Nd^{3+} doped crystals, and again enhances the efficiency and ease of operation.

The 1064nm transition was the first transition shown to lase [149]. It is the most commonly exploited transition because of its four level nature and the highest branching efficiency from the $^4S_{3/2}$ metastable level (~0.5) [150]. It has become the standard workhorse of many high-power laser systems with innumerable applications.

The second most probable transition radiates at 1320nm. It has a branching efficiency that varies dramatically with host material. For example in Nd:YVO_4 the branching ratio is 42.2%, whereas in Nd:YAG it is 25% [150]. Slope efficiencies and thresholds similar to the 1064nm transition have been shown in materials with high branching efficiencies for this transition [151], though applications are not as numerous.

The third transition lasing at 940nm terminates on the upper sub-level of the ground state, giving quasi four-level lasing operation. Cooling the crystal reduces the thermal population in the upper sub-level, decreasing reabsorption losses and lowering the threshold. The splitting of the $^4I_{9/2}$ level is the main factor in determining the lasing performance of this transition. For example in Nd:YAG the upper sub-level is $848cm^{-1}$ above the ground level and the transition will operate with 33% slope efficiency at room temperature [152]. However in Nd:YVO_4 the upper sub-level is $245cm^{-1}$ above the ground level and so the transition barely reaches threshold [153].

The branching ratio for the fourth and final transition is approximately one

hundredth that of the 1064nm transition, giving a very small stimulated emission cross-section. Although this transition has been shown to lase at 1833nm in Nd:YAG below room temperature [154], this transition is generally ignored because other active ions (e.g. Tm^{3+}) have more intense transitions in the same spectral region.

Although these are the four main radiative transitions from the $^4S_{3/2}$ level, transitions to different terminating sub-levels can be made to lase by the use of wavelength selective elements, such as tunable etalons. To date more than 20 transitions have been shown to lase in Nd:YAG in this way [155,156,157].

2.2.1.2 **Development of Nd:YVO_4, Nd:SFAP, Nd:YOS and Nd:SVAP**

The work in this chapter is concerned with the characterising of four Nd^{3+} doped crystals: Nd:YVO_4, Nd:YOS, Nd:SFAP and Nd:SVAP. Each of these hosts modifies the characteristics of the doped Nd^{3+} ions according to the crystal field of the dopant site. We will consider the differing properties of these laser materials after a brief historical overview of the development of each of the hosts.

The crystal structure of yttrium orthovanadate (YVO_4) was first experimentally measured in 1933 by Broch [158] and later used as a host for Eu^{3+}, giving very efficient red-emitting phosphors used in colour televisions [159]. In 1965 the first growth of large crystals of Nd:YVO_4 for use as laser crystals was carried out by Rubins and Van Uitert who also reported the successful lasing of Tm:YVO_4 [160]. A year later O'Connor demonstrated efficient laser action in Nd:YVO_4 attributed to the small Stark splitting of the lasing levels [161]. Phonon assisted energy transfer between the lattice and Nd^{3+} ions was also inferred from fluorescence measurements, which is important in considerations of gain migration and efficiency.

Problems with growing good quality crystals hampered further development of Nd:YVO_4 as a laser material until the late 1980's. However some important spectroscopic work was carried out in the mid-1970's [162,163,164], recognising the that emission cross-sections at 1064nm and 1342nm were many times those of Nd:YAG. The development of reliable, high power laser diodes in the 1980's lead to the first demonstration of an efficient, end-pumped Nd:YVO_4 laser in 1987 [165]. Monolithic Nd:YVO_4 microchip lasers have been shown to have low thresholds (~5mW) and high slope efficiencies (57%) with single frequency operation (~100mW tuned over 107GHz) [166].

Nd:SVAP (Nd:$Sr_5(VO_4)_3F$) and Nd:SFAP (Nd:$Sr_5(PO_4)_3F$) are both fluoroapatite compounds with the chemical formula $A_{10}(BO_4)_6F_2$ where A=Sr, Ca etc. and B=P, V etc. Apatite crystals were shown to be efficient hosts for rare-earth ions with flashlamp pumping in 1968 [167], but the combination of poor thermal properties and difficulties in crystal growth meant little attention was paid to them until the early 1990's when efficient laser diodes became available. Bruce Chai and his group at CREOL, Florida, have led the resurgence of interest in these materials, examining their structure and lasing properties [168,169,170,171,172].

The main difference between Nd:SFAP and Nd:SVAP is the sites occupied by the Nd^{3+} ions; in Nd:SFAP the ions occupy one site, but in Nd:SVAP a number of different sites can be occupied, which normally limits efficiency. However efficient energy transfer from ions in these multiple sites to the metastable upper laser level of one site can occur giving good laser performance. Nd:SVAP is the easier crystal to grow with lower intrinsic loss and higher yield, but the maximum Nd^{3+} doping concentration of both crystals is limited by fluorescence quenching [173]. SFAP has recently been shown to be a good host for Yb^{3+} ions pumped at 899nm and lasing at 1047nm with slope efficiencies of 78% and the possibility of short pulses [174].

The final crystal examined is the disordered oxide host, neodymium doped yttrium orthosilicate (Nd:Y_2SiO_5 or Nd:YOS). Kaminskii and his group in Moscow demonstrated emission at 1074nm and 1358nm from Nd:YOS with flashlamp pumping in 1973, with further spectroscopic work in 1976 [175]. Nd:YOS is an unusual gain material in that it is a positive biaxial crystal with a complicated structure and it has a greater absorption cross-section than emission cross-section. This is a characteristic of ground-state depleted (GSD) lasers [176], where a very large fraction of the ions can be pumped into the metastable state, giving efficient energy storage for Q-switching, or reducing reabsorption losses for laser transitions terminating near the ground level. Correspondingly, efficient Q-switched operation of the 912nm transition has been demonstrated based on Nd:YOS [177]. As with the other crystals, Nd:YOS is normally grown using the Czochralski method but it has relatively poor mechanical and thermal properties for an oxide.

2.2.1.3 Characteristics of Nd:YVO_4, Nd:SFAP, Nd:YOS and Nd:SVAP

Table 6 overleaf details some of the important optical and physical properties of the

gain materials used in this chapter with Nd:YAG added for comparison.

Nd^{3+} Host Material:	YAG	YVO_4	YOS	SFAP	SVAP
Thermal / Optical Properties					
Crystal Class	Isotropic	Uniaxial	Biaxial	Uniaxial	Uniaxial
Refractive Index	1.84	1.958σ 2.168e	1.772x 1.773y 1.793z	1.6314σ 1.6252e	1.824σ 1.809e
dn/dT (*10^{-6}/°C)	+7.3	+3/+8.5	+3.5	negative	-11/-8
Thermal Cond. (W/m.K)	13	5.1	4.5	2.0	1.7
Absorption / Emission Properties					
Emission X-section σ_{em} (*10^{-19} cm^2)	3.3	15.6	0.9	5.4	5
Emission Lifetime τ_{em} (μs) [low conc.]	240	115	250	298	215
$\sigma_{em}\tau_{em}$(*10^{-17}μs.cm^2)	7.92	17.9	2.25	16.2	10.8
Abs.X-section 810nm σ_{abs} (*$10^{-19}$$cm^2$)	0.7	2.7	0.99	2.26	1.8
λ (pump) nm	808.7	808.5	808.9	805.2	809.6
Δλ (pump) nm	0.8	1.7	1.6-2.4	1.6	1.6
λ (laser) nm	1064	1064.3	1074	1058.5	1065
Δλ (laser) nm	0.7	1.3	1.75	0.6	1.4
Measured Properties					
Nominal Size /mm	-	5x5x0.5	3x3x0.4	3x3x0.35	3x3x0.5
Length /mm	-	0.52	0.41	0.32	0.53
Doping Conc. (% At.)	-	3	0.7	0.71	0.75
Output Coupling (%)	-	1,5,10	1	2	1

Table 6 - Physical and Optical Properties of Laser Materials [after 178]

As can be seen, Nd:YAG, Nd:YVO_4, Nd:YOS, Nd:SVAP and Nd:SFAP offer quite different operating characteristics, although all have previously been shown to be efficient laser hosts. Nd:YAG in an isotropic crystal with good thermal and mechanical properties, making it the most suitable material for higher power work. Its absorption around 810nm is however quite weak and narrow band, placing limitations on diode pumping, in particular wavelength control of the pump light. The narrow emission band offsets this disadvantage in that longer cavities can be used before the free spectral range is comparable to the gain bandwidth. The relatively long upper

state lifetime is attractive for Q-switching and gives Nd:YAG an average $\sigma\tau$ figure of merit.

In contrast, Nd:YVO_4 is more suited to microchip geometries. Its broad and strong absorption at 810nm allows easy diode pumping of thin crystals (<1mm). Doping concentrations of up to 3% are possible, giving absorption coefficients in excess of $10mm^{-1}$, however further sacrificing the upper-state lifetime through increased fluorescence quenching. The relatively short lifetime and large emission cross-section would limit the Q-switched operation of these devices to lower peak powers at high repetition rates.

Nevertheless the large stimulated emission cross-section of Nd:YVO_4 does give low thresholds and the possibility of larger output couplings to promote single frequency operation. Unfortunately the broad emission spectrum limits inherent single frequency operation to crystals less than 0.2mm long. For an oxide, Nd:YVO_4 exhibits poor thermal properties which limit its application to larger laser systems and introduces concern about thermal constraints. The uniaxial crystal structure does however give a strongly polarised output in contrast to the unpolarised output of Nd:YAG. Overall Nd:YVO_4 has the highest figure of merit with the most suitable characteristics for diode-pumped microchip lasers.

The second oxide examined, Nd:YOS, has similar thermal and mechanical characteristics to Nd:YVO_4. The biaxial nature introduces a complicated range of operating possibilities depending on crystal orientation. The output is however always polarised. The long upper state lifetime and the low stimulated emission cross-section make Nd:YOS more attractive for Q-switching than CW operation. This is compounded by a larger absorption cross-section than emission cross-section. Nd:YOS has the lowest figure of merit and therefore was expected to be the most difficult to operate.

The apaptites, Nd:SFAP and Nd:SVAP have similar thermal and mechanical properties. The strong negative change in refractive index with temperature is in contrast to the positive change for the oxides and affects the cavity stability of these materials. Nd:SFAP is the more attractive of the two materials, because of the wide, strong absorption band at 810nm and the narrow emission bands at 1058.5nm, making it well suited to diode pumping and a microchip geometry. The long upper state

lifetimes of both materials make Q-switching attractive, in particular for Nd:SFAP. In conclusion, the figure of merit for Nd:SFAP is close to that of Nd:YVO_4 and is expected to operate in a similar way, with Nd:SVAP slightly more difficult to use.

The Nd:YVO_4 crystals used for this work were purchased from Casix and coated by Laseroptik for either 1064nm or 1342nm operation. The Nd:YOS, Nd:SFAP and Nd:SVAP crystals were provided by CREOL and coated by Virgo Optics.

The pumping laser diodes used were from the SDL-2350 range; a 0.5W diode with emitting dimensions of 50x1μm or a 1.2W diode with a 100x1μm active region. The spectral width of the output of these diodes is around 2nm with tunability from 802-812nm by varying the temperature of the thermoelectric cooler. The output of the diodes was collimated using an 8mm lens and focused using a 6.5, 8, or 14.5mm Melles Griot lens.

2.2.2 Absorption Characteristics

The absorption band of the $^4S_{5/2}$ energy level of Nd^{3+}, typically around 810nm, can be easily accessed by these AlGaAs diodes. The wavelength of a 0.5W laser diode was tuned, using its thermoelectric cooler, to measure the absorption properties of each of our materials from 802-812nm. The crystals used were at room temperature and uncoated, with allowance made for surface reflectivities. In each case the crystal was orientated to measure the absorption along the axis with the most intense absorption.

Figure 14 illustrates the absorption coefficient measured for each material over the operating range of the laser diode. The absorption coefficient for Nd:YVO_4 is much greater than the other materials because it is doped with 3% Nd^{3+}, in contrast to the other materials with nominally 1% doping. This is highlighted by Nd:SFAP which has an equivalent absorption coefficient to a crystal of Nd:YVO_4 with the same doping concentration and dimensions.

The low absorption coefficients of Nd:YOS and Nd:SFAP, combined with their short length meant that at the optimum pump wavelength only 37% and 49% of the pump power was absorbed respectively. In contrast the Nd:YVO_4 crystal absorbed more than 95% of the incident pump power. In the case of Nd:SVAP the broad absorption is attributed to absorption of the diode radiation by dopant ions in multiple

sites.

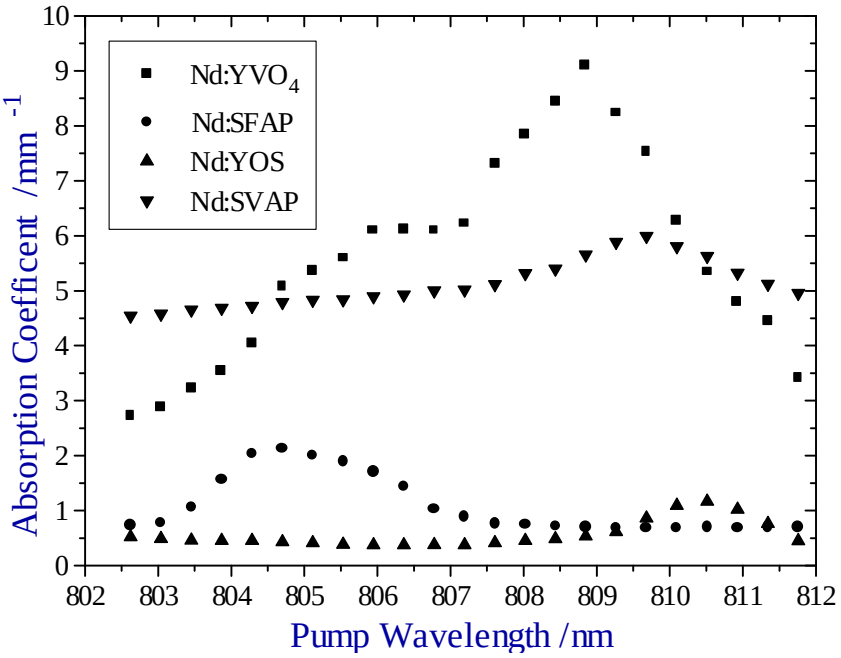

Figure 14 - Absorption coefficient of Nd:YVO_4, Nd:SFAP, Nd:YOS and Nd:SVAP measured from 802-812nm using 0.5W laser diode ($\Delta\lambda$=2nm).

The height and width of the absorption peaks in Figure 14 differ slightly from those quoted in Table 6. This is primarily because of the 2nm spectral width of the laser diode used to take the measurements in Figure 14 and the wavelength uncertainty associated with the optical spectrum analyser used (Anritsu MS96). The use of a laser diode generally diminishes, but broadens the absorption characteristics. For example, the Nd:YVO_4 crystal has an absorption coefficient of 11.2mm^{-1} when pumped by a correctly tuned Ti:sapphire laser and an absorption bandwidth of 1.7nm, in contrast to the 9.1mm^{-1} and 6.5nm for diode pumping.

For the remaining work in this thesis, the wavelength of the pumping laser diode was tuned to the peak absorption of the material being used. In the case of Nd:YOS this required the laser diode to be operating substantially below room temperature (~-2^{o}C), causing concern about condensation. The other materials all operated with the laser diode above room temperature.

2.2.3 Fluorescence Characteristics

The fluorescence excited in these uncoated crystals by the 0.5W laser diode was also examined using the optical spectrum analyser, with a resolution of 0.lnm. No

splitting, or additional fluorescence lines were recorded around the $^4S_{3/2}$ to $^4I_{11/2}$ (1064nm) transition for any of the crystals examined to within 20dB of the peak fluorescence. This indicates the Stark splitting of the transition levels is weak and should not inhibit the lasing performance of any of the materials. Fluorescence around 1320nm was also observed for Nd:YVO_4, Nd:SFAP and Nd:SVAP, but not for Nd:YOS. The 940nm and 1820nm transitions were not examined.

Crystal	Centre of Fluorescence /nm	FWHM of Fluorescence /nm	Fluorescence Lifetime /μs
Nd:YVO_4	1064.0 1342.1	0.68 0.66	55
Nd:YOS	1073.9	1.5	525
Nd:SFAP	1059.0 1328.2	0.9 0.85	427
Nd:SVAP	1065.6 1338.7	1.1 1.3	333

Table 7 – Measured fluorescence characteristics of Nd:YVO_4, Nd:SFAP, Nd:YOS and Nd:SVAP at room temperature with 400mW incident power from a 0.5W laser diode.

Table 7 shows how the crystal field of the host can modify the properties of doped Nd^{3+} ions. The lifetime of the fluorescence from the ions was measured by modulating the laser diode pump power (fall time <2μs) and recording the decay of the fluorescence using a fast photodiode.

Further work has shown the fluorescence of the 1064nm transition in Nd:YVO_4 to behave in unexpected ways. Experimental work has shown both an increase (~20%) in lifetime with temperature ($\Delta T=20^oC$) and a non-exponential decay rate. These effects are attributed to a decrease in fluorescence quenching and intensity dependent effects, however no attempt was made to take this work further for this thesis.

The measured upper-state lifetimes in Table 7 are different from the lifetimes quoted in Table 6. As mentioned earlier the lifetime varies strongly as a function of doping concentration and the figures quoted in Table 6 are for 1% doped materials in the case of Nd:SVAP, Nd:SFAP and Nd:YOS and 3% in the case of Nd:YVO_4. The former three materials have doping concentrations less than one percent and therefore would be expected to have longer lifetimes, as was observed. The dramatic increase in lifetime of Nd:YOS is attributed to a lower doping concentration than nominally

attributed to it from the melt composition.

2.3 Lasing Characteristics

In the previous section the basic optical and mechanical properties of Nd:YVO_4, Nd:YOS, Nd:SFAP and Nd:SVAP were described, with an overview of the properties which make them attractive as the gain material in a monolithic microchip laser. This section will now consider the CW lasing characteristics of these materials with laser diode pumping. We will begin by comparing these four gain materials and then move to considering the 1064nm and 1342nm transitions of Nd:YVO_4 in more detail.

2.3.1 Comparison of Lasing Performance of Nd^{3+} Doped Materials

The CW lasing performance of monolithic Nd:YVO_4, Nd:SFAP, Nd:YOS and Nd:SVAP microchip lasers was characterised for pumping by a 0.5W and 1.2W laser diodes. The nominal properties of these lasers are listed in Table 6. The rear surface of each crystal was coated to be anti-reflecting at the pump wavelength and highly reflecting at the signal wavelength. The opposite surface of each crystal was coated for an output coupling, listed in Table 6, forming the microchip cavity.

These crystals were then mounted on brass rings, which acted as heat sinks and pumped with either a 0.5W (50x1μm emitter) or 1.2W (100x1μm emitter) laser diode through an 8mm collimating lens, and 8mm focussing lens. This gave up to approximately 450mW and 1.1W of pump power respectively, incident on the crystals. There was no attempt made to ‘shape’ the pump beam to provide a more symmetric pump spot, or to double pass the pump light. The approximate pump spot sizes in each case were 30x100μm and 60x160μm.

The diode was tuned to the maximum absorption for each crystal and a low power absorption measurement taken to calculate the absorbed power for each crystal. The Nd:YVO_4 and Nd:SVAP absorbed 98% and 94% of the pump light respectively. Approximately half the pump power was absorbed by the Nd:SFAP crystals and a third by the Nd:YOS crystals.

The measured thresholds and slope efficiencies for all the monolithic microchip lasers examined are illustrated in Figure 15 and tabulated in Table 8.

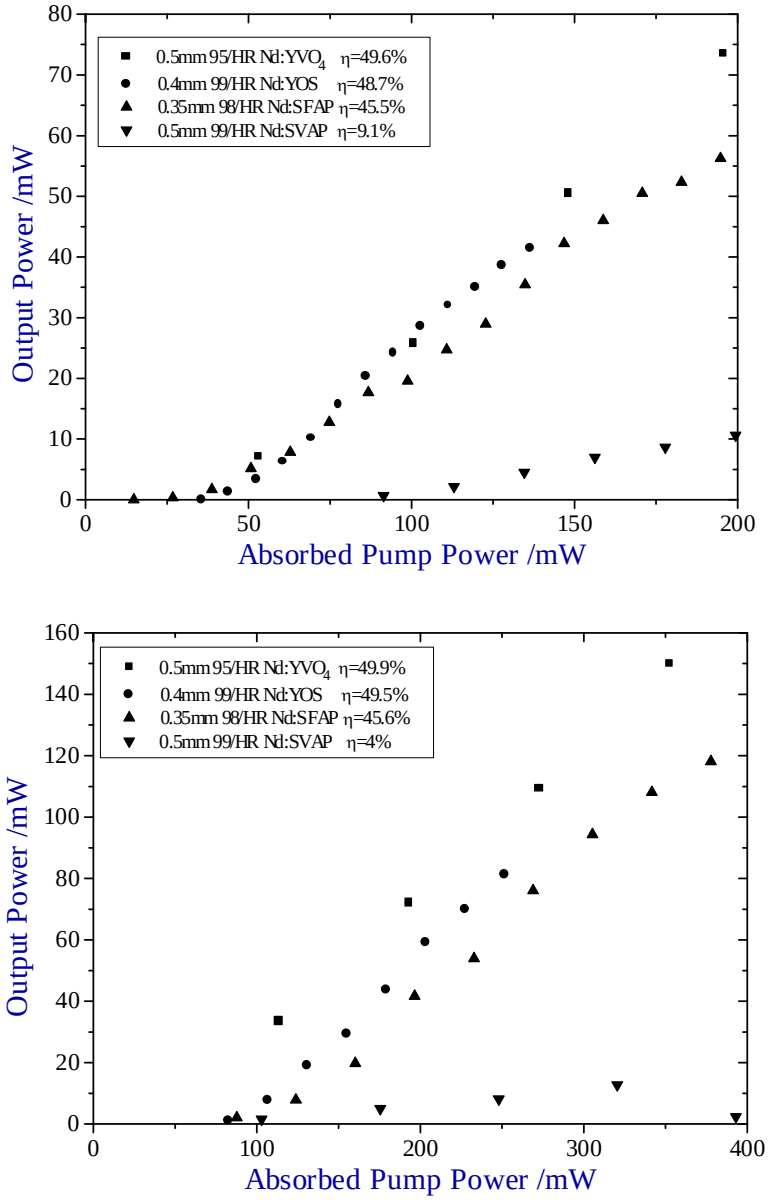

Figure 15 - Comparison of the CW lasing performance for a) 0.5W and b) 1.2W laser diode pumping through an 8mm collimating lens and 8mm focussing lens.

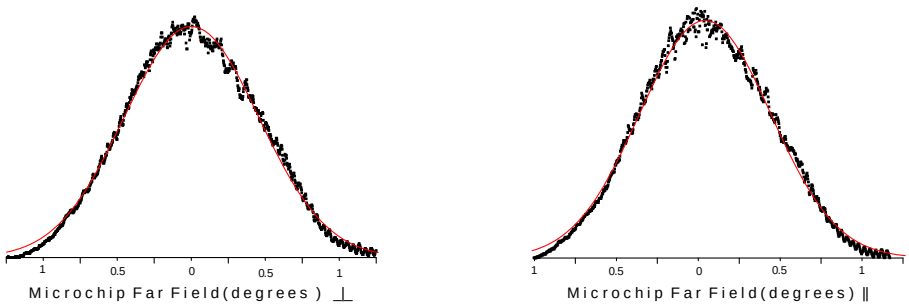

Figure 16 - Far-field energy distribution of a Nd:YVO_4 microchip.

All the materials, with the exception of Nd:SVAP, operated with high slope efficiencies and low thresholds for both 1.2W and 0.5W pump sources. As an indication, Nd:YVO_4, Nd:YOS, Nd:SFAP and Nd:SVAP had slope efficiencies of 50%, 49%, 45% and 9% respectively, with thresholds less than 100mW.

The output of all the devices was uniform to within approximately 20% over a large fraction of the crystal faces, except for Nd:SVAP which had extensive cracks visible. The parallelism of the crystal faces was examined using a He-Ne based Fizeau interferometer. This showed the Nd:YVO_4 crystal to have the best parallelism, with no wedging visible. The other crystals had wedging less than 0.05^o, which effected the mode quality at very low pump power levels. However choosing a part of the crystal with little or no wedging could compensate for this. CW threshold pump powers as low as 14mW for Nd:YVO_4, 29mW for Nd:YOS and 21mW for Nd:SFAP were measured at different crystal positions, although with lower slope efficiencies.

All the devices operated in a near-TEM_{00} mode, as shown Figure 16. M^2 measurements, based on the near and far-field output, indicated values of 1.2 $^+/_-$ 0.2 for all these lasers [179]. With the exception of Nd:SVAP, the devices operated in a single transverse mode over their entire operating range. The mechanisms for cavity formation in monolithic microchip lasers will be discussed further in the next chapter.

The output beam in each case was approximately circular for pumping with the 0.5W laser diode. For Nd:YVO_4 the output became more elliptical with a ratio of up to 1:1.4 when pumped by the 1.2W laser diode. This increasing ellipticity is attributed to the increasingly high temperature of the pumped region and the differing thermal conductivities of the two crystal axes of Nd:YVO_4. The output of all the devices was polarised better than 100:1 in the same plane as the peak absorption of the crystal.

All the devices operated in a single longitudinal mode (SLM) at low pump powers. The maximum SLM powers obtained are given in Table 8. The wavelength separation between longitudinal modes corresponded to a free spectral range; 1.1nm for Nd:SFAP, 0.6nm for Nd:SVAP, 0.8nm for Nd:YOS and 0.45mm for Nd:YVO_4. At high powers Nd:YVO_4, Nd:YOS and Nd:SVAP all operated on three longitudinal modes and Nd:SFAP on two. With shorter cavity lengths and greater output couplings, higher SLM operation should be possible from these materials. The wavelength tuning of these lasers will be considered in the final section of this

chapter.

2.3.2 Monolithic 1064nm Nd:YVO_4 Microchip Lasers

In addition to the microchip lasers already described, a number of monolithic Nd:YVO_4 microchip lasers operating at 1064nm and 1342nm were characterised with a variety of output couplings (1, 5, 10, 15%) and crystal lengths (0.25, 0.5mm). The CW lasing performance of the 1064nm devices is illustrated below in Figure 17 and tabulated in Table 8.

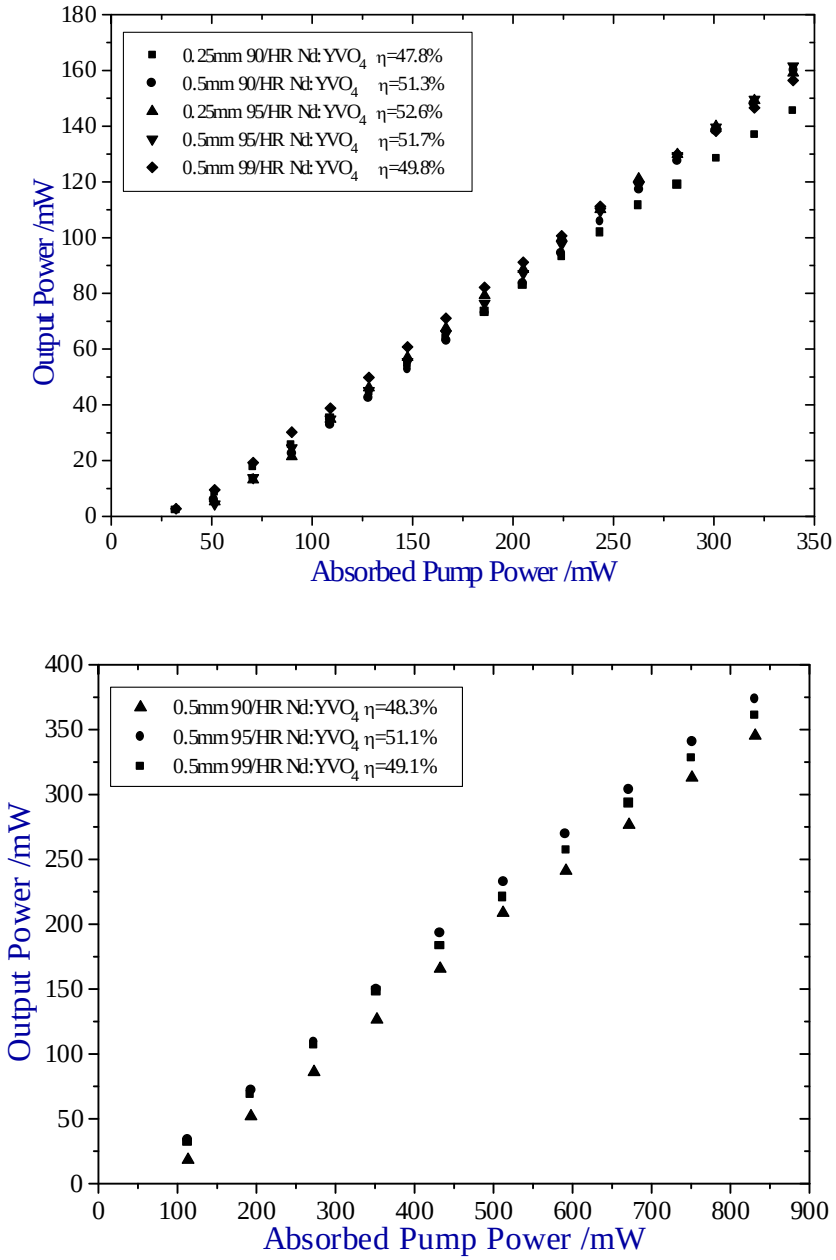

Figure 17 - Comparison of the CW lasing performance at 1064nm of 3% doped, 0.25mm and 0.5mm long Nd:YVO_4 microchip lasers with 1, 5 or 10% output

coupling for a) 0.5W and b) 1.2W laser diode pumping.

For operation at 1064nm there were six different microchip lasers available; three 0.25mm long and three 0.5mm long, one of each with a 1%, 5% and 10% output coupling. These lasers were pumped in the same fashion as described earlier for the comparison of Nd^{3+} doped materials.

There was only a small variation in the slope efficiencies of these devices as can be seen from Figure 17 and Table 8. These values compare favourably to the maximum reported efficiencies for similar Nd:YVO_4 monolithic devices [166]. Slope efficiencies as high as 59-61% were measured from these devices when operating in a non-TEM_{00} transverse mode, indicating these devices are limited by the overlap between the pumping mode volume and that of a stable TEM_{00} mode. Therefore beam shaping of the diode output would potentially enhance these results.

The lasing threshold increased with increasing output coupling, as expected, though was not directly proportional to the cavity loss. This is because thermal considerations, as well as loss considerations, determine the threshold. For low output couplings thermal considerations primarily define the threshold value with output coupling more prominent with increasing loss. Indeed, we have demonstrated AR/HR Nd:YVO_4 microchip lasers with a discrete output coupler, lasing with more than 60% output coupling, indicating the high gain available.

Pumping with a 2W-laser diode (200x1μm emitter) proved catastrophic for both 0.25mm and 0.5mm long crystals as discussed in Chapter Two. Crystals with lower doping levels of Nd^{3+} are therefore required if more than 500mW of power are required at 1064nm from a microchip and this has implications for the lasing properties of the microchip.

It was also found that the 0.25mm crystals would crack when exposed to more than 800mW of absorbed power and therefore these results are not included with the 0.5mm long crystals in Figure 17b. The limitations of these devices due to thermal failure is described further in the next chapter, with illustrations of the change in behaviour of these devices close to their thermal fracture points.

The maximum single frequency power available from each laser varied significantly with increasing output coupling as can be seen from Table 8. Taking the 0.5mm long crystals as an example, the maximum SLM power increases from 1.2mW to 52mW to

123mW for an increase in output coupling from 1% to 5% to 10%. These figures do not agree with the theoretical modelling for the limit of single frequency power for a standing-wave laser [180]. This discrepancy is attributed to two factors: the model used does not take account of any gain diffusing effects, which may be significant in Nd:YVO_4 [161], and relies on the threshold values measured being proportional to the cavity loss. Temperature tuning of the microchip lasers can enhance the maximum single frequency powers available from these lasers by as much as 100% by tuning the lasing frequency to the centre of the gain bandwidth, in order to minimise the gain available to the next longitudinal modes.

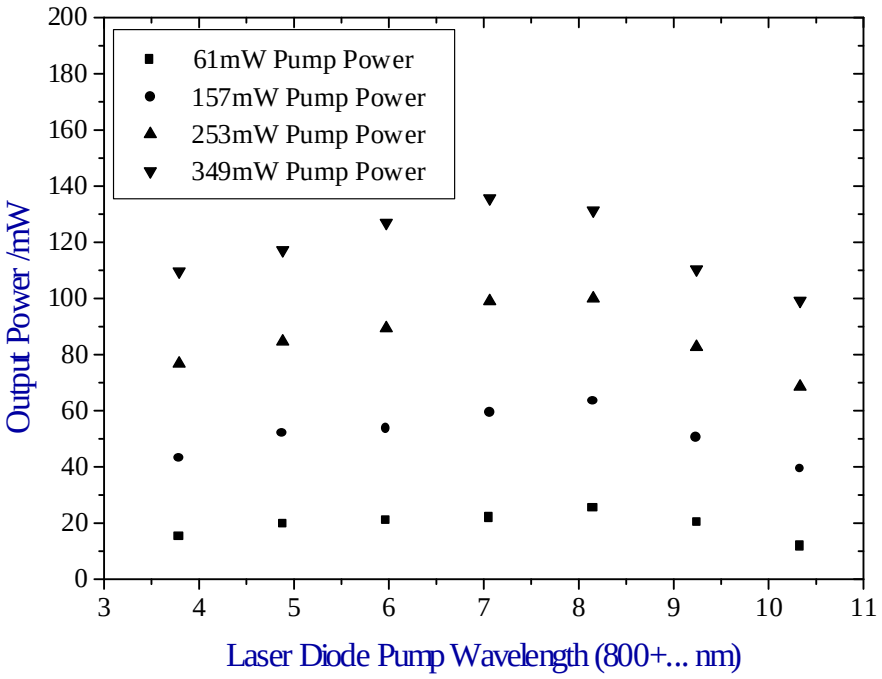

Figure 18 – Change in output power of 0.5mm long 95/HR Nd:YVO_4 monolithic microchip laser with pump detuning from peak absorption.

The effect of detuning the pump wavelength from maximum absorption was examined for Nd:YVO_4 to determine how critical diode stability is. A variation of approximately 30% was observed over the entire wavelength range of the diode, indicating relative insensitivity to the wavelength of the diode. There was also an indication that the absorption peak increased in frequency with increasing pump power, and hence temperature of the pumped region.

The amplitude stability of these microchip lasers was typically 0.5% peak-to-peak with a characteristic noise peak in the 0.5-5MHz region. The deliberate modulation of the pump to produce relaxation oscillations from these monolithic microchip lasers

will be discussed later in this chapter.

2.3.3 Monolithic 1342nm Nd:YVO_4 Microchip Lasers

In a similar fashion, the performance of a range of Nd:YVO_4 monolithic microchip lasers operating at 1342nm was examined, with output couplings of 1%, 5%, 10% and 15%, lengths of 0.25mm and 0.5mm and with doping concentrations of 1% and 3%. The results are illustrated below in Figure 19 and overleaf in Figure 20 and tabulated at the end of this section in Table 8.

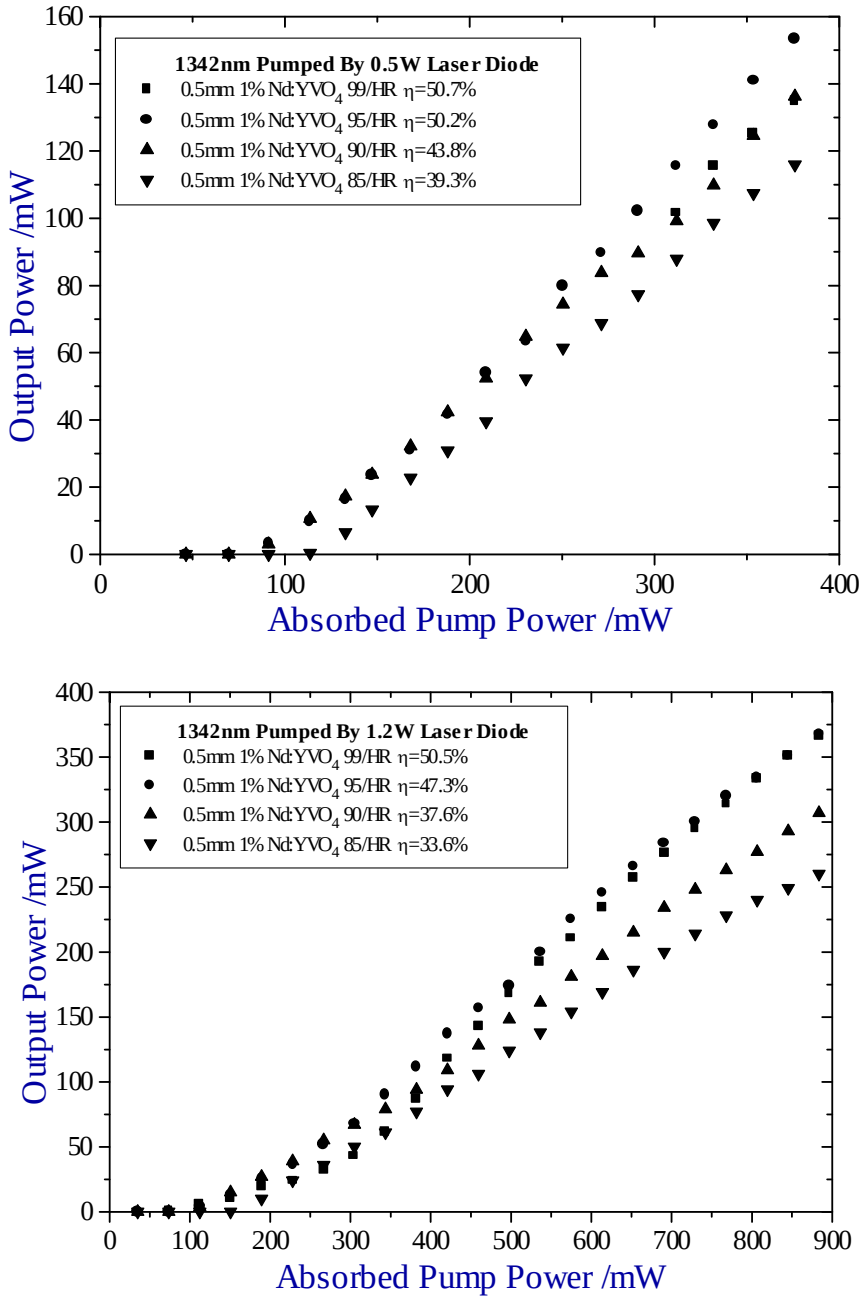

Figure 19 - Comparison of the CW lasing performance at 1342nm of 1% doped,

0.5mm long Nd:YVO_4 microchip lasers with 1, 5, 10 or 15% output coupling for a) 0.5W and b) 1.2W laser diode pumping.

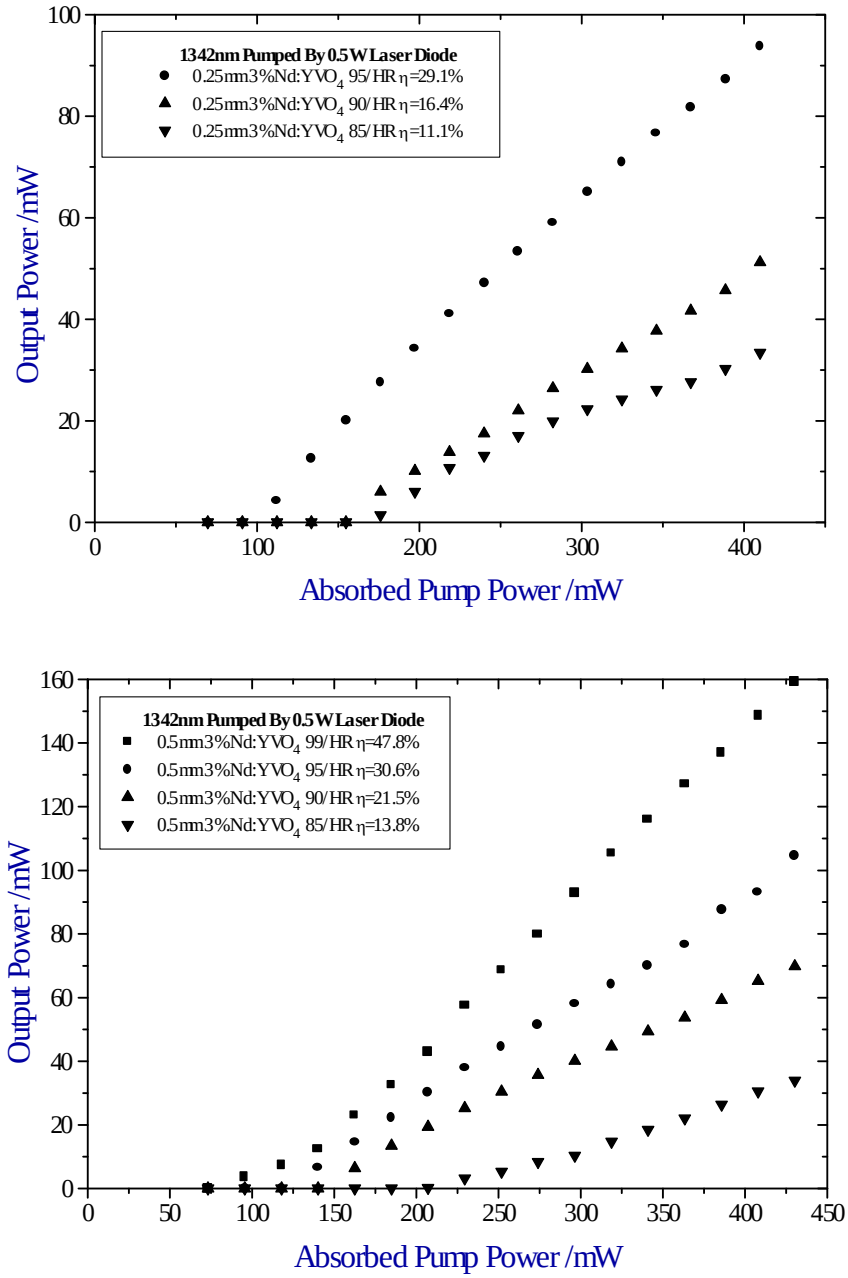

Figure 20 - Comparison of the CW lasing performance at 1342nm of 3% doped, a) 0.25mm and b) 0.5mm long Nd:YVO_4 microchip lasers with 1, 5, 10 or 15% output coupling for 0.5W laser diode pumping.

The performance of the 1342nm-microchip lasers varied more significantly than the 1064nm lasers for a number of reasons. The crystals with 5%, 10% and 15% output coupling were from a different boule and coating run than the 1% devices, and there is some evidence they have inferior coatings and increased cavity losses. The lower stimulated emission cross-section of the 1342nm transition ($5.6x10^{-19}cm^2$) is more

sensitive to increasing cavity loss and will not lase with more than 20% output coupling. Indeed the theoretical optimal output coupling is between 5-10%.

The 1% doped lasers did not exhibit the expected linear relationship between pump power and output power as shown in Figure 19. Further analysis showed that at absorbed pump powers below 100mW these lasers operated on a multi-transverse mode with low slope efficiency. This mode of operation arises from poor cavity mode definition because of the smaller thermal lensing due to the lower doping concentration. Unusually, in the region where the mode changes to a TEM_{00} output the slope efficiency can exceed the quantum limit of 60% (determined by the ratio between pump and signal photon energies) as the cavity becomes optimised due to the increasing thermal lensing (the gain/loss ratio increases more rapidly than due to only the increasing pump rate, giving rise to this effect). The intensity stability of the output also decreased to below 0.5% peak-to-peak.

There was also an indication of roll-off in the performance of these devices when pumped with the 1.2W laser diode, in particular for the higher output couplings. Similar behaviour occurred for some of the 3% doped, 0.25mm long crystals in Figure 20a giving smaller slope efficiencies at high powers. This behaviour is in part attributed to the poor coatings and in part to the increased temperature of the pumped region in each case because of the larger quantum defect heating (~40%).

The three crystals with 1% output coupling all exhibited very similar operating characteristics at moderate pump powers. Indeed their efficiency exceeds that of the 1064nm devices, taking the quantum defect into account (40% at 1342nm and 26% at 1342nm). These also represent the highest slope efficiencies ever reported for the 1320nm transition of Nd^{3+} materials.

Up to 93mW of single frequency power was generated from the 3% doped, 0.25mm long crystal with 5% output coupling. This figure was only limited by the available pump power. Comparison of the measured maximum single frequency powers shown in Table 8 and theoretical predictions [180] give relatively good agreement.

In conclusion a range of Nd:YVO_4 monolithic microchips operating at 1064nm and 1342nm, in addition to the Nd^{3+} doped materials Nd:YOS, Nd:SFAP and Nd:SVAP have been demonstrated. With the exception of Nd:SVAP, all of these devices offered low threshold, high efficiency operation with polarised, single transverse mode

output. Output powers up to and exceeding 350mW and single frequency powers in excess of 90mW have been measured at both wavelengths.

2.3.4 Summary of CW Lasing Performance

Crystal	Length	Output Coupling	Threshold /mW		Slope Efficiency		Max SLM /mW
			0.5W	1.2W	0.5W	1.2W	
Nd:SFAP, Nd:SVAP, Nd:YOS ~ 1064nm							
Nd:SFAP	0.35mm	2%	23.2	74.3	45.5%	45.6%	24
Nd:SVAP	0.5mm	1%	64.3	64.8	9.1%	4%	4
Nd:YOS	0.4mm	1%	37.6	82.5	48.7%	49.5%	35
$Nd:YVO_4$ – 1064nm							
3% doped	0.25mm	10%	43.4	-	47.8%	-	>140
3% doped	0.5mm	10%	42.9	79.8	51.3%	49.7%	123
3% doped	0.25mm	5%	34.6	-	52.6%	-	94
3% doped	0.5mm	5%	33.5	46.5	51.7%	51.1%	52
3% doped	0.25mm	1%	24.1	-	49.8%	-	18
3% doped	0.5mm	1%	16.7	39.7	52.1%	49.1%	1.2
$Nd:YVO_4$ – 1342nm							
3% doped	0.25mm	15%	171.4	-	11.1%	-	>33.4
3% doped	0.5mm	15%	210.2	-	13.8%	-	11.3
1% doped	0.5mm	15%	109.5	165	39.3%	33.6%	6.5
3% doped	0.25mm	10%	155.4	-	16.4%	-	>51.2
3% doped	0.5mm	10%	158.5	-	21.5%	-	51.3
1% doped	0.5mm	10%	87.3	114	43.8%	37.6%	105
3% doped	0.25mm	5%	107.9	-	29.1%	-	>93.7
3% doped	0.5mm	5%	104.7	-	30.6%	-	11.2
1% doped	0.5mm	5%	83.1	111	50.2%	47.3%	17.8
3% doped	0.5mm	1%	34.0	-	47.8%	-	5.2
1% doped	0.5mm	1%	41.2	76	50.7%	50.5%	1.7

Table 8 – Summary of lasing performance of monolithic microchip lasers.

The table above summaries the CW lasing performance of the microchip lasers described in this section. In conclusion $Nd:YVO_4$, Nd:SFAP and Nd:YOS have all shown efficient operation as monolithic microchip lasers, with slope efficiencies in excess of 45% and low thresholds. The high doping concentration of Nd:SVAP limited its performance because of fluorescence quenching. The 1342nm transition of $Nd:YVO_4$ has been shown to be as efficient as the 1064nm, with slope efficiencies in

excess of 50% and low thresholds. The poor coatings limited the performance of 1342nm devices with higher output couplings.

2.4 Intensity Modulation of Monolithic Microchip Lasers

2.4.1 Introduction

In the first parts of this chapter we examined the characteristics and CW lasing performance of a number of different monolithic microchip lasers. The second half of this chapter is concerned with the modulation of these devices, first in the time domain and then in the frequency domain. Modulation is more attractive than CW operation for many applications because the output can then be used for time or frequency resolution, or to carry information. The higher peak powers also are advantageous for nonlinear effects and as a pump source for other transitions.

Intensity modulation of the output will occur if the gain or loss of the laser cavity is changed. Every laser exhibits modulation when it is switched on as the population inversion builds up. This modulation is damped however for a CW pump source, and the output of the laser will tend to a CW operating level determined by the power coupled out of the cavity reducing the overall gain of the cavity to one.

Many of the intensity modulation techniques used today arise from the introduction of a time-varying loss into the cavity. Two forms of these composite cavity techniques, passive Q-switching and active Q-switching will be described in Chapter Four of this thesis. For the modulation of a monolithic device however, only the properties of the gain material, cavity, or pumping rate can be varied in time to change the gain/loss ratio. Inherent modulation of the first two can occur in the form of self Q-switching, a form of which will be described in the next chapter.

The third possibility for a monolithic laser is to modulate the pumping rate to give a temporal variation in the gain available. This form of modulation is generally called ‘gain switching’. Gain switching is often considered an unwanted side effect on the output of a laser with a noisy pump source, and is also referred to as ‘relaxation oscillations’.

However, pulses as short as 760ps for Nd:YAG and 80ps for LNP have been measured, using a gain-switched Ti:sapphire pump source [181]. In this section we

will describe the generation of short pulses using modulation of a laser diode to give gain switched operation of a range of monolithic microchip lasers.

2.4.2 Gain Switching Theory

Figure 21 shows how gain-switched pulses are generated from a laser oscillator. When there is a rapid increase in the pumping rate, the population of the upper state, N_2, increases as shown in the lower diagram. As the threshold level is reached there is a build up of photon flux as the round-trip small signal gain exceeds the cavity losses.

The photon flux, ϕ, will then increase rapidly until it reaches a maximum level (marked with dotted vertical line) where it has depleted the upper state population back to the threshold level through stimulated emission. The flux will then decay to a level below the steady state level to balance the cavity losses with the available gain.

This process is repeated, producing a train of damped relaxation oscillations as the upper state population continues to oscillate towards the threshold level.

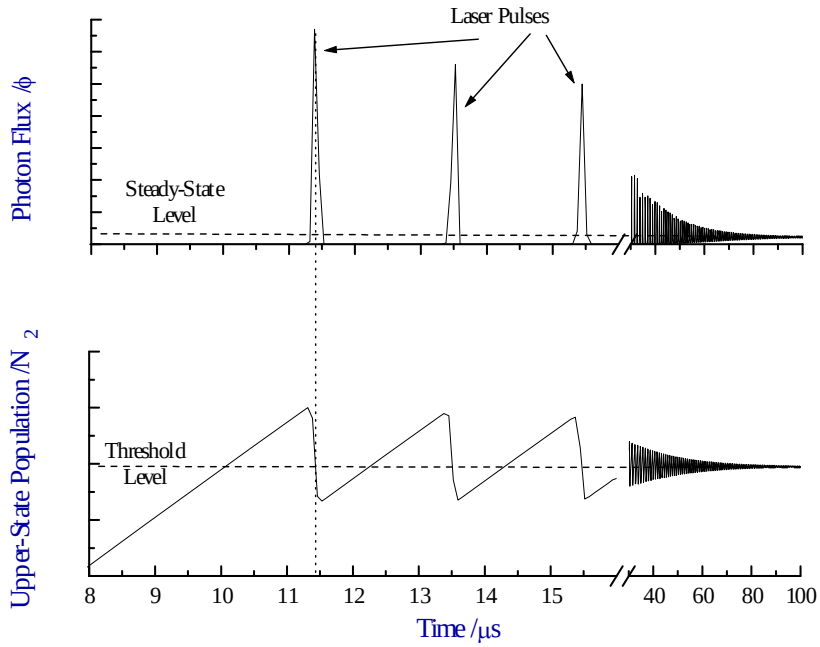

Figure 21 – Numerical simulation of gain switched pulses from a 0.5mm 95/HR Nd:YVO_4 microchip laser pumped ten times above threshold.

Therefore qualitatively, to produce short, high intensity pulses it is desirable to increase the pumping rate as quickly as possible to as high a rate as possible. This will have the effect of increasing the upper state population further above threshold before a pulse can build up. By modulation of the pump at a suitable repetition rate, it should

be possible to produce a train of single pulses, by preventing the build-up of the second pulse in the relaxation oscillation train.

Quantitatively these effects can be modelled in the form of small perturbations to the steady state to give an analytical solution, or by numerical solution of the laser rate equations. We will now consider both of these approaches with reference to our monolithic microchip lasers.

2.4.2.1 Theoretical Modelling of Relaxation Oscillations

A gain switched system can be modelled analytically if two approximations are made: the first is that the perturbations of the upper state population and photon flux are small (relaxation oscillations) and that the cavity mode is a plane wave. Both of these approximations become less valid the further above threshold we pump the monolithic devices, but we can still gain a useful insight into their expected operation.

The coupled rate equations for a laser can be expressed as [182]:

$$\frac{dN_2}{dt} = R - \frac{N_2}{\tau_2} - N_2\phi\sigma_e\frac{c}{n}$$
$$\frac{d\phi}{dt} = N_2\phi\sigma_e\frac{c}{n} - \frac{\phi}{\tau_c}$$

Equation 1

where N_2 and ϕ are the upper state population and photon flux respectively, R is the pumping rate in ions per second per unit volume, τ_2 is the upper state lifetime, σ_e is the stimulated emission cross section, c is the speed of light in a vacuum and n is the refractive index. τ_c is the cavity decay time given by:

$$\tau_c = \frac{2nL}{c}(-\ln(R_1R_2 + 2\alpha L)^{-1}$$

Equation 2

where R_1 and R_2 are the reflectivities of the cavity mirrors and α is the parasitic loss coefficient for the cavity.

In the steady state, there is no temporal variation in the photon flux or upper state population so:

$$\frac{dN_2}{dt} = 0 = R - \frac{N_{02}}{\tau_2} - N_{02}\phi_0\sigma_e\frac{c}{n}$$
$$\frac{d\phi}{dt} = 0 = N_{02}\phi_0\sigma_e\frac{c}{n} - \frac{\phi_0}{\tau_c}$$

Equation 3

Rearranging gives the steady state upper state population N_{02} and photon flux ϕ_0:

$$N_{02} = \frac{n}{c\sigma_e\tau_c}$$
$$\phi_0 = \frac{R\sigma_e\tau_c - \frac{n}{c\tau_2}}{\sigma_e}$$

Equation 4

If we now introduce a small perturbation ΔN_{02} into the steady state value of the population inversion N_{02}, and a similar perturbation $\Delta\phi_0$ into the steady state photon density ϕ_0, we can rewrite Equation 1 as:

$$\frac{d(\Delta N_{02})}{dt} = -R\frac{c}{n}\sigma_e\tau_c\Delta N_{02} - \frac{\Delta\phi_0}{\tau_c}$$

Equation 5

and

$$\frac{d(\Delta\phi_0)}{dt} = (R\frac{c}{n}\sigma_e\tau_c - \frac{1}{\tau_2})\Delta N_{02}$$

Equation 6

Taking the derivative of Equation 5 and substituting into Equation 6 gives:

$$\frac{d^2(\Delta\phi_0)}{dt^2} + R\frac{c}{n}\sigma_e\tau_c\frac{d(\Delta\phi_0)}{dt} + (R\frac{c}{n}\sigma_e - \frac{1}{\tau_2\tau_c})\Delta\phi = 0$$

Equation 7

which is the equation for a damped simple harmonic oscillator.

The threshold-pumping rate, R_{th}, is given from Equation 6 when $\Delta\phi_0=0$:

$$R_{th} = \frac{n}{c\sigma_e\tau_2\tau_c}$$

Equation 8

Substituting this into Equation 7 gives:

$$\frac{d^2(\Delta\phi_0)}{dt^2} + \frac{R}{R_{th}\tau_2}\frac{d(\Delta\phi_0)}{dt} + (\frac{R}{R_{th}} - 1)\frac{\Delta\phi_0}{\tau_c\tau_2} = 0$$

Equation 9

A solution for the damped simple harmonic oscillator differential equation can be expressed in the form $\Delta\phi_0 = A\exp(Bt)$. Substituting this into Equation 9 gives:

$$B^2 + \frac{R}{R_{th}\tau_2}B + (\frac{R}{R_{th}} - 1)\frac{1}{\tau_c\tau_2} = 0$$

Equation 10

where

$$B = -\frac{R}{2R_{th}\tau_2} \pm i\sqrt{(\frac{R}{R_{th}} - 1)\frac{1}{\tau_2\tau_c} - (\frac{R}{R_{th}})^{\frac{1}{2}}\frac{1}{\tau_2}}$$

Equation 11

The real part of this solution describes the damping rate of the oscillations:

$$\frac{R}{2R_{th}t_2}$$

Equation 12

and the imaginary part describes the oscillation frequency:

$$\sqrt{(\frac{R}{R_{th}} - 1)\frac{1}{\tau_2\tau_c} - (\frac{R}{R_{th}})^{\frac{1}{2}}\frac{1}{\tau_2}}$$

Equation 13

Thus, for an increasing pumping rate, we would expect to see an increase in the relaxation oscillation frequency and a more rapid decay time. For materials with longer upper-state lifetimes we would also expect to see lower oscillation frequencies and long decay time.

The decay rate of the relaxation oscillations will not considered here for two reasons. The modelling above assumes single frequency operation, though in reality these monolithic devices often operate with multiple longitudinal modes. Each subsequent longitudinal mode will begin to gain-switch whenever it reaches its own threshold, often only a few microseconds after the first mode begins to oscillate. Thus the first mode is not able to decay before further longitudinal modes, with different thresholds, different decay rates and oscillation frequencies begin to oscillate.

The second reason is that energy diffusion between Nd^{3+} ions in the lattice can cause

a drastic increase in the damping constant but only a small change in the relaxation oscillation frequency, particularly in high gain materials [183]. Detailed work by Otsuka on miniature LNP lasers has helped to explore this effect and add an effective diffusion parameter to the rate equations in Equation 1 [184].

2.4.2.2 Numerical Modelling of Relaxation Oscillations

The alternative approach is to solve Equation 1 using numerical techniques. The coupled laser rate equations can be rewritten for finite time steps as:

$$N_{t+1} = N_t + \Delta t\left(R - \frac{N_t}{\tau_2} - N_t\phi_t\sigma_e\frac{c}{n}\right)$$

$$\phi_{t+1} = \phi_t + \Delta t\left(N_t\phi_t\sigma_e\frac{c}{n} - \frac{\phi_t}{\tau_c}\right)$$

Equation 14

Using suitable parameters these coupled equations can be solved using a computer. The advantage of a numerical method is that other information can be extracted from the generated data, such as the expected peak power of the pulses and their duration, and it is not limited by the approximations used for the analytical modelling.

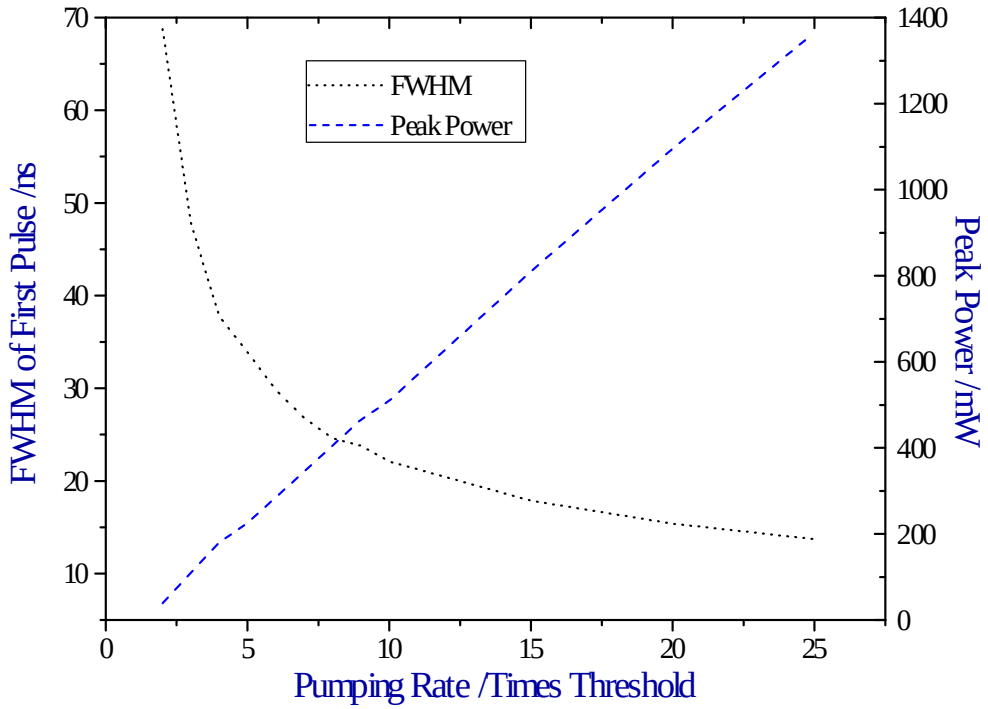

Figure 22 – Numerical modelling of the expected pulse widths and peak powers from a gain switched 0.5mm. 3% doped, 95/HR Nd:YVO_4 microchip laser.

The gain switched behaviour of a 0.5mm long, 3% doped crystal of Nd:YVO_4 coated

for 5% output coupling was modelled using the 'Relaxation Oscillations and Q-Switching' program written by Alastair Gillies as part of the Psst! Project. The results were analysed to determine the peak power and FWHM of the first pulse of the relaxation oscillations as shown in Figure 22.

With the good absorption properties of Nd:YVO_4 and its low threshold in a microchip geometry (~30mW), we can expect to pump the microchip up to 25 times above threshold with a 0.5W laser diode modulated over its full range. Under these conditions pulses as short as 13ns and peak powers of up to 680mW are indicated by the numerical solution. Similarly the decay rate falls from 113μs at twice threshold, to 9.4μs twenty-five times above threshold, producing very short bursts of relaxation oscillations.

Both the analytical and numerical techniques have shown how gain switching can be modelled to give an indication of the pulses that can be produced from a monolithic microchip laser. These theoretical results will now be compared to experimental results using the microchip lasers described earlier in this chapter.

2.4.3 Gain Switching of Nd^{3+} Doped Monolithic Microchip Lasers

To gain switch the monolithic microchip lasers, a pulse generator was connected to the analogue input of an SDL-800 driver. This enabled full-scale switching of the drive current to a 0.5W SDL-2352 laser diode at up to 100kHz with pulse durations down to 5μs. For this work the pulse generator was operated with a 50% duty cycle at 5kHz repetition rate. The rise time of the resulting pulse from the laser diode was 900ns for a change from zero to 400mW. Fast silicon photodiodes (bandwidth ~1GHz) were used to measure the pulsed output of both the laser diode and monolithic microchip. Although higher power laser diodes were examined as pump sources, the limitation of the switching speed of the current from the larger drivers (typically >20μs) failed to improve the results reported in this section.

For each material the laser diode was tuned to the peak absorption of the material. The absorbed peak power was then divided by the threshold for each material to normalise the pump power. The lower pump absorption of the Nd:SFAP and Nd:YOS samples and the poor lasing performance of the Nd:SVAP sample, limited the number of times above threshold these devices could be pumped to single figures. The

Nd:YVO_4 sample could be pumped up to more than twenty times above threshold and will be considered separately later.

The measured relaxation oscillation frequencies are shown in Figure 23 for each of the materials, together with the theoretical analytical results from Section 2.4.2.1.

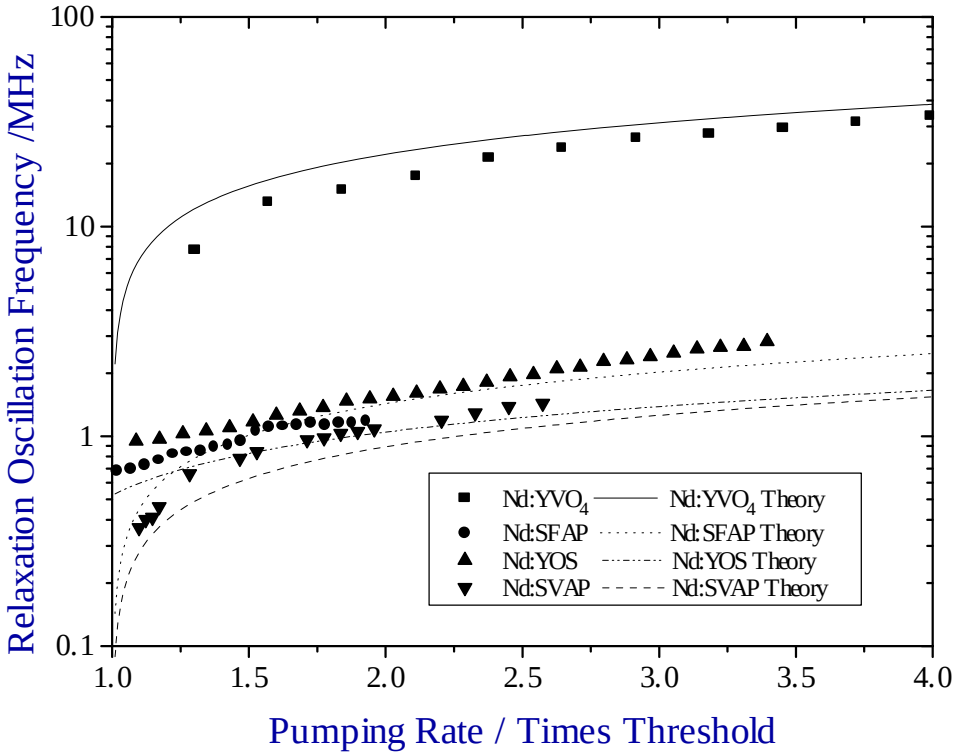

Figure 23 - Measured relaxation oscillation frequency of gain switched Nd:YVO_4, Nd:SFAP, Nd:YOS and Nd:SVAP microchip lasers pumped by 0.5W laser diode. The theoretical analytical results from Section 2.4.2.1 for each material are included.

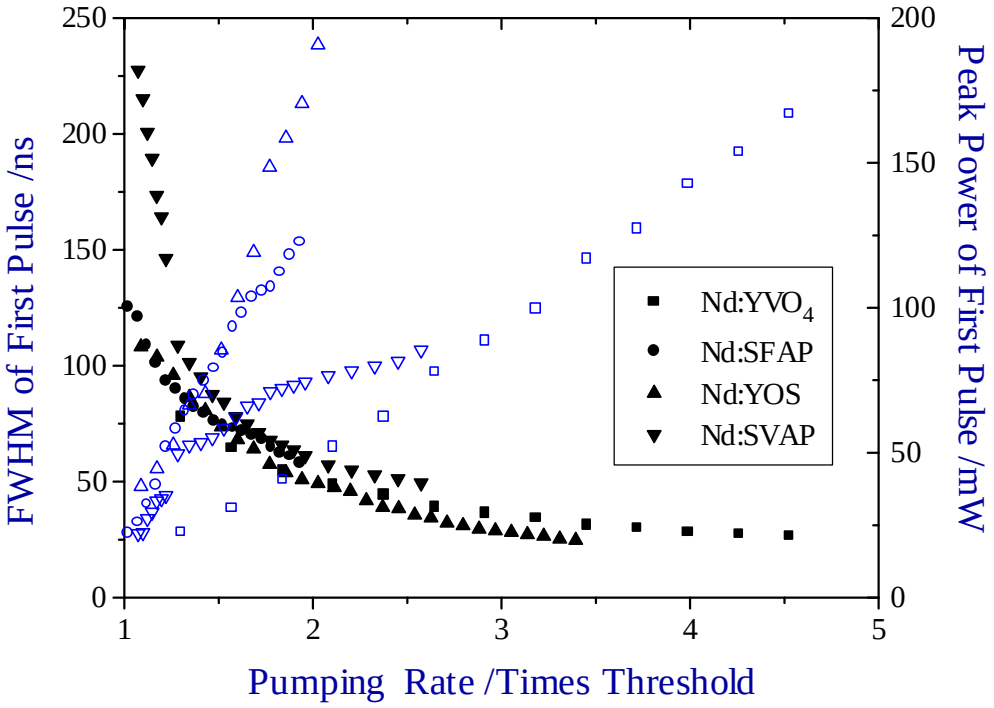

Figure 24 - Peak power (hollow) and FWHM (solid) of the first pulse of gain switched output for Nd:YVO_4, Nd:SFAP, Nd:YOS and Nd:SVAP microchip.

There is good agreement between the calculated and measured relaxation oscillation frequencies for each of the materials. The oscillation frequency for Nd:YVO_4 is much greater than the other materials because of its much shorter upper state lifetime (55μs) The variation between the other materials is mainly due to the slight variation in crystal lengths and the variation of upper state lifetime.

The peak power and duration of the first pulse of the relaxation oscillation train was also measured and the results are shown in Figure 24. The pulse durations of all the microchip lasers are similar because they all have similar cavity round-trip times. Pulses down to 20ns were measured for Nd:YOS and Nd:YVO_4.

The peak power of the first pulse is determined by how efficiently energy can be stored in the upper state and how quickly a pulse will build up. The large stimulated emission cross-section of Nd:YVO_4 combined with its short upper state lifetime gives low intensity pulses because of its poor storage capability and fast pulse build up time. In contrast Nd:YOS has a long upper state lifetime and low stimulated emission cross-section and produces the highest peak power pulses.

The effect of the increasing thermal heating of the materials is not considered here though it would effect the operation of the lasers in parallel with the increasing pump

intensity. At low pump powers the number of times threshold the microchip operates increases more rapidly than expected because the minimum beam waist in the cavity is larger than optimal, whereas at higher pump powers the converse is true.

2.4.3.1 Gain Switching of Nd:YVO_4 Microchip Lasers

As mentioned earlier, the 1064nm Nd:YVO_4 microchip lasers used could be pumped more than twenty times above threshold and we will now consider them separately. The further above threshold a microchip laser can be pumped before its starts to lase, the shorter the pulses and higher the peak power. The only caveat is that the switching time of the pump needs to be much faster than the build-up time of the first pulse.

The range of monolithic 1064nm Nd:YVO_4 devices described earlier were used to consider the effect of different crystal lengths and output couplings on the resulting gain switched pulses. As with the previous section, measurement of the decay rate was hampered by other longitudinal modes reaching threshold before the decay of the first mode was complete and for this reason decay rates are not considered here.

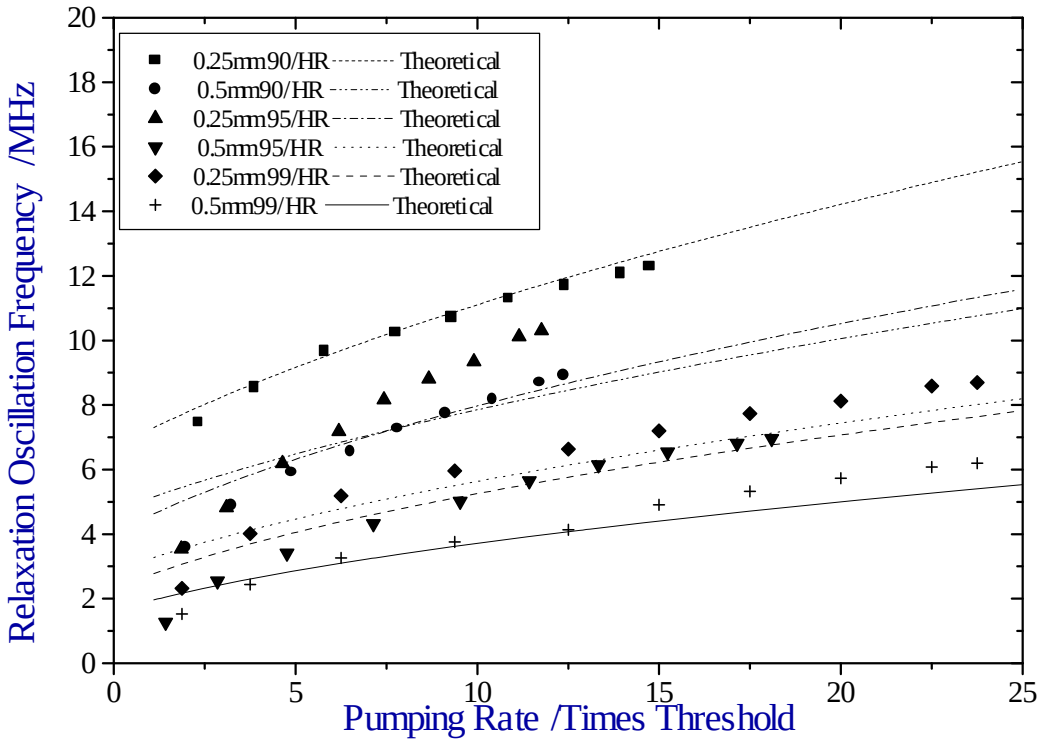

Figure 25 - Measured relaxation oscillation frequency of gain switched Nd:YVO_4, microchip lasers with 10, 5, 1% output coupling and 0.25,0.5mm long. The theoretical analytical results from Section 2.4.2.1 for each laser are included.

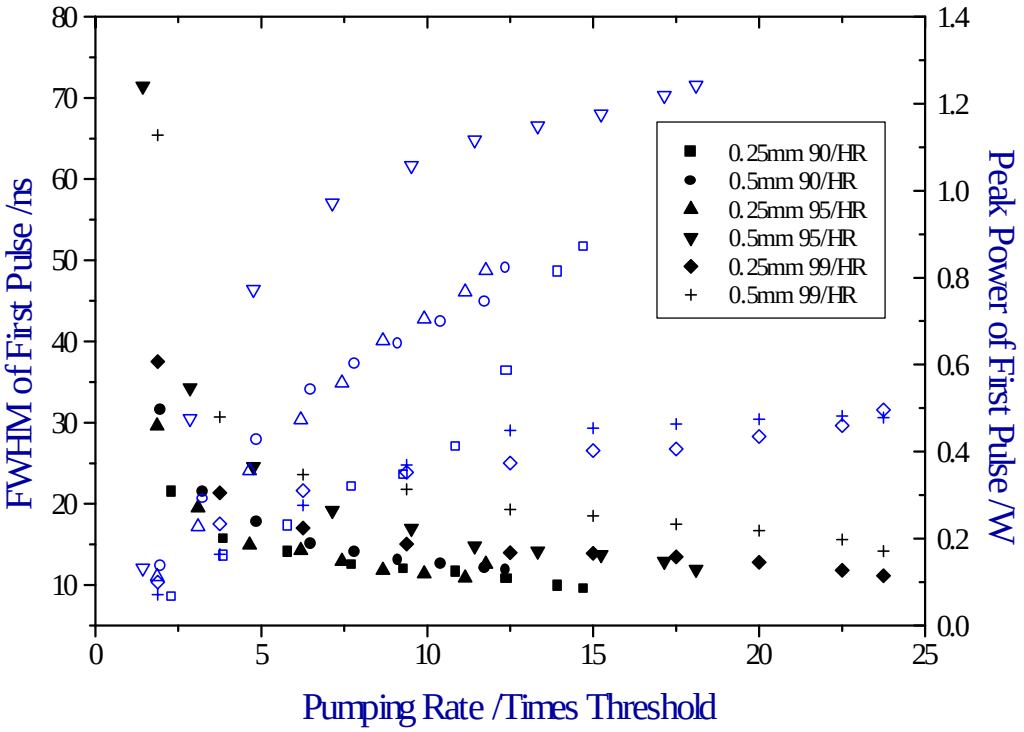

Figure 26 - Peak power and FWHM of the first pulse of gain switched output for gain switched Nd:YVO_4, microchip lasers with 10, 5, 1% output coupling and 0.25,0.5mm long.

Figure 25 shows how the relaxation oscillation frequency for each microchip varied as it was pumped further above threshold. As before, there is good agreement between the small perturbation theory and the observed experimental results. The frequency of the pulses in the relaxation oscillation train exceeded 10MHz, further indicating how far above threshold these devices were being pumped and the large emission cross-section of Nd:YVO_4. It is worth noting that characteristic spikes around 2-5MHz in the frequency spectrum of a CW Nd:YVO_4 laser are often an indication of small scale relaxation oscillations in the output due to small pump fluctuations.

The FWHM and peak power of the first pulse of the relaxation oscillation trains were also measured as indicated in Figure 26. Pulses as short as 9.1ns were recorded with peak powers of over 1.25W, approximately 8 times the normal CW power. These results show good agreement with those from numerical modelling in Figure 22.

The devices with 1% output coupling showed the worst performance, with the 5% output coupling devices showing the best, as expected from the theory of optimal output coupling [182]. However care had to be taken to differentiate these results from the effect of self Q-switching described in the next chapter which could also

produce shorter, higher intensity pulses during gain switched operation.

The delay between the start of pumping and the first pulse from the microchip was measured to be as short as 1.8μs with 450mW of incident pump power for a 0.5mm 95/HR microchip. This is much faster than predicted by theory and could account for the roll off in peak power of the first pulse as its build-up time occurs earlier in the build-up of the pump pulse.

Although these results are of interest, most applications require a single pulse to be generated on demand, instead of a series of relaxation oscillations. A further extension to gain switching is 'repetitive gain switching' where the pumping is stopped quickly enough after the first pulse to produce just a single pulse.

2.4.4 Repetitive Gain-Switching

In order to achieve repetitive gain switching the fall time of the pump source must be faster than the reciprocal of the relaxation oscillation frequency of the device of interest. This would indicate that a fall time of less than 1μs would be required for all our monolithic lasers.

The fall time of the laser diode pulses used was slightly longer 1μs. Therefore to prevent the generation of a second pulse, the pump pulse duration had to be altered so that the single pulse from the microchip laser was generated on the fall edge of the pump pulse. This decreased the efficiency below that of normal gain switched operation described in the previous section.

Table 9 shows the results obtained for the repetitive gain switching of each of our Nd^{3+} doped materials. The diode was modulated over part of its power range (0-250mW) and the pulse width and repetition rate of the laser diode was altered to provide an optimised single pulse output. The peak power of the diode could not be increased without lengthening the pulse width. In all cases it was less than 2μs, though for example Nd:YVO_4 required a shorter pump pulse than Nd:YOS to prevent a second pulse from the microchip laser.

Crystal	Pulse FWHM /ns	Repetition Rate /kHz	Peak Power /mW
Nd:YOS	51.7	85.76	161
Nd:SFAP	49.6	75.36	244
Nd:SVAP	54.3	84.3	163

Nd:YVO_4 (1064nm)	16.79	85.8	676
Nd:YVO_4 (1342nm)	26	82.3	462

Table 9 – Peak power and FWHM of pulses generated from repetitive gain switching of Nd:YVO_4, Nd:SFAP, Nd:YOS and Nd:SVAP using a 0.5W laser diode.

Single pulse generation was possible from all the devices for an increase in pulse width and slight decrease in peak power over normal gain switching. Nd:YVO_4 again showed the best performance because of its stronger absorption characteristics.

In conclusion we have demonstrated both normal gain switching and repetitive gain switching for a range of different Nd^{3+} doped, monolithic microchip lasers. Pulses as short as 9.1ns were measured with peak powers in excess of 1.25W at relaxation oscillation frequencies up to 10MHz, in agreement with analytical and numerical modelling. Gain switching has been shown to be a very basic method of generating short pulses with relatively low peak powers from monolithic lasers, when intensity modulation is required.

2.5 Frequency Modulation and Tuning

The second form of modulation of interest is frequency modulation. Frequency modulation has a number of different applications, from spectroscopy to telecommunications. Frequency modulation techniques can also be used to precisely tune the laser frequency for high-resolution applications.

The frequency of a laser is determined by the oscillator cavity around the gain material. Constructive interference is required for amplification, limiting the wavelengths of the longitudinal modes to those that are an integer fraction of the optical path length of the cavity and fall within the gain bandwidth. If the optical path length of the cavity is increased, then the wavelength of the longitudinal modes must increase to remain in resonance.

Such a change in cavity length is the basis of most of the frequency tuning and modulation techniques. Changes in the cavity length normally occur through three processes: thermal, mechanical or electrical change of a cavity element. We will now consider modulation and tuning of microchip lasers via each of these processes.

2.5.1 Pump Power Frequency Tuning

The first of these processes is thermal modulation of the cavity length. Thermal effects are generally long term, with a maximum effective modulation rate of 1kHz. Therefore for frequency modulation, pump power modulation is not commonly used. However the pump power can be used successfully to tune the wavelength of a laser over its free spectral range.

Slow modulation of the pump power can change the average temperature of the gain material. The temperature of a material and its refractive index are related through the thermo-optical effect. With the inclusion of thermal expansion, the change in frequency of a longitudinal mode with temperature is given by [185]:

$$\frac{d\upsilon}{dT} = -\upsilon_0\left(\frac{1}{n}\frac{dn}{dT} + \frac{1}{L}\frac{dL}{dT}\right)$$

Equation 15

where ν is the laser oscillator frequency, ν_0 is a known oscillator frequency at a given temperature, n is the refractive index and L is the length of the crystal. An approximation to the average temperature in the pumped region of a monolithic microchip laser is [186]:

$$\text{Average Temperature} = \frac{Q}{4\pi kL}\left(-2\ln(A) + 0.5\right)$$

Equation 16

where k is the thermal conductivity, Q is the thermal power absorbed by the crystal and A is the ratio of the pump radius to the crystal radius. The derivation of this equation and its implications will be discussed in the next chapter.

If we combine Equation 15 and Equation 16 the pump power tuning rate is:

$$\frac{d\upsilon}{dQ} = \left(\frac{\left(2\ln(A) - 0.5\right)\upsilon_0}{4\pi kL}\right)\left(\frac{1}{n}\frac{dn}{dT} + \frac{1}{L}\frac{dL}{dT}\right)$$

Equation 17

Thus the pump power frequency-tuning rate is dependent on absorption distribution of the pump power and on four material properties:

1. Thermal expansion coefficient ($^{dL}/_{dT}$),
2. Thermo-optical coefficient ($^{dn}/_{dT}$),
3. Thermal conductivity (k)

4. Crystal size. (A,L)

From the thermal characteristics listed in Table 6 we would expect significantly different temperatures and tuning rates for Nd:YVO_4, Nd:YOS, Nd:SFAP, and Nd:SVAP.

The fluro-apatites, Nd:SFAP and Nd:SVAP, have low thermal conductivities, approximately half those of the oxides, Nd:YOS and Nd:YVO_4, giving much larger average temperatures for a given pump power. This is offset in terms of tuning rate by negative thermo-optical coefficients. The thermal expansion coefficients are however greater than the thermo-optical coefficients, providing a stable cavity and giving negative pump power frequency tuning.

The oxides in contrast have lower average temperatures but have both positive thermo-optical and thermal expansion coefficients. Therefore, although oxides may have considerably lower temperature rises, their tuning rates can be comparable to the fluro-apatites because of the combination of these effects.

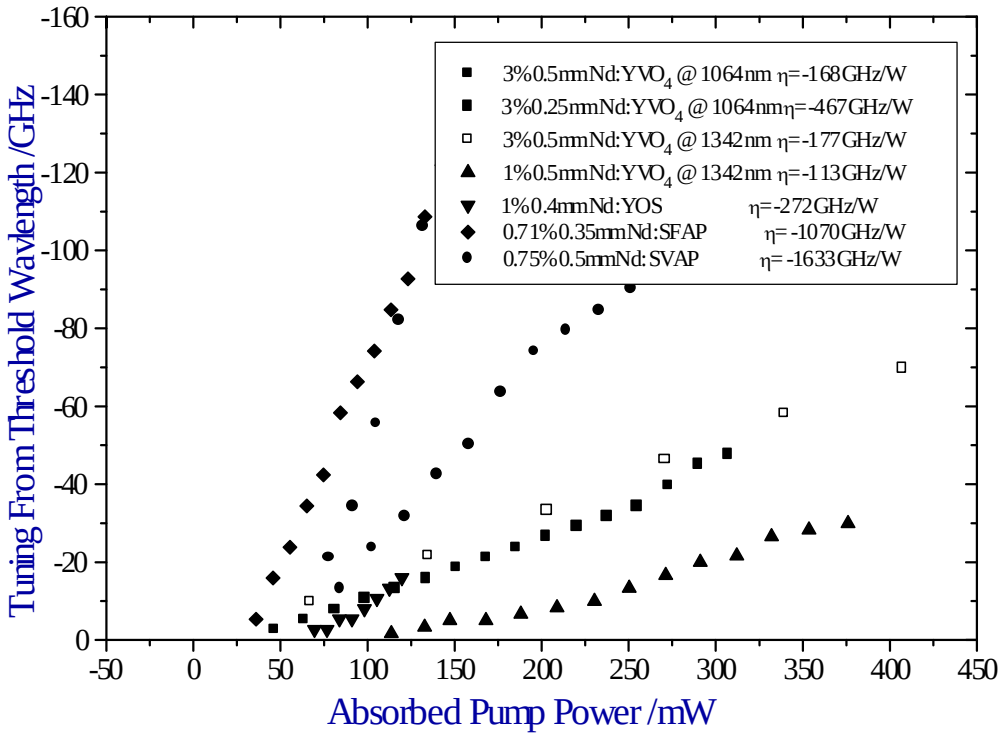

Figure 27 – Frequency tuning of Nd:YVO_4, Nd:YOS, Nd:SFAP and Nd:SVAP as a function of absorbed pump power. The tuning rate of 0.25mm long 3% Nd:YVO_4 and 0.5mm long 1&3% Nd:YVO_4 at 1342nm are also considered.

Crystal	Average Temperature (^oC/W)	Calculated Tuning Rate GHz/W		Measured Tuning Rate	
		GHz/W	GHz/^oC	GHz/W	GHz/^oC
Nd:YVO_4 (5x5x0.5mm)	100.02	-164	-1.64 [185]	-168	-1.68
Nd:YVO_4 (5x5x0.25mm)	200.05	-328	-	-467	-2.33
Nd:YOS (3x3x0.4mm)	141.7	-257	-1.82	-272	-1.91
Nd:SFAP (3x3x0.35mm)	364.3	-	-	-1070	-2.93
Nd:SVAP (3x3x0.5mm)	300.1	-	-	-1633	-5.44

Table 10 – Calculated and measured tuning rates for temperature and pump power tuning of Nd:YVO_4, Nd:SFAP, Nd:YOS and Nd:SVAP. The temperatures are calculated assuming 40% quantum defect heating, in a 75μm pump spot.

With moderate pump powers and short crystals, large frequency tuning ranges can be achieved. The large free spectral range arising from the short microchip laser can give tuning ranges greater than 100GHz. Indeed, a 0.25mm long 3% doped Nd:YVO_4 microchip with 5% output coupling was tuned over 660GHz before the temperature gradient from the pumped region caused the crystal to fail. This tuning range is larger than the gain bandwidth (257GHz FWHM), though can be explained because the gain centre tunes as well, at a rate of 0.53GHz/^{o}C [185].

The tuning rate of the 0.25mm long Nd:YVO_4 crystal is larger than that expected by theory because of the use of nominal crystal lengths in the modelling and the assumption of no axial variation in the temperature profile of the crystal. There was however good agreement between the tuning rate of similar devices operating at 1064nm and 1342nm. The 1% doped material showed a lower tuning rate than expected, again because of the assumptions used in the thermal modelling.

Nd:YOS had similar tuning characteristics to Nd:YVO_4 because of their similar thermal properties as discussed earlier. In contrast the apatites exhibited tuning rates up to an order of magnitude greater than the oxides, indicating strong thermal expansion. Qualitative work on examining the optical path distortion of Nd:SFAP and Nd:SVAP when pumped, showed the change in optical path length was several times that of an equivalent Nd:YVO_4 microchip laser confirming this.

Fluctuations in the amplitude of the pump can cause gain switching as discussed

earlier. More importantly it can determine a lower limit to the frequency stability of the laser output. In this respect Nd:YVO_4 is expect to be the least sensitive of our materials to thermal fluctuations and transients in the pump power level.

A heterodyne technique was used to measure the beat frequency between two free running 0.5mm long Nd:YVO_4 microchip lasers operating at 1064nm. The linewidth was measured to be less than 300kHz, limited by detector. The beat frequency was stable to within 100MHz over several minutes when the microchip lasers were isolated from air-flows. A similar result was obtained for the same experiment using two 1342nm Nd:YVO_4 microchip lasers. The linewidth of a Nd:YVO_4 microchip should be of the order of 100Hz [187].

This stability is equivalent to a pump power fluctuation of 0.5mW which is equivalent at high powers to the 0.7% peak-peak noise signal on the laser diode output.

2.5.2 Mechanical Tuning

The second form of cavity length modulation is through mechanical processes. Mechanically applied stress or strain can alter the optical path of a monolithic laser causing the frequency to tune proportionally to the applied pressure.

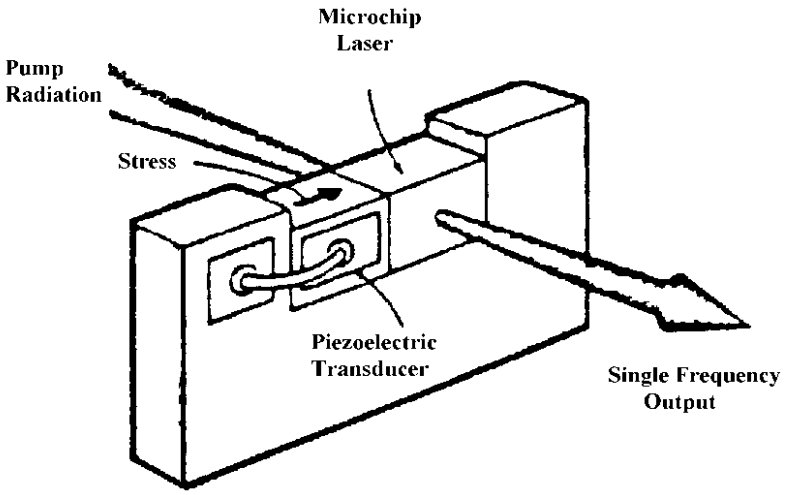

Figure 28 - Mechanical Frequency Tuning [after 188]

By applying a small transverse stress to a monolithic Nd:YAG crystal, Owyoung and Esherick showed in 1987 that it was possible to change the cavity length sufficiently to tune the device over a large portion of the 1064nm transition [189]. Zayhowski

subsequently showed, using the system illustrated in Figure 28, single frequency operation from a 0.65mm long monolithic Nd:YAG microchip laser tuned over 300MHz at frequencies of up to 25MHz [188]. The response of these devices was limited by mechanical and acoustic considerations with acoustic resonances limiting the frequency tuning range. The fragility of some gain materials would limit the wide spread implementation of this technique.

In a similar fashion strain could be used to modulate the output of a microchip laser in and this mechanical control of the output could potentially be used to feedback information about the microchip environment in a sensor system.

Compression and rarefaction can also be achieved by launching acoustic waves into the laser crystal. To date this has not explored as a frequency modulation technique for monolithic lasers, though could potentially offer improved performance over the mechanical compression techniques described above.

2.5.3 Electrical Modulation

The third and final form of frequency tuning is to alter the optical path length by an applied electric field. For a monolithic device, the electro-optic properties of a doped non-centrosymmetric crystal can be used to change its refractive indices. Previous work in St.Andrews by MacKinnon and Sinclair has shown a diode-pumped electro-optically tuneable Nd:MgO:$LiNbO_3$ microchip laser [190]. Frequency tuning ranges of up to 1.7GHz were achieved in a multi-longitudinal mode by applying 200V across the crystal to access the r_{33} non-linear coefficient in $LiNbO_3$.

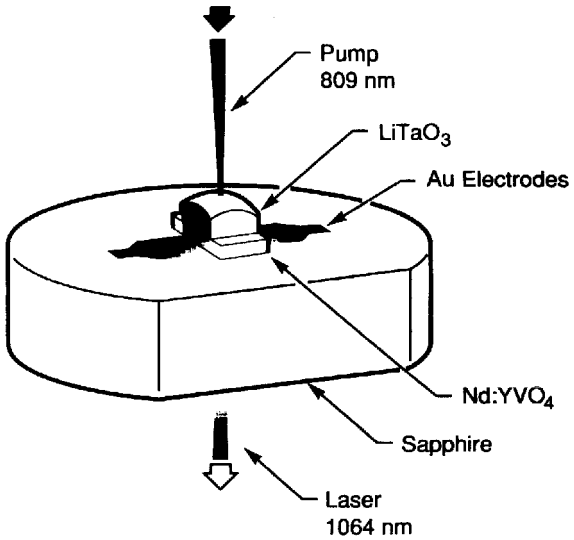

Figure 29 - Electro-Optically Tuned Composite Microchip [after 192]

Other frequency modulation techniques have been demonstrated using composite microchip devices. Zayhowski reported an electro-optically tuned device based on a sandwich of lithium tantalate and Nd:YAG with a tuning range of 30GHz [191]. Robrish reported a similar device using Nd:YVO_4, shown in Figure 29, to achieve tuning ranges of up to 120GHz [192]. Tuning by use of a discrete output coupler mounted on a piezoceramic has be used to modulated the output of a 1320nm Nd:YAG hybrid microchip over 58GHz without polarisation switching [193].

In conclusion, this section has reviewed a number of different frequency modulation techniques, which can be applied to monolithic microchip lasers. Pump power tuning of a range of Nd^{3+} doped materials has been demonstrated, with tuning ranges of up to 660GHz.

2.6 Summary & Conclusions

Crystal	**Nd:YVO_4**		**Nd:SFAP**	**Nd:YOS**	**Nd:SVAP**
	1064nm	**1342nm**			
Dimensions /mm	5x5x0.25 / 0.5		3x3x0.35	3x3x0.4	3x3x0.5
Doping Concentration	3%		0.71%	0.7%	0.75%
Output Coupling	1,5,10%		2%	1%	1%
Absorption Characteristics					
Orientation	π (|| C Axis)		π (|| C Axis)	y Axis	π (|| C Axis)
Peak Absorption Coefficient /mm^{-1}	9.1		2.12	1.17	5.98
Centre of Absorption Peak	808.85		804.7	810.51	809.68
FWHM of Peak /nm	6.5		3.3	2	-
Gain Characteristics					
Centre of Fluorescence /nm	1064.0	1342.1	1059.0 1328.2	1073.9	1065.6 1338.7
FWHM of Fluorescence /nm	0.68	0.66	0.9 0.85	1.5	1.1 1.3
Lifetime /μs	55	55	427	525	333
CW Lasing: 0.5/1.2W Pumping					
Threshold /mW	16.7 / 39.7	34 / 76	23 / 74	38 / 83	64 / 65
Slope Efficiency	52.1 / 51.1	50.7 / 50.5	46% / 46%	49% / 50%	9% / 4%

Max SLM /mW	>140	>105	24 / 17	35 / 25	4 / 3
Gain Switching					
Pulse FWHM /ns	9.1	15.2	24.7	58.2	49.3
Peak Power /ns	1240	760	539	123	85.3
Repetitive Gain Switching					
Pulse FWHM /ns	16.8	26	49.6	51.7	22.3
Peak Power /mW	676	462	244	361	163
Rep Rate /kHz	85.8	82.3	75.4	85.8	84.3
Pump Power Tuning					
Tuning Rate GHz/W	-167	-177	-1070	-355	-1633
Tuning Rate GHz/^{o}C	-1.77	-1.41	-1.97	-1.95	-2.22

Table 11 – Summary of the properties measured in this chapter for Nd:YVO_4, Nd:SFAP, Nd:YOS and Nd:SVAP monolithic microchip lasers.

In conclusion this chapter has characterised a range of Nd^{3+} doped monolithic microchip lasers. These characteristics are summarised in Table 11 for the Nd:YVO_4, Nd:SFAP, Nd:YOS and Nd:SVAP crystals used.

The basic absorption and emission properties were measured, indicating that Nd:YVO_4 and Nd:SFAP were the most promising materials, with Nd:SVAP the least favourable. The wide, strong absorption bands for diode pumping around 810nm and the intense, narrow fluorescence of the former two materials mean they are more suited to diode-pumped microchip geometries than Nd:YAG.

Low threshold (<100mW) and high slope efficiencies (>40%) were measured for all the gain materials, with the exception of Nd:SVAP. This poor performance was attributed to strong fluorescence quenching in Nd:SVAP and poor crystal quality. The laser output was diffraction limited and strongly polarised in each case. Significant single frequency powers were measured, indicating the advantages of a monolithic microchip laser design. The CW lasing properties of all these microchip lasers was summarised in Table 8.

Nd:YVO_4 was investigated more thoroughly because it exhibited the best lasing properties. The 1064nm and 1342nm transitions were examined and the effect of different output couplings, doping concentrations and crystal lengths considered. Single frequency powers in excess of 100mW were measured, with slope efficiencies exceeding 50% and thresholds less than 20mW.

The intensity and frequency modulation of these lasers was also considered. Intensity modulation, in the form of gain switching, was examined. Pulses as short as 10ns were measured with peak powers up to 1.3W, in agreement with analytical and numerical modelling. Repetitive gain switching showed single low intensity pulses could be produced at repetition rates around 85kHz.

Pump power tuning could be used to tune all the monolithic lasers over significant fractions of their gain bandwidths without mode jumping. In the case of Nd:YVO_4, a tuning range in excess of 650GHz was achieved.

Finally, the performance of monolithic Nd:YVO_4 described here formed the reasoning for the continuation of its use in the subsequent chapters of this thesis. Similar studies of monolithic microchip lasers based on other active ions and new and novel Nd^{3+} doped materials would enhance these results and indicate new possibilities.

References:

[148] T. Kushida and J.E. Geusic, Phys. Rev. Lett., **21**, 1172 (1968)

[149] L.F. Johnson and K. Nassau, Proc. I.R.E., **49**, 1704 (1961)

[150] ITI Electro-Optics Data Sheet on Nd:YVO_4 (1994)

[151] R.S. Conroy, N. MacKinnon, D.G. Matthews and B.D. Sinclair, OSA Tech. Digest ECLEO'96, Paper CFH1, 334 (1996)

[152] W.A. Clarkson, R. Koch and D.C. Hanna, Opt. Lett., **21:10**, 737 (1996)

[153] D.G. Matthews, N. MacKinnon, R.S. Conroy and B.D. Sinclair, Private Communication (1996)

[154] T.S. Kubo and T.J. Kane, IEEE J. Quantum Electron., **28:4**, 1033 (1992)

[155] R.G. Smith, IEEE J. Quantum Eelectron., **4**, 505 (1968)

[156] S. Singh, R.G. Smith and L.G. Van Uitert, Phys. Rev. B, **10**, 2566 (1974)

[157] J. Marling, IEEE J. Quantum Electron., **14**, 56 (1978)

[158] E. Broch, Z. Physik. Chem. B, **20**, 345 (1933)

[159] A.K. Levine, F.C. Palilla, Appl. Phys. Lett., **5:6**, 118 (1964)

[160] J.J. Rubin and L.G. van Uitert, J. Appl. Phys., **37**, 2920 (1966)

[161] J.R. O'Connor, Appl. Phys. Lett., **9:11**, 407 (1966)

[162] P.P. Yaney, L.G. DeShazer, J. Opt. Soc. Am., **66:12**, 1405 (1976)

[163] A.W. Tucker, M. Birnbaum, C.L. Fincher and J.W. Erler, J. Appl. Phys., **48:12**,

4907 (1977)

[164] T.S. Lomheim and L.G. DeShazer, J. Appl. Phys., **49:11**, 5518 (1978)

[165] R.A. Fields, M. Birnbaum and C.L. Fincher, Appl. Phys. Lett., **51:23**, 1885 (1987)

[166] T. Taira, A. Mukai, Y. Nozawa, T. Kobayashi, Opt. Lett., **16:24**, 1955 (1991)

[167] R.C. Ohlmann, K.B. Steinbruegge and R. Mazelsky, Appl. Opt., 7, 905 (1968)

[168] G.B. Loutts, B.H.T. Chai, S.P.I.E. Proc., **18:63**, 31 (1993)

[169] B.H.T. Chai, OSA Proc on ASSL'94, **41**, 20 (1994)

[170] R.E. Peale, P.L. Summers, H. Weidner, B.H.T. Chai and C.A. Morrison, J. Appl. Phys., **77:1**, 270 (1995)

[171] J.B. Gruber, C.A. Morrison, M.D. Seltze, A.O. Wright, M.P. Nadler, T.H. Allik, J.A. Hutchinson and B.H.T. Chai, J. Appl. Phys., **79:3**, 1746 (1996)

[172] X.X. Zhang, M. Bass, B.H.T. Chai, P.J. Johnson and J.C. Oles, J. Appl. Phys., **80:3**, 1280 (1996)

[173] P. Hong, J. Appl. Phys., 77, 294 (1995)

[174] M.R. Dickinson, L.A.W. Gloster, N.W. Hopps and T.A. King, Opt. Comm., **132**, 275 (1996)

[175] A.A. Kaminskii, "Laser Crystals - Their Physics and Properties" (2^{nd} Ed), Springer-Verlag, 252 (1993)

[176] W.F. Krupke and L.L. Chase, Opt. & Quantum Electron., **22**, S1 (1990)

[177] R. Beach, G. Albrecht, R. Solarz, W. Krupke, B. Comaskey, S. Mitchell, C. Brandle and G. Berkstresser, Opt. Lett., **15:18**, 1020 (1990)

[178] D.G. Matthews, J.R. Boon, R.S. Conroy and B.D. Sinclair, J. Mod. Opt., **43:5**, 1079 (1996)

[179] J.R. Boon, "Comparison of Nd:YVO_4, Nd:YOS, Nd:SFAP and Nd:SVAP Microchip Lasers", Senior Honours Report, Physics Department Library, University of St.Andrews, 48 (1995)

[180] J.J. Zayhowski, IEEE J. Quantum Electron., **26:12**, 2052 (1990)

[181] R.S. Conroy, N. MacKinnon and B.D. Sinclair, OSA Tech. Digest CLEO'95, Paper CTuP2, **13** (1995)

[182] W. Koechner, "Solid-State Laser Engineering" (3^{rd} Ed.), Springer-Verlag (1992)

[183] K. Otsuka, IEEE J. Quantum Electron., **13**, 520 (1977)

[184] K. Otsuka and K. Kubodera, IEEE J. Quantum Electron., **16:4**, 419 (1980)

[185] T. Taira, A. Mukai, Y. Nozawa, T. Kobayashi, Opt. Lett., **16:24**, 1955 (1991)

[186] A.K. Cousins, IEEE J. Quantum Electron., **28:4**, 1057 (1992)

[187] J.J. Zayhowski, Lincoln Lab Journal, **3** (1990)

[188] J.J. Zayhowski and A. Mooradian, Opt. Lett., **14:12**, 518 (1989)

[189] A. Owyoung, P. Esherick, Opt. Lett., **12**, 999 (1987)

[190] N. MacKinnon, C.J. Norrie and B.D. Sinclair, J.O.S.A. B, **11:3**, 519 (1994)

[191] J.J. Zayhowski, P.A. Schulz and S.R. Henion, OSA Technical Digest CLEO'93, Paper CThR4 (1993)

[192] P. Robrish, Opt. Lett., **19:11**, 813 (1994)

[193] F. Zhou and A.I. Ferguson, Elect. Lett., **26:7**, 490 (1990)

Chapter 3 - TRANSVERSE MODE DEFINITION IN MICROCHIP LASERS

3.1 Introduction

In the previous chapter we characterised a variety of different gain crystals as monolithic microchip lasers, in particular Nd:YVO_4. It is perhaps surprising that such a high quality and efficient output is produced given the poor quality and asymmetry of the diode pump light. This chapter is an investigation of the two major mechanisms, thermal and gain guiding, which can define the transverse mode in a monolithic microchip laser.

The cavity of a monolithic microchip laser is typically formed by coating suitable dielectric mirrors on two near-parallel faces of the gain crystal. This plane-plane cavity is on the edge of stability and provides a good starting point for observing both thermal and gain guiding effects. Pumping with a laser diode causes distortion of the optical path in the lasing mode volume, through a number of effects, generally giving a more stable cavity and promoting a single transverse mode. These effects include thermal expansion, change in the refractive index with temperature and dispersion caused by detuning from the centre of the gain.

This chapter will begin by considering what is meant by cavity stability and then move on to consider how the cavity stability can be affected by heat diffusing from the pumped region. A number of different modelling techniques are described and compared highlighting the expected operating characteristics. The following section then describes a range of experiments to characterise the thermal distortion of monolithic Nd:YVO_4 microchip lasers and these experimental results are compared to the theoretical modelling.

The final section introduces the effect of gain distribution on the definition of the transverse mode. The circumstances under which gain-induced refractive index guiding can dominate are described and a basic model derived, modifying the 1D analytical thermal model. In particular a gain-related effect, self Q-switching, is examined and modelled. However first we will consider why thermal modelling is important and how cavity stability effects the transverse mode.

3.1.1 Behaviour at High Pump Powers

The need for an understanding of thermal effects is best illustrated by the behaviour of monolithic microchip lasers with high CW pump powers. In the previous chapter we considered the operation of 0.25mm and 0.5mm long Nd:YVO_4 microchip lasers pumped by a 0.5W laser diode and mentioned that pumping by a 1.2W laser diode has also been attempted but the 0.25mm long crystal had cracked. These results will now be considered in more detail to highlight the upper-limit of the operating envelope of these lasers.

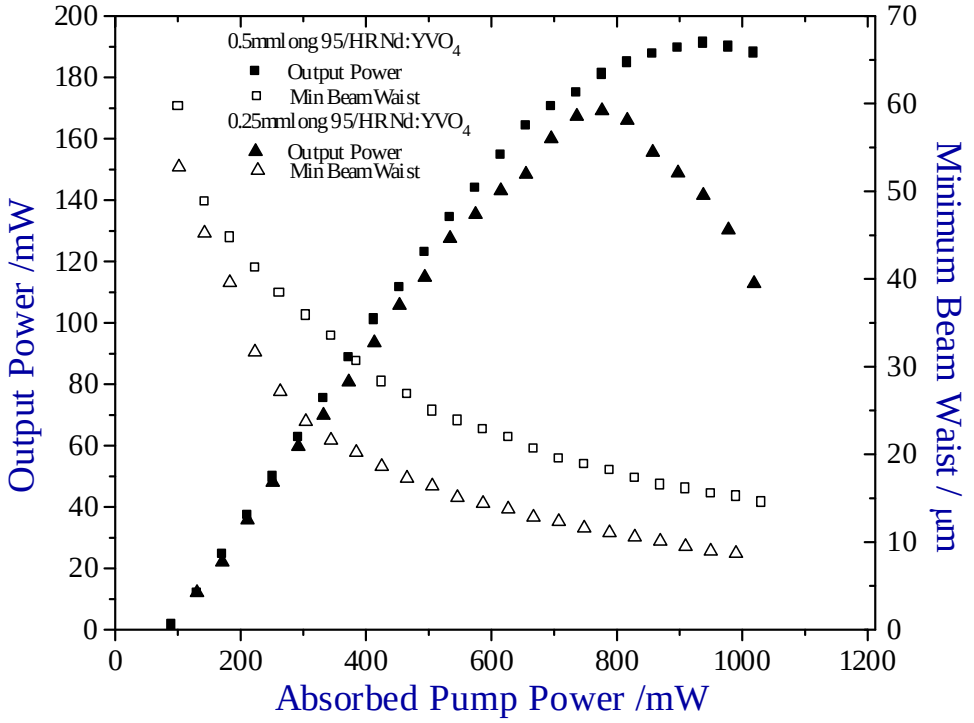

Figure 30 – Minimum beam waist and output power from a) 0.5mm and b) 0.25mm long 95/HR Nd:YVO_4 microchip laser pumped with a 1.2W laser diode, through 8mm collimating lens, and 6.5mm focussing lens.

As can be seen there is a substantial decrease in the efficiency of the 0.25mm long microchip laser as it approaches fracture. This is matched by a rapid increase in the frequency tuning rate of the cavity with pump power, giving an overall tuning in excess of 660GHz from room temperature to fracture. If material properties were independent of temperature, this would equate to a temperature rise in the pumped region in excess of 500^{o}C! Even small temperature rises can significantly distort the operation of a laser; therefore, an understanding of the effect of heating is essential in understanding the limitations and optimisation of a microchip laser system.

3.1.2 Cavity Stability

The geometry of a laser resonator primarily determines the mode structure of the resulting laser output. A laser cavity can be described by its Fresnel number, N, and cavity parameters g_1 and g_2 defined as:

$$N = \frac{\omega_0^{\,2}}{\lambda d}$$

$$g_1 = 1 - \frac{d}{R_1}, g_2 = 1 - \frac{d}{R_2}$$

Equation 18

where ω_0 is the minimum beam radius in the cavity, λ is the laser wavelength in the cavity medium, d is the cavity length, and R_1 and R_2 are the radii of curvature for the two end mirrors of the cavity. The Fresnel number can also be thought of as the ratio of the acceptance angle of one mirror as viewed from the centre of the other, to the diffraction angle of the beam.

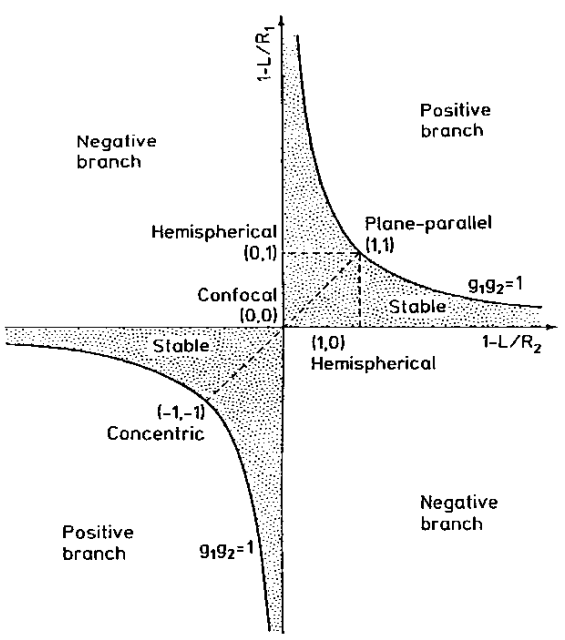

Figure 31 - Stability diagram for a passive laser resonator [after 196]

The condition for a stable cavity can be expressed as:

$$0 < g_1 g_2 < 1$$

Equation 19

Figure 31 shows the types of resonators that fall within the stable region (shaded). A plane-plane cavity, that of an unpumped microchip laser, is marked at (1,1). When the

laser is pumped by a laser diode, heat flows from the hotter pumped region to the cooler edges of the crystals, resulting in a temperature gradient. This temperature gradient in turn induces a refractive index and thermal expansion profile. Generally, the combination of these effects provides a net increase in the optical path length with increasing temperature, equivalent to a concave mirror on one or both ends of the cavity. In Figure 31 this equates to a geometry lying within the region bounded by hemispherical, plane-parallel and confocal cavities.

Therefore thermal effects are beneficial in defining a stable cavity, however as we have also seen, thermal effects ultimately limit performance as well. One of the most attractive features of microchip lasers is that they form a self-aligning, stable cavity, in contrast to other solid-state lasers that require careful alignment of cavity mirrors. However, the pump-power dependence of the cavity geometry also limits its scalability at both very low and very high average pump powers.

A stable cavity is particular attractive because it can lead to a lower lasing threshold and a diffraction-limited (TEM_{00}) transverse mode, qualities which are desirable for our microchip lasers. However, for a cavity with end mirrors of small radii of curvature, diffraction is significant and there is poor overlap between pumping and lasing mode volumes, as indicated experimentally by the roll-off in output power at high pump powers in Figure 30. Therefore, to define a stable cavity, though not necessarily one that is inefficient, there are three parameters of a laser system we must consider: pumping geometry, heat sinking and material parameters.

The aim of this chapter is to look at mechanisms through which a stable cavity can be formed in a monolithic microchip laser, and the limitations these impose on the laser's operation. We have already indicated how heat flow can define a stable cavity, and we will consider this guiding mechanism in the first half of this chapter. The thermal work has been divided into two sections, one investigating the modelling of thermal effects and the second how these effects can be measured and related to this modelling. The second half of this chapter will investigate how gain can also effect the cavity stability of a laser. This is then integrated into our thermal work, to produce an overall picture how the transverse mode is defined in a monolithic microchip laser.

3.2 Thermal Modelling of Microchip Lasers

3.2.1 Introduction

The first guiding mechanism we will consider is the flow of heat from the pumped region. All laser systems experience heating of the gain medium through a number of different processes. There are three main sources of this heating. Fundamentally for a laser, the relaxation of an electron from the state into which it is excited by a pump source involves at least one non-radiative transition and this provides so-called 'quantum defect heating'. Further heating can occur when the quantum efficiency of the lasing transition is less than unity, for example where alternative quenching mechanisms exist, providing non-radiative phonon decay. These quenching mechanisms often determine the maximum concentration of an active ion in a laser host. The third source of heating occurs when the gain medium is pumped with a broad band source, such as a flashlamp. Significant absorption can occur at many wavelengths exciting undesirable processes and adding to the heating of the medium.

End pumping with a laser diode is an efficient way of minimising thermal effects because of the diode's narrow spectral bandwidth and the good overlap between the pumped and lasing regions. For these reasons typically the thermal load of a diode-pumped solid-state laser is only a third that of an equivalent flashlamp pumped system.

This heating is useful in a microchip laser, providing a mechanism by which a stable cavity is formed as described in the previous section. However, it is also desirable to minimise the effect of this heating at higher pump powers to avoid decreasing efficiency and ultimately fracture or breakdown of the medium.

This aim of this section is to consider how the thermal effects in an end-pumped microchip laser can be modelled, analytically and numerically, to predict its behaviour and limitations. We will begin by reviewing the development of thermal models and some basic properties of laser crystals, before describing some of the basic features of all thermal models. Then a comprehensive 1D analytical model is presented, which is used to compare different gain crystals and pumping geometries. This section concludes with an examination of numerical models and their input into our understanding of thermal guiding in microchip lasers.

3.2.1.1 Historical Review of Thermal Modelling

Koechner was amongst the first to study and model thermal effects in lasers [194]. Using the approximations of an infinitely long rod to remove axial heat flow, no transient temperature perturbations, and without addressing the issues of stress, strain or birefringence, he derived an analytical solution for the temperature distribution within a laser rod. In two further publications, he added stress-induced birefringence [195] and two-dimensional temperature variations and stress effects under uniform pumping [196] to his initial work to produce a more comprehensive model.

Early work on thermal effects in flashlamp pumped Nd:YAG systems showed the focal length of the induced thermal lens varied inversely and nonlinearly with the absorbed power [197]. This thermal lensing was also shown to introduce thermal bifocusing and birefringence, which greatly affected the operation of the laser.

Kane et al. [198] and Eggleston et al. [199] both analytically investigated thermal effects in slab lasers, concentrating on lamp-pumped slabs. Further work by Kane et al. developed numerical solutions in two dimensions based on his earlier analytical work and compared it to experimentally measured results [200]. Later work by Hello et al. [201] on side pumping of slabs with laser diodes produced a three dimensional model based on the complex summation of harmonic functions.

The use of a pump light collector for laser diode side-pumped Nd:YAG lasers was modelled and compared to experimental results by Jackson and Piper [202]. All-round cooling of the rod was possible using the collector and different heat sinking materials were compared.

Although useful in concept, these early models assumed side pumping of the laser material and are therefore not directly applicable here. The improvement of laser diode technology and the development of end-pumped solid state lasers in the 1980's however provided the impetus to model systems more directly relevant to this work.

3.2.1.2 Thermal Modelling of DPSSLs

Refinement of the modelling to take account of finite length laser rods subject to Gaussian and 'top-hat' pump profiles was made by Farrukh et al. in the late 1980's [203]. Eigen-mode solutions were derived for various pumping geometries although the study focused on transient rather than CW effects and did not consider thermal stress. Further refinements, including side and end-pumping with consideration to

particular laser systems were made in a later paper, using computer models to solve equations numerically in time for pulsed systems [204].

Work has been done in St.Andrews to produce a Mathcad computer document from which thermal lensing in laser rods can be modelled, based on Farrukh's work [205]. The computing power required for this model, typically twenty minutes on a 100MHz Pentium processor, increased substantially with precision. Therefore, this model was considered to be of limited value and not pursued further for this thesis.

A more simplistic solution for finite-length end-pumped laser rods was derived by Cousins [206]. This work will form the basis of the analytical solution derived in the next section. It is based on the aspect ratio of the rod and includes stress and strain effects for a one-dimensional cylindrical solution.

The effect of thermal lensing on the mode matching between the lasing and pump modes was considered by Frauchiger et al. with particular interest in the extreme cases where higher order ring modes can oscillate [207]. They found that to maintain fundamental transverse mode operation in a stable resonator the laser mode size should not exceed 1.3 times the pump mode size for top-hat (laser diode) pumping and 0.75 times for Gaussian beam excitation. Further work by this group modelled the one dimensional solution to the standard heat equation using finite element analysis, taking account of finite rod size, cooling and stress and compared it to measured optical path differences from a Twyman-Green interferometer for Nd:YAG, Nd:GSGG and Nd:YLF [208]. They found that face-cooling decreased the overall thermal lens though increased stress and strain, in particular for more highly doped materials and higher thermal conductivities. Highly doped materials were also found to have better spatial overlaps with divergent pump sources, such as laser diodes. Even with face cooling, the magnitude of the thermal lensing was still an order of magnitude higher for Nd:YAG and Nd:GSGG than for Nd:YLF. This was attributed to the small net optical path distortion in Nd:YLF due to its negative thermal dispersion.

Thermally induced optical distortion in end-pumped rod lasers was considered by Sutton and Albrecht for both Gaussian and super-Gaussian pump profiles [209]. Analytical and numerical solutions in two dimensions were derived for end-cooled rods based on the aspect ratio of the rod.

3.2.1.3 Thermal Modelling of Microchip Lasers

Zayhowski was the first to report on thermal guiding in Nd:YAG microchip lasers. He derived an expression whereby the minimum beam waist in the cavity varies with the inverse fourth root of the pump power which he supported with experimental results [210]. This work did not find any evidence for gain guiding and did not take account of surface distortion.

Work in St.Andrews using LNP microchip lasers, which experience a negative change in refractive index with temperature, found that surface distortion through thermal expansion could form a stable cavity even with a negative thermal lens present [211]. Again, this work reported no evidence of gain guiding.

Omatsu et al. investigated thermal effects in a monolithic, self-frequency-doubled, diode pumped NYAB microchip laser [212]. As well as thermal lensing, the heating of the gain material caused a phase mismatch for the second harmonic power and this was investigated using a Michelson interferometer. There is a similar, though less severe, problem with composite frequency-doubled devices, in particular those with narrow temperature bandwidths and this is discussed in chapter five of this thesis.

Harrison and Martinsen investigated the modelling of monolithic crystals of Nd:YAG and Tm,Ho:YLF pumped with a one dimensional array of pump spots, theoretically with a finite element method, and experimentally with a diode bar array [213]. They found an upper limit in pump power below which the arrays would lase in a single transverse mode, though computational problems restricted their ability to model this.

More recently work by our group in St.Andrews reported evidence of both thermal and gain guiding in Nd:YVO_4 microchip lasers [214]. This work forms the basis of the experimental evidence used in this chapter and represented our first attempt at quantifying thermal effects in microchip lasers and their influence on the operation of the laser.

This chapter extends our earlier work by building on the work described in this sub-section to develop a comprehensive range of modelling and experimental techniques for studying thermal effects and transverse mode definition in microchip lasers. Before considering the effect of different pumping and heat-sink geometries, we will consider how material parameters influence the operation of a monolithic laser.

3.2.1.4 Thermal Properties of Common Laser Materials

As mentioned previously, the material properties of the gain crystal are one of the three main parameters which can influence the temperature distribution and hence the transverse mode definition in a monolithic laser. The most significant of these properties is the thermal conductivity, which determines how efficiently heat can flow from the pumped region. A material with a high thermal conductivity will have a relatively low maximum temperature with a low temperature gradient to the cooled edges. Conversely, a material with low thermal conductivity will have a substantial temperature rise in the pumped region with a sharp temperature gradient, significantly increasing the possibility of thermal fracture.

	Nd:YAG	**Nd:YVO_4**	**Nd:YLF**	**Cr:LiSAF**	**Ti:sapphire**
Crystal Type	Cubic	Uniaxial	Uniaxial	Uniaxial	Uniaxial
Absorption Coefficient (cm^{-1})	0.85% = 7.1	1.1% = 31 3% = 120	-	-	-
Thermal Expansion Coefficient ($*10^{-6}$ K^{-1})	7.5	a = 4.43 c = 11.37	a = 1.3 c = 8	a = 19 c = -10	8.4
Thermal Optical Coefficient ($*10^{-6}$ K^{-1})	7.3	a = 8.5 c = 3	a = -2.0 c = -4.3	-	14
Thermal Conductivity ($WcmK^{-1}$)	0.13	a = 0.051 c = 0.0523	0.06	a = 0.0458 c = 0.0514	0.33/ 0.35
Specific Heat Capacity ($Jg^{-1}K^{-1}$)	0.6	0.51	0.79	0.842	0.775
Density (gcm^{-3})	4.55	4.22	3.99	-	3.99
Refractive Indices (@1064nm)	1.82	a = 1.96 c = 2.165	a = 1.45 c = 1.47	-	1.76

Table 12 - Thermal properties of common laser crystals.

From Table 12, the exceptionally high thermal conductivity of Ti:sapphire gives rise to the ability to pump a relatively small crystal with a focussed argon ion beam of tens of watts, impractical for the other gain materials. At the opposite extreme, the unusual thermal expansion coefficients of Cr:LiSAF and its much lower thermal conductivity limit CW pump powers to a few hundred milliwatts.

Of the Nd^{3+} doped materials, Nd:YAG has the most attractive thermal properties, though a Nd:YAG laser is potentially more susceptible to thermally induced birefringence because of its isotropic structure. The properties of Nd:YLF and $Nd:YVO_4$ are similar, except for the negative thermo-optical coefficient in Nd:YLF, characteristic of fluoroapatites.

Although not so critical for rare-earth ions like Nd^{3+}, the temperature of the pumped region can also significantly alter the absorption and emission properties of the ions. For example, the lifetime of the Cr^{3+} ions in Cr:LiSAF decreases more than 80% for a 80^oC increase in temperature of the pumped region, significantly inhibiting lasing. Such a drop in performance is common for transition metal ions, though similar effects can be seen in quasi-four level rare-earth ion systems because of thermal population of the lower lasing level. However, these quasi-four level systems remain attractive because the quantum defect heating can be less than 10% of the absorbed pump power, therefore limiting the temperature rise experienced. In contrast, the quantum defect heating for the 1064nm transition pumped at 810nm is 24%, rising to 40% for the 1342nm transition, providing significant heating.

The crystals used for this work were the same monolithic $Nd:YVO_4$ microchip lasers as described in Chapter Two. With larger temperature variations however, the thermal properties of $Nd:YVO_4$ can alter substantially. A peculiarity of $Nd:YVO_4$ is the decrease in the thermal expansion coefficient along the c axis with increasing temperature. However, for the orientation of $Nd:YVO_4$ used in devices here, the a axis is in the axial plane, and thus with increasing temperature we would expect to see an increasing tuning rate with temperature due to the increasing thermal expansion coefficient. Indeed, in Chapter Two, when 0.25mm thick pieces were operated close to their fracture limit, a rapid increase in the temperature-tuning rate was observed. The density, thermo-optical coefficients, specific heat capacity and thermal conductivity also show marked variations with temperature, which needs to be considered when a device is operated close to its fracture limit, although have not been quantified.

For the remaining work in this chapter, it is assumed the material properties are independent of temperature. For large frame lasers, this is a realistic approximation because of the small temperature rises. However for microchip lasers, with temperature rises exceeding 100^oC this is clearly a substantial approximation.

3.2.2 Standard Heat Equation

To understand how a stable laser cavity can be formed from heating of the gain medium, the temperature rise and flow of heat from the pumped region must be considered. The temperature profile can then be used to determine the effect of thermal expansion and change in refractive index with temperature on the optical path length profile in the laser cavity. Analytical and numerical models to determine the temperature profile can be derived from the standard heat equation and this is the starting point for all the modelling in this chapter.

The standard heat equation describes the general effect of a heat source, Q(r,t), in time and space on a material such that:

$$\rho(T)c(T)\frac{\partial T}{\partial t} - k(T)\nabla^2 T = Q(r,t)$$

Equation 20

where T is the temperature and is determined by these temperature-dependent material properties: $\rho(T)$ is the density of the material being heated, c(T) is specific heat capacity and k(T) is the thermal conductivity.

A physical interpretation of this equation can help in understanding how it may be solved analytically. The first term describes how the region of the heat source experiences a temperature change over time. Therefore, for a steady-state solution we can set this term equal to zero, simplifying our analysis. However, for a numerical solution, or pulsed system, this term needs to be considered and requires a more detailed knowledge of the material properties of the gain medium.

The second term describes the flow of heat, in three dimensions, from the region of the heat source. This flow is due to the temperature gradient from the heated (cooled) pump region to the surrounding material. For analytical purposes, this term can be simplified in terms of the number of dimensions considered and the temperature dependence of the material properties can be approximated by a constant value.

The third term describes the heat source, and if we assume a CW diode or Ti:sapphire pump source, we can approximate these pump sources using a top-hat or gaussian function respectively. We will now consider some of the basic properties that arise when we apply these simplifications to a CW end-pumped, monolithic microchip laser.

3.2.3 Parabolic Temperature Profile in Pumped Region

If we remove the time dependence, from Equation 20 and convert to working in radial co-ordinates then the standard heat equation can be reduced to:

$$\frac{d^2T}{dr^2}+\left(\frac{1}{r}\right)\left(\frac{dT}{dr}\right)+\frac{Q(r)}{k}=0$$

Equation 21

if we assume there is no temperature dependence for the thermal conductivity.

This differential equation can be solved with relative ease. In this sub-section, we will consider the solution of Equation 21 within the pumped region (ie. Q(r)<>0) and in the next sub-section the solution outside the pumped region (Q(r)=0) to determine a characteristic temperature profile in each region.

If we assume our heat Q is deposited uniformly within a circle of radius r_0 and zero outside, then the temperature inside the pumped region, T(r) where $r<r_0$, can be expressed relative to the temperature at the edge of the pumped region, $T(r_0)$, as [196]:

$$T(r)=T(r_0)+\frac{Q}{4k}(r_0^2-r^2)$$

Equation 22

assuming there is only symmetrical radial heat flow from the pumped region.

Therefore, to a first approximation, the temperature profile inside the pumped region is parabolic. To some extent, this temperature profile is independent of the intensity profile of the heat source, as can be seen by introducing different heat sources, though ultimately is dependent on its size and shape. This relative insensitivity to the pumping intensity profile goes part way to explaining why the output of a DPSSL does not inherit an equivalent intensity profile to the pumping laser diode. This ability to use thermal effects to determine the mode quality of a laser is very important in the design of diode-pumped lasers. It is particularly fortuitous in the case of diode-pumped microchip lasers as it provides a mechanism to give self-aligning, stable cavities with single transverse mode outputs. The effect of different pump intensity profiles is considered in more detail in Section 3.2.8.

The parabolic temperature profile described in Equation 22 can be directly related to the change in optical path length induced in the pumped region of the gain material through thermal expansion and thermo-optical effects. The radial optical path length in the pumped region can be expressed as:

$$n(r)l(r) = \left[n_0\left(1+\tfrac{dn}{dT}T(r)\right)\right]\left[\left(1+\alpha_e T(r)\right)l_0\right]$$

Equation 23

where n_0 is the normal refractive index, $^{dn}/_{dT}$ is the thermo-optical component, l_0 is the normal cavity length and α_e is the thermal expansion component. This equation ignores stress and strain induced refractive index variations, which are typically only a few percent of the overall change in optical path length. Although we will continue to ignore stress/strain effects in this section, the validity of this approximation is discussed in more detail in the next section.

Treating each of these thermal effects separately, we can examine their contribution to the thermal lensing within the gain material. Looking first at the thermal-optical effect then the equivalent focal length lens induced can be found, by rewriting the refractive index change as:

$$\Delta n_T(r) = -\frac{Q}{4k}\frac{dn}{dT}r^2$$

Equation 24

where dn/dT is the thermo-optical coefficient. This radial refractive index profile induces a quadratic spatial phase variation across a propagating beam equivalent to the effect of a spherical lens [196]. The focal length of a medium with a refractive index which varies according to:

$$n(r) = n_0\left(1-\frac{2r^2}{g^2}\right)$$

is given by :

$$f_T \approx \frac{g^2}{4n_0 l_0} = \frac{k}{Ql_0}\left(\frac{1}{2}\frac{dn}{dT}\right)^{-1}$$

Equation 25

This value is approximate because it assumes the focal length is much greater than the length of the gain material. The focal length can be seen to vary inversely with gain material length, thermo-optical coefficient and pump power density and linearly with thermal conductivity.

Considering the thermal expansion contribution now, the deviation from flatness of the end faces of the gain material is given by:

$$l(r) = \alpha_0 l_0 \Delta T(r) = -\frac{\alpha_0 r_0 Q}{4k} r^2$$

Equation 26

where α_0 is the thermal expansion coefficient and l_0 is the length of the end section of the laser material over which the expansion occurs and in this case $l(r_0)=l_0$. The focal length of a material with an end-face curvature of R is obtained from the thick-lens formula of geometric optics [196]:

$$f_e = \frac{R}{2(n_0 - 1)}$$

where the end – face curvature is :

$$R = -\left(\frac{d^2 l}{dr^2}\right)$$

Equation 27

From these equations, the focal length of the gain material due to thermal expansion can be expressed as:

$$f_e = \frac{k}{\alpha_0 r_0 Q(n_0 - 1)}$$

Equation 28

As with the thermo-optical case, the focal length varies inversely with material length and pump power density and linearly with thermal conductivity.

Combining Equation 27 and Equation 28, to produce an overall expression for the focal length of the induced thermal lens gives:

$$f = \frac{k}{Q}\left(\frac{l_0}{2}\frac{dn}{dT} + \alpha_0 r_0 (n_0 - 1)\right)^{-1}$$

Equation 29

Therefore, for a 500μm long Nd:YVO_4 microchip laser, where $dn/dT=3*10^{-6}K^{-1}$, $k=0.0515WcmK^{-1}$, and $\alpha_0=4.4*10^{-6}K^{-1}$ pumped by a 50μm spot then thermal expansion contributes 26% to the total thermal lens. For a microchip of half this length, it contributes 41%. Normally the aspect ratio and low absorption coefficient of the gain material in a DPSSL means thermal lensing dominates. For a microchip laser

however, thermal expansion can lead to the creation of a stable cavity geometry, particularly so in materials with a negative dn/dT, such as in LNP [211].

For 1W of absorbed pump power in a 0.5mm long Nd:YVO_4 crystal, the quantum defect heating of the 1064nm transition would give a thermal lens with a focal length of 7.6cm. For the 0.25mm long crystal, 1W of pump power would give a focal length of 5.9cm. These figures assume there is no parasitic heating through quenching effects and in practice, one would expect a thermal lens with a shorter focal length.

3.2.4 Logarithmic Temperature Profile Outside Pumped Region

If we consider the flow of heat from the edge of the pumped region to the cooled edge of the laser crystal, then the rate of flow of heat is:

$$Q = -2\pi rlk\frac{dT}{dr}$$

Equation 30

Re-arranging and integrating gives:

$$\frac{Q}{2\pi lk}\ln(r_0 - r) = T - T_0$$

Equation 31

Therefore, outside the pumped region there is a logarithmic decay in the temperature from the edge of the pumped region to the cooled extremities.

For short absorption depth materials, the temperature profile outside the pumped region does not significantly contribute to the definition of the transverse mode in a microchip, because the size of the lasing mode volume is comparable or smaller than the pumping mode volume. This logarithmic decay will however produce the highest stress and strain on the crystal just beyond the pumped region and is therefore important in determining the maximum operating characteristics.

3.2.5 Minimum Beam Waist and Pump Power Dependence

An alternative way of expressing the strength of the thermal-induced cavity is as the minimum beam waist of the laser field produced by the cavity. In general for a stable cavity, the minimum beam waist will lie within the cavity as shown in Figure 32.

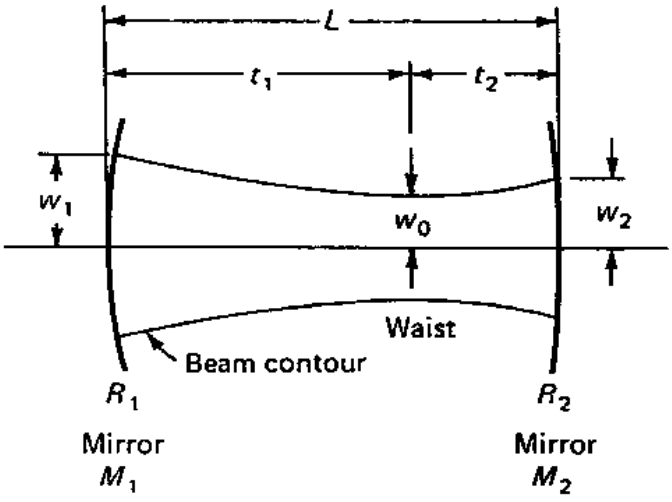

Figure 32 - Mode parameters of interest for stable resonators [after 196]

The most common design of laser resonator is shown above. If the net curvature of both mirrors is positive, then a stable cavity is formed which can produce a TEM_{00} mode. A Gaussian beam with a wavefront curvature of R_1 at distance t_1 from the beam waist will not experience any alteration in its mode shape if it its radius of curvature of the mirror matches the curvature of the wavefront. Similarly, a mirror with a suitable radius of curvature can be placed at distance t_2 without distortion of the wavefront to form a stable cavity. Kogelnik and Li derived a relationship between the mode parameters and resonator parameters such that the minimum beam waist is [215]:

$$w_0^4 = \left(\frac{\lambda_0}{\pi n}\right)^2 \frac{L(R_1 - L)(R_2 - L)(R_1 + R_2 - L)}{(R_1 + R_2 - 2L)^2}$$

Equation 32

with the distances t_1 and t_2 between the waist and mirrors:

$$t_1 = \frac{L(R_2 - L)}{R_1 + R_2 - 2L}, t_2 = \frac{L(R_1 - L)}{R_1 + R_2 - 2L}$$

Equation 33

For a simple plano-concave resonator then Equation 32 reduces to:

$$w_0^2 = \left(\frac{\lambda}{\pi n}\right)\sqrt{L(R-L)}$$

Equation 34

A similar equation can be obtained for the minimum beam waist induced because of the total optical path distortion in a microchip laser due to both thermal expansion and thermal 'lensing'. This distortion can be modelled as either entirely due to end-face curvature or as a thin lens in a plane-plane cavity or a combination of both. Analysis has shown that the minimum beam waist predicted by each of these techniques for a microchip laser is identical because of the short cavity lengths involved [216]. The focal length of the induced thermal lens is equivalent to a radius of curvature R=2f. If the focal length from Equation 29 is substituted into Equation 34 then:

$$w_0^2 = \left(\frac{\lambda}{\pi n}\right)\sqrt{L\left[\frac{k}{Q}\left(\frac{L}{2}\frac{dn}{dT} + \alpha_0 r_0 (n_0 - 1)\right)^{-1} - L\right]}$$

Equation 35

The focal lengths quoted in the previous section for the two microchip lasers described equate to a minimum beam waist of 36μm for the 0.5mm long crystal and 29μm for the 0.25mm long crystal.

The stable propagation of a Gaussian beam with planar phase fronts and constant spot size in a medium with a quadratic refractive index profile is given by [217]:

$$w = \left(\frac{n_0}{n_2}\right)^{\frac{1}{4}}\sqrt{\frac{\lambda}{\pi n_0}}$$

Equation 36

where w is the constant beam waist size, λ is the free space wavelength of the beam and n_0 and n_2 describe the Gaussian duct such that $n(r) = n_0 - \frac{1}{2}n_2 r^2$. Equation 36 does not take account of spatial gain or absorption variations. For many laser systems, the gain or absorption distributions do not significantly alter the guiding of the transverse mode. However, for microchip lasers gain guiding can be significant and the implications of this will be discussed further in the second half of this chapter.

For a Gaussian refractive index duct set up by the diffusion of heat from the pump region due to dn/dT, as described previously then:

$$n_2 = \frac{Q}{2k}\frac{dn}{dT}$$

therefore the minimum beam waist is given by :

$$w = \left(\frac{2k\lambda^2}{\pi^2 n_0 Q \frac{dn}{dT}} \right)^{\frac{1}{4}}$$

Equation 37

This is the minimum beam waist in the absence of other thermal effects and is dependent on the fourth root of the pump power density. Zayhowski derived a similar expression and showed it could be used to describe thermal guiding in Nd:YAG microchip lasers [210]. For scaling purposes, the beam waist varies with the square root of the pump radius and with the fourth root of the crystal length.

For the Nd:YVO_4 microchip laser described previously of length 0.5mm, then the minimum beam waist predicted by Equation 37 is 40μm and is 34μm for the 0.25mm long crystal. It is worth nothing that these predicted beam waists are greater than those predicted if end-face curvature is considered, but are still less than the radius of the pump beam (50μm).

In the previous three sub-sections, we started with the standard heat equation and showed techniques which could potentially be employed to solve it numerically and analytically. This equation represents the starting point for all thermal modelling and for the modelling in this chapter. Developing an analytical solution for a steady state, CW end-pumped laser, we showed that in the limit of our approximations, the temperature profile is parabolic within the pumped region and logarithmic outside. This is consistent with previous thermal models. We will now consider how this basic model can be expanded to give a more complete, yet simple solution to the temperature profile. Then this model will be used to model a variety of laser systems before considering how the standard heat equation can be solved numerically.

3.2.6 1-D Analytical Solution to Standard Heat Equation

An analytical solution can be derived for the standard heat equation if a number of assumptions are made about the laser system to simplify its operation. Following the work of Cousins [206], who derived a set of equations for thin laser discs, the equations relating to the temperature profile in end-pumped microchip lasers will be derived here.

If we assume that we are dealing with an isotropic gain material, such as Nd:YAG, which is pumped with a top-hat pump beam of finite radius a, we can re-write the standard heat equation in cylindrical co-ordinates as:

$$\frac{1}{r}\frac{\delta}{\delta r}\left(r\frac{\delta T}{\delta r}\right)+\frac{\delta^2 T}{\delta z^2}=\begin{cases}-\dfrac{Q(\alpha L)e^{-\alpha z}}{(\pi a^2 Lk)(1-e^{-\alpha L})}, r \le a\\ 0, r \ge a\end{cases}$$

Equation 38

where Q is the thermal power absorbed by the gain material, α is the absorption coefficient at the pump wavelength, L is the axial length of the gain material and k is the thermal conductivity of the gain material. The equation for the heat source expression within the pumped radius a, is derived from the absorption of the thermal heat power in both the transverse and axial planes such that:

$$q(r,z)=\frac{2Q\alpha}{\pi a^2}\frac{e^{-\alpha z}}{k\left(1-e^{-\alpha L}\right)}$$

Equation 39

where q is thermal power density. Outside the pumped region, there is no heat input and the equation is equal to zero.

The top-hat geometry, where only part of the cross-sectional area of the gain crystal experiences pumping, as illustrated in Figure 33, is appropriate to the pumping profile from the pumping laser diodes used in this work. The difference between isotropic and anisotropic materials will be discussed in the next section, though for most materials this approximation to isotropy is not unreasonable.

The boundary condition for this system can be expressed as:

$$h(T-T_\infty)+k\frac{\delta T}{\delta n}=0$$

Equation 40

where n is the local normal to the boundary, h is the heat transfer coefficient and T_∞ is the background temperature. This boundary condition allows for different cooling conditions ranging from having an insulated boundary, where no heat is lost to the surroundings h→0, to having an edge kept at the same temperature as the background by active cooling, h→∞. This work will use this latter condition for reasons discussed later.

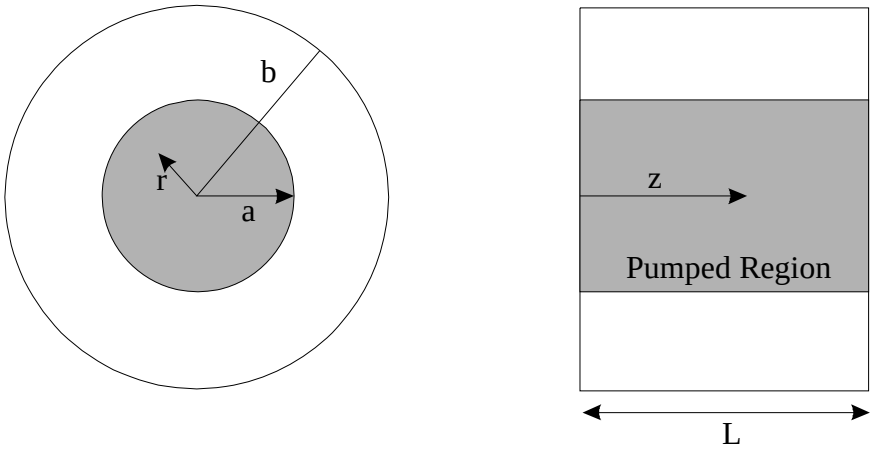

Figure 33 - Geometry of End-Pumped Microchip Laser

The variables relating to the physical geometry of the gain crystal are illustrated above. To simplify the analysis the variables used can be normalised such that:

$$r^* = \frac{r}{b}, z^* = \frac{z}{L}, a^* = \frac{a}{b}, L^* = \frac{L}{2b}, T^* = \frac{T - T_\infty}{Q \diagup (4\pi kL)}$$

Equation 41

Thus Equation 38 becomes:

$$\frac{1}{r^*}\frac{\delta}{\delta r^*}\left(r^* \frac{\delta T^*}{\delta r^*}\right) + \frac{1}{4}\left(\frac{1}{L^*}\right)^2 \frac{\delta^2 T^*}{\delta z^{*2}} = \begin{cases} -\dfrac{4(\alpha L)e^{-\alpha L z^*}}{a^{*2}(1-e^{-\alpha L})}, r^* \le a \\ 0, r^* \ge a \end{cases}$$

Equation 42

and the boundary condition, Equation 40, becomes:

$$(Bi)T^* + \frac{\delta T^*}{\delta n} = 0$$

Equation 43

where Bi is the Biot modulus, defined as $\mathrm{Bi} = \frac{hL}{k}$.

By assuming a fixed absorption value of 95% of the pump power, which is a good approximation for a 3% doped Nd:YVO_4 microchip laser and either an infinite or zero Biot modulus depending on the cooling technique used, dimensional analysis shows that a solution can be expressed dimensionally in the form:

$$T^* = f(r^*, z^*, a^*, L^*)$$

Equation 44

Therefore, in this analysis the temperature profile is only dependent on the size of the pumped region with respect to the crystal width, and on ratio of the length to width of crystal.

The equilibrium equations in cylindrical co-ordinates for the stress induced in a gain crystal are:

$$\frac{d\sigma_r}{dr} + \frac{d\tau_{rz}}{dz} + \frac{\sigma_r - \sigma_\theta}{r} = 0,$$
$$\frac{d\tau_{rz}}{dr} + \frac{d\sigma_z}{dz} + \frac{\tau_{rz}}{r} = 0$$

Equation 45

where σ is the normal component of the stress tensor and τ is the shear component of the stress tensor where the subscript represent the cylindrical planes. The strains and displacements are related by:

$$\varepsilon_r = \frac{du}{dr}, \varepsilon_\theta = \frac{u}{r}, \varepsilon_z = \frac{dw}{dz}, \gamma_{rz} = \frac{du}{dz} + \frac{dw}{dr}$$

Equation 46

where u is the radial and w is the axial displacement component and e is the normal and γ the shear component of the strain tensor. The stresses, strains and temperature are related by the generalised Hooke's laws:

$$\varepsilon_r = \frac{\left[\sigma_r - v(\sigma_\theta + \sigma_z)\right]}{E} + \alpha_T (T - T_\infty),$$
$$\varepsilon_\theta = \frac{\left[\sigma_\theta - v(\sigma_r + \sigma_z)\right]}{E} + \alpha_T (T - T_\infty),$$
$$\varepsilon_z = \frac{\left[\sigma_z - v(\sigma_\theta + \sigma_r)\right]}{E} + \alpha_T (T - T_\infty),$$
$$\gamma_{rz} = \frac{2(1+v)}{E}\tau_{rz}$$

Equation 47

where α_T is the thermal expansion coefficient, v is Poisson's ratio and E is the modulus of elasticity. At the boundaries of the laser crystal, we will assume there is zero-displacement so:

$$\sigma_r = 0, \sigma_\theta = 0, \sigma_z = 0, \tau_{rz} = 0, u = 0, w = 0$$

Equation 48

This problem can be nondimensionalised by using the following substitutions:

$$\sigma_i^* = \frac{\sigma_i}{Ef}, \tau_{rz}^* = \frac{\tau_{rz}}{Ef}$$
$$\varepsilon_i^* = \frac{\varepsilon_i}{f}, \gamma_{rz}^* = \frac{\gamma_{rz}}{f}$$
$$u^* = \frac{u}{bf}, w^* = \frac{w}{Lf}$$
$$\text{where :}$$
$$f = \frac{\alpha_T Q}{4\pi kL}$$

Equation 49

So Equation 45-Equation 48 can be rewritten as:

$$\frac{d\sigma_r^*}{dr^*} + \frac{d\tau_{rz}^*}{dz^*} + \frac{\sigma_r^* - \sigma_\theta^*}{r^*} = 0,$$
$$\frac{d\tau_{rz}^*}{dr^*} + \frac{d\sigma_z^*}{dz^*} + \frac{\tau_{rz}^*}{r^*} = 0$$

Equation 50

$$\varepsilon_r^* = \frac{du^*}{dr^*}, \varepsilon_\theta^* = \frac{u^*}{r^*}, \varepsilon_z^* = \frac{dw^*}{dz^*}, \gamma_{rz}^* = \frac{du^*}{dz^*} + \frac{dw^*}{dr^*}$$

Equation 51

$$\begin{aligned}
\varepsilon_r^* &= \left[\sigma_r^* - v(\sigma_\theta^* + \sigma_z^*)\right] + T^*, \\
\varepsilon_\theta^* &= \left[\sigma_\theta^* - v(\sigma_r^* + \sigma_z^*)\right] + T^*, \\
\varepsilon_z^* &= \left[\sigma_z^* - v(\sigma_\theta^* + \sigma_r^*)\right] + T^*, \\
\gamma_{rz}^* &= 2(1+v)\tau_{rz}^*
\end{aligned}$$

Equation 52

$$\sigma_r^* = 0, \sigma_\theta^* = 0, \sigma_z^* = 0, \tau_{rz}^* = 0, u^* = 0, w^* = 0$$

Equation 53

If we assume that Poisson's ratio has the value of 0.3, which is true for Nd:YAG and does not vary much for other crystalline materials, and all other material properties are constant, then examination of Equation 47 shows stress and strain are only dependent on the temperature profile. Therefore, the stress and strain induced in the laser crystal can be expressed in the same dimensions as Equation 44 and are only dependent on the aspect ratio of the crystal and size of the pump spot.

As previously, these assumptions of constant material parameters are only valid for small perturbations to the system. Therefore, they are perhaps unreasonable assumptions for a microchip laser system, where there is a substantial temperature profile and consequently large stresses and strains.

3.2.6.1 Edge-Cooled Microchip Laser Crystals

If we limit our analysis initially to edge cooling, Equation 42 can be formally integrated in the axial direction, z, using the appropriately modified boundary condition from Equation 43:

$$\frac{1}{r^*}\frac{\delta}{\delta r^*}\left(r^*\frac{\delta\langle T\rangle^*}{\delta r^*}\right) + \frac{1}{4}\left(\frac{1}{L^*}\right)^2 (Bi)(-T_{z=0}^* - T_{z=1}^*) = \begin{cases} -\dfrac{4}{a^{*2}}, r^* \le a \\ 0, r^* \ge a \end{cases}$$

Equation 54

For a typical edge-cooled Nd:YVO_4 microchip laser the convective heat transfer coefficient at the end faces is h~10^{-3} and the black body radiative transfer h = $4\varepsilon T^3$ = $0.7*10^{-3}$. With a thermal conductivity of 0.05W/cmK, this gives a Biot modulus of the order of 0.01. For active cooling at the edges the heat transfer coefficient h~1, giving a Biot modulus of order 10, three orders of magnitude greater than the heat loss from the faces, and sufficient that a constant temperature boundary condition at the crystal

edges is a good approximation.

For a microchip of dimensions 5x5x0.5mm the value of the second term in Equation 54 is approximately 0.15 compared to the other terms which are typically greater than 1. Thus the heat flux from the end faces is in general very small or negligible compared to the radial heat flow and the problem can be reduced to a mean temperature distribution in only the radial direction. It is worth noting that as the aspect ratio, L*, of the microchip crystal decreases then this passive face cooling term becomes more significant, implying that edge-cooling is not the most satisfactory technique for cooling thin crystals with an aspect ratio less than 0.2.

Solving the remaining partial differential equation for the mean normalised temperature <T*>, yields:

$$\left\langle T^{*}\right\rangle = \begin{cases} -2\ln(a^{*}) + 1 - \left(\frac{r^{*}}{a^{*}}\right)^{2}, r^{*} \le a^{*} \\ -2\ln(r^{*}), r^{*} \ge a^{*} \end{cases}$$

Equation 55

Rewriting this as the temperature change from ambient and denormalising gives:

$$\left\langle T\right\rangle = \begin{cases} \frac{Q}{(4\pi kL)}\left[-2\ln(\frac{a}{b}) + 1 - \left(\frac{r}{a}\right)^{2}\right], r \le a \\ \frac{Q}{(4\pi kL)}\left[-2\ln(\frac{r}{b})\right], r \ge a \end{cases}$$

Equation 56

From these equations we can see that within the pumped region, r<a, the temperature profile is dominated by the quadratic term and out with this region there is an logarithmic decay of temperature to the edge. Coincidentally this quadratic function within the pumped region makes the analysis of the resulting thermal lensing straightforward to solve analytically as discussed earlier and it can be modelled by a simple lens. The thermal lens outside the pumped region cannot be corrected easily because of the logarithmic shape and this can lead to undesirable and unacceptable losses at high pump powers.

As the length of the rod tends to zero the axial stress, σ_z^*, in the crystal approaches zero. If we assume this is the case for a microchip laser with small aspect ratio, L^*, this plane stress approximation indicates the shear stress vanishes as well. This leads to a plane mean stress solution for the case of traction-free rod boundaries [206]:

$$\left\langle \sigma_r^* \right\rangle = \int_0^1 \left\langle T^* \right\rangle r^* dr^* + \frac{1}{r^{*2}} \int_0^{r^*} \left\langle T^* \right\rangle r^* dr^*$$
$$\left\langle \sigma_\theta^* \right\rangle = -\left\langle T^* \right\rangle + \int_0^1 \left\langle T^* \right\rangle r^* dr^* + \frac{1}{r^{*2}} \int_0^{r^*} \left\langle T^* \right\rangle r^* dr^*$$

Equation 57

Substituting for the mean temperature profile from Equation 55 and integrating gives the following equations for the mean stresses:

$$\left\langle \sigma_r^* \right\rangle = \begin{cases} \ln(a^*) - \frac{a^{*2}}{4} + \left(\frac{r^*}{2a^*} \right)^2, r^* \le a^* \\ \ln(r^*) - \frac{a^{*2}}{4} + \left(\frac{a^*}{2r^*} \right)^2, r^* > a^* \end{cases}$$
$$\left\langle \sigma_\theta^* \right\rangle = \begin{cases} \ln(a^*) - \frac{a^{*2}}{4} + 3\left(\frac{r^*}{2a^*} \right)^2, r^* \le a^* \\ \ln(r^*) - \frac{a^{*2}}{4} - \left(\frac{a^*}{2r^*} \right)^2 + 1, r^* > a^* \end{cases}$$

Equation 58

The mean axial strain distributions can be found from the stress-strain relations in Equation 52 and from the equation above such that:

$$\left\langle \varepsilon_z^* \right\rangle = \begin{cases} \left[-2\ln(a^*) + 1 - \left(\frac{r^*}{a^*} \right)^2 \right] [1+\nu], r^* \le a^* \\ \left[-2\ln(r^*) \right] [1+\nu], r^* \ge a^* \end{cases}$$

Equation 59

The scaling of microchip lasers is often limited by thermal problems. Equation 56 shows that the temperature varies linearly with absorbed power and inversely to the volume of the pumped region. Thus by increasing the pumped volume, through either longer crystals, a larger pump spot or a lower absorption coefficient it is possible decrease the magnitude of the temperature profile and consequently the stress and strain on the crystal.

3.2.6.2 Face-Cooled Microchip Laser Crystals

An alternative to cooling the crystal from the edges is to cool the crystal through one of the end faces. This method is particularly attractive for very thin crystals with an aspect ratio of less than 0.1. Cousins showed that it is possible to derive a general expression for the mean temperature without further approximation by means of a Fourier-Bessel expansion of Equation 42 and Equation 43 in the radial co-ordinate. The resulting three-dimensional temperature distribution can then be integrated through the rod thickness to give the mean temperature. This temperature field can be expressed as:

$$< T^{*} >= C_0 + \sum_{n=1}^{\infty} C_n J_0\left(\beta_n r\right)$$

Equation 60

where the β_n are the roots of $J_1(\beta_n)=0$, n=1,2,... and the coefficients C_n are given by:

$$C_0 = \frac{F_0 a^{*2}}{(\alpha L)^2}\left(\frac{e^{-\alpha L}-1}{\alpha L} + e^{-\alpha L} + \frac{\alpha L}{2}\right)$$

$$C_n = \frac{F_n}{(2L^{*}\beta_n)^2 - (\alpha L)^2}\left(\frac{1-e^{-\alpha L}}{\alpha L} + \frac{e^{-\alpha L}}{2L^{*}\beta_n}\tanh(2L^{*}\beta_n) + \frac{\alpha L}{(2L^{*}\beta_n)^2}\left[\cosh(2L^{*}\beta_n) - \tanh(2L^{*}\beta_n)\sinh(2L^{*}\beta_n) - 1\right]\right)$$

where:

$$F_0 = 4\frac{\alpha L}{1-e^{-\alpha L}}(2L^{*})^2$$

$$F_n = F_0 \frac{2}{a^{*}\beta_n}\frac{J_1(a^{*}\beta_n)}{J_0^2(\beta_n)}$$

Equation 61

By assuming a large aspect ratio so that the heat flux on the cooled face is uniform and the edge boundaries are insulated, Equation 42 can be integrated and using the appropriately modified boundary condition from Equation 43 then:

$$\frac{1}{r^{*}}\frac{\delta}{\delta r^{*}}\left(r^{*}\frac{\delta\langle T^{*}\rangle}{\delta r^{*}}\right) = \begin{cases} -\dfrac{4}{a^{*2}} + 4, r^{*} \le a \\ 4, r^{*} \ge a \end{cases}$$

Equation 62

Solving this equation, the resulting differential mean temperature profile in this aspect limit is:

$$\left\langle T^{*}\right\rangle =\begin{cases} -2\ln(a^{*})+\left(1-\dfrac{1}{a^{*2}}\right)r^{*2}, r^{*}\le a^{*} \\ r^{*2}-2\ln(r^{*})-1, r^{*}\ge a^{*} \end{cases}$$

Equation 63

Comparing the edge-cooled solution Equation 55 and the face-cooled solution Equation 63, the temperature differential between the centre and edge of the crystal is greater for edge-cooled systems. This greater differential is carried through into greater stress, strain and optical aberrations within the crystal.

As with the edge-cooled case, in the limit of an infinitely short crystal, the axial stress, s_{z}^{*}, and the mean shear stress, t_{rz}^{*}, become vanishingly small [206]. Using this same plane stress approximation with the temperature distribution in Equation 63 gives:

$$\left\langle \sigma_{r}^{*}\right\rangle =\begin{cases} \dfrac{1}{4a^{*2}}\left(a^{*2}-1-a^{*2}r^{*2}+r^{*2}\right), r^{*}\le a^{*} \\ \ln(r^{*})-\dfrac{r^{*2}}{4}+\dfrac{1}{4}, r^{*}>a^{*} \end{cases}$$

$$\left\langle \sigma_{\theta}^{*}\right\rangle =\begin{cases} 1\dfrac{1}{4a^{*2}}\left(a^{*2}-1-3a^{*2}r^{*2}+3r^{*2}\right), r^{*}\le a^{*} \\ \ln(r^{*})-\dfrac{3r^{*2}}{4}+\dfrac{5}{4}, r^{*}>a^{*} \end{cases}$$

$$\left\langle \varepsilon_{z}^{*}\right\rangle =\begin{cases} \left[-2\ln(a^{*})+\left(1-\dfrac{1}{a^{*2}}\right)r^{*2}\right]\left[1+v\right], r^{*}\le a^{*} \\ \left[r^{*2}-2\ln(r^{*})-1\right]\left[1+v\right], r^{*}\ge a^{*} \end{cases}$$

Equation 64

for the mean stress and strain distributions. Qualitatively, the shapes of these distributions are the same as the edge cooled crystals. However it is worth noting that in the limiting case where the pump size tends to the size of the crystal, $a^{*}\rightarrow 1$, the mean temperature, stress and strain distributions become uniform across the radius, implying that induced optical aberrations and birefringence effects vanish. Also as the aspect ratio of the rod tends to zero, $L^{*}\rightarrow 0$, the temperature, stress and strain magnitudes decrease due to the smaller conduction paths to the cooling surface.

3.2.7 Results of Analytical Models

In the previous sub-section we derived a series of equations which can be used to analytically calculate the temperature profile created by end-pumping of a microchip laser crystal by a diode laser. These temperature profiles can then be related to the guiding of the transverse mode through the equations derived earlier in this section. We will now consider how this modelling can be applied to predict the behaviour of a range of microchip lasers and pumping conditions, and how it compares with other analytical models.

3.2.7.1 Thermal Modelling of Monolithic Nd:YVO_4 Microchip Lasers

Equation 55 and Equation 63 were solved using Mathcad for a variety of different Nd:YVO_4 microchip lasers, such as the four shown below.

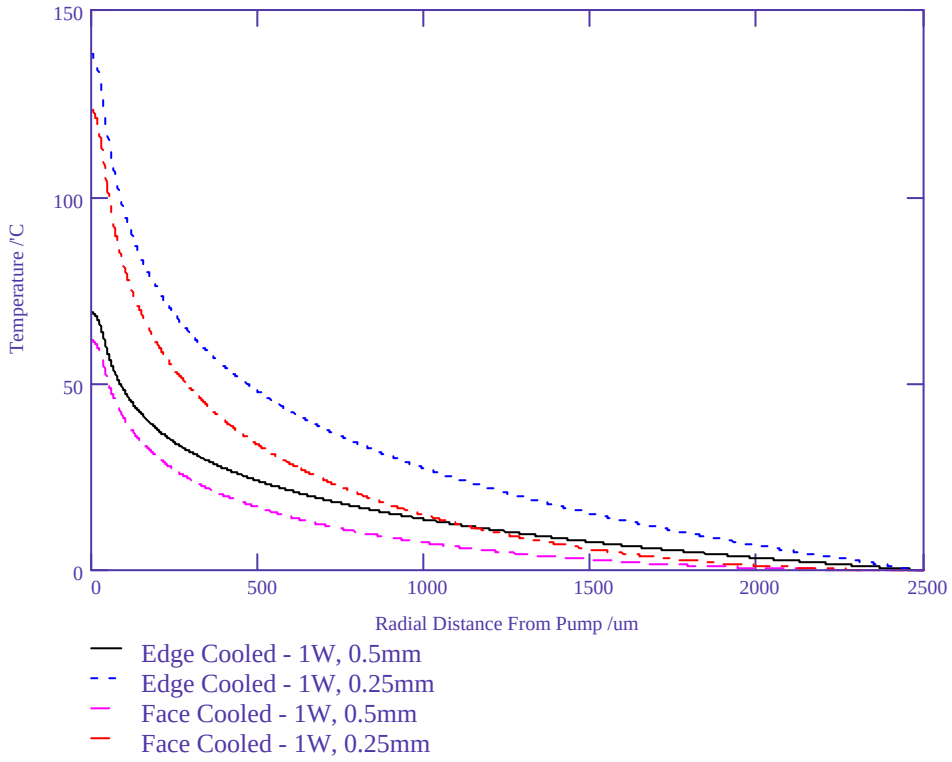

Figure 34 – Thermal modelling of different crystal lengths and cooling geometries for a Nd:YVO_4 microchip laser pumped by a 1W laser diode.

Figure 34 shows the temperature profile solutions for both edge and face cooled cases of 0.5mm and 0.25mm long crystals pumped by a 1W-laser diode. Within the pump radius of 50μm, the quadratic profile can clearly be seen, with an logarithmic decay outside the pumped region to the crystal edge. The advantage of face cooling is

more obvious for the 0.25mm long crystal, where the temperature at the centre of the pumped region is approximately 20°C less than the edge cooled case. The temperature profile in the pumped region is of particular interest because it ultimately determines the nature of the thermal guiding. The Mathcad model was extended to consider the impact of crystal length and pump power on the temperature rise from edge to centre, as illustrated below in Figure 35.

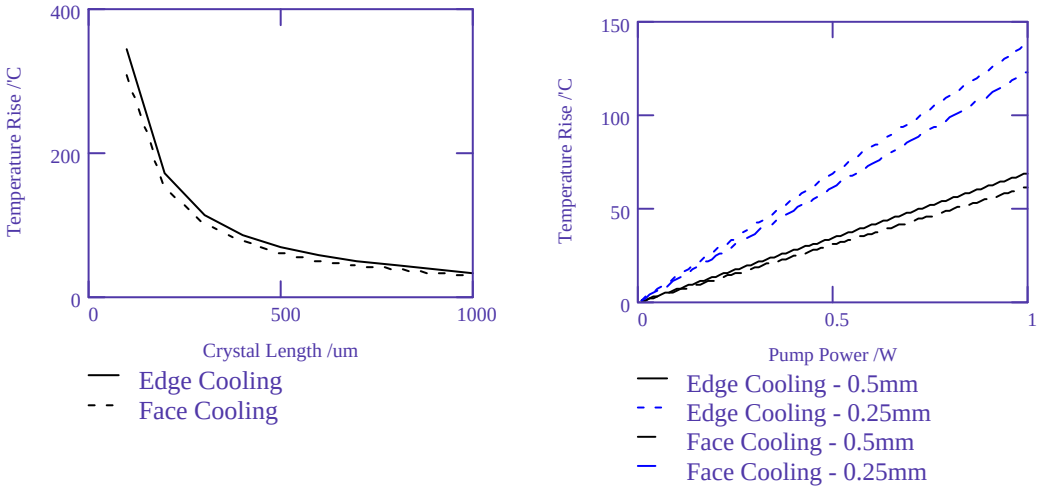

Figure 35 – Temperature at centre of pumped area with a) crystal length for 1W of pump power and b) pump power.

The advantage of longer crystals and face cooling can be seen more clearly in Figure 35. The inverse relationship between crystal length and temperature from Equation 56 is highlighted in Figure 35a), while the linear relationship with pump power is illustrated in Figure 35b). However, at low pump powers and for longer crystals there is little advantage in face cooling, supporting our case for using edge cooling in the experimental work of this thesis.

In the experimental work described at the beginning of this chapter, in Section 3.1.1, the 0.25mm long crystal used cracked with approximately 1W of pump power. Our modelling would indicate that this corresponds to an average temperature rise of 140°C over the entire pumped volume. In reality, there is a temperature gradient present along the axis of the crystal, and this will be supported by the numerical thermal modelling in the next section. This gradient dramatically increases the temperature rise in the region of the pumped surface to several times this value and close to the melting point of the crystal.

If we now consider the stress and strain predicted by this model, using Equation 58

and Equation 59, then we can estimate the conditions required for thermal fracture.

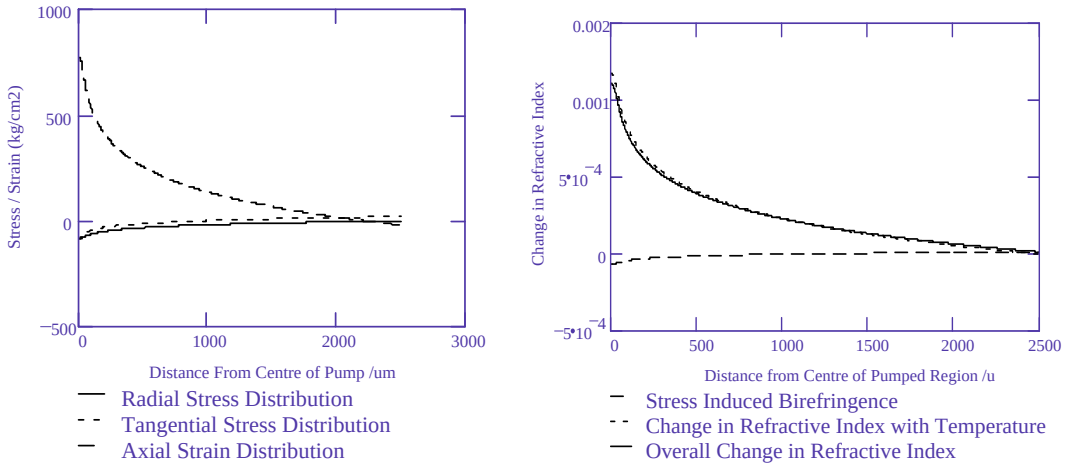

Figure 36 – Calculated a) stress and strain and b) effect of stress induced birefringence for a 5x5x0.5mm 3% Doped Nd:YVO_4 crystal pumped with a 1W laser diode in a 50μm pump spot.

The tensile strength of Nd:YVO_4 is unknown, and therefore it is difficult to compute an upper limit to the pump power. However, as a guide the tensile strength of Nd:YAG is 1800-2100kg/cm^2 and 340 kg/cm^2 for Nd:YLF. Working with a value of 1700 kg/cm^2, and a 0.25mm long crystal, one watt of incident pump power will strain the material to nearly 50% of this value. Again, this assumes there is no axial temperature gradient, though only a factor of two increase would bring us within the thermal fracture limit. Indeed, this is what was observed in Section 3.1.1. Therefore as a rule of thumb from this model, crystals can be successfully used up to a temperature profile creating stress or strain approximately 25-30% of their tensile strength.

A softer limit to the usable ceiling of the microchip system can be found from examining the effect of stress induced birefringence. Unfortunately the photoelastic coefficients for Nd:YVO_4 have not so far been measured. Again as a guide, the values of Nd:YAG have been used for our modelling. From Figure 36b) it can be seen that stress induced birefringence in Nd:YVO_4, which is naturally very birefringent, is not significant compared to changes in refractive index from thermo-optical effects. However in isotropic materials such as Nd:YAG, stress induced birefringence can be an undesirable effect leading to elliptical output and higher order transverse modes.

3.2.7.2 Comparison of Analytical Models

As mentioned in the introduction to this section, several thermal models exist which can be applied to microchip lasers. Complementary Mathcad documents were developed to compare some of these models to the analytical model derived earlier.

In particular, the models chosen were based on the work of Frauchiger [207], Zayhowski [210], and Innoncenzi [218]. The temperature profile from the Cousins model was also interpreted in two ways, one using the optical path difference calculation (OPD), described in Section 3.2.5, and the other using Koechner's equations for a thermal lens [196].

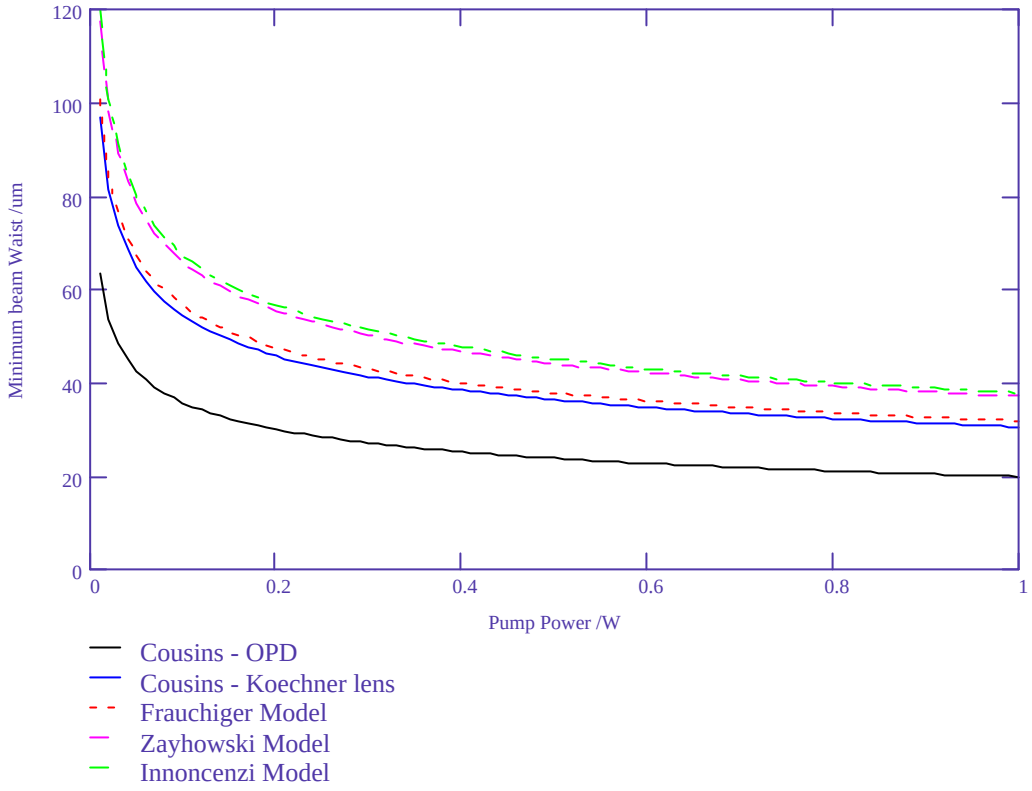

Figure 37 – Comparison of minimum beam waist predicted by several different thermal models for a 5x5x0.5mm 3% doped Nd:YVO_4 microchip laser pumped with a 50μm pump spot size.

For each of the models, the same starting conditions were used, namely a 5x5x0.5mm 3% doped Nd:YVO_4 crystal operating at 1064nm pumped by a laser diode with a pump spot radius of 50μm. All of the results were produced in terms of the dependence of the minimum beam waist on pump power, the standard conclusion of many thermal models.

Frauchiger's model of thermal lensing gives a very similar result to that of

Koechner's thermal lens although using a very different procedure. This indicates that the Cousins model solely taking into account thermal lensing is in good agreement with a more complicated model using fewer assumptions, supporting our use of this model as the basis of our analytical work.

Using a value of 50μm in Zayhowski's empirical model, very similar results to those of the derived from the work of Innocenzi were obtained. Both of these models indicate that the minimum waist size within the microchip does not decrease much below that of the pumping beam, even at high pump powers. This is inconsistent with the roll-off in slope efficiency observed in microchip lasers pumped with high average powers, and therefore these models were not considered appropriate for the modelling of thermal effects in Nd:YVO_4 microchip lasers.

The Cousins - OPD model, where both thermal expansion and change in refractive index are accounted for, predicted the smallest beam waists. The beam waists were approximately half those of from the Koechner interpretation of the Cousins model, indicating that in Nd:YVO_4 the curvature of the end faces due to thermal expansion contributes significantly in the guiding of the transverse mode. The smaller beam waists are consistent with the low thresholds observed, the relatively large divergences and the behaviour described in Section 3.1.1.

Therefore, of the models examined, the Cousins-OPD model was considered the most comprehensive and accurate for the modelling of our microchip lasers.

3.2.7.3 Modelling of Different Nd^{3+} Doped Crystals

If we now consider the application of our Cousins - OPD model to a range of different gain materials, we can be guided as to how they will perform in a microchip format.

The gain materials chosen, were Nd:YVO_4 operating at both 1064nm and 1342nm, Nd:YAG, Nd:YLF and LNP, all commonly used Nd^{3+} doped crystals. These materials also represent the three main classes of gain crystal, Nd:YAG and Nd:YVO_4 are oxides with good thermal properties, Nd:YLF is a fluoride with negative $^{dn}/_{dT}$, and LNP is a stiochiometric crystal. Each crystal was modelled as being 0.5mm long and pumped by a 50μm spot. The results for this modelling are shown in Figure 38.

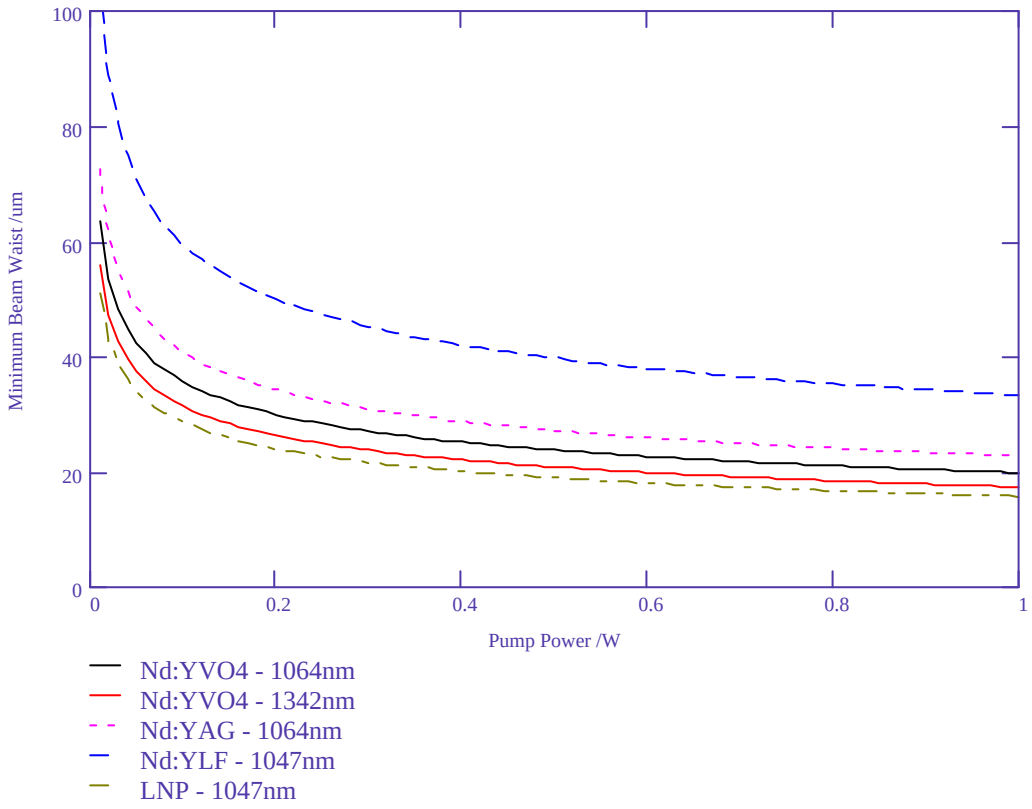

Figure 38 – Comparison of beam waists predicted by Cousins-OPD model for different gain materials. Each materials was modelled as a 5x5x0.5mm crystal pumped with a 50μm spot from a laser diode.

The negative thermo-optical coefficients of Nd:YLF lead to it having the largest minimum beam waists, although it has a temperature profile close to that of Nd:YVO_4 at 1064nm. Nd:YAG has the lowest maximum temperature, because of its good thermal conductivity and has the next largest beam waists. In contrast the 1342nm transition in Nd:YVO_4 and LNP both have small predicted beam waists. In the case of the 1342nm line, this is because of the increased quantum defect heating, approximately 66% greater than for the 1064nm transition. For LNP, the poor thermal conductivity gives a large temperature rise. This combined with the short absorption depth and large thermal expansion coefficients, suggest that LNP has a very limited operating range.

In conclusion, we have developed a 1D analytical model to predict the effect of pump power heating on a microchip laser. Several models, gain materials and pumping geometries have been compared, and used to indicate the operating envelope of our microchip lasers.

3.2.8 Numerical Solutions to the Standard Heat Equation

Analytical solutions to the standard heat equation normally involve some degree of simplification of the system and generally only yield a steady-state solution. While analytical models are useful in deriving relationships between variables, numerical models can provide a more accurate and representative solution for almost all laser systems.

In the first part of this sub-section we will look at the use of numerical methods to compare the effect of different pump source functions on the solution to the one dimensional standard heat equation. Then we will go on to look at the use of a finite element modelling to investigate the thermal effects in a microchip laser and consider some problems beyond the scope of an analytical solution.

3.2.8.1 Comparison of Pump Sources

The one dimensional steady-state standard heat equation (Equation 21) can be solved numerically for different thermal heat sources (Q(r)). This analysis is useful in understanding the independence of the output intensity profile of a solid-state laser from the intensity profile of the pump source and for comparison with the previously described analytical expressions. At either extreme of the pumping range this analysis is no longer valid due to the dominance of other effects, in particular the decrease in overlap efficiency between the pump and lasing mode volumes. For much of the operating range however the output can be observed theoretically and experimentally to independent of the pump profile.

If the intensity profile of a laser diode is treated as a top-hat function and a Ti:sapphire laser as having a Gaussian profile, then the heat source functions can be expressed as:

$$Q_{diode} = \begin{cases} \dfrac{Q}{\pi l r_p^2}, r \le r_p \\ 0, r > r_p \end{cases}$$

$$Q_{gaussian} = \frac{2Q}{\pi l r_p^2} e^{\frac{-2r^2}{r_p^2}}$$

Equation 65

Using these functions as the heat sources, Equation 21 can be solved numerically to compare pump sources. A Mathcad document was developed for this purpose using a

fourth order Runge-Kutta method and the results are shown in Figure 39.

Outside the pumped region (50μm) there is excellent agreement between the numerical diode and Gaussian solutions and the 1D analytical solution described in Section 3.2.6. In each case, the temperature profile is approximately parabolic with a logarithmic decay from the edge of the pumped region to the edge of the crystal.

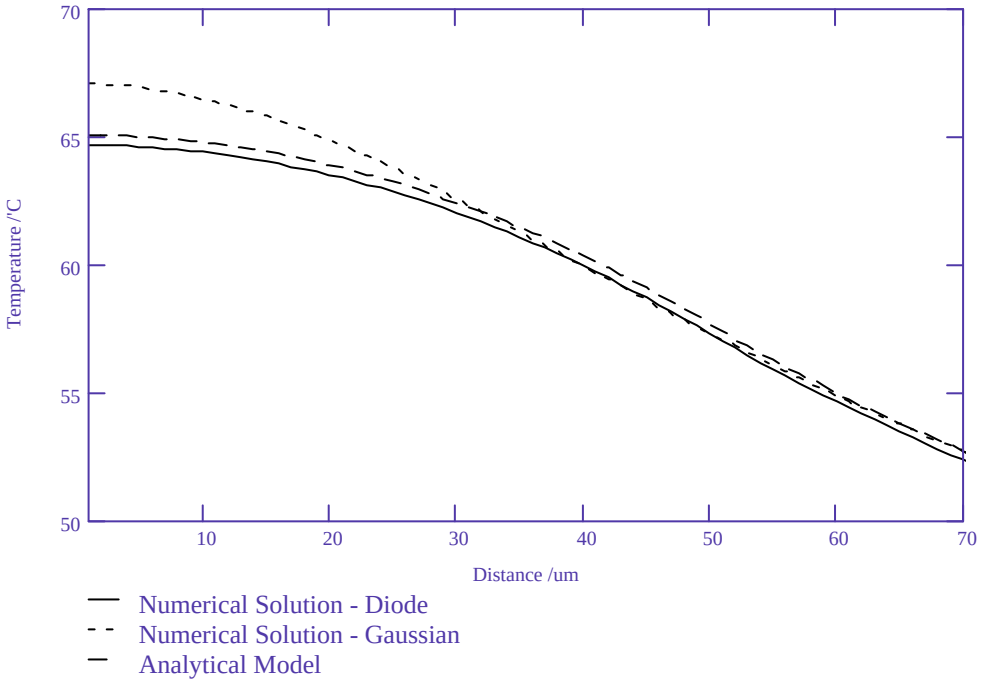

Figure 39 – Temperature profile within the pumped region (50μm) for different pumped sources a) Diode (solid), b) Gaussian (short dashed), c) Analytical solution (long dashed). 0.5mm long Nd:YVO_4 microchip laser pumped with 0.5W laser diode.

The temperature profiles from Figure 39 were evaluated using Equation 23 and Equation 34 to give the minimum beam waists. The diode heat source function and the analytical model both predict beam waists of 31.8μm. However, the Gaussian pump beam with the same pump power gives a minimum beam waist for the laser mode of 29.7μm. The increased temperature in the central region is due to the higher thermal loading from the pumping intensity profile. As the distance from the centre of the pumped region tends to the pump radius, the heat emanating from the enclosed region to the cooled edges converge for both diode and Gaussian pump sources.

3.2.8.2 Finite Element Analysis

A powerful method of evaluating complex numerical systems is to use finite element

analysis. The calculating power of computers has allowed otherwise impossible problems to be broken down into simple components which can be evaluated independently and then the relationship between the components considered at finite time steps. The flow of heat in a crystal can be considered in such a way.

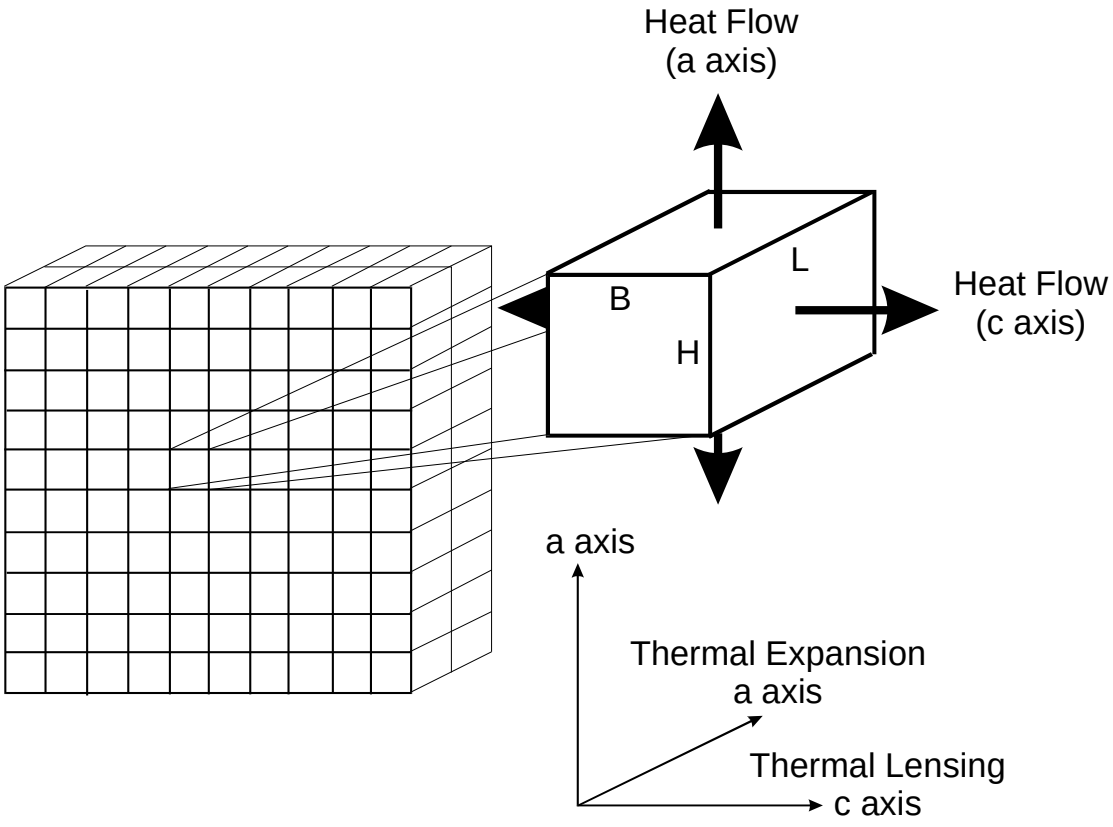

Figure 40 - Finite Element Model for Nd:YVO_4 Microchip Laser

If a microchip laser is decomposed by a grid into a large number of smaller crystal elements of size BxHxL, each of these smaller crystals can be considered independently. The elements around the edge of the crystal can be kept at a constant temperature to mimic active edge cooling of the crystal.

A heat source can then be applied to several of these elements to simulate heating from a diode laser. This forms part of an iterative loop in discrete time intervals, which continues until a steady state solution is reached. The heat added to an element is calculated from the power it absorbs in its volume from the pump power in the time interval Dt and the temperature rise created by this energy can be evaluated. The final step of the loop is to consider the heat flow between elements. Energy will be transferred through each of the faces of the element according to the temperature differential to the respective adjacent element. After a number of iterations, the matrix

will reach a pseudo-steady-state and this can be taken to be an approximate solution.

This method can be used to take account of anisotropic crystal properties and to simulate pumping anywhere on the crystal and with more than one source. Pulsed pumping can also be considered along with different cooling geometries. The technique can be applied equally as well to solving the problem in one, two or three dimensions. Thus, finite element modelling can be used to study a number of systems beyond the scope of an analytical solution.

Computer programs were written in QuickBasic to simulate a Nd:YVO_4 microchip laser pumped by a laser diode under various conditions using the method described above. Three versions were written, for one, two and three-dimensional simulations. The diode pump source is treated as having a top-hat intensity profile to offer a direct comparison with the analytical modelling.

One of the important considerations in coding a finite element model is determining the finite element sizes. If the crystal elements are made small, the time step interval needs to be correspondingly small to avoid thermal run-away in the heated region. Therefore, in going to smaller step sizes the computational time for the model increases exponentially. Alternatively, with a coarse element size, the detail of the thermal profile cannot be convincingly determined, although the computational time is minimal. How strict the condition is for stopping the calculation loop can also have a bearing on the time taken for a system to be evaluated. It is important that thought is given to the optimisation of the modelling and the choice of parameters in order to have reasonable computation times, yet have sufficient detail.

3.2.8.3 One Dimensional Finite Element Modelling

As before, the laser gain material can be treated as a series of cylinders in the radial plane to produce a one-dimensional model for the heat flow from the pumped region to the cooled edges. This introduces some complexity into the finite element model in determining element sizes and area through which the heat will flow between elements, though a comparatively small number of elements can allow detailed temperature profiles to be calculated.

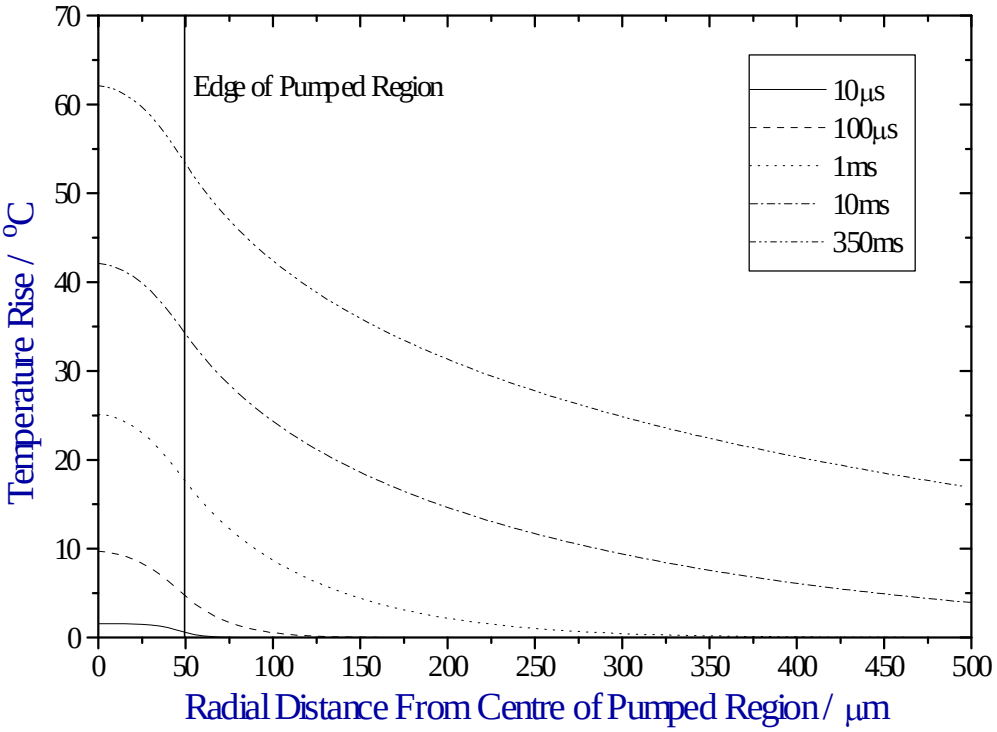

Figure 41 – Temperature Distributions at Different Time Intervals

The one-dimensional finite element program was used to simulate the pumping of a 5x5x0.5mm 3% crystal of Nd:YVO_4 with a 1W diode pump source to examine the temporal development of the thermal lens. Within the pump radius of 50μm, the characteristic quadratic temperature dependence can be seen, with the logarithmic decay of temperature to the cooled crystal edges. The model was run with time steps of 0.5μs with elements 2μm wide and a steady state condition of less than 0.001°C temperature change anywhere during this time step. Computation time was of the order of 30 minutes on a 100MHz pentium processor.

The development of an almost constant temperature difference between the centre and edge of the pumped region can be seen, which evolves over an increasing background. This is illustrated more clearly in Figure 42. The main graph shows how this temperature difference rapidly stabilises in comparison to the absolute temperature of these two points. Indeed, it takes 350ms for a pseudo-steady state to be reached for the absolute temperature, however only a few milliseconds for the temperature difference to stabilise. Ultimately it is the temperature difference, which determines the formation of a transverse mode, however the absolute temperature will impact the longitudinal mode structure and the intensity and frequency stability of the

laser.

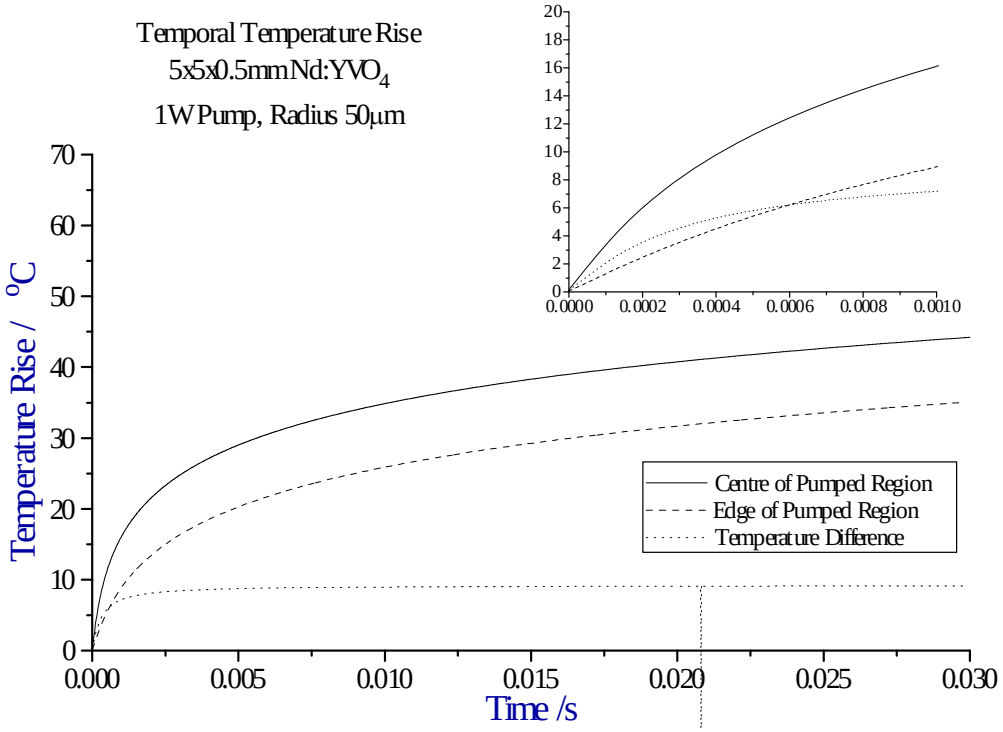

Figure 42 – Temporal temperature rise at the centre and edge of the pumped region.

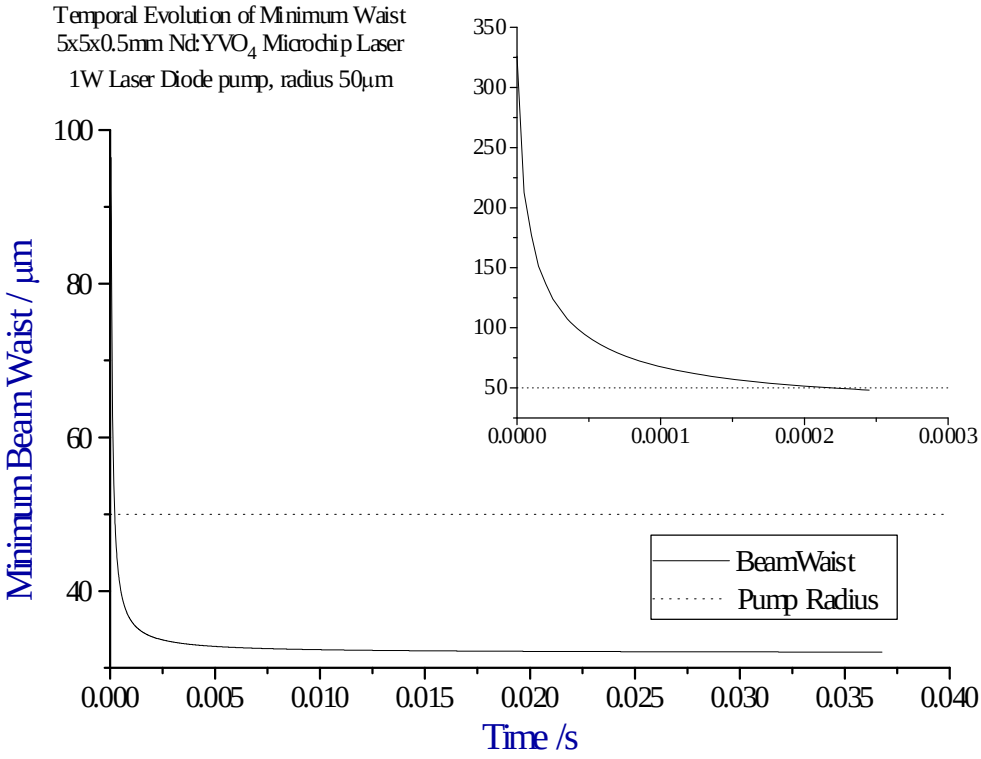

Figure 43 – Temporal development of minimum beam waist

More importantly, the temporal evolution of the transverse mode definition can be

modelled using Equation 35 as shown in Figure 43.

The flow of heat from the pumped region leads to a rapid build up of a stable cavity. Within 200μs from when the 1W of pump power is incident on the microchip, the waist size is already equivalent to the pump waist, and the microchip would begin lasing. After around 10ms the beam waist has reached a pseudo steady state.

Thus, the one dimensional finite element modelling has given us a guide as to how quickly the thermal lens is formed and how quickly thermal equilibrium is reached. Both these values are useful in consideration of quasi-CW pumped lasers, where the period between pulses should be sufficiently short as to prevent deleterious effects from thermal relaxation.

3.2.8.4 Two Dimensional Finite Element Modelling

By extending the matrix of elements to two dimensions, it is possible to consider a number of problems that cannot be solved analytically. Associated with this increase in dimensions is an increase in the computing power required to provide sufficient iterations to reach a steady state. Typically these solutions take several hours to compute, depending on element size and termination conditions.

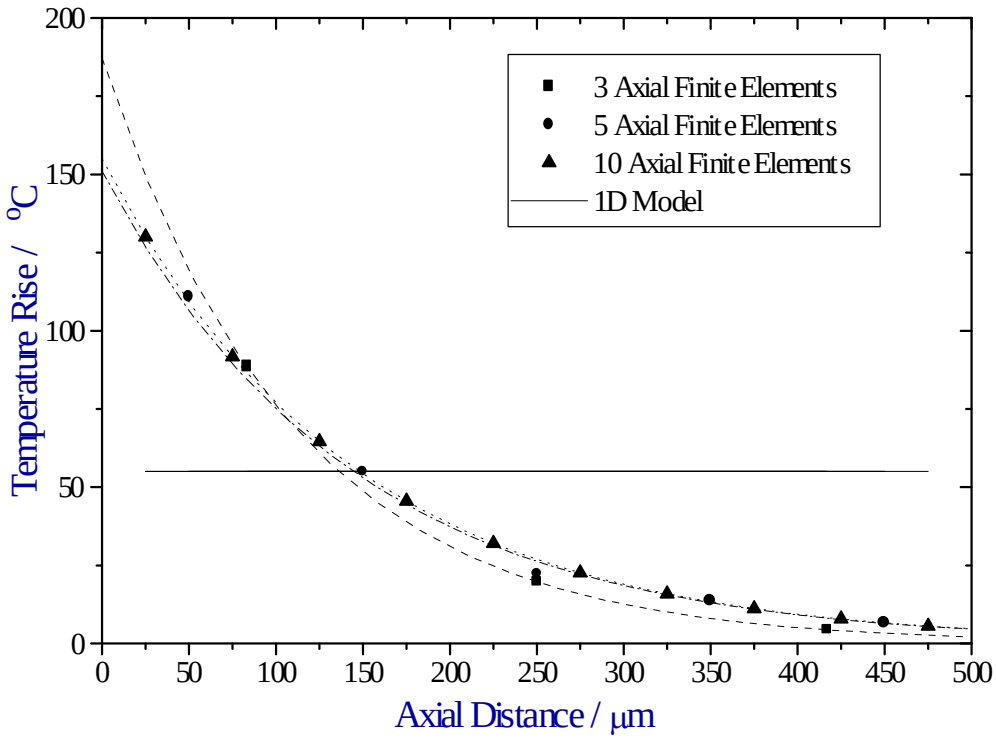

Figure 44 – Axial Temperature Variation from 2D Cylindrical Finite Element Model. 5x5x0.5mm 3% Doped Nd:YVO_4 Crystal Pumped with 1W in a 50μm

Spot.

The radial model described previously can be extended to a cylindrical model to examine the axial temperature gradient. In this chapter, it has been assumed there is a constant temperature profile in the axial plane. This is an unreasonable assumption given the short absorption depth in Nd:YVO_4 which would provide strongly localised heating to the pumped surface. Figure 44 shows the axial temperature profile in the centre of the pumped region from our finite element model, calculated with different element sizes. The data is fitted with an exponential decay, which would match the absorption profile of the pump light. From the data, a matrix with 5 axial elements is sufficient to give a good indication of the maximum temperature at the face of microchip, in this case about 150^{o}C, nearly three times the average temperature.

This result correlates well with the observed fracture point of a 0.25mm crystal, which occurred at slightly less than half the temperature predicted by the 1D analytical model. With further work, it would be possible to calculate the exact form of the maximum axial temperature profile, which empirically is:

$$T_{max} = \frac{-\alpha_0 mL\langle T\rangle}{\left(1-e^{c-\alpha_0 mL}\right)}$$

Equation 66

Where c and m are fitted constants and <T> is the average temperature from the analytical model. I hope future work will derive a more analytical solution.

The second form of 2D finite model is to use a x,y co-ordinate system to consider thermal effects in uniaxial and biaxial crystals. In the case of Nd:YVO_4, the thermal conductivities of the a and c axes are similar, which lead to an almost symmetric temperature distribution [219] and therefore this modelling was not pursued in depth.

It is possible to extend the finite element modelling to 3D and combine all these effects, again with a leap in the computing power required. Although simple forms of a 3D model have been calculated, they do not indicate any new insights or effects that have not already been discussed.

In conclusion, we have derived a range of models for understanding thermal effects within microchips, ranging from analytical solutions to numerical calculations. These models have provided a basis for the understanding of thermal guiding and now we will consider how this work relates to experimental measurements of the guiding.

3.3 Measurement of Optical Distortion

In the previous section, we considered how distortion of a gain crystal could be caused by optical pumping. Several models were described indicating how the flow of heat from the pumped region could cause both refractive index guiding ('thermal lensing') and guiding by thermal expansion.

This section will explore the measurement of this optical path distortion and compare it to the models derived in the previous section. Two techniques were used for this work, one a direct measurement of the change in optical path length using a Fizeau interferometer and the other indirect, through the change in divergence of the laser output. We will now consider these two methods in turn before considering the relative magnitudes of the two thermal guiding mechanisms.

3.3.1 Far-Field Measurement of Optical Distortion

A TEM_{00} mode emitted from a stable microchip laser cavity, which has a minimum beam radius w_0 inside the cavity, has a half divergence angle in the far-field of [196]:

$$\theta = \tan^{-1}\left(\frac{\lambda_0}{\pi n w_0}\right)$$

Equation 67

where λ_0 is the wavelength of the emerging beam and n is the refractive experienced by the propagating rays. As a rule of thumb, a beam can be considered to be in the far field after a few Rayleigh ranges [220], where the Rayleigh range is defined as:

$$z_R = \frac{\pi n w_0^2}{\lambda}$$

Equation 68

For a Nd:YVO_4 microchip laser with a beam waist of 50μm this equates to a Rayleigh range of 1.6cm, and therefore the beam can be considered to be far-field beyond approximately 5cm from the microchip laser.

The waist of this beam in the far field, at a distance z from the minimum beam waist,

is given by:

$$w(z) = w_0\left[1+\left(\frac{\lambda z}{\pi n w_0^2}\right)^2\right]^{\frac{1}{2}}$$

Equation 69

This expression can be simplified such that when:

$$w(z) >> w_0$$

$$\text{then}:$$

$$w(z) = \frac{\lambda z}{\pi n w_0} = \theta z$$

Equation 70

Thus by measuring the size of the emitted beam sufficiently into the far-field, the minimum beam waist experienced by the mode within the cavity can be deduced.

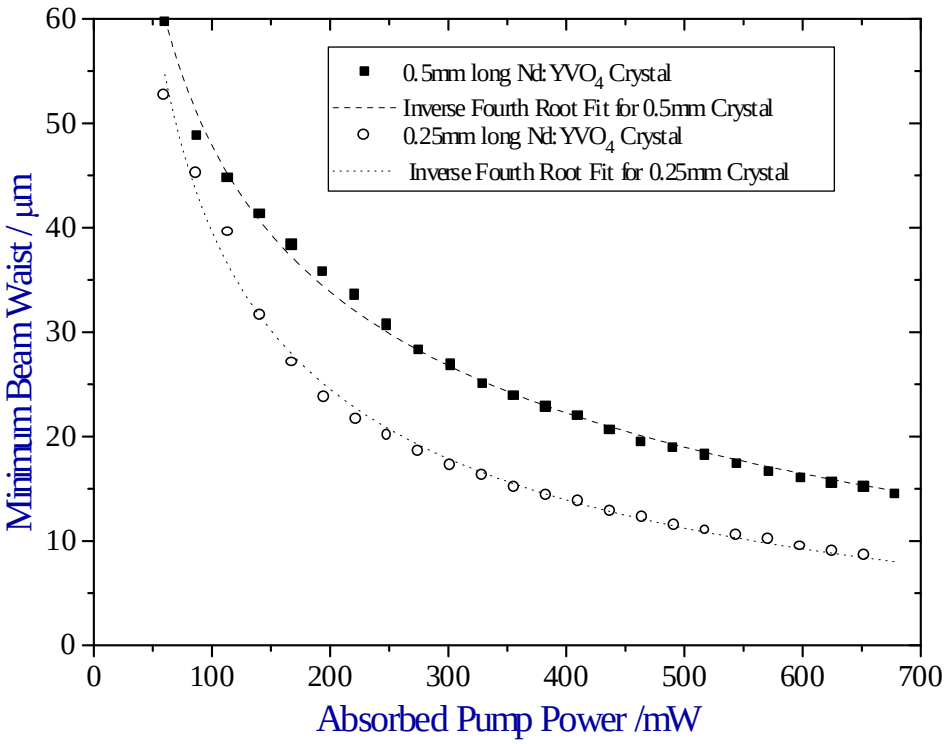

Figure 45 – Minimum beam waists of a 0.25mm and 0.5mm long Nd:YVO_4 microchip laser with increasing pump power. The beam waists were calculated from measurements of the output beam in the far field. The results are fitted with the fourth inverse root dependence hypothesised in Section 3.2.3. A 1.2W laser diode was used to pump both lasers.

Using a CCD camera to measure the spot sizes at a distance of approximately one metre from the microchip, the pump power dependence of the minimum beam waist

for a 0.25mm and 0.5mm long Nd:YVO_4 microchip laser was calculated. The results are shown in Figure 45. The dotted lines represent the best fit of an inverse fourth root dependence of the beam waist on the absorbed pump power. This is the relationship predicted by Equation 35 for laser modes equal to or smaller than the pump size.

As can be seen, there is good agreement between the observed results and this predicted dependence, indicating the size of the lasing mode is smaller than the pumping diode mode. This is indeed the case, with the pump spot having a radius of approximately 50μm.

Therefore, potentially one of the most important factors in determining the threshold of a microchip laser is that the lasing mode forms a stable cavity giving a smaller beam waist than that of the pump beam. However too small a beam waist will also cause low efficiency due to poor overlap between the diode and lasing mode volumes.

There is a smaller beam waist than predicted by the Cousins model discussed earlier because of a number of factors. The high doping concentration leads to significant fluorescence quenching, giving up to 40% of the incident power to phonon heating. The short absorption depth will also lead to non-uniform axial heating, as discussed in the section on finite element modelling and cause larger than expected lensing and end-face curvature.

The approximation for the pump spot size is taken from fluorescence measurements of the pumped area and is therefore an integrated value for the pump size. Previous measurement of the pump spot using a scanning photodiode showed the pump spot to be approximately 30x80μm in size at its focal point. Considering all these factors, a good fit can be achieved between the Cousins model and the measured results.

The effect of polarisation dependent pump absorption was investigated in a Nd:YVO_4 microchip using a CW Ti:sapphire pump source. The pump beam was focussed using a 250mm lens to give an 85μm pump radius and the microchip rotated so as it could be pumped parallel or perpendicular to the c axis. As can be seen from Figure 46 the beam radius is greater for a pump polarisation perpendicular to the c axis of the microchip. The longer absorption depth and decrease in absorbed power account for this effect, with less pronounced surface deformation and more shallow axial temperature gradient.

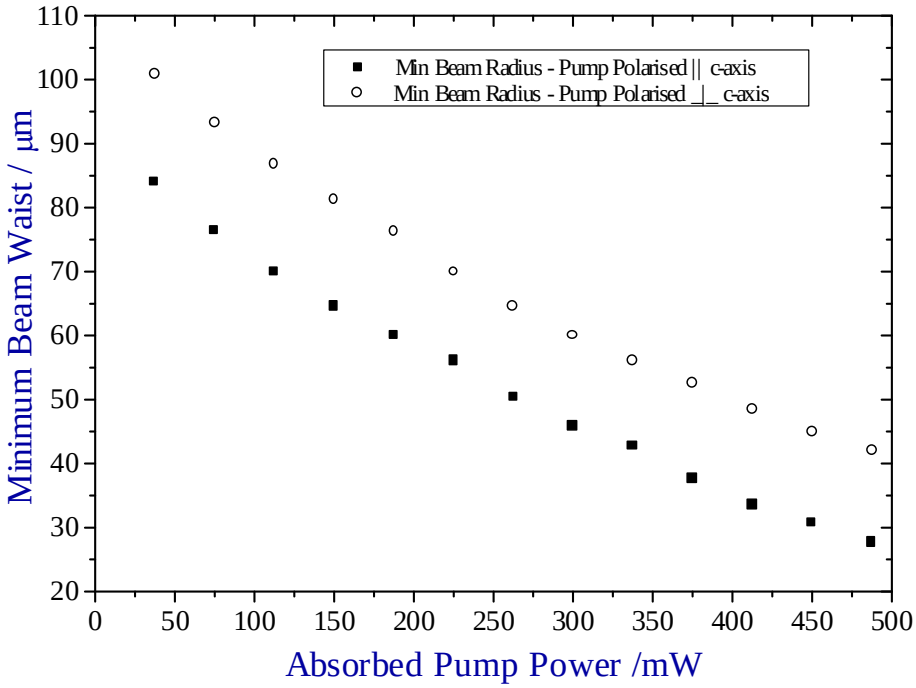

Figure 46 – Minimum beam waist of a 99%/HR 0.5mm long Nd:YVO_4 microchip laser pumped by a polarised Ti:sapphire along each axis. The pump spot from Ti:sapphire was 85μm.

The accuracy of the technique of measuring the far-field divergence relies on the assumption that the transverse mode is always diffraction limited. Measurement of the near field intensity profiles in the previous chapter indicated for monolithic microchip lasers pumped with a 0.5W laser diode the transverse mode was always near diffraction limited (M^2<1.2) and therefore this assumption was carried forward. This assumption can be checked by consideration of the effect of a higher order transverse mode. A higher order mode has a higher divergence, giving a smaller than expected beam waist. No discontinuities were observed, which would indicate that no mode jumps take place, and that the beam waists were of the order expected, suggesting the assumption was valid.

In conclusion, far field measurement of the divergence provides a fast and simple method to calculate the minimum beam waist with the cavity of a microchip laser. The results are consistent with the trends predicted by out thermal modelling and absolute differences can be accounted for if quenching and gain effects are included in the modelling. We will now consider the second technique, interferometric measurement, before describing further work comparing these two techniques.

3.3.2 Interferometric Measurement of Optical Distortion

The second technique used to measure the optical distortion is based on interferometric measurement of the microchip crystal. A Fizeau interferometer, like the one illustrated in Figure 47, was used to measure the optical distortion caused by the absorption of the pump light in the microchip laser. The interferogram is formed from the reflection of light from both the front and back surfaces of the microchip laser. One of the requirements for an efficient microchip laser is that the two surfaces forming the laser cavity are approximately parallel. Typically this parallelism is better than 0.1mrad, which equates to one fringe different in optical path length between the two faces of the crystal. The two near-parallel reflections from these faces can be easily imaged onto a CCD camera to form the interferogram and the image captured by a computer.

The light used to probe the crystal was typically from a HeNe laser, which has a coherence length of approximately 30cm, much longer than the 0.2-1mm coherence length required to produce an interferogram. This long coherence length was problematic in that reflections from other surfaces, in particular the pumping lens close to the front surface of the microchip caused unwanted disturbance to the interferogram. To minimise this noise, various other light sources were investigated as alternatives to a HeNe laser, including filtered white light sources, diode lasers, and arc lamps. Overall, however, the uniform and high brightness illumination provided by the HeNe laser, or a green microchip laser were found to be the most suitable light sources for these experiments. To minimise the reflections from the pumping lens a suitable glass filter was employed which would transmit the pumping radiation at 810nm and absorb any incident 632.8nm HeNe light.

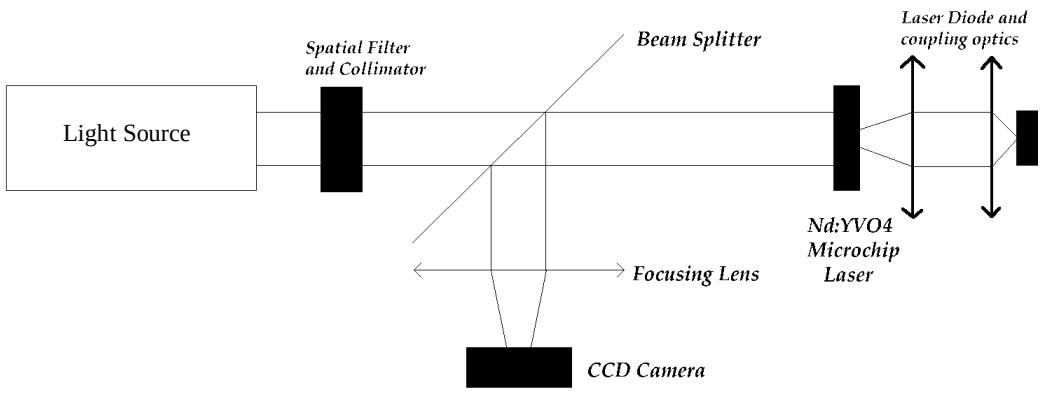

Figure 47 – Fizeau Interferometer for Measuring Optical Path Distortion

A second major limitation on this form of measurement is the requirement that the residual pump and lasing wavelengths be filtered before the CCD camera. Typically, their intensity is greater by up to two orders of magnitude than the incident HeNe radiation. Both dielectric mirrors and glass filters were investigated as methods for blocking the pump and lasing wavelengths. Dielectric mirrors were found to introduce less distortion to the image, though provided less attenuation and problems with interference if badly aligned in the beam path. Glass filters were used for most of this work, often in conjunction with an initial dielectric mirror. This initial mirror was used to attenuate the pump and lasing wavelengths to a suitable power level so that thermal effects caused by the heating of the filters through absorption of the light were minimised.

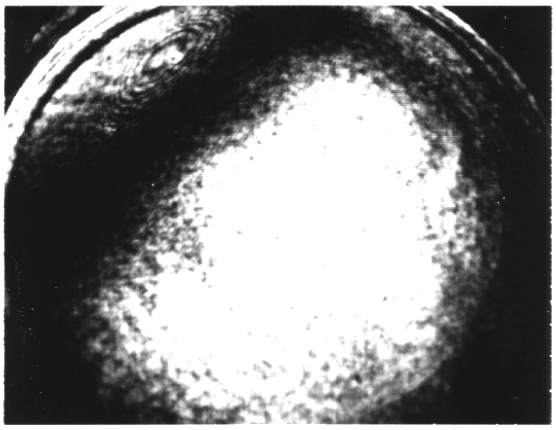

a) Interferogram of 0.25mm Nd:YVO4 Microchip
The width of the microchip is 5mm

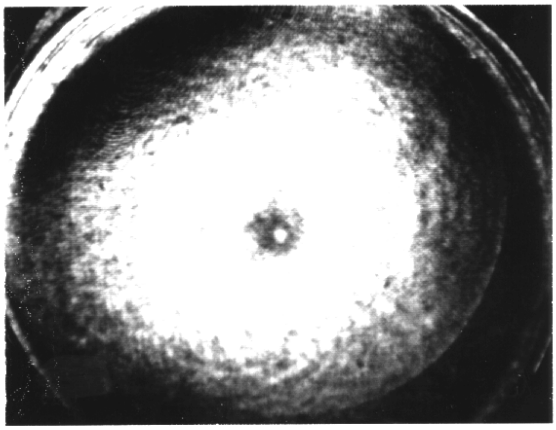

b) Deformation caused by 500mW of Diode Power

Figure 48 – Optical deformation interferogram of a 0.5mm 3% Nd:YVO_4 Microchip Laser by 0.5W laser diode. The bright ring around the edge marks

the edge of the dielectric coatings (5mm diameter).

Typical whole chip interferograms are shown in Figure 48. They show the effect of pump light from a 500mW laser diode incident on the centre of a 5x5x0.5mm 3% doped Nd:YVO_4 crystal. The pumped region forms the main area of interest for this work as it defines the lasing mode and maximum temperature and stress/strain regions. For analysis of this region, long focal length lenses are used to image the pumped region onto the CCD camera to provide a larger working image, typically several centimetres across. This imaging system ultimately determines the resolution of this form of interferometric measuring system. It is limited by the quality of the lens used (typically a large area doublet to minimise image distortion) and the intensity and homogeneity of the light source used. The setup of the camera was also important, to ensure linearity of its response and proper gamma control.

The change in optical path length was analysed relative to the background, unpumped case using an image analysis program, such as Image Tool. Line intensity profiles from an unpumped background were subtracted from the profiles through the centre of the distorted region to give the resultant change in optical path length as a series of interference fringes. These fringes were then analysed as $\cos^2\theta$ intensity fringes over the pumped region with maximum or minimum intensity nodes providing the inflection points.

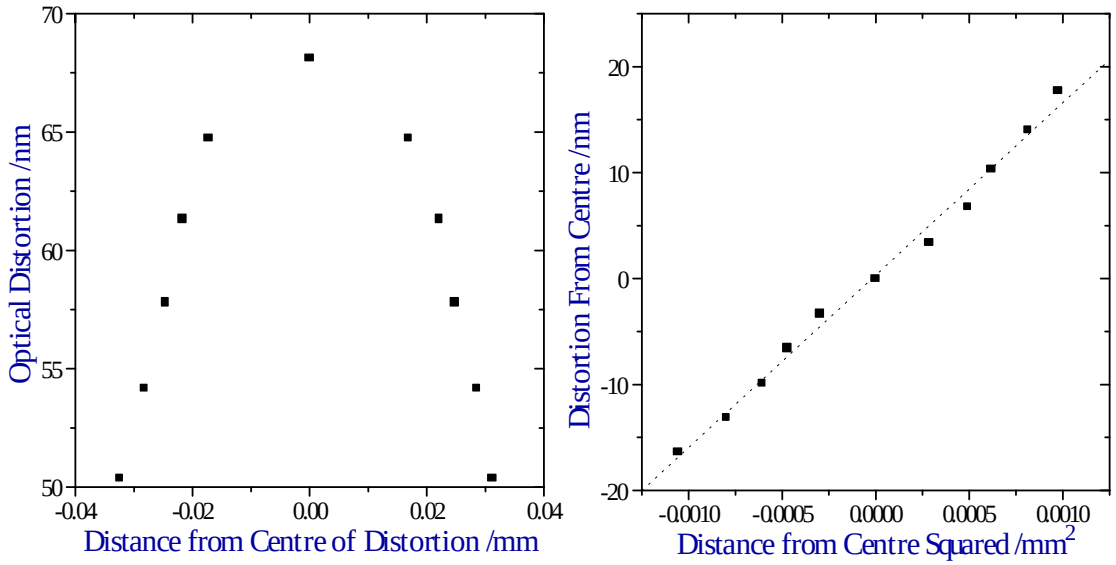

Figure 49 – Measured Change in Optical Path Length around Centre of Pumped Region for 0.5mm 3% Nd:YVO_4 Crystal pumped with 0.5W. The distortion is

parabolic (R^2=0.97) and symmetric around the Centre.

Figure 49 shows the change in optical path length measured around the centre of the pumped region for a 5x5x0.5mm 3% doped Nd:YVO_4 crystal pumped with a 0.5W laser diode. The second graph shows the excellent correlation between the distortion and a quadratic function. This indicates that the parabolic approximation we used in the earlier modelling is valid over the pumped region.

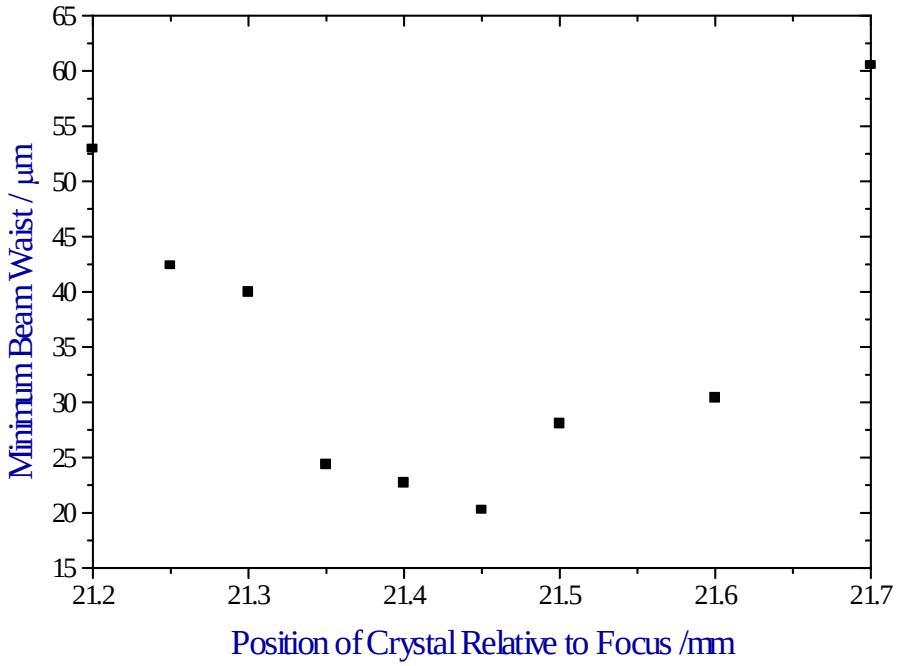

Figure 50 – Minimum beam waist measured from optical distortion as the microchip laser translated through pump focus.

The change in optical path length was measured as the microchip laser was translated through the focus of the pump light to investigate how the waist varied with pump spot size. Figure 50 records the minimum beam waists calculated from the optical distortion measurements. Close to the focus of the pump spot incident on the surface of the microchip (~21.45mm) there is little variation in the minimum beam waist. Further from the focus, there is a sudden rise in the beam waist size, which correlates well with the results from far field measurements described in Figure 58.

We will now consider these two techniques in relation to each other and to the theoretical modelling in the previous section. We will then conclude this section on the measurement of optical distortion by considering the relative contributions of

thermal expansion and thermal lensing to the guiding of the transverse mode.

3.3.3 Comparison of Measurement Techniques

If we compare these two measurement techniques for measuring the minimum beam waist, there is a constant and unaccountable difference between the measurements as shown in Figure 51.

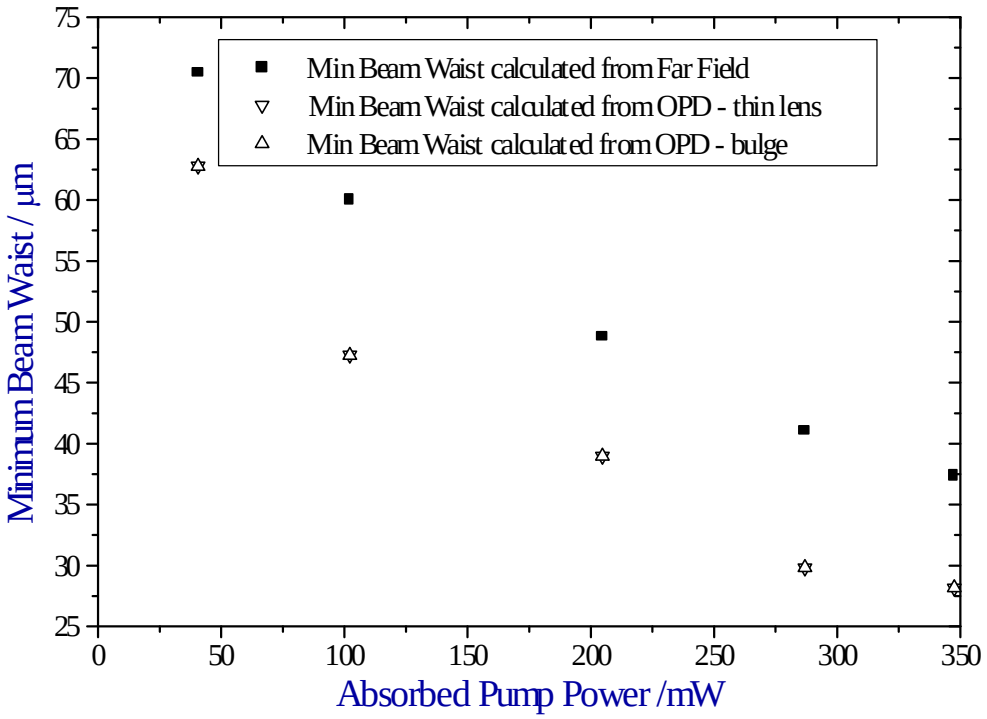

Figure 51 – Comparison of minimum beam waist from OPD and far-field measurements of a 95%/HR 0.5mm long Nd:YVO_4 microchip laser pumped by 0.5W laser diode.

Consideration was given to modelling of both methods to account for this discrepancy, as illustrated by the two OPD minimum beam waist calculations in Figure 51. One treated the distortion as solely thermal expansion (i.e. using Equation 34) and the other as a plane-plane cavity with a thin thermal lens (i.e. using Equation 37). This was found to be insignificant as illustrated.

Experimental assumptions similarly cannot account for this discrepancy, such as non-TEM_{00} operation. In this case, the beam waist from the far-field measurements would be smaller than that from the OPD measurements. The only explanation, which will be discussed later, is if there is anti-guiding of the oscillating mode due to the saturated gain present in the cavity, which would not be evident from measurements

using the non resonant HeNe radiation.

3.3.4 Comparison of Theoretical and Experimental Results

The second comparison of interest is between the theoretical models derived in the previous section and the measurement techniques described in this section. Good agreement was shown between the 1D analytical model and the far field technique, for the relationship between minimum beam waist and pump power, as illustrated in Figure 45. Figure 52 below compares the measured OPD caused by 350mW of absorbed pump power with that predicted by the 1D analytical model and the finite element model described in the previous section.

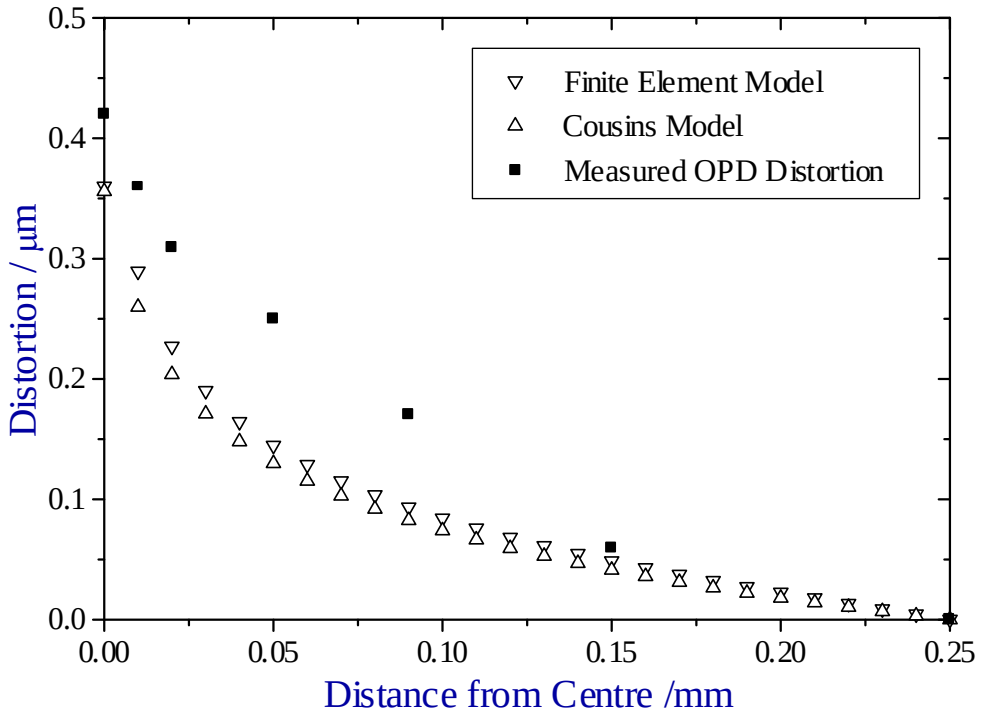

Figure 52 – Comparison of measured and predicted distortion of 5x5x0.5mm 3% doped Nd:YVO_4 microchip laser pumped with 350mW of absorbed power.

As expected there was good agreement between the models, predicting similar distortion profiles. However, the measured OPD measured was larger than expected with a lower gradient profile. This can be explained through two effects. The models assumed only quantum defect heating, although in reality the heating is more substantial due to effects including fluorescence quenching, accounting for the larger distortion. The shallower gradient may arise due to larger than expected thermal conductivity, and stress and strain considerations not accounted for in the modelling.

However in general, good trend correlation was observed between predicted beam waists and the measured beam waists from optical path distortion.

3.3.5 Surface Distortion

The final comparison of interest is the relative contributions of guiding by thermal expansion and refractive index guiding to the overall guiding of transverse mode in a Nd:YVO_4 microchip laser. In the case of LNP thermal expansion dominates the definition of the transverse mode [211] although is insignificant in Nd:YAG [210]. From Table 12 the thermo-optical coefficient of Nd:YVO_4 is approximately twice the thermal expansion coefficient and therefore it would be expected that thermal lensing would be more significant. The short absorption depth, providing strong localised heating of the pumped surface, could however favour thermal expansion as the dominant guiding mechanism.

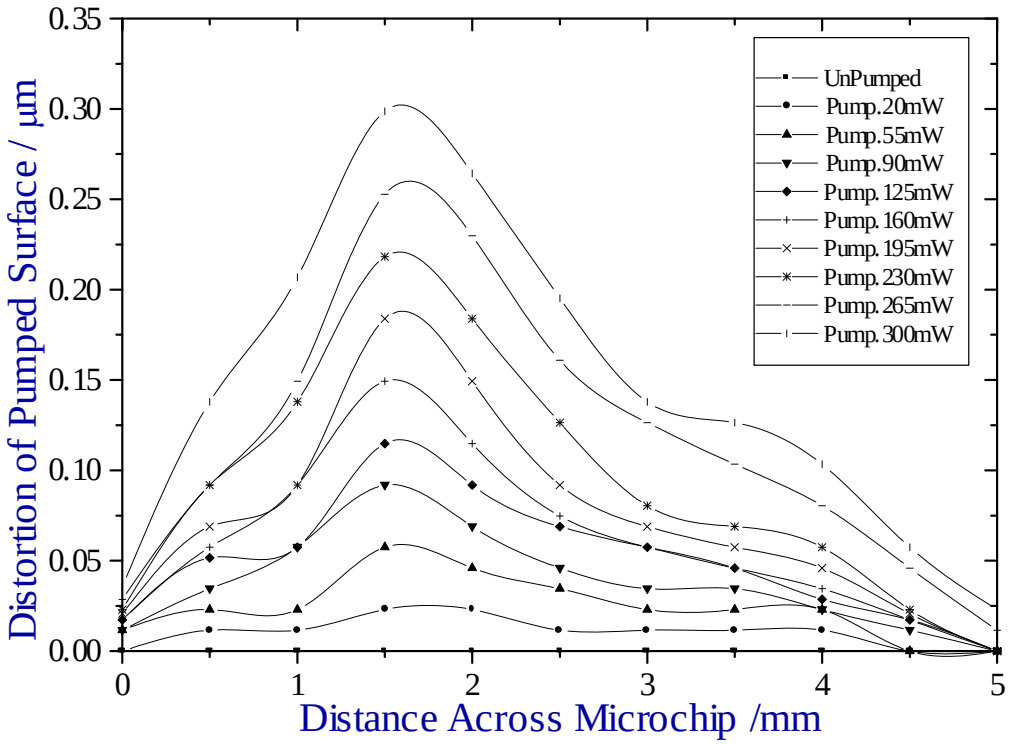

Figure 53 – Distortion of the pumped surface of a 5x5x0.25mm 3% doped Nd:YVO_4 microchip laser due to thermal expansion. The microchip was pumped by a 0.5W laser diode through a 6.5mm-focussing lens.

Initially, the development of the surface bulge, due to thermal expansion, on the pumped surface of a 0.25mm long Nd:YVO_4 microchip laser was characterised as shown in Figure 53. The distorted surface was measured by inserting a $^{\lambda}/_{10}$-flat glass

plate between the pump lens and the pumped surface of the microchip laser. The change in the fringe structure between the flat and distorted surface was used to calculate the distortion in a similar method to that described previously for measurement of the total optical path distortion. The distortion was determined to be out from the material, giving positive and significant guiding. However, the smaller magnitude and the additional spurious interference fringes, from the increased number of surfaces, lead to poorer resolution than for the OPD measurements.

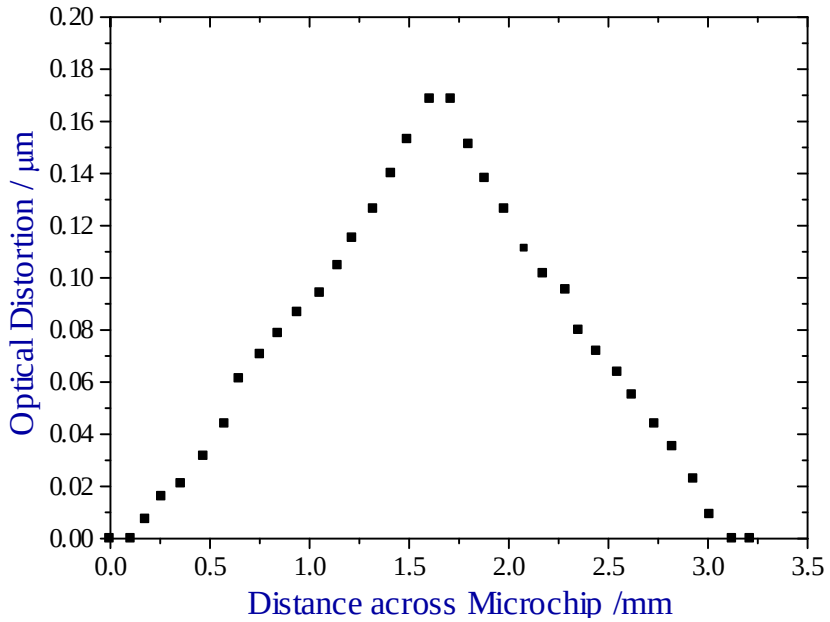

Figure 54 – Measurement of optical distortion of the surface of a 3% 5x5x0.5mm Nd:YVO_4 pumped with 350mW from a 0.5W laser diode.

The second experiment used the same experimental system as Figure 52. The optical distortion in this case was less than for the 0.25mm crystal used in Figure 54, in agreement with the expected distortion from our modelling. Comparing the overall OPD from Figure 52 with surface distortion in Figure 54, indicates that thermal expansion of the pumped surface contributes approximately 40% to the total change in optical path length. Therefore, both guiding mechanisms make a significant contribution to the confinement of the transverse mode. No attempt was made to measure the distortion of the unpumped surface, though potentially a small distortion may occur at that face as well, but beyond the resolution of our current interferometer.

In conclusion, we have described two independent methods for measuring the optical path distortion, which arises from optical pumping of a monolithic microchip laser.

Initial comparison of these methods and with the models derived in the previous section has been made, indicating unexplained offsets, though with good general agreement of trend. Further experimentation may clarify the nature of these offsets.

3.4 Gain-Guiding of Transverse Modes

3.4.1 Introduction

In the previous two sections, we have considered how thermal effects can determine the transverse mode structure of a CW monolithic microchip laser. However, for some materials and pumping conditions, the distribution of gain and loss within the cavity can also become a significant factor in determining the transverse mode structure.

Monolithic Nd:YVO_4 microchip lasers are one of the most attractive solid-state lasers in which to observe gain-related effects. Their monolithic nature, where dielectric coatings are directly applied to two near-parallel surfaces of a sub-millimetre sized crystal, combined with the short absorption depth and large stimulated emission cross-section of Nd:YVO_4, offer high gain in a cavity on the edge of stability. Gain guiding can then arise from the wavelength-dependent refractive index profile due to dispersion around the gain centre and preferential amplification in the high gain regions.

Typically however, thermal effects dominate the definition of the transverse mode in a CW microchip laser. Previous work in St. Andrews, using monolithic LNP microchip lasers, found no evidence of gain guiding [221]. However, when thermal effects are minimised and in the presence of high gain, or re-absorption losses, it is possible to observe alternative guiding mechanisms. Previous experimental work has shown high gain in Nd:YVO_4 lasers to be significant in guiding the transverse mode [222,223]. Similarly, for a three-level laser system, Fan found the re-absorption losses at the edges of the pumped region could dominate the definition of the transverse mode [224].

Substantial theoretical modelling of gain and its ability to guide the cavity mode of a microchip laser has been carried out by Harkness and Firth [225] and Longhi et al. [226]. The effect of cavity detuning on the optimisation of pump spot sizes has also been considered by Sanchez and Chardon, predicting a decrease in laser efficiency for

positive cavity detuning, and an increase for negative detuning [227].

We will begin this section by considering the conditions under which gain-guiding effects can be observed, and then consider a consequence of gain-guiding, self-Q-switching, before describing how our thermal modelling can be extended to take account of gain-guiding.

3.4.2 Experimental Evidence of Gain-Guiding

To examine gain guiding it is first necessary to consider the circumstances under which it will be evident as a guiding mechanism. In order to minimise the effect of thermal guiding and increase the contribution of other guiding mechanisms, pulse-pumping with high peak powers and low duty cycles was chosen as the most likely conditions for observing gain induced refractive index guiding.

The 0.5W SDL-2542 laser diode used for this work was modulated by using a pulse generation to modulate the current to the diode via the analogue input of the SDL-800 driver. The light from the diode laser was collimated using an 8mm focal length lens and focussed into the microchip laser using a 6.5mm lens. The rising edge of the diode pump pulses was ~1μs, giving possible repetition rates of 0-90kHz and average pump powers from 100μW to 400mW with a maximum peak power of 400mW.

For all gain-guiding work monolithic Nd:YVO_4 microchip lasers were used operating at 1064nm, to take advantage of the high gain associated with this transition. In particular a 5x5x0.5mm 3% doped Nd:YVO_4 microchip laser, coated 99%R/HR at 1064nm was used for this exploratory work in the sub-section determining the conditions under which gain-guiding becomes significant.

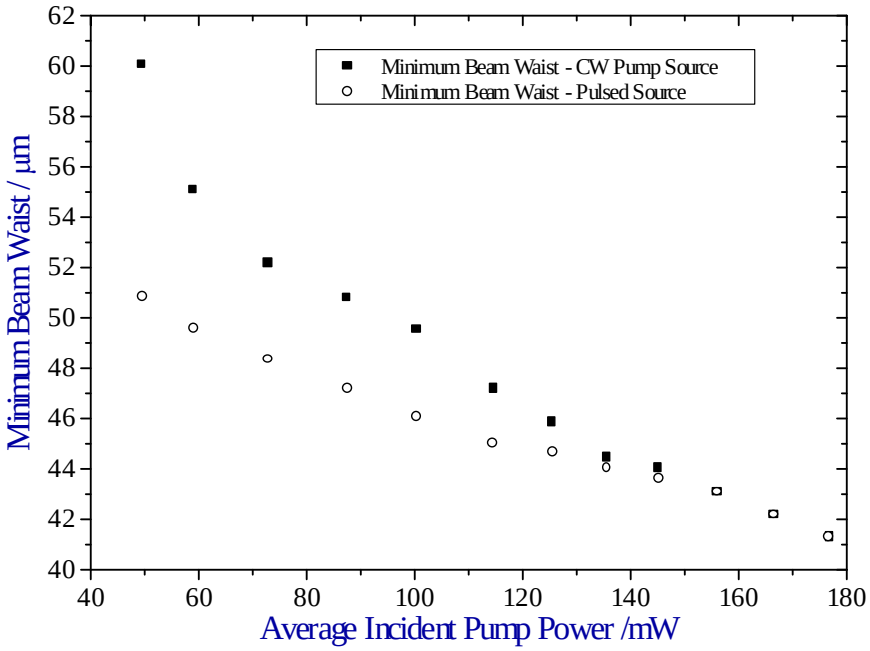

Figure 55 – Beam waist from microchip laser as function of average incident power for a) CW and b) pulsed 0.5W diode laser. The peak power of the pulsed source was 400mW with the pulse period varied to give different average powers.

The first experimental evidence of gain guiding in monolithic Nd:YVO_4 microchip lasers came from examining the divergence of the output under different pumping conditions. The divergence could then be used to determine the minimum beam waist within the cavity using the methods described in Section 3.3.1 and comment made on the magnitude of guiding within the cavity. This first experiment is analogous to the previous work carried out in St.Andrews with monolithic LNP microchip lasers [211] that showed no evidence of gain guiding.

As can be seen from Figure 55, the minimum beam waist for the CW pumped microchip (filled squares) followed an inverse fourth root dependence to the pump power, as predicted earlier in Section 3.2.4. However, when the peak power was kept constant at 400mW and the pulse repetition rate varied to achieve equivalent average powers, the minimum beam waist was found to diverge from the CW case (open circles). If gain guiding was not present, both lines would follow the same dependence, but a positive gain guiding effect would cause a smaller beam waist. Therefore, as the contribution of the thermal lensing decreases at lower average powers, the contribution of the gain induced refractive index guiding becomes more significant.

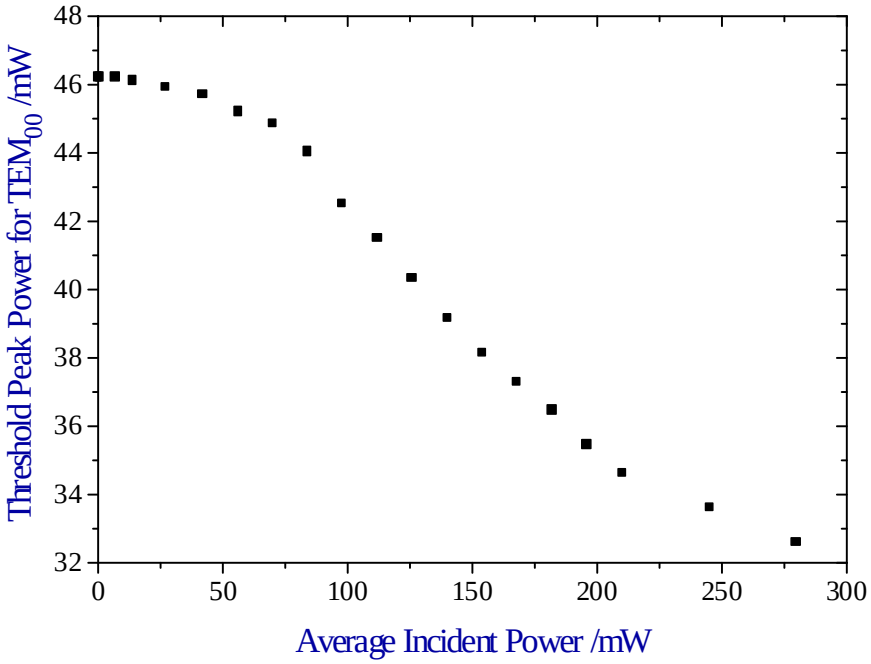

Figure 56 – Peak pump power required to reach threshold for a TEM_{00} mode at different average powers. The duty cycle of a quasi-CW 0.5W laser diode (max. incident power 400mW) was fixed at 1kHz and the pulse width varied to give different average powers at full peak power. The peak power was then decreased to measure the threshold peak power required at that duty cycle.

For the same system, the peak power was varied at different average power levels to measure the peak pump power required to reach threshold of a TEM_{00} mode at different average powers. The results are shown in Figure 56. This graph illustrates the region between thermal guiding and gain guiding. With no gain effects, the threshold would tend to infinity as the average incident power decreases, because of the decreasing overlap between the pumped mode volume and the lasing mode volume. Conversely if guiding was solely due to the presence of gain, the threshold peak power would be independent of the average pump power. Therefore this experiment indicates that both mechanisms are important, gain-guiding dominating at lower average powers and thermal guiding dominating at high average powers,

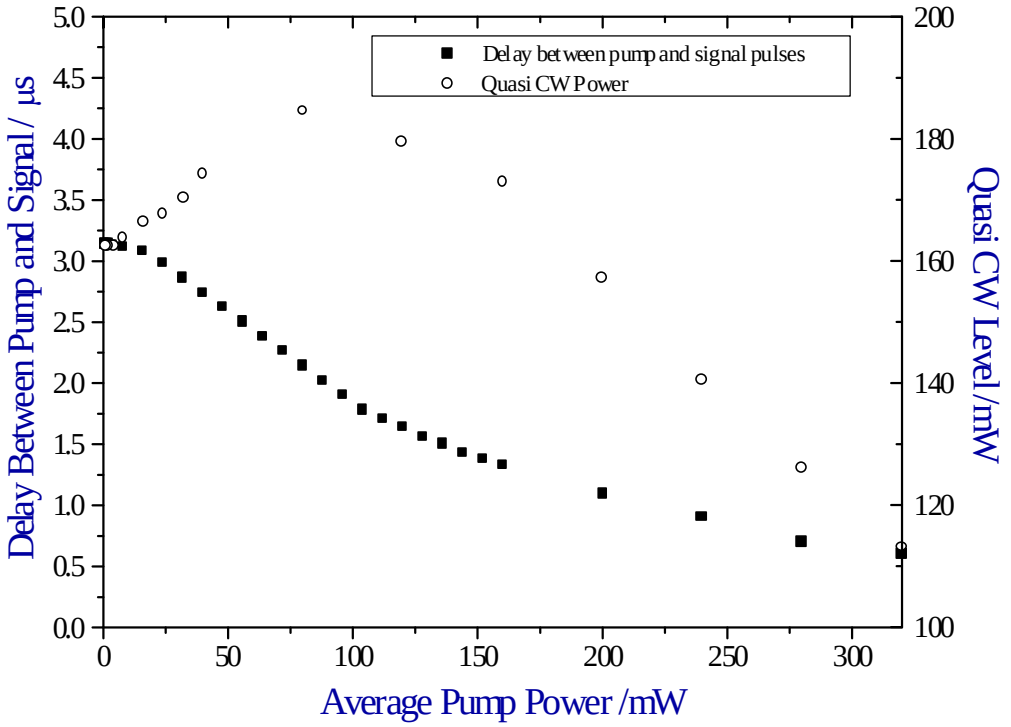

Figure 57 – Quasi-CW output power and delay between pump and signal pulses of pulse pumped 0.5mm long Nd:YVO_4 99/HR microchip laser. Different average powers were achieved by varying the period between 50µs, 400mW peak power diode pump pulses.

Returning to the use of a constant peak power of 400mW, the mode matching and efficiency of our microchip laser were considered as a function of average power. These characteristics were interpreted from the lasing output of the microchip laser. The efficiency was taken to be described by the peak power of the quasi-CW part of the lasing output from the microchip laser and the delay between the pump pulse and the start of the microchip gain switching (pulse build-up time) was used as a measure of the amount the gain available exceeded the losses for the lasing mode.

The results for this experiment are shown in Figure 57. The peak power of the quasi-CW level can be seen to peak around an average power of 75mW, indicating the conditions under which there is optimal coupling between the pump and lasing mode volumes. This indicates the lasing mode volume is generally less than the pumping mode volume for CW systems operating well above threshold, limiting their efficiency. The use of a 6.5mm focal length lens to image the diode pump light into the microchip laser was therefore a non-optimal choice of focussing lens. This is in

agreement with the observations in the previous chapter that longer focal length lenses (e.g. 8mm) provide higher efficiency through better mode overlap. However, a 6.5mm lens was used here to provide a smaller pump spot size within the crystal which potentially would offer a region of higher gain.

The relationship between the delay between the pump and microchip pulses and the average thermal power is similar in shape to that of the previous experiment (Figure 56), again indicating the transition between thermal and gain guiding. At high average powers, there is excellent overlap between the high gain region in the centre of the pumped volume and a small lasing beam waist within the microchip laser. This gives a high gain/loss ratio and consequently a short pulse build-up time. With decreasing thermal load, the beam waist increases to include lower gain regions and unpumped regions, leading to a longer build-up time. At very low average powers, the build-up time tends to a fixed values determined by the gain induced refractive index guiding of the lasing mode due to the fixed peak power. Although not fully considered here, the preferential amplification of the oscillating mode in the central portions of the lasing mode will also contribute to the confinement of the lasing mode.

The final experiment carried out repeated an experiment described by Longhi et al. [222]. Their theoretical modelling of gain-guiding using the Maxwell-Bloch equations hypothesised that cavity detuning in a cavity with two longitudinal modes would cause hopping between the two modes, observable by a change in the beam waist. This change in beam waist arises from one of the longitudinal modes being positively detuned from line centre and therefore anti-guided by the negative dispersion, giving a large minimum beam waist within the cavity. The converse is true for the negatively detuned second longitudinal mode, which would have a smaller beam waist. This hypothesis was experimentally verified using a 0.7mm long 94%R/HR Nd:YVO_4 microchip laser operating at 1064nm pumped by a Ti:sapphire laser. The cavity detuning was achieved both with different focal length lens to give different pump spot sizes, and by displacing the microchip laser from the focal point of the lenses.

For our verification of this experiment, we used a 0.5mm long 5%R/HR Nd:YVO_4 microchip laser coated for 1064nm pumped with a CW 0.5W laser diode through an 8mm collimating lens and 6.5mm focussing lens. The microchip laser was then

translated through the focus of the 6.5mm lens to simulate different pump spot sizes. The far-field divergence of the resulting output was used to calculate the minimum beam waists as described previously. The results from this experiment are shown below in Figure 58, and agree with the observations and modelling of Longhi et al.

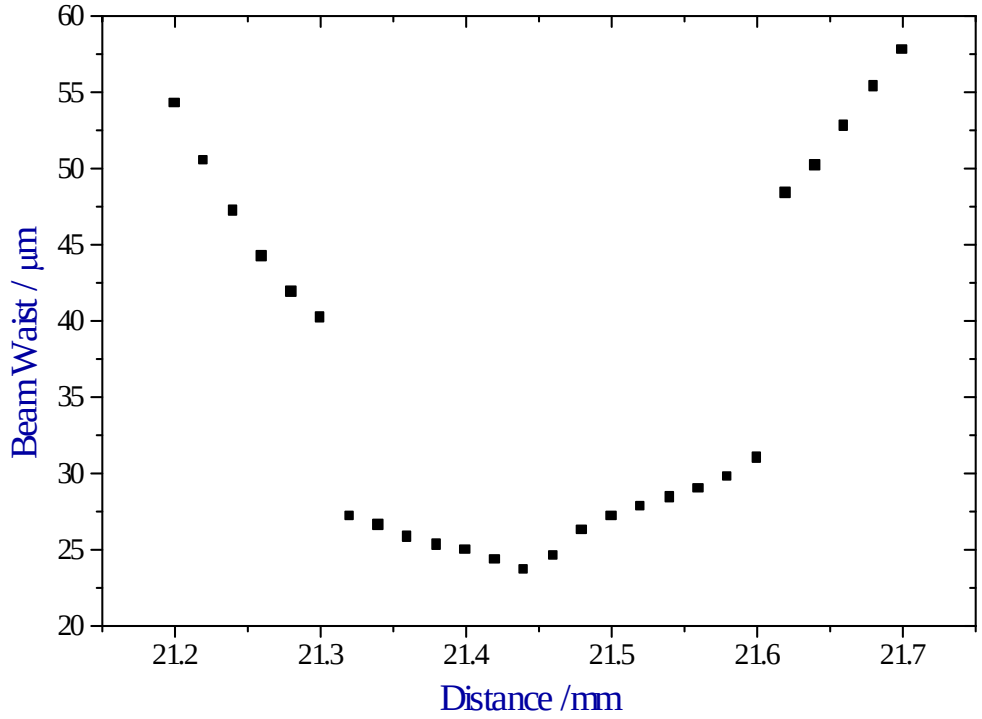

Figure 58 – Minimum beam waist as a function of the 6.5mm focal length pump lens position (relative). The beam waists were calculated from far field divergence measurements. The 5x5x0.5mm 95%R/HR Nd:YVO_4 microchip laser was pumped with 300mW of absorbed power.

As with Longhi's microchip laser, our microchip laser operated on two longitudinal modes, either side of the gain centre. The laser operated on a single lobed intensity profile in the far field over the experimental range (21.2-21.7mm) and on an obviously multi-mode output outside this region. No attempt was made to verify the single-lobbed output was a single transverse mode in the near field, though the calculations are consistent with this assumption. There was also evidence of increased elliptically in the output with detuning from the focal point, though again this was not quantified for this experiment.

The focal point was incident on the back surface of the microchip laser at approximately 21.44mm in Figure 58. This is characterised by a dip in both the

minimum beam waist and output power of the microchip laser. This dip is attributed to an increased heating of the rear surface by the strong absorption within the smallest pump spot size. Further characterisation of this effect could provide further insight into the relative contributions of both thermal expansion and thermal lensing to the guiding of the transverse mode.

In summary, we have carried out a range of experiments examining the conditions under which gain guiding of the transverse mode is observable. The transitional period between thermal and gain guiding has been investigated, with thermal guiding dominating in CW high average power systems and gain guiding dominating in high peak power, low average power systems. Although these experiments were carried out using Nd:YVO_4 microchip lasers operating at 1064nm to take advantage of their high gain, in principle the same effects should be observable in other monolithic microchip lasers, though perhaps with weaker gain guiding.

Our results also agreed with previous work showing how gain can effect the transverse mode of a Nd:YVO_4 microchip laser. This final experiment indicates a mechanism by which the Q of the cavity can be altered by cavity detuning. This 'self Q-switching' could arise from the different guiding properties of the two longitudinal modes providing different gain/loss ratios for each mode. Indeed we observed large inexplainable spikes from monolithic Nd:YVO_4 microchip lasers which we will now consider in the context of self Q-switching through gain induced refractive index guiding and cavity detuning.

3.4.3 Self Q-Switching in Monolithic Nd:YVO_4 Microchip Lasers

While working on gain-switched Nd:YVO_4 microchip lasers [228], we observed large spiking behaviour from our monolithic devices which could not be accounted for by normal gain switching theory. Gain-switching, where the upper state population is altered rapidly, often through modulation of the pump power, can produce peak powers in excess of a watt with pulses as short as 5ns, as described in Chapter Two. However, the large spikes we observed were several hundred times the CW level with peak powers in excess of 25W and pulses as short as 1.85ns, more similar in nature to Q-switched pulses. These pulses are potentially useful and we

believe we are the first to report on their generation and the mechanism by which they arise.

Q-switched operation of solid-state lasers is generally achieved through the addition of intra-cavity components to alter, either passively or actively, the quality of the cavity in time, to selectively allow the build up of pulses. Active Q-switching of microchip lasers has produced pulses as short as 115ps with peak powers in excess of 10kW [229] while passive Q-switching using saturable absorbers has produced pulses as short as 56ps [230] and peak powers in excess of 28 kW [231]. The active and passive Q-switching of microchip lasers will be described in more detail later in Chapter Four.

Q-switched operation can also occur through a number of intrinsic properties of the laser medium and cavity itself without the addition of additional elements. This 'self Q-switching' has been observed in a number of materials including ruby [232], Nd:YAG at 77K [233], and Nd:YVO_4 [234] though no explanation of the mechanism was given. Co-doped laser materials, such as Nd,Cr:YAG also exhibit self Q-switching in much the same way as separate gain and saturable crystals in a cavity give passive Q-switching [235]. The injection of sinusoidally frequency-modulated light back into a Nd:YVO_4 microchip laser has also produced pulses several hundred times the CW level, similar in nature to the giant pulses we have observed [236].

We will begin by considering the experimental evidence of the nature of these giant spikes. Here we present simplistic arguments to show how gain guiding can act as a mechanism for self Q-switching in monolithic Nd:YVO_4 microchip lasers. Following this experimental evidence we will consider a basic model for this self Q-switching and how the thermal modelling described earlier can be expanded to include the effect of gain induced refractive index guiding.

3.4.3.1 Experimental Evidence of Self Q-Switching

A 0.25mm long, 3% doped Nd:YVO_4 microchip laser was used for this work, coated for 5% output coupling at 1064nm. A 0.5W SDL-2542 laser diode, controlled by a SDL-800 driver, was used to pump this microchip through a 8mm collimating and 6.5mm focussing lens, which were adjustable to provide different pump spot sizes within the crystal.

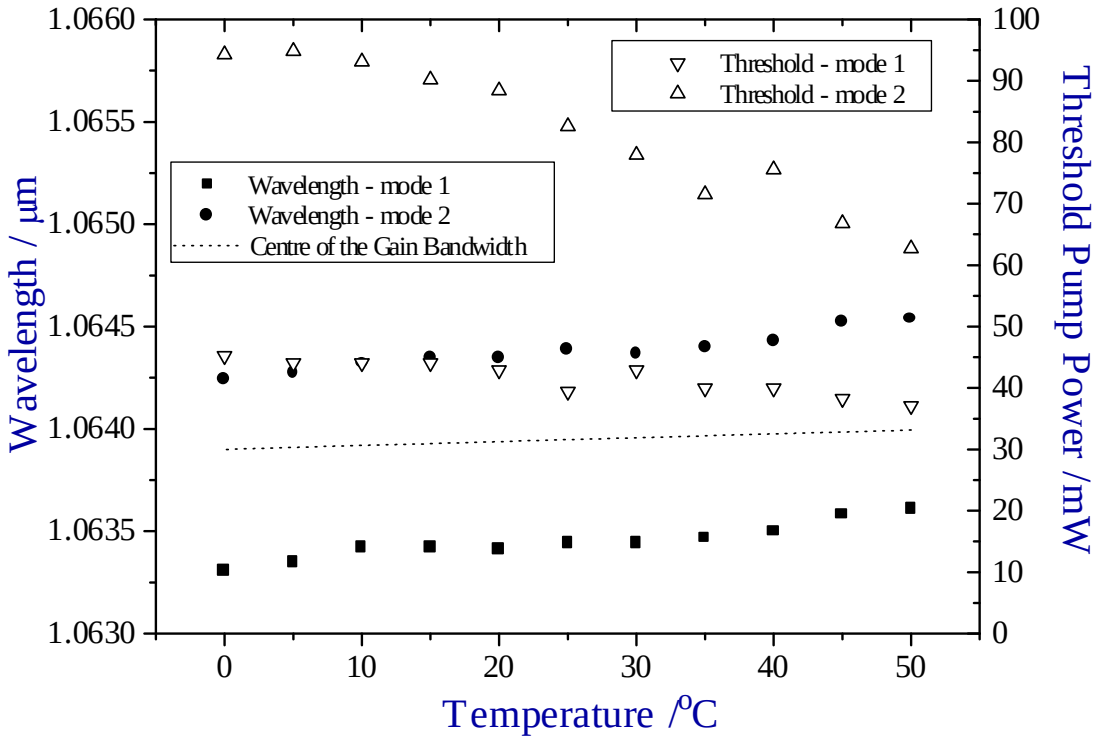

Figure 59 - Threshold (open) and lasing wavelength (solid) of both longitudinal modes (mode 1 squares, mode 2 triangles) of a 3% doped, 0.25mm long, 95%/HR Nd:YVO_4 microchip laser as peltier temperature was varied.

At room temperature, pumping with a CW laser diode, the microchip laser reached threshold first with the longitudinal mode around 1063.4nm. At around two times the threshold of the first mode, the second longitudinal mode reached threshold and had a measured wavelength of 1064.2nm. The temperature tuning of the wavelength and threshold for both these modes are plotted in Figure 59. The fluorescence from an uncoated piece of Nd:YVO_4 cut from the same boule showed the centre of the gain bandwidth to be at 1064.0nm at 20°C with a FWHM of 0.8nm. The centre of the gain profile is also plotted in Figure 59 using the tuning rate reported by Taira et al. [237].

We recorded some experimental evidence for a small discontinuity in the wavelength of the two longitudinal modes at the threshold for mode 2. This is thought to be due to the change in mode pulling/pushing associated with the change in dispersion around the line centre due to depletion of the residual gain. This change in wavelength however could not be satisfactorily characterised because of its small magnitude, though it is noted this would be expected theoretically.

Normally mode 2 would reach threshold first, as it is closer to the centre of the gain profile, however this was not observed and is attributed to anti-guiding of this mode causing greater loss.

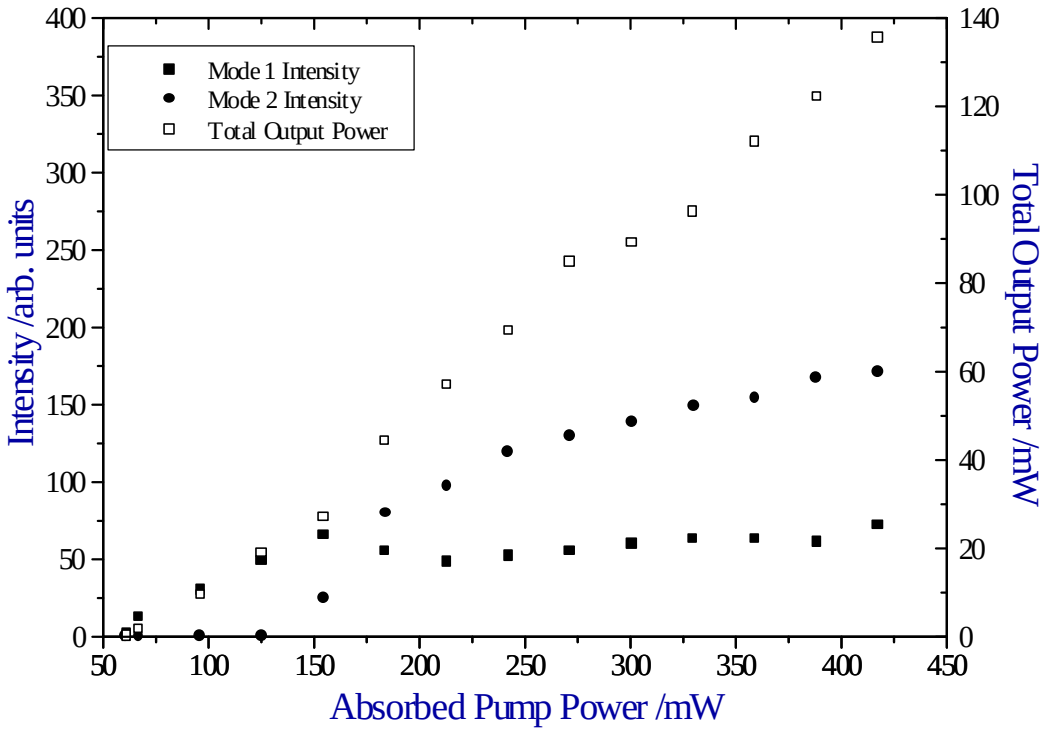

Figure 60 - Intensity of longitudinal modes (Mode 1 - solid squares, Mode 2 – solid circles) and total output power (hollow squares) of a 0.25mm 95/HR Nd:YVO_4 microchip laser as a function of pump power.

An optical spectrum analyser (Anritsu MS96A) was used to measure the relative intensity of the two longitudinal modes as a function of pump power. The results are shown in Figure 60 plotted as peak spectral density. The total output power of the microchip laser varied linearly with pump power with a slope efficiency of 41%. Once mode 2 reached threshold, its intensity increased rapidly with pump power and it dominated the output. Mode 1 appeared to be partially suppressed at higher pump powers.

Initially the giant spikes were observed when the diode power was modulated with a square wave, such that the laser first under went spiking as mode 1 started and later produced the giant spike associated with the introduction of mode 2. It was found however that pulses could also be generated using a carefully configured CW pump source. In this case, the repetition rate of the giant pulses and subsequent relaxation oscillations was approximately 10kHz. The pulses were measured to have peak

powers up to 28W and pulse lengths as short as 1.85ns, corresponding to peak powers 430 times the CW level.

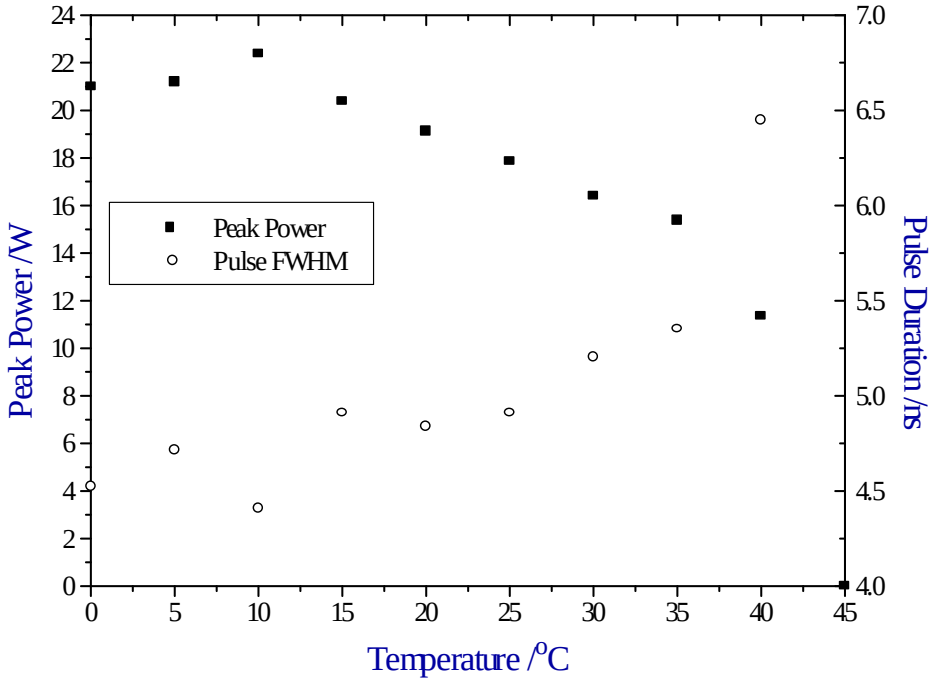

Figure 61 – Measured temperature dependence of pulse duration and peak power of 'giant spikes' attributed to self Q-switching.

The temperature dependence of the peak power and pulse duration of the observed giant pulses is shown in Figure 61. The intensity of the pulses was maximised when the temperature of the heat sink of the Nd:YVO_4 laser was stabilised at 10°C, with a rapid fall off in peak intensity above a heat sink temperature of 40°C. At 10°C, pulses with peak powers up to 28W and pulse lengths as short as 1.85ns were measured, corresponding to peak powers approximately 400 times the CW level. This pulse length was close to the maximum bandwidth of the photodetector and sampling oscilloscope used (1GHz) and therefore potentially was shorter, though there was no strong evidence for this. The tuning range of this effect is approximately 70GHz (FWHM) or approximately 0.27nm.

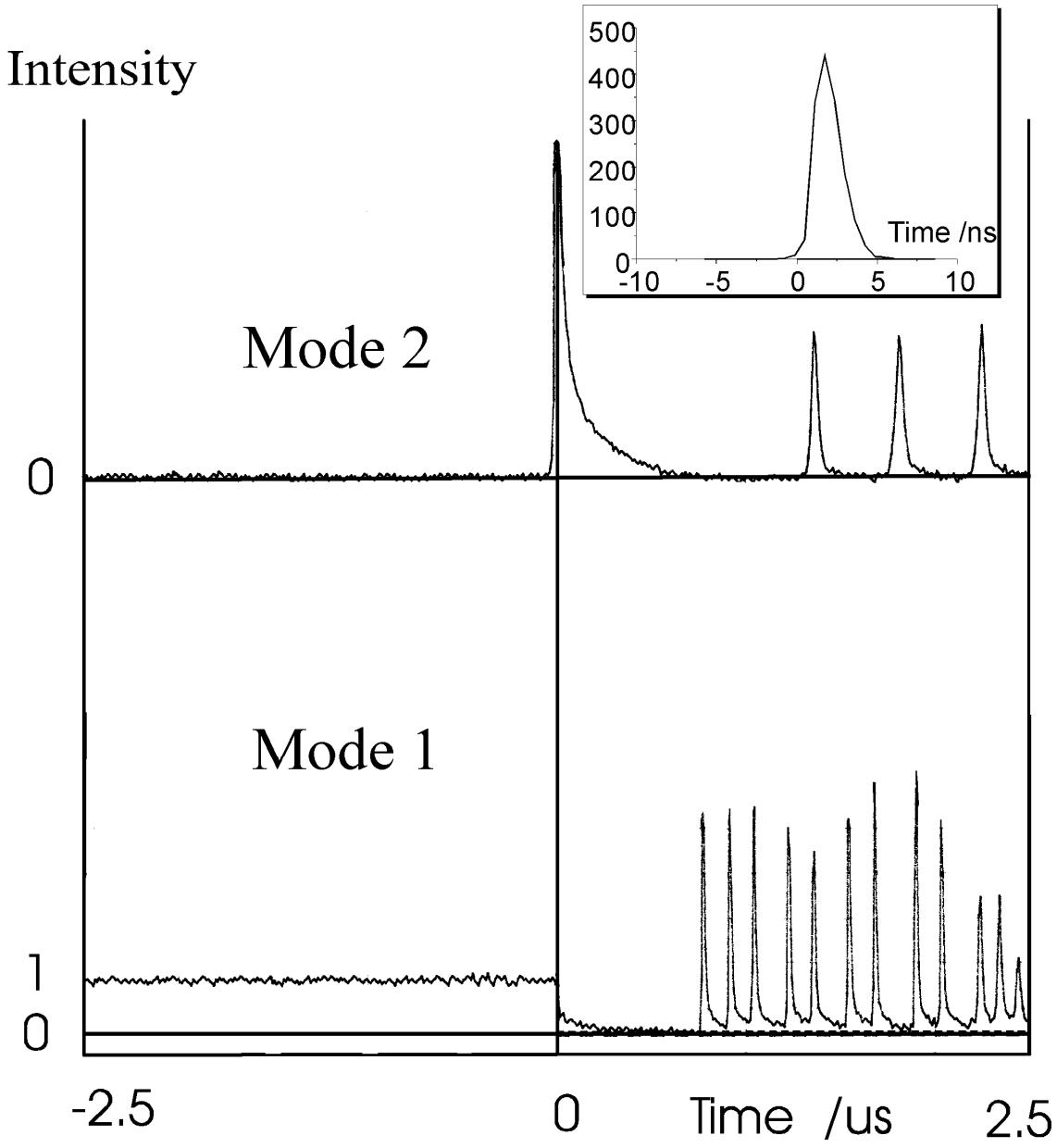

Figure 62– Intensity Fluctuations of mode 1 (lower) and mode 2 (upper trace). The intensity of the giant pulse at t=0 in the 2nd Mode is more than 100 times greater than the following relaxation oscillations. The inset shows a typical giant pulse.

The temporal structure of the giant pulse and the following relaxation oscillation trains was examined using a ¼ metre monochromator (Cromex 250IS/SM) which separated the longitudinal modes spatially onto a fast (1GHz) photodetector. Figure 62 shows the intensity of the two axial modes around the production of the Q-switched pulse (the two traces shown were not taken simultaneously). The higher frequency mode (mode 1) lases at a CW level, until a Q-switched pulse occurs in the lower frequency mode (mode 2), at which point it stops lasing. The population

inversion then takes several hundred nanoseconds to recover from the depletion caused by the giant pulse, after which point the two longitudinal modes go into coupled relaxation oscillations, with the sort of modulation depth expected from standard rate-equation spiking theory [238].

The microchip laser operated on a TEM_{00} mode at all pump power levels. The minimum beam waist was calculated from the divergence of the output beam in the far-field as shown in Figure 63. At the threshold pump power of the second longitudinal mode (70mW) there is a significant increase in the measured beam waist. The beam waist beyond the threshold for the second mode decreases as the inverse fourth root of the pump power as predicted by Zayhowski [239].

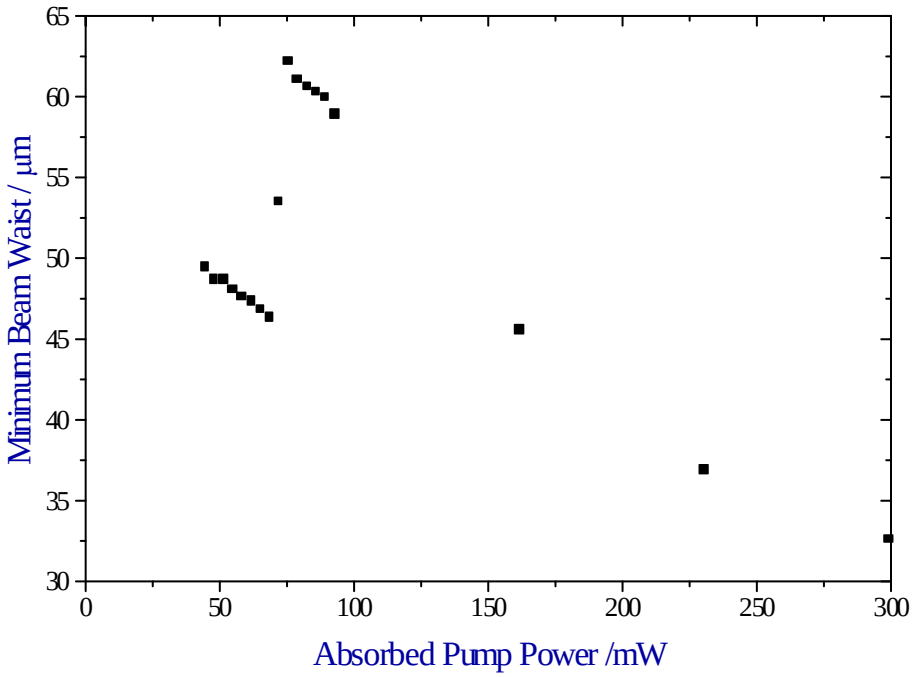

Figure 63 - Change in the minimum beam waist of a 0.25mm 95/HR Nd:YVO_4 microchip laser from far-field measurements around the threshold for the second longitudinal mode (~70mW).

Although the best results were achieved with the 0.25mm crystal with 5% output coupling, giant spiking was also observed in monolithic 0.5mm long crystals with 1% and 5% output coupling. Similar giant spiking was also observed in a 3% doped. 0.5mm Nd:YVO_4 microchip operating at 1342nm, with 1% output coupling, producing pulses as short as 5ns and peak powers of up to 18W. Indeed, potentially such self Q-switching is observable for any high gain transition in a similar cavity geometry.

3.4.4 Modelling of Gain Guiding

These results can be explained through the introduction of gain related effects into the modelling of the cavity and its stability. The inversion density created in a four-level laser when pumped optically by a gaussian intensity profile is given by [240]:

$$N_0(r,z) = \left(\frac{2\alpha f P \tau}{h\nu_0 \pi w_p^2} \right) e^{-\alpha z} e^{\frac{2r^2}{w_p^2}}$$

Equation 71

Where α is the absorption coefficient, P is the pump power, τ is the upper state lifetime, f is the fraction in the upper laser multiplet, $h\nu_0$ is the energy per pump photon and w_p is the radius of the pump beam. A gaussian profile is not an unreasonable first approximation for the pump beam, although ideally it should be modelled as a super-gaussian.

Above the threshold P_{th1} of the first longitudinal mode to lase, the intensity of this mode within the cavity is approximately:

$$I_1(r,z) = \frac{4(P - P_{th1}) \frac{\lambda_p}{\lambda_0}}{(1-R)\pi w_l^2} e^{-\frac{2r^2}{w_l^2}} \sin^2(k_1 z)$$

Equation 72

where λ_p is the pump wavelength, λ_0 is the lasing wavelength, w_l is the radius of the lasing mode and R is the reflectivity of the output coupler. The residual inversion density remaining after the first mode lases is:

$$N_1(r,z) = \frac{N_0(r,z)}{1 + \frac{I_1(r,z)}{I_{sat}}}$$

Equation 73

where l is the length of the crystal and I_{sat} is the saturation intensity for the transition in the gain material. Gain diffusion has been neglected here, as we believe the effect not to be significant from the good agreement seen for threshold calculations in chapter 2. For a double or multi-pass laser amplifier, if the size of the lasing waist is approximately the same size or greater than the pump waist, the transverse variation in residual population inversion is still peaked at the centre of the pumped area. This is true at both the nodes and anti-nodes of mode 1 [241].

Mode 2 at frequency n_2 below threshold will see a small signal gain given by:

$$g_2(\nu_2, r, z) = \frac{N_1(r,z)c^2}{8\pi n_0^2 \tau \nu_2^2} \frac{\Delta\nu}{2\pi\left[(\nu_2 - \nu_0)^2 + \left(\frac{\Delta\nu}{2}\right)^2\right]}$$

Equation 74

where n_0 is the refractive index, ν_0 is the centre of the gain profile, and $\Delta\nu$ is the gain bandwidth for the transition. This gain will induce a distortion in the refractive index for a second mode below threshold equal to [242]:

$$\Delta n(r, z, \nu_2) = \frac{c(\nu_2 - \nu_0)}{2\pi\nu_2\Delta\nu} g_2(\nu_2, r, z)$$

Equation 75

Therefore, in the presence of a population inversion longitudinal modes at a higher frequency than the centre of the gain bandwidth will experience a positive change in refractive index. This is more clearly illustrated in Figure 64. As the magnitude of this population inversion is greater in the centre of the beam than at the edges, these higher frequency modes will be positively guided. In contrast, longitudinal modes with frequencies lower than then gain centre will be anti-guided.

From Figure 59, the longitudinal mode around 1063.4nm (mode 1) would experience positive guiding in the presence of gain and the mode at 1064.3nm (mode 2) would experience anti-guiding. This anti-guiding results in a poor mode overlap between the lower frequency mode (mode 2) and the pump volume. This prevents mode 2 lasing first, even though it is closer to the centre of the gain profile than mode 1.

If Equation 74 and Equation 75 are now solved for the microchip system used to carry out the experimental work, we can calculate expected orders of magnitude. Figure 64 illustrates how the small signal gain and dispersion vary with wavelength around the gain centre of the 1064nm transition in Nd:YVO_4. The small signal, single pass gain for our 0.5mm long, 3% doped Nd:YVO_4 crystal, with 5% output coupling at 1064nm, pumped with 70mW is 0.317 at the centre of the gain profile. Mode 1 experiences a small signal gain of 0.194 and mode 2 a gain of 0.237. In the centre of the pump beam at the pumped face, mode 1 experiences a refractive index increase of

$5x10^{-5}$, and conversely mode 2 experiences a decrease in refractive index of approximately the same amount.

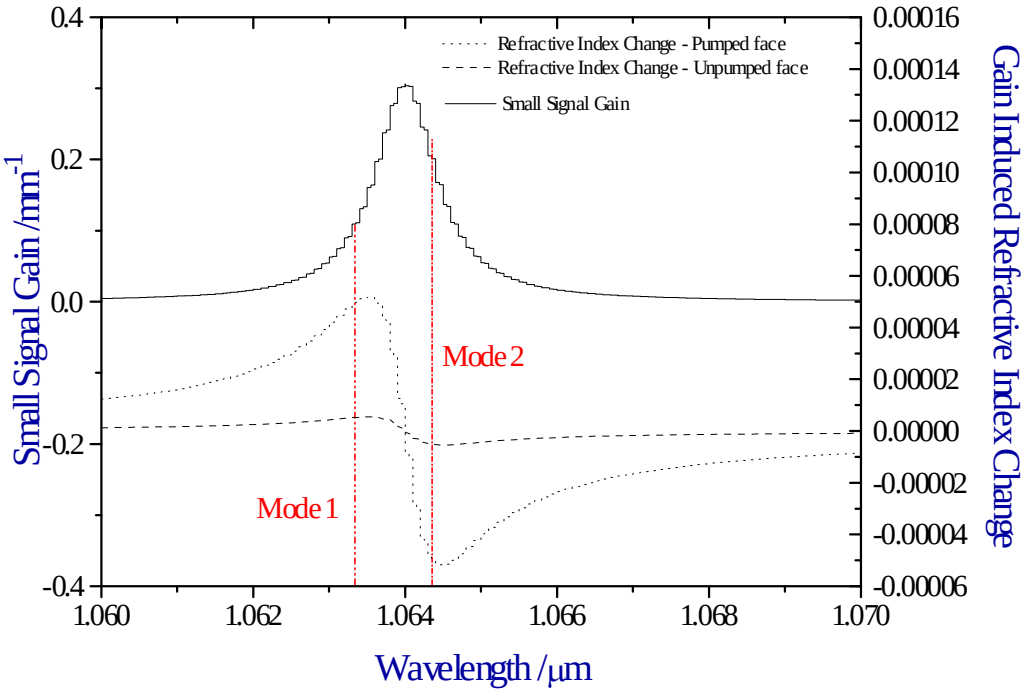

Figure 64 – Calculation of Small Signal Gain and Refractive Index Change due to Dispersion for 0.5mm 3% doped Nd:YVO_4 Microchip Laser. The dotted lines indicate the wavelengths of the longitudinal modes 1 and 2.

We can now compare the order of magnitude of thermal and gain-guiding effects in the formation of a stable cavity. The thermal effects can be modelled using Equation 56, which we derived earlier for an edge-cooled microchip laser. Again, we make the approximations used in both the thermal modelling and converting the temperature profile into a minimum beam waist.

For a microchip operating with 70mW of absorbed pump power in a spot size of 70μm, the temperature rise above ambient in the centre is 8.5°C, and at the edge of the pumped region is 7.5°C. Thus, the expected change in optical path length between the centre and edge of the pump beam is 12nm. If thermal effects were the dominant guiding mechanism, this would suggest a minimum beam waist of 52μm.

If we include the effects of change in refractive index associated with the gain from a gaussian pump, the change in optical path length is given by:

$$\Delta l_{gain}(r) = \left[(1+\alpha_1 T(r))l\right]\left[\left(1+\frac{dn}{nT}T(r)\right)n_0 + \Delta n(r,z)\right] - n_0 l$$

Equation 76

and the minimum beam waist can be calculated accordingly. In our estimations we approximate the gaussian profile of the gain induced change in refractive index to be quadratic, simplifying the analysis to allow the use of the same equations as derived for the thermal change in optical path length.

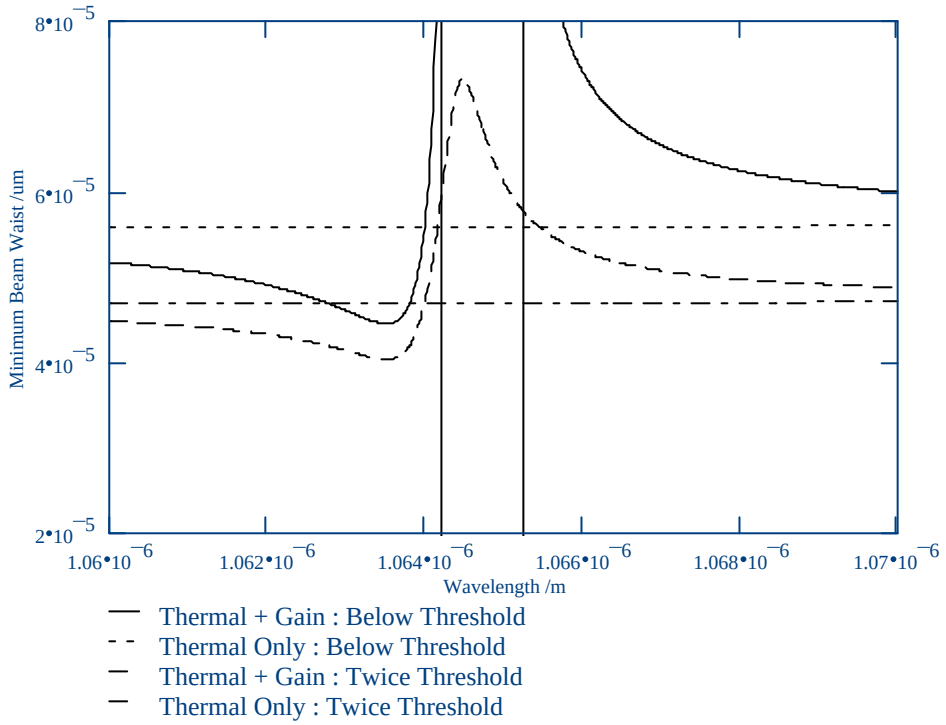

Figure 65 – Predicted wavelength dependence of minimum beam waists around line centre of 1064nm transition in Nd:YVO_4. The blue lines represents the beam waists expected due to only thermal effects just below threshold of mode 2 (solid) and twice the threshold of mode 2 (dotted). The red lines represent the minimum beam waists given by both thermal and gain guiding (Equation 76) just below threshold of mode 2 (solid) and twice this threshold (dotted).

With these simplifications in mind, we can estimate the magnitude of the change in beam waist expected from this effect, as illustrated above in Figure 65. Just below the threshold for mode 2, at around 70mW of absorbed power, the beam waist of mode 1 in the presence of residual inversion is calculated to be 44μm. This is similar to the measured beam waist of 46μm in Figure 63. The predicted beam waist for mode 2 in the presence of the residual gain is 121μm. This mode has a much larger volume than might otherwise be expected and has a poor overlap with the pumped volume and the

pump-induced lens, reducing the effective gain for this mode. If one artificially removes the effects of the residual inversion, the predicted beam waist for both modes reverts to the beam waist of 52μm, predicted by thermal effects only.

Figure 65 also indicates that mode 2 would need to lie within a 0.5nm range to experience this anti-guiding effect around 1064.5nm. This is consistent with the experimental results described in the previous section. An optimal system would have one longitudinal mode at the maximum and minimum of the dispersion curve respectively. In this respect, a crystal of length 0.25mm is almost ideal, whereas a crystal 0.5mm has a smaller free spectral range and therefore two adjacent longitudinal modes straddling the gain centre will not experience such a large refractive index variation. This is consistent with the observation of less efficient self Q-switching in the 0.5mm long 95/HR microchip used.

There will also be an output coupling restriction on the operation of this effect. A small output coupling will provide little discrimination between the threshold of mode 1 and mode 2, preventing sufficient gain to build up to cause self Q-switching. With a larger output coupling, the higher threshold condition for the laser is more likely to be reached first by mode two, as the beam waist of mode 1 becomes inefficiently small. This restriction is again consistent with observing much weaker self Q-switching in microchip lasers with 1% and 10% output couplings.

The anti-guiding of mode 2 at low pump powers is sufficient to increase the population inversion required for it to reach threshold above that normally expected from consideration of the gain profile. Once mode 2 begins to oscillate however, gain saturation reduces the effects of anti-guiding and the second mode finds itself well above threshold. Indeed, the second mode will experience more gain than the first because it is closer to the centre of the gain profile. This sudden realisation of gain leads to the self Q-switching effect discussed in the next section. At higher pump powers, and in the presence of significant gain diffusion, these gain-related effects would not be so prominent due to the dominance of thermal cavity definition over gain guiding.

3.4.5 Gain-Induced Self Q-Switching

As mentioned, the anti-guiding of mode 2 due to the residual inversion density

causes it to have an artificially higher threshold. The sinusoidal variation in the refractive index in the axial plane can act as a Bragg reflector for the second axial mode, with a reflectivity of approximately 0.3% for the conditions of operation already described. This longitudinal variation will not be considered, though it is noted that this could contribute to the change in Q of the cavity.

With the removal of the anti-guiding, the overlap between pump and lasing mode volumes will increase with the decrease in lasing mode volume, proving more gain for the second longitudinal mode than the first mode. Thus, when this inversion is removed the effective threshold for the second mode is lower than with the inversion present. This change in threshold can be thought of as a change in the quality of the cavity for the second mode caused by the presence of a population inversion.

Again, we can use simple laser theory to determine the order of magnitude of the effects involved. In a plane wave approximation, where spatial hole burning is ignored, the population inversion and cavity photon number are related through the coupled laser rate equations [243]:

$$\frac{dn(t)}{dt} = KN(t)n(t) - \tau_c n(t)$$
$$\frac{dN(t)}{dt} = R_p - \frac{N(t)}{\tau} - KN(t)n(t)$$

Equation 77

where n(t) is the cavity photon number, N(t) is the population inversion, R_p is the pumping rate to the upper lasing level, K is a constant associated with stimulated emission, and τ_c is the cavity decay time. These coupled equations can be solved numerically using finite time steps to simulate the effect of Q-switching.

We suggest that as mode 2 goes above threshold, its self Q-switching behaviour rapidly brings it to be 1.1 times threshold. At the same time mode 1 will be pushed below threshold and it will be extinguished. The simple rate equation model predicts that a pulse would be produced of peak power 450 times that of the equilibrium value, and with a width of 1.8ns. This would extract 15% of the population inversion, bringing both modes 1 and 2 below threshold. The time constants associated with gain saturation, repumping and mode competition would then lead to coupled spiking between the two modes on a microsecond time scale.

These predictions are similar to those measured in Figure 62, indicating that such a

change in the inversion population can be sufficient to produce giant pulses such as are reported here.

To conclude, in this section we have shown how gain guiding can influence the operation of a microchip laser. In particular, it can dominate the definition of the transverse mode in a monolithic microchip laser when pumped with high peak, and low average powers. The transition between gain and thermal guiding has been characterised to illustrate the connectivity between this work and the work described in the previous sections.

One consequence of gain guiding arises from the wavelength dependent refractive index variation around the centre of the gain transition. In a high gain system, this variation can significantly alter the guiding of a cavity mode. This variation was confirmed and found to be in agreement with previous experimental and theoretical work on gain guiding.

Self Q-switching was explored in depth as a phenomenon associated with this wavelength dependent guiding. This represents the first time such a self Q-switched system has been observed and characterised and explained. Pulses as short as 1.85ns and peak powers in excess of 25W were observed at a repetition rate of approximately 10kHz. Although lacking the peak powers of active and passive Q-switching, this technique of pulse generation could potentially be applied to diode and polymer lasers or extended to provide proper Q-switching of microchip lasers.

Other potential phenomena arising from this refractive index variation include higher single frequency powers. If the second longitudinal mode was kept suitably anti-guided, or over-guided to produce an extremely small beam waist, then higher power single frequency operation would be possible because of the improved discrimination between the thresholds of the longitudinal modes. The anti-guiding could also potentially be used to optimise the beam waist of the lasing mode to that of the pump mode.

3.5 Conclusions and Future Work

In this chapter, the guiding of the transverse mode in monolithic microchip lasers has been explored. Two forms of guiding have been identified and characterised, thermal

guiding and gain guiding. This work is ongoing within our group in St.Andrews to address some of the outstanding issues raised, though it still represents an exciting advance towards a more complete understanding of the definition of cavity within a monolithic laser.

An area not considered in this chapter, though potentially important, especially for quasi-four level lasers, is the role of absorption and aperture guiding in defining the transverse mode. These effects are not thought to be significant in Nd:YVO_4 operating at 1064nm or 1342nm, though would be extremely relevant for Nd:YAG microchip lasers operating at 946nm or Yb^{3+} doped materials and I hope will be incorporated in future work.

For CW operation, thermal effects generally dominate in the formation of a stable cavity and ultimately limit the maximum pump power that can be used. As well as the hard limitation of thermal fracture, anisotropy of the gain material can lead to softer maximum ceilings. These limitations have been explored with an indication of how they can be calculated for a microchip laser. Two independent methods of measuring the thermal lensing have been presented and compared with the theoretical modelling described in the first third of this chapter. There was generally good agreement between theory and experimental work, however further work is required to clarify the role of gain guiding at higher pump powers.

Around threshold in particular, gain effects can be observed experimentally. We have presented a basic model of how residual gain can effect the cavity stability of a monolithic Nd:YVO_4 microchip laser through gain induced refractive index guiding. This was initiated by our observation of self Q-switched pulses and subsequent work to model this phenomenon, the first time such a phenomenon has been observed or described. The region between thermal and gain guiding has been explored to indicate the circumstances under which both guiding mechanisms are important. This work is in good agreement with previously observed results and I hope will be developed into a fully integrated, generalised model for transverse mode definition in microchip lasers.

References:

[194] W. Koechner, J. Appl. Phys., **44:7**, 3162 (1973)

[195] W. Koechner, D.K. Rice, IEEE J. Quantum Electron., **6**, 557 (1980)

[196] W. Koechner, "Solid State Engineering" (3rd Ed.), Springer-Verlag, 381 (1992)

[197] J.D. Foster and L.M. Osterink, J. Appl. Phys., **41:9**, 3656 (1970)

[198] T.J. Kane, R.C. Eckardt and R.L. Byer, IEEE J. Quantum Electron., **10**, 1351 (1983)

[199] J.M. Eggleston, T.J. Kane, K. Kuhn, J. Unternahrer and R.L. Byer, IEEE J. Quantum Electron., **20**, 289 (1984)

[200] T.J. Kane, J.M. Eggleston and R.L. Byer, IEEE J. Quantum Electron., **21:8**, 1195 (1985)

[201] P. Hello, E. Durand, P.K. Fritschel, C.N. Man, J. Mod. Opt., **41:7**, 1371 (1994)

[202] S.D. Jackson and J.A. Piper, Appl. Opt., **34:12**, 2012 (1995)

[203] U.O. Farrukh, A.M. Buoncristiani, C.E. Byvik, IEEE J. Quantum Electron., **24:11**, 2253 (1988)

[204] U.O. Farrukh, P. Brockman, Appl. Opt., **32:12**, 2075 (1993)

[205] H.G. Feise, "Thermal Lensing in Laser Rods", Senior Honours Report, Physics Department Library, University of St. Andrews (1994)

[206] A.K.Cousins, IEEE J. Quantum Electron., **28:4**, 1057 (1992)

[207] J. Frauchiger, P. Albers and H.P. Weber, IEEE J. Quantum Electron., **28:4**, 1046 (1992)

[208] C. Pfistner, R. Weber, H.P. Weber, S. Merazzi and R. Gruber, IEEE J. Quantum Electron., **30:7**, 1605 (1994)

[209] S.B. Sutton and G.F. Albrecht, Appl. Opt., **32:27**, 5256 (1993)

[210] J.J. Zayhowski, OSA Proc. on ASSL'90, **6**, 9 (1991)

[211] N. MacKinnon and B.D. Sinclair, Opt. Comm., **94:4**, 281 (1992)

[212] T. Omatsu, Y. Kato, M. Shimosegawa, A. Hasegawa and I. Ogura, Opt. Comm., **118**, 302 (1995)

[213] J. Harrison and R.J. Martinsen, IEEE J. Quantum Electron., **30:11**, 2628 (1994)

[214] R.S. Conroy, A.J. Kemp, D.G. Matthews and B.D. Sinclair, OSA Tech. Digest CLEO'96, Paper CTuP4 (1996)

[215] K. Kogelnik and T. Li, Appl. Opt., **5**, 1550 (1966)

[216] A.J. Kemp, "Thermal Distortion in Laser Diode Pumped Nd:YVO_4 Microchip Lasers", Private Communication (1995)

[217] C.C. Davis, "Lasers and Electro-Optics - Fundamentals and Engineering",

Cambridge University Press, 372 (1996)

[218] M.E. Innocenzi, H.T. Yura, C.L. Fincher and R.A. Fields, Appl. Phys. Lett., **56:19**, 1831 (1990)

[219] R.S. Conroy, A.J. Kemp, E. Marks, N. MacKinnonand B.D. Sinclair, "Advances in Solid State Lasers" – IOP Quant. Electron. Group Meeting, Paper 12 (1996)

[220] N. MacKinnon, PhD Thesis, St.Andrews University (1994)

[221] N. MacKinnon and B.D. Sinclair, Opt. Comm., **94**, 281 (1992)

[222] S. Longhi, G. Cerullo, S. Taccheo, V. Magni and P. Laporta, Appl. Phys. Lett., **65:24**, 3042 (1994)

[223] J.E. Bernard, E. McCullogh and A.J. Alcock, Opt. Comm., **109**, 109 (1994)

[224] T.Y. Fan, Opt. Lett., **19:8**, 554 (1994)

[225] G.K. Harkness and W.J. Firth, J. Mod. Opt., **39:10**, 2023 (1992)

[226] S. Longhi, J. Opt. Soc. Am. B, **11**, 1098 (1994)

[227] F. Sanchez and A. Chardon, Opt. Comm., **136**, 405 (1997)

[228] R.S. Conroy, N. MacKinnon and B.D. Sinclair, OSA Tech. Digest CLEO'95, Paper CTuP2 (1995)

[229] J.J. Zayhowski and C. Dill, Opt. Lett., **20:7**, 716 (1995)

[230] B. Braun, F.X. Kartner, G. Zhang, M. Moser and U. Keller, Opt. Lett., **22:6**, 318 (1997)

[231] J.J. Zayhowski and C.Dill, Opt. Lett., **19:18**, 1427 (1994)

[232] A. Szabo and L.E. Erickson, IEEE J. Quantum Elect., **4:10**, 692 (1968)

[233] M. Birnbaum and C.L. Fincher, Proc. IEEE, 804 (1969)

[234] A.W. Tucker, M. Birnbaum, C.L. Fincher and J.W. Erler, J. Appl. Phys., **48:12**, 4907 (1977)

[235] P. Wang, S.H. Zhou, K.K. Lee and Y.C. Chen, Opt. Comm., **114**, 439 (1995)

[236] A. Uchida, M. Takeoka, T. Sato and F. Kannari, OSA Tech. Digest QELS'97, Paper QW8 (1997)

[237] T. Taira, A. Mukai, Y. Nozawa, T. Kobayashi, Opt. Lett., **16:24**, 1955 (1991)

[238] A.E. Siegman, "Lasers", University Science Books, 958 (1986)

[239] J.J. Zayhowski, OSA Proc. on ASSL, 382 (1990)

[240] J.J. Zayhowski, IEEE J. Quantum Electron., **26:12**, 2052 (1990)

[241] G.J. Friel, PhD Thesis, Southampton University (1998)

[242] A. Maitland and M.H. Dunn, "Laser Physics", North Holland Publishing Company, 20-21 (1969)

[243] A.E. Siegman, "Lasers", University Science Books, Chpt. 26 (1986)

Chapter 4 – Q-SWITCHED MICROCHIP LASERS

4.1 Introduction

Many applications require a high intensity, pulsed output as opposed to a continuous output. In these areas, solid-state lasers can offer significant advantages over other laser types. The main benefit of a solid-state laser gain material arises from the relatively long upper-state lifetime of the active ion, of the order 1μs-1ms; much longer than the excited st ate of atoms in a gas or charge carriers in a semiconductor laser, which typically have an upper-state lifetime of the order 1ns-1μs. This longer lifetime allows efficient energy storage in the upper laser level giving the ability to produce short, high intensity pulses. This chapter describes two ways in which short pulses can be generated from composite microchip lasers, using a method called 'Q-switching'.

In Chapter Two a simple form of pulse generation from monolithic microchip lasers, 'gain-switching', was described and shown to produce pulses of peak power several times the continuous wave (CW) level with pulse duration of tens of nanoseconds. This technique is normally limited by the rate change of pump power achievable and generally can only produce pulses several times the intensity of the normal CW level.

A more powerful technique relies on introducing a temporal variation into the quality of the cavity, where the quality, or 'Q', of a cavity is the ratio of the energy stored to the loss in a cavity. This form of modulation is generally referred to as 'Q-switching'. In Chapter Three a novel form of 'self Q-switching' in monolithic Nd:YVO_4 microchip lasers was described, caused by residual gain. This Q-switching was capable of producing pulses down to 1.85ns and peak powers in excess of 25W, more than 400 times the CW level.

The most common form of Q-switching, active Q-switching, generally uses the acousto-optic or electro-optic properties of a crystal to increase the loss in the cavity and prevent lasing. To produce a pulse, a voltage is either applied to, or removed from the crystal to restore the cavity to a high Q state and allow the build up of a pulse. This is particularly suitable for pulse-pumped lasers as the Q-switching can be synchronised with the pumping source to produce an optimised output. In this chapter, novel forms of electro-optic Q-switch will be described which produce pulses

of less than 1.1ns and peak powers in excess of 10kW, 20000 times the normal CW level.

A passive mechanism for Q-switching can also be realised using a material with non-linear absorption properties. Such a material exhibits lower absorption for high intensity pulses than low intensity pulses through a bleaching process. This can be used to selectively allow the build up of pulses in preference to CW lasing. This technique is less controllable because it relies on the bleaching of the saturable absorber and therefore is inherently noisy, making it less reproducible than active Q-switching. However it does not require complicated electronics and can be achieved with the use of a sub-millimetre sized crystal. It is an almost ideal way in which to preserve the advantages of a microchip laser and produce short, high intensity pulses. In this chapter passive Q-switching is investigated and is shown to produce pulses of less than 1.4ns and peak powers of nearly 1kW, 2000 times the CW level.

To produce pulses substantially below a nanosecond in duration or higher peak powers, a more recent technique has been developed, 'mode-locking'. Here the longitudinal cavity modes of the laser are locked together in phase. The addition of these modes within the cavity provides a solution, which gives a single pulse output at a period of the cavity round-trip time. Therefore the more modes within the cavity and the gain bandwidth, the potentially shorter the pulses produced can be.

The short pulse length of mode-locked lasers have allowed pulses in excess of 10TW to be produced, through post-amplification of selective mode-locked pulses, often by chirped pulsed amplification. In a microchip environment however, mode-locking is generally impractical because of the inherent single-frequency nature of the short cavity and the very short round-trip time, of the order 10ps, which would prevent the storage of significant power for each pulse. In spite of this, mode-locking of a Nd:MgO:$LiNbO_3$ microchip laser has been demonstrated, by applying a microwave sub-carrier to metallic coatings on the surface of the microchip [244].

The work of this chapter however focuses on Q-switching as a means for pulse generation, because of it ease of implementation and the many potential applications for the nanosecond, multi-kilowatt peak power pulses it produces. We will first consider a novel form of active Q-switching and then move to consider passive Q-switching of both the 1064nm and 1342nm transitions of Nd:YVO_4 in the second half

of the chapter.

4.2 Active Q-Switching of Microchip Lasers

4.2.1 Introduction

The first form of active Q-switching employed in a microchip laser geometry exploited the large cavity mode spacing associated with the short cavity of a semi-monolithic device. A 0.65mm long Nd:YAG crystal coated for partial output coupling (50% reflective) was used in conjunction with a discrete output coupler (98.5% reflective) mounted on a piezoelectric actuator to form a coupled cavity [245]. The cavity formed between the crystal and mirror acted as a Fabry-Perot etalon, whose reflectivity at the lasing wavelength depended strongly on the etalon thickness. The total cavity length was approximately 1.8mm with a tuning of 0.5μm/kV applied to the piezoelectric to Q-switch the device. When pumped with 120mW from a Ti:sapphire, 5ns pulses were demonstrated with a peak power of ~7W. The limitation of slow switching speed due to the piezoelectric response reduces the possibility of significant improvement on these figures using this technique. However, the novel coupled cavity design provided a new technique, which could offer low loss, compact Q-switches which operate at low voltages.

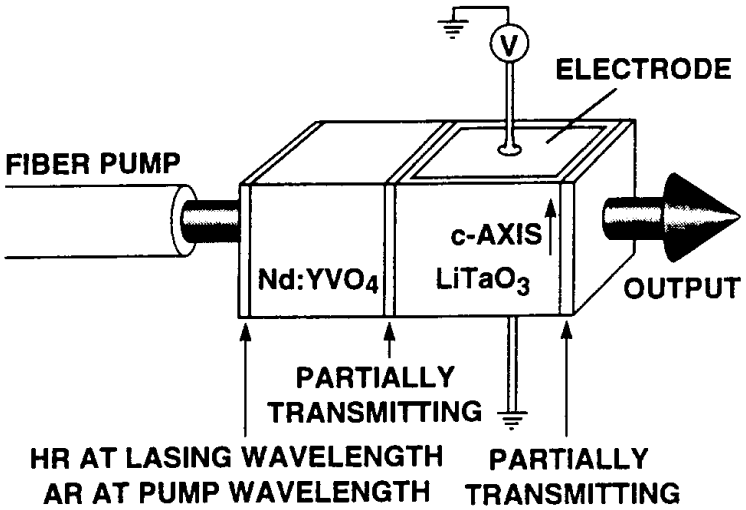

Figure 66 - Electro-Optic Mirror Q-Switch (after [246])

Zayhowski demonstrated an extension of this coupled cavity idea, using an electro-optic crystal to provide constructive and destructive feedback in the cavity, in 1992 [247,246]. A 1x1x0.5mm piece of Nd:YAG was bonded to a 1x1x0.9mm piece of

$LiTaO_3$ to form the coupled-cavity, as shown in Figure 66. By applying a 600V pulse of 100ns duration to the electrodes on the $LiTaO_3$, 55mW of single frequency average power at 1064nm was produced. At 1kHz repetition rate, pulses as short as 270ps were obtained, with energies of 6.8μJ and peak powers of more than 25kW. Pulse repetition rates of up to 500kHz showed useful operation over a wide frequency range with timing jitter of 0.5ns and amplitude jitter of less than 0.5%. Further improvement of the construction of this laser and greater pump powers yielded pulses less than 115ps with peak powers in excess of 90kW at a rate of 1kHz [248]. At higher frequencies, the pulse width varied from 1ns at 300kHz to 8.8ns at 2.25MHz.

An alternative to using the electro-optic properties of a crystal is to use acousto-optic properties. In this case, sound waves travelling through a crystal can produce compression and rarefaction of the material; this gives a time varying change in refractive index through the photo-elastic effect. The sound wave is launched into the crystal using an ultrasonic transducer and its frequency defines the grating period experienced by the laser beam travelling in the transverse plane.

Generally, acousto-optically Q-switched lasers have been limited to producing pulses in the 1-10ns region. However recently a diode end-pumped laser system with a cavity length of 7mm, has produced 600ps pulses of 5kW peak power at 1kHz using 1064nm Nd:YVO_4, 700ps pulses of 15kW peak power at 1kHz from Nd:YLF and 3.3ns pulses of 0.8kW peak power at 1kHz from 1342nm Nd:YVO_4 [249]. The Q-switch was operated with a 2W driver at 108MHz giving a switching speed of 18ns.

These results are at the forefront of Q-switch design and miniaturisation. Typical Q-switches employed in large frame lasers use a Pockels cell in combination with a polariser to provide loss modulation. By applying a voltage to the Pockels cell, the polarisation of the light is rotated and rejected by the polariser. By removing the voltage, the polarisation matches that orientation of the polariser and the laser returns to the high Q-state. These modulators are bulky, require high voltages and introduce significant residual loss into the cavity. The aim of this work was to develop a new alternative to traditional Q-switching, which was compact, low-loss, worked with low voltages and was easily scalable.

4.2.2 Laser Rate Equations

To model the Q-switched operation of a laser we can start with the rate equations determining the upper state photon density and cavity flux. If we assume the Q-switched pulse duration is small, we can neglect spontaneous emission and optical pumping during the pulse build-up and oscillation to give [250]:

$$\frac{\delta\phi}{\delta t} = \phi\left(\frac{c}{n}\sigma_e N\frac{l}{l'} - \frac{\varepsilon(t)}{\tau_R}\right)$$

and

$$\frac{\delta N}{\delta t} = -\gamma N\phi\sigma_e\frac{c}{n}$$

Equation 78

Where ϕ is the photon flux in the cavity, N is the upper state population density, σ_e is the stimulated emission cross-section, l is the length of the gain material, l' is the cavity length, $\varepsilon(t)$ is the fractional round-trip loss function, τ_R is the round-trip time, c is the speed of light, n is the refractive index, and γ is the degeneracy factor.

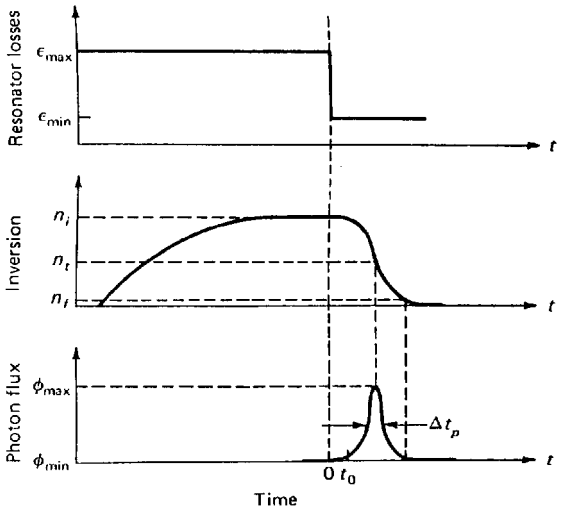

Figure 67 – Development of a Q-Switched Laser Pulse (after [250])

Q-switching is achieved through the temporal modulation of the loss parameter, $\varepsilon(t)$, of the cavity, as shown in Figure 67. If the gain material is pumped for a time longer than the upper state lifetime, then the upper state population density, or inversion, tends to a steady state value, n_i. This inversion is determined by the spontaneous decay rate. If at time t=0 the resonator losses are reduced, the laser finds itself well above threshold and there is a sudden build up of the photon flux. This photon flux

rapidly depopulates the inversion density, increasing to a maximum, ϕ_{max}, when the inversion density equals the threshold for CW lasing, n_t. Below this value, the flux will drop rapidly as the cavity losses exceed the available gain. Intuitively it can be seen that the final inversion n_f is inversely related to the maximum photon flux. Thus, qualitatively it can be seen that when the gain and/or the stimulated emission cross-section are large, the upper-state will decay more rapidly, producing shorter, higher intensity pulses.

The two simultaneous rate equations in Equation 78 can be solved either numerically or analytically by making assumptions about the laser system. The use of the boundary conditions in Figure 67 can help to realise an exact solution for a given laser system and we will now consider these two methods.

4.2.2.1 Numerical Solutions to Q-Switching

A step function in the loss, as in Figure 67, where there is a fast switching speed, can be modelled easily using a computer to solve the laser rate equations. Re-writing the rate equations as an iterative loop for a four level laser system yields:

$$\phi_{t+\Delta t} = \phi_t \left[1 + \Delta t \left(c\sigma_e N_t \frac{l}{l'} - \frac{\varepsilon(t)}{\tau_R} \right) \right]$$

and

$$N_{t+\Delta t} = N_t - \Delta t \left(N_t \phi_t \sigma_e c \right)$$

Equation 79

These coupled equations can be solved with careful choice of the loss function and of the time step. One problem worthy of note is the requirement to add in the pulse build-up period some photons corresponding to spontaneous emission in order to initiate the build-up of a photon flux.

A program written by Dr Alaistair Gillies, as part of the ‘Psst! Software Suite’ was used to simulate the Q-switched operation of a microchip laser. These results are shown in Figure 68. As can be seen there is an exponential decay in both the pulse width and build-up time as the laser is pumped further above threshold. At ten times threshold, the pulse widths fall to around 600ps with a pulse build-up time of 20ns, limited by the cavity decay rate and single pass gain available respectively.

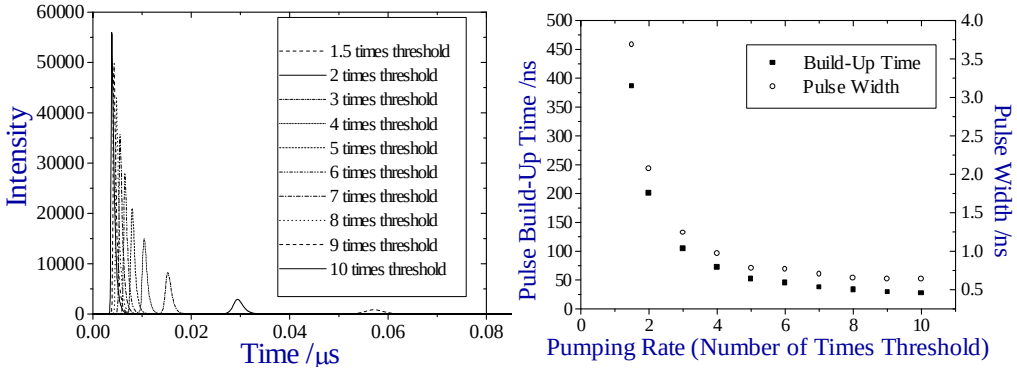

Figure 68 – Numerical modelling of Q-switched performance of a 0.5mm long 3% doped Nd:YVO_4 crystal in a 2mm long cavity with 5% output coupling at 1064nm.

If the switching speed of the Q-switch is longer than the pulse build-up time, then a pulse can be produced before the cavity is in its high Q-state. This presence of non-useful intracavity loss reduces the efficiency of the laser and is generally undesirable. Therefore, it is important that the Q-switch can switch faster than the build-up time of the laser pulse. For modelling of laser systems which exhibit this 'slow Q-switching' an extra-term can be included into Equation 79 to account for this effect, providing more realistic modelling.

4.2.2.2 Analytical Solutions to Q-Switching

The first attempt to theoretically model Q-switched or 'giant pulse' lasers was carried out by Wagner and Lengel [251]. They showed the energy of the Q-switched pulse could be expressed as:

$$E = \frac{h\nu A}{2\sigma_e \gamma} \ln\left(\frac{1}{R}\right) \ln\left(\frac{N_i}{N_f}\right)$$

Equation 80

Where A is the effective beam cross-sectional area and hν is the laser photon energy. The initial and final population inversions, N_i and N_f respectively, are related through the transcendental equation:

$$N_i - N_f = N_t \ln\left(\frac{N_i}{N_f}\right)$$

Equation 81

where N_t is the population inversion at threshold for CW lasing. The pulse width, t_p, can also be expressed as a function of these inversion populations such that:

$$t_p = \tau_c \frac{N_i - N_f}{N_i - N_t\left[1 + \ln\left(\frac{N_i}{N_t}\right)\right]}$$

Equation 82

The transcendental relationship between the different inversion boundary values means that general solutions cannot be realised, though solutions can be considered for particular laser systems.

These equations assume the switching time between the low and high Q states of the laser is negligibly small as before with the numerical modelling. The effect of slow Q-switching on these equations has also been considered and modelled in a similar, though more complicated fashion [252].

Degnan derived a series of analytical expressions for the optimisation of laser systems using Lagrange multipliers to assist in the modelling of passively Q-switched lasers [253]. He defined a dimensionless parameter z, to be the ratio of small signal gain to roundtrip dissipative loss:

$$z = \frac{2g_0 l}{\varepsilon}$$

Equation 83

where g_0 is the small signal gain. This parameter could then be used to describe the Q-switched operation of the any laser system. The optimum output coupler reflectivity is given by:

$$R_{opt} = \exp\left[-\varepsilon\left(\frac{z - 1 - \ln(z)}{\ln(z)}\right)\right]$$

Equation 84

For this output coupling the optimised output energy is:

$$E_{max} = \frac{h\nu A\varepsilon}{2\sigma_e \gamma}\left[z - 1 - \ln(z)\right]$$

Equation 85

With an energy extraction efficiency of:

$$\eta_e = 1 - \frac{(1+\ln(z))}{z}$$

Equation 86

Therefore, beyond choosing a suitable output coupler, laser efficiency can only be increased by increasing the gain with respect to the loss. For a value of z greater than 20 the laser is more than 80% efficient, which does not dramatically increase for higher pumping rates. Therefore optimisation of the overlap of the pumped and lasing mode volumes is an equally important consideration in optimising the process for high z systems as the optimisation of the output coupling and minimising parasitic losses.

The threshold inversion for our optimally coupled laser is given by the expression:

$$N_t = \frac{\varepsilon}{2\sigma_e l}\left(\frac{z-1}{\ln(z)}\right)$$

Equation 87

The peak power extracted can also be expressed analytically:

$$P_{max} = \frac{h\nu A\varepsilon^2}{2\sigma_e \gamma \tau_r}\left[\frac{z-1-\ln(z)}{\ln(z)}\right]\left\{z - \left(\frac{z-1}{\ln(z)}\right)\left[1+\ln\left(\frac{(z\ln(z))}{z-1}\right)\right]\right\}$$

Equation 88

And the FWHM pulse width:

$$t_p = \frac{\tau_r}{\varepsilon}\left\{\left[\frac{\ln(z)}{z}\right]\left[\frac{1}{1-\left(\frac{z-1}{\ln(z)}\right)\left[1+\ln\left(\frac{(z\ln(z))}{z-1}\right)\right]}\right]\right\}$$

Equation 89

If we use the above equations to model the one millimetre long quadrupole deflector system described later in this chapter, the results are shown below. The values of the peak power and pulse widths are calculated using the optimal output coupling for each pump power, and therefore cannot be directly compared to the experimental performance described later.

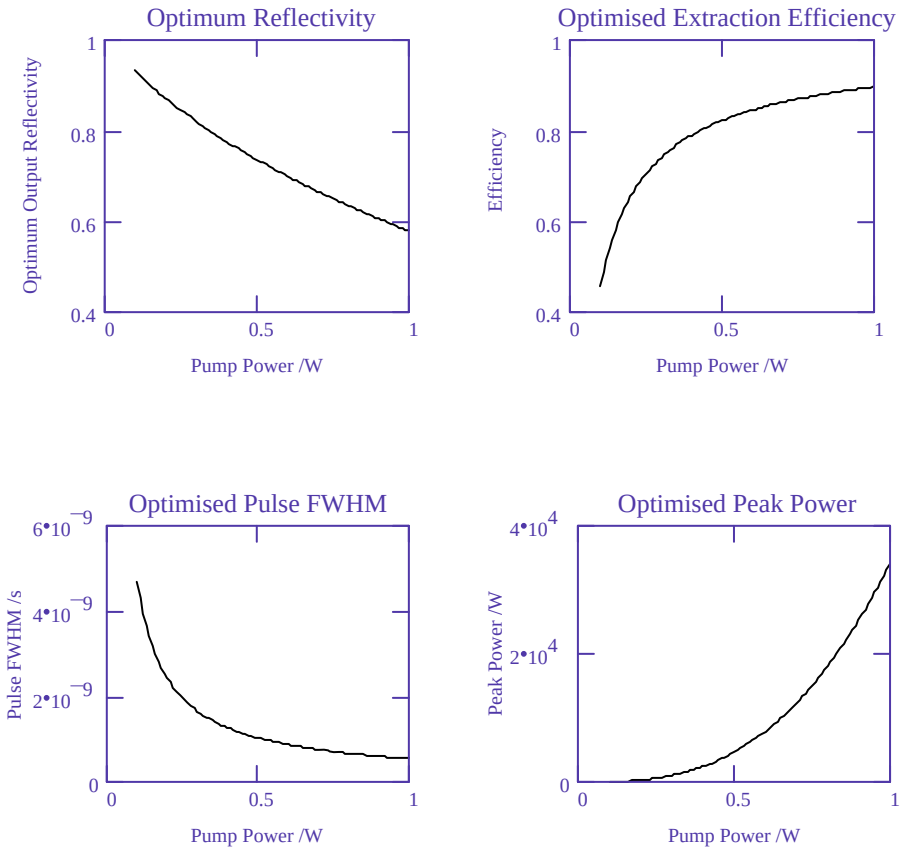

Figure 69 – Theoretically Optimised Performance of 1mm QPD System

As can be seen, we would expect to see an active Q-switch system, which could produce pulses of less than one-nanosecond and peak powers of tens of kilowatts if the system was fully optimised. The optimum output coupling varies significantly over the operating range considered here because of the high emission cross-section of Nd:YVO_4 combined with small pumped volume, providing high round trip gain values. The extraction efficiency for a fully optimised system approaches 90%. These values are similar to the values reported by Zayhowski for his shorter Nd:YAG based system which offered the same pulse energies with half the pulse length.

Generally, optimisation of the output coupling is attractive because it results in maximum laser output or efficiency. However, for some applications this is traded off against shorter pulse widths or higher peak powers which can be achieved through the use of other output couplings. However, there can be a significant loss in efficiency in order to gain a relatively small drop in pulse width. Therefore, in practice many Q-switched lasers are operated near their optimal output coupling.

4.2.3 Electro-Optic Deflection

The novel form of active Q-switching to be described in this chapter arises from deflection of the beam within the cavity, using an electro-optic crystal, to modulate the loss. The electro-optic effect was discovered in 1949, though the main stimulus for the development of this field came after the development of the laser in the 1960's. The effect arises in non-centrosymmetric crystals, where an applied electric field can alter the polarisation of the material. In a centrosymmetric crystal, such as YAG for example, the symmetry is generally not broken and no polarisation is achieved. The induced change in polarisation is in turn related to the refractive index through the dielectric properties of the material. The refractive index variation along a particular crystal axis can be expressed as a function of the applied dc electric field, E, through the Pockels relationship [250]:

$$\Delta(n)_i = n_0 \sum_{j=1}^{3} r_{ij} E_j$$

Equation 90

where i,j are the direction indices, n_0 is the refractive index, and r is the electro-optic tensor. Considering crystal symmetry, the 18 electro-optic tensor elements can be reduced to four for $LiNbO_3$. The largest of these, r_{33}, is generally employed as the basis of electro-optic devices. Thus the change in refractive index for a dc electric field applied to a correctly orientated piece of $LiNbO_3$ can be expressed as:

$$\Delta n = n_0 r_{33} E_x$$

Equation 91

Several forms of active Q-switch have been fabricated using the electro-optic effect; the most common exploiting polarisation rotation by the change in refractive indices in combination with a polariser to give a voltage dependent loss. These Q-switches are generally bulky, require high switching voltages and suffer from high insertion losses. As described previously, the change in refractive index has also been exploited to change the resonance conditions of a coupled cavity laser. These Q-switches are susceptible to cavity fluctuations, are difficult to scale to higher powers and require interferometrically controlled construction. The electro-optic Q-switches here address all of these disadvantages in a compact, low cost, low loss novel form.

For the work in this chapter, we are utilising the electro-optic effect to give beam deflection by two methods: through an induced refractive index gradient and through an active prism. Both of these schemes will be illustrated in more detail later in this chapter. Work by Ireland and Ley [254] showed the deflection of both a prism and gradient deflector is given by:

$$\Delta\phi = L\frac{\Delta n}{wn}$$

Equation 92

where L is the difference in path length between the two edges of the beam through the active region, w is the beam waist, n is the normal refractive index of the crystal and Δn is the change in refractive index given by Equation 91. Therefore, by applying an electric field, it is possible to achieve beam deflection in an electro-optic material.

This deflection angle varies linearly with the applied electric field if Equation 91 and Equation 92 are combined. For a gradient deflector, the active region can be the full length of the crystal, giving superior performance, over a single shaped prism electrode, where the active area is generally a fraction of the total crystal length. To some extent this can be compensated for by using multiple prism electrodes over the length of the crystal, however in reality problems with tracking and domain boundaries would limit the performance of such a device.

4.2.3.1 Deflective Requirements of a Q-Switch

Initially work was carried out to consider how much deflection was required in order to prevent the lasing of a semi-monolithic laser with a discrete highly reflecting output coupler. A cavity was constructed with a 3x3x1mm 1% doped crystal of Nd:YVO_4 with a discrete HR output coupler at 1064nm. The cavity length could be varied via a translation stage and the gain crystal was pumped by a 0.5W laser diode, through an 8mm collimating lens and 6.5mm focussing lens.

For a cavity length of 35mm, the output coupler had to be tilted more than 1.13mrad in the vertical plane and 1.46mrad in the horizontal plane to prevent lasing as shown in Figure 70. When the cavity length was decreased to 20mm, the required angle increased to 2.27mrad in the vertical plane and 3mrad in the horizontal.

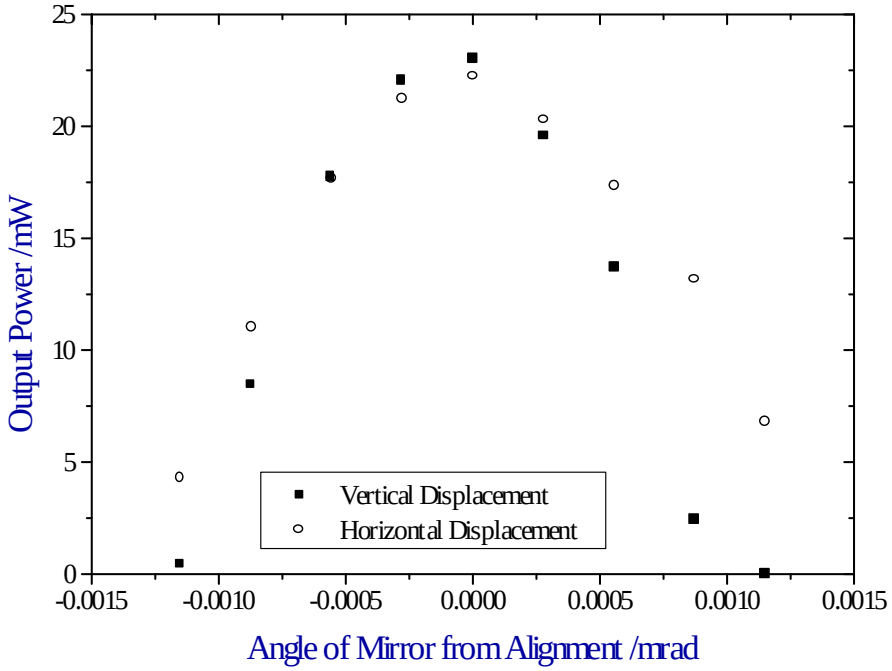

Figure 70 – Measurement of angular displacement required in vertical and horizontal planes to prevent lasing in a 20mm cavity, composed of 3x3x1mm 1% doped Nd:YVO_4 and a HR output coupler, pumped by 0.5W laser diode.

Calculations based on a $LiNbO_3$ prismatic Q-switch indicated that for a 0.5x1x10mm crystal with 1kV applied to the electrode, exploiting the r_{33} electro-optic coefficient, a beam deflection of 0.85mrad was possible. This indicated that such a rhombic electrode geometry with 2kV switching voltage should be sufficient to prevent lasing and give active Q-switching of a relatively long cavity. A quadrupole design of similar dimensions was considered to give more than sufficient deflection, based on the work of Ley [254].

It is worth noting from the work in Chapter Three, that the stability of a semi-monolithic laser increases with increasing pump power, and its efficiency falls with increasing cavity length. This, combined with the position of the deflector within the cavity, could account for the difficulties encountered when it was discovered larger than expected deflection angles were required for efficient operation.

4.2.3.2 Triangular (Prism) Deflector

The concept of a prismatic or triangular Q-switch is illustrated in Figure 71. In its simplest form, this type of deflector could be implemented in a cavity by a prism made from an electro-optic material. By applying an electric voltage across the prism, and changing its refractive index, a different refraction angle can be realised. The

change in angle could be used to misalign the cavity, switching the Q-state. In addition to Q-switching, this type of electro-optic prism could be used to actively mode-lock a laser system, or to give optimised dispersion compensation.

For this work, a thin slab of 0.5x5x10mm $LiNbO_3$ was patterned with rhombic electrodes on opposite faces separated by the smallest dimension to give a prism of different refractive index within the bulk crystal. The use of a rhombic electrode gives two refractive index boundaries in the beam path where refraction can take place. Ideally, the surface would have multiple rhombi to exaggerate the deflection, although for our work this was not possible for practical reasons.

A single prism of the type used is illustrated below. There is an indication of how the path of a ray is deviated when an electric field is applied to the rhombic electrodes. The $LiNbO_3$ was orientated to exploit the large r_{33} ($30.8x10^{-9}$mm/V) electro-optic coefficient, giving the largest possible deflection. When a voltage is applied, the area between the electrodes has a lower refractive index than the bulk material, giving a deflection in the vertical direction as shown in the diagram below. The flat end faces of the slab were coated AR@1064nm and allowed the $LiNbO_3$ slab to be used with a gain crystal and discrete output coupler in a linear cavity.

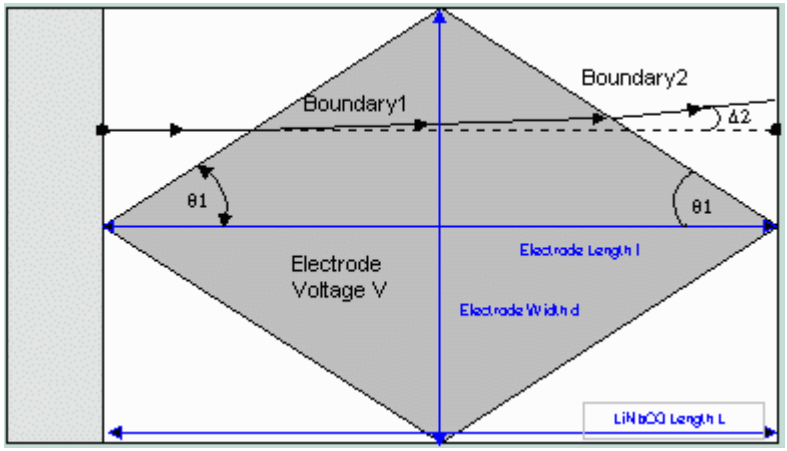

Figure 71 - Schematic of $LiNbO_3$ Triangular (Prism) Q-Switch (0.5x1x10mm)

To examine the Q-switched operation of these beam deflectors, a driver was constructed based on a chain of high speed transistors. The transistors were biased near their breakdown voltage, to give the maximum voltage across the Q-switch from a variable voltage Brandenburg supply. When a signal voltage was applied to the chain from a pulse generator, the chain was grounded to provide a fast switch. The switching rate of the chain was 10-20ns depending on the number of transistors in the

chain and their matching. The response of the refractive index of the material was typically slower than this because of the piezo-optic effect. From the numerical modelling earlier, this would indicate the optical pulse would start to build-up in a non-optimised cavity, with a loss in performance.

By removing transistors, it was possible to bias the chain for operation between 0-2kV. The charging rate for the chain was approximately 1.5µs, because of the significant current available from the HT supply. This set-up was found to be the most satisfactory, giving repetition rates up to 100kHz.

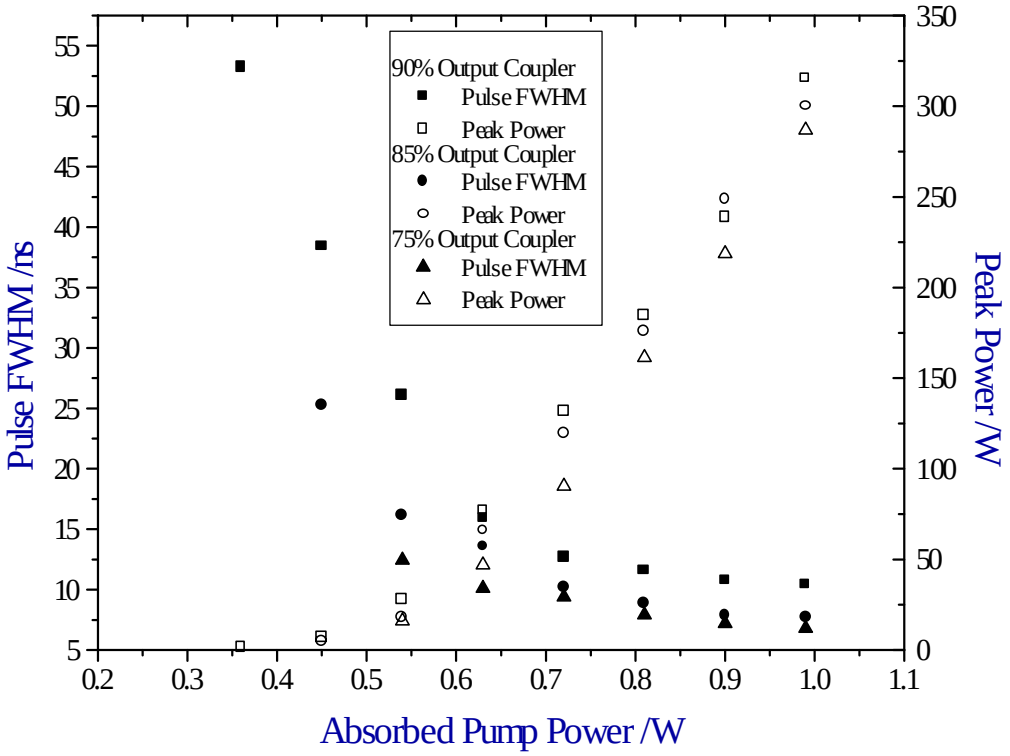

Figure 72 – Peak power and pulse FWHM of triangular Q-switch with pump power. The cavity was 45mm long consisting of 3x3x1mm 1% doped Nd:YVO_4 crystal, 0.5x1x10mm $LiNbO_3$ Q-switch and output coupler. The pulse repetition rate was 5kHz.

The diagram above shows the performance achieved from the 0.5x1x10mm $LiNbO_3$ prismatic Q-switch in a 45mm long cavity composed of a 3x3x1mm 1% doped Nd:YVO_4 crystal and a discrete output coupler. The Q-switch was operated with a repetition rate of 5kHz and an applied voltage of 1.8kV. The system was pumped by a 1.2W laser diode through an 8mm collimating lens and 8mm focussing lens. Minimisation of the cavity length was frustrated by the mounting for the Q-switch as potentially it could have been less than half this length.

The small deflection offered by this deflector was barely sufficient to stop lasing, unless the cavity was biased right on the edge of stability. This required the output coupler to be angled carefully to prevent residual lasing and caused the efficiency of the laser to drop rapidly. With increased output coupling, residual lasing was found to be less of a problem, though it still severely limited performance.

The pulses were measured using reverse biased fast (BPX65) photodiodes (10-90% rise time of 0.4ns) and a 1GHz digital scope. Pulse timings were measured by averaging over multiple pulses and errors by persistence of repetitive pulses. Triggering was controlled by the switching voltage of the Q-switch on a second channel.

Using this system, pulses as short as 5.8ns were achieved, with peak power of up to 320W, without evidence of after pulsing or CW lasing. Shorter pulses and high peak powers were observed with after pulsing and a CW background, indicating the deflection from the Q-switch was not sufficient. The pulse-to-pulse timing jitter (~5ns) was significant and indicated the instability of the laser. The amplitude instability was also significant with as much as 20% variation from peak-to-peak.

In addition to the 1064nm output, approximately 1μW of non-phase matched green light was observed when the system operated with a high peak power (>100W). Although useful for optimising the laser, $LiNbO_3$ is susceptible to damage from high intensity green light. This limitation would be of concern at higher powers in addition to other forms of optical damage with the high intensities potentially achievable.

The best performance was observed with a 90%R output coupler, indicating that the gain/loss ratio was less than that considered in the theoretical modelling. The coatings of the Q-switch introduced a very significant 3% single pass loss into the cavity, indicating the problems associated with the manufacture of this first generation of deflective Q-switches. These losses, in combination with the extended cavity length, strong thermal lensing and the need to offset the cavity alignment, part-way explains why the gain to loss ratio and performance are not as good as indicated from the theoretical modelling.

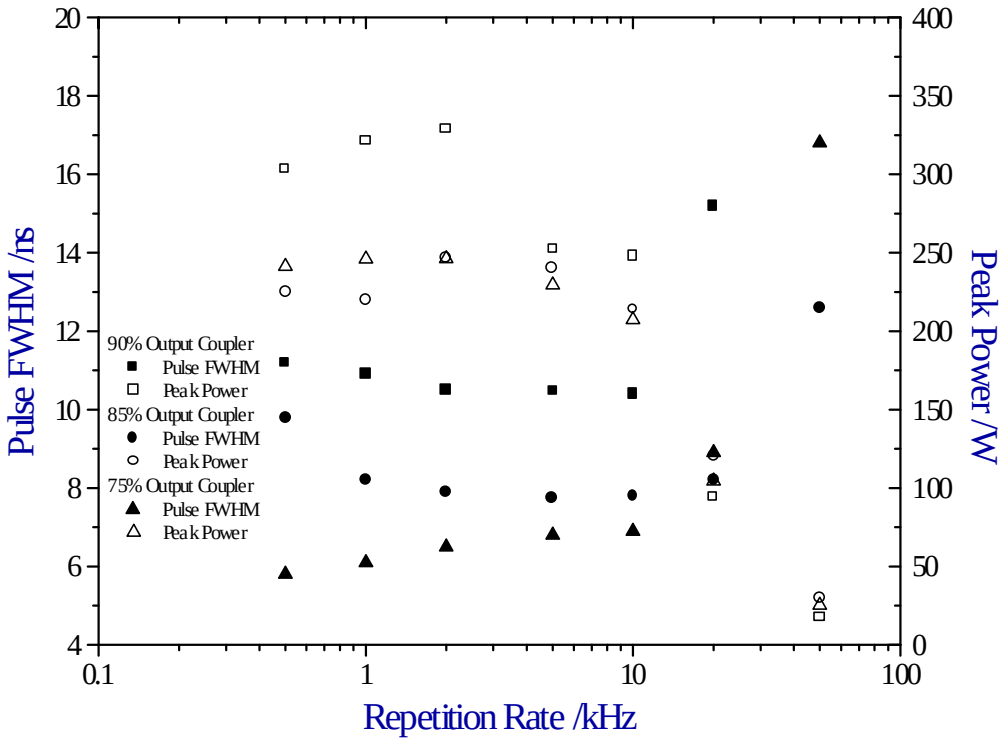

Figure 73 – Peak power and pulse FWHM of 0.5mm triangular Q-switch as a function of pulse repetition rate. The cavity was 45mm long consisting of 3x3x1mm 1% doped Nd:YVO_4 crystal, 0.5x1x10mm $LiNbO_3$ Q-switch and output coupler. The pump power was 1W.

At maximum pump power, the pulse widths were found not to vary significantly for repetition rates up to the inverse of the upper-state lifetime. When the repetition rate exceeded the inverse of the upper-state lifetime, a noticeable degradation in performance was observed. The peak performance was observed at several kilohertz. At lower frequencies, thermal considerations may become important in determining efficiency, and for a high gain material, such as Nd:YVO_4, depopulation by stimulated emission in the low Q-state may be a significant limiting factor in the Q-switched performance observed.

In conclusion, the first use of a prism deflector as a Q-switch has been demonstrated, indicating its potential use as a successful Q-switch in a modified form. This first generation of device has shown deflection is possible, though not significant enough to give optimal performance. Further work on the next generation of these devices using multiple rhombic electrodes can potentially enhance these results.

4.2.3.3 Quadrupole Deflector

The second form of deflector examined was a quadrupole deflector. The design of a

typical quadrupole deflector is illustrated below. These deflectors were initially developed for use in steak cameras and scanning applications that required rapid deflection of laser beams [255]. However their properties are superior to the prismatic deflectors and are almost ideal for use as deflective Q-switches and this was proposed as a possible application more than a decade ago [254]. For this work we used three deflectors, with 5mm, 2mm and 1mm apertures.

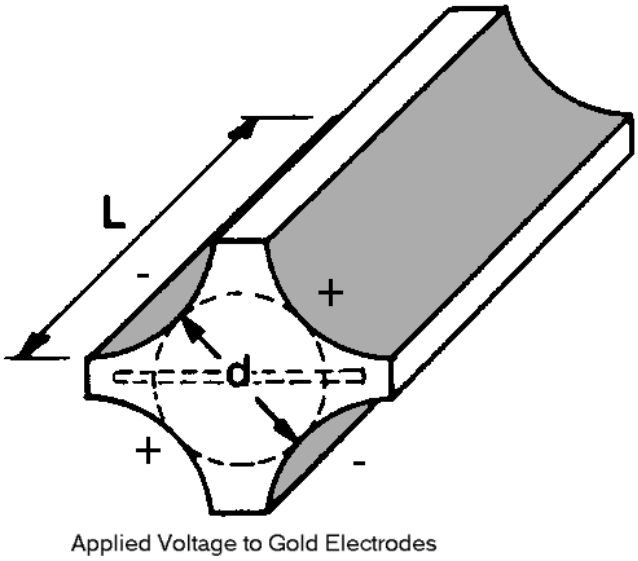

Figure 74 - Schematic of quadrupole deflector.

Our devices were fabricated by Leysop Ltd from x-cut $LiTaO_3$, polished into the form above. This process is non-trivial and perhaps is responsible for inducing stress and strain damage in the crystal. Again, the cut of the crystal used allowed access to the relatively large r_{33} electro-optic coefficient in $LiTaO_3$ ($30x10^{-9}$mm/V). In contrast to the prism deflectors, deflection was achieved through a linear gradient in refractive index when a voltage is applied. This gradient is more easily visualised by considering the interferograms in Figure 82 and is discussed in more detail later. The refractive index gradient causes a phase delay to one side of a beam propagating through the deflector with respect to the other, giving a deflection proportional the gradient. As with the prism deflector, the Q-switch was orientated to give vertical deflection within the cavity.

The circular surfaces of each quadrant of the $LiTaO_3$ were coated with thin layers of gold to act as electrodes. Opposing faces of the deflector were electrically connected,

giving opposite voltages applied to adjacent faces. The same driver as described previously was used to create the refractive index gradient in these Q-switches.

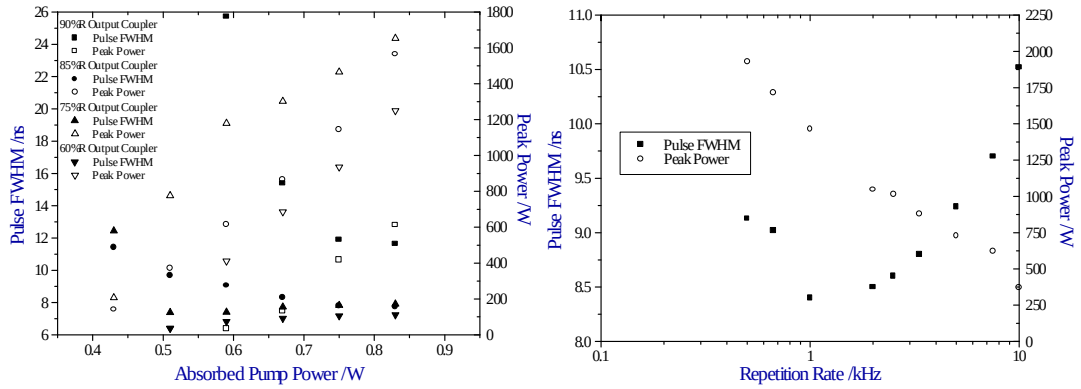

Figure 75 – Q-switched operation of 2mm aperture quadrupole deflector in a 40mm long cavity with 3x3x1mm 1% doped Nd:YVO_4 crystal and output coupler, pumped by 1.2W laser diode. The resulting pulse FWHM and peak power was measured a) as a function of pump power at 5kHz repetition rate and b) as a function of repetition rate at a pump power of 0.84W and 85% reflective.

The first quadrupole deflector examined was 26mm long with a 2mm aperture and used the same driver as the prism Q-switch. The insertion loss of the Q-switch was measured to be less than 2% single pass. This device was operated with 1kV applied to the electrodes in a cavity 40mm long and pumped by a 1.2W laser diode. The light from the diode was collimated using a 8mm lens and focussed into the Nd:YVO_4 crystal using a 8mm focal length lens, giving a pump spot size of approximately 120x80μm. A range of discrete output couplers was used to examine the Q-switched performance, and the results are illustrated above. Peak powers of up to 2kW and pulse widths down to 6.4ns were measured. The optimal output coupling for the system was approximately 20-25%, indicating an improvement on the gain/loss ratio over the prism deflector. The stability of the pulses was similarly improved, with a 10% fluctuation in the pulse duration and a similar fluctuation in the peak-to-peak intensity. The pulse build-up time was 30-40ns.

In many respects, the operation of the two forms of deflective Q-switch is similar. To achieve the best operation with no after pulsing and no CW background level, it is necessary to change the alignment of both from the optimal CW case. If less deflection is available, then the cavity needs to be balanced more closely to edge of stability, reducing the performance of the laser.

The smallest aperture quadrupole deflector gives the largest deflection and would

therefore be expected to give the best performance and this is what was observed with the 1mm aperture quadrupole deflector. The electrode surfaces of the fabricated device had circular profiles of 0.75mm radius. The insertion loss for the Q-switch was measured to be less than 1% single pass. The smaller aperture also allows a shorter length of electro-optic crystal (11mm) and cavity (13mm) to be used, improving the laser performance. Without the deflector present and with a 95% output coupler in an optimally aligned cavity, the slope efficiency of the laser was 41%. As with the other deflectors, on occasions the cavity had to be misaligned to ensure there was no evidence on after-pulsing of a CW background.

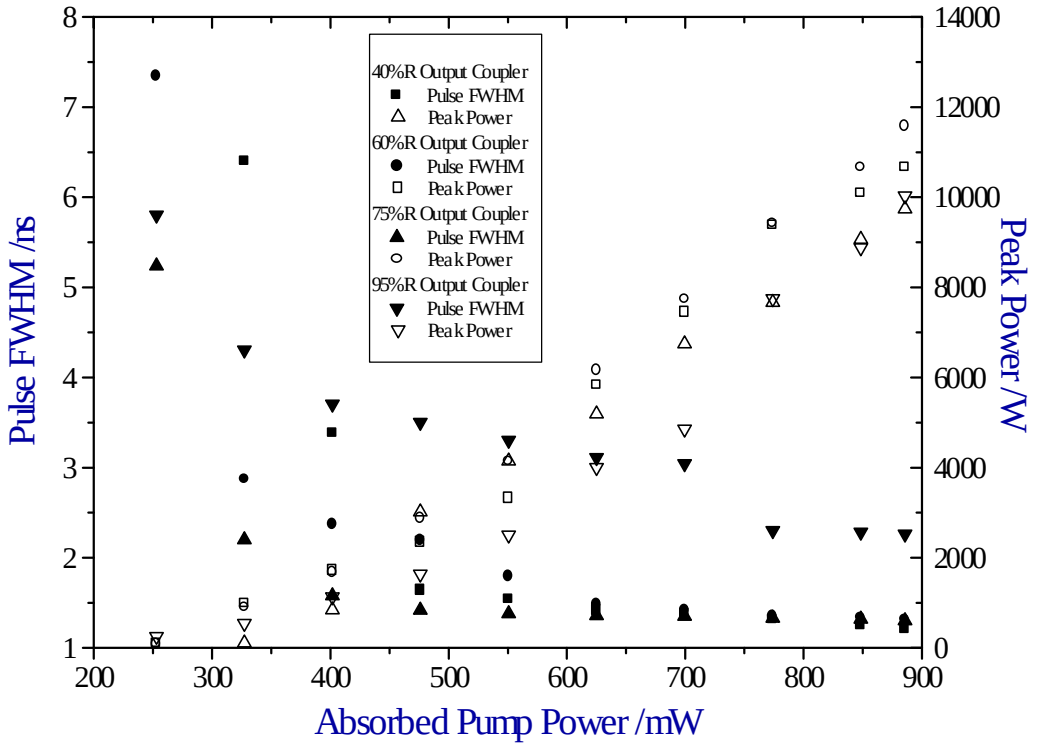

Figure 76 – Peak power and pulse width at 1064nm from 1mm aperture quadrupole deflector with pump power from 1.2W laser diode. The cavity was 13mm long composed of 2x11mm deflector, 3x3x1mm 1% doped Nd:YVO_4 and a discrete output coupler. The Q-switch was operated at 1kHz.

When the Q-switch was used in a similar fashion to the 2mm aperture deflector with 600V applied to the electrodes, peak powers of up to 11.6kW were measured with pulse widths down to 1.08ns as illustrated in Figure 76 and Figure 77. The pulse-to-pulse jitter was less than 0.2ns with a peak-to-peak stability of better than 5%. Over longer periods of operation, some deflectors showed evidence of a slow drop in power due to induced damage in the deflector. Further work is required to quantify these effects and determine suitable compromises for future systems.

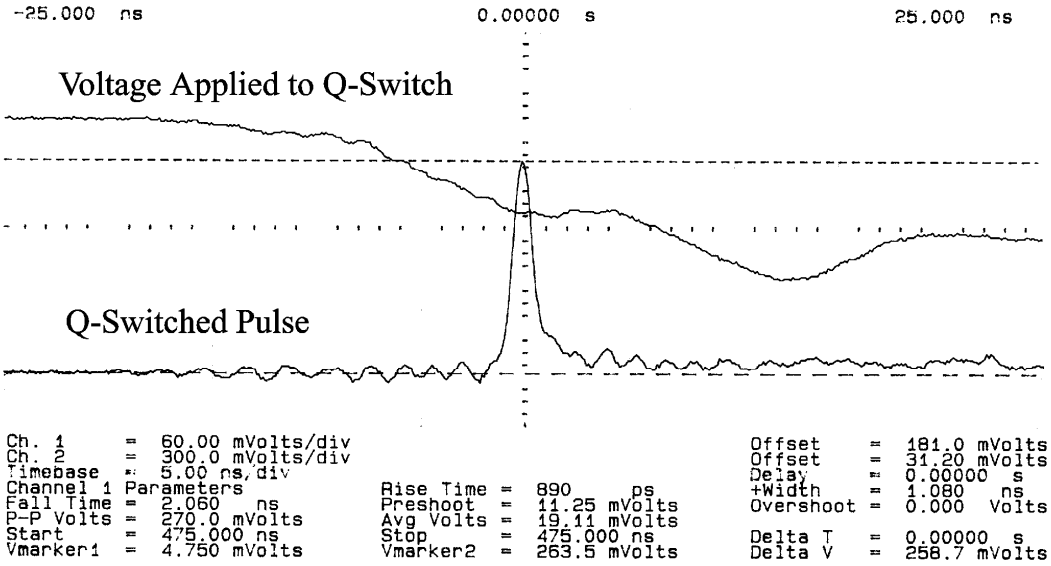

Figure 77– Time averaged pulse of 1.08ns from 1mm aperture quadrupole deflector pumped with 1W at a repetition rate of 5kHz.

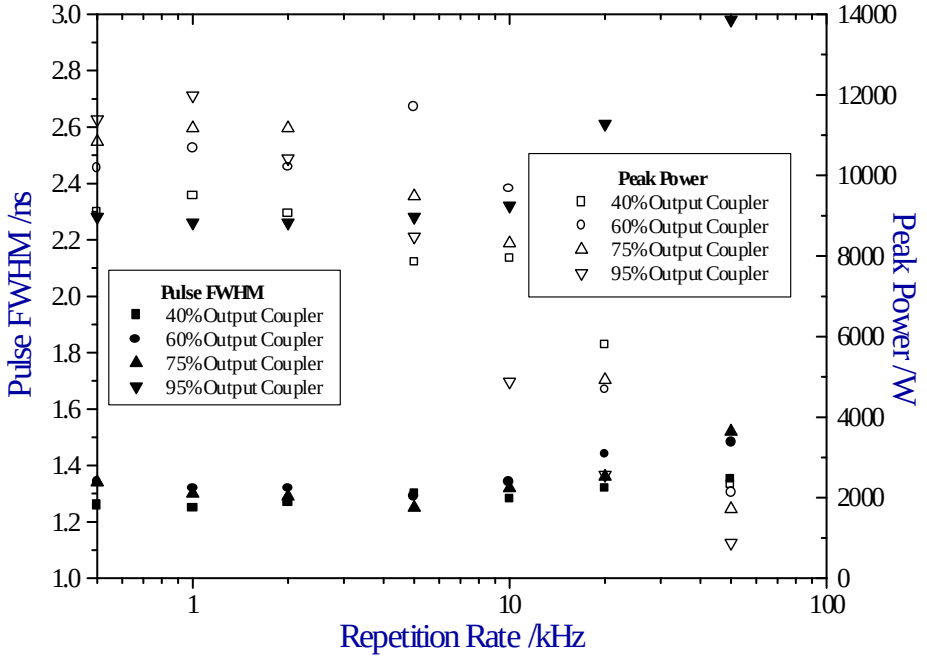

Figure 78 – Peak power and pulse width at 1064nm from 1mm quadrupole deflector with repetition rate. The cavity was 13mm long composed of 2x11mm deflector, 3x3x1mm 1% doped Nd:YVO_4 and a discrete output coupler. The laser was pumped with 1W from 1.2W laser diode.

The optimal performance was achieved with the 60% reflective output coupler, in good agreement with the optimum as predicted from the theory in the previous section. The pulse lengths observed are approximately three times the theoretical optimum, which compromises the peak powers from Figure 69, although the pulse

energies are similar to those predicted by theory. The measured pulse build-up times of 15-20 nanoseconds for operation at maximum pump power are in good agreement with those predicted by the numerical modelling in Figure 68. The discrepancies between predicted and observed potentially originate from the slow Q-switching nature of the deflective Q-switch in comparison to the fast build-up time of a Nd:YVO_4 laser.

As with the 2mm aperture device, the 1mm aperture device was operated with a repetition rate from 0.5-50kHz. The slight drop in performance at low repetition rates is attributed to thermal effects, while at high rates the performance decreases due to a decrease in the population inversion available. The optimal performance was achieved for a pulse rate of several kilohertz, in agreement with the other deflector Q-switches.

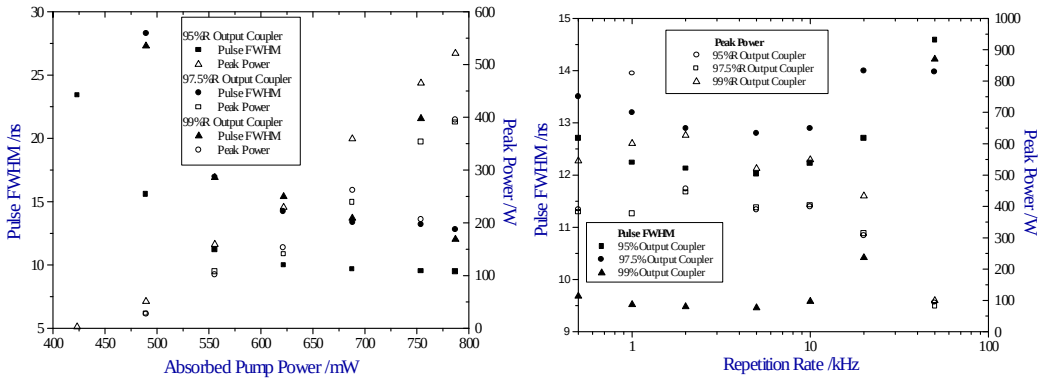

Figure 79 – Q-switched operation of 1342nm transition.

The operation of the 1mm aperture quadrupole deflector was also examined in a 1342nm-laser system of the same geometry as the 1064nm system described previously. The single pass losses (~2%) from the anti-reflection coatings were more significant because they were designed for 1064nm, though the device operated with creditable performance when aligned properly. The stability of this device was similar to that described for 1064nm operation. Pulse widths down to 9.5ns were obtained, with peak powers up to 520W. The build-up time for this system was typically 60ns, much longer than the 1064nm because of the smaller emission-cross section and greater parasitic cavity losses for 1342nm.

In conclusion, we have demonstrated a set of novel single element active Q-switch devices that are easily scalable, compact and low loss. Pulses of over 10kW peak power were obtained with pulse durations down to 1.1ns at 1064nm and pulses over 500W peak power with duration 9.5ns at 1342nm.

4.2.3.4 Comparison of Deflective Properties

The deflecting strength of the two forms of deflective Q-switches were considered using similar techniques to those used in the previous chapter for analysing the deformation of pumped monolithic crystals. The electric field gradient for a quadrupole device is twice that of a prism deflector with similar aperture and applied voltage, offering improved performance for same size. With this in mind, we would expect superior deflection characteristics from the quadrupole deflectors.

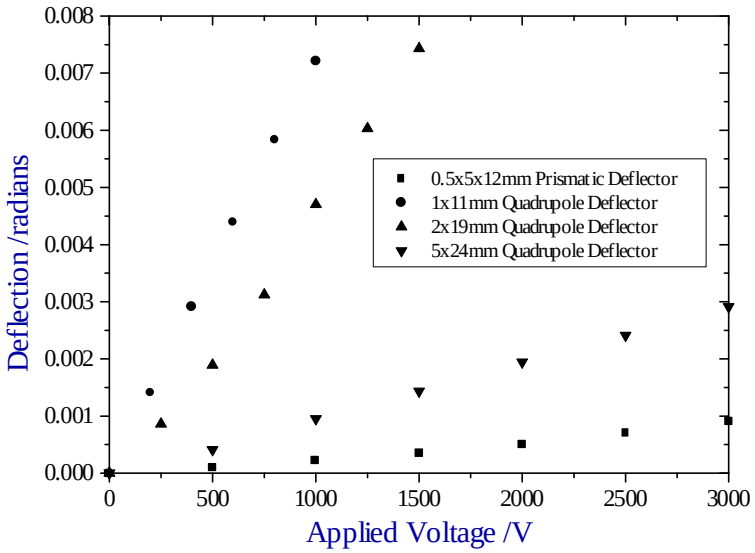

Figure 80 – Deflective angle induced in prismatic and quadrupole deflectors with applied voltage. Measured using a HeNe laser and CCD camera.

The first technique used to measure the deflection was to examine the effect on a HeNe laser beam passed through the deflector. All the devices exhibited measurable deflection over their operating voltage range. As expected the prismatic deflector provided the least deflection, 0.9mrad for 3kV of applied voltage. From Figure 70 this deflection is not sufficient to prevent lasing in a cavity. However, coupled with this there is an increase in the spreading of the beam with increasing voltage due to the increasingly phase difference across the beam path. At 3kV, the beam is approximately three times that of with no applied voltage, increasing the loss sufficiently to provide a small region where Q-switched operation is possible.

If the length of the deflector crystals is included, the performance of the prismatic deflector (3.1×10^{-5}mrad/kVmm) is similar to that of the quadrupole with 5mm aperture (3.7×10^{-5}mrad/kVmm). In contrast, the performance of the smaller aperture quadrupoles is an order of magnitude better; 2.11×10^{-4}mrad/kVmm for the 2mm

aperture and $6.59x10^{-4}$mrad/kVmm for the 1mm aperture. These deflections vary inversely with aperture size as expected.

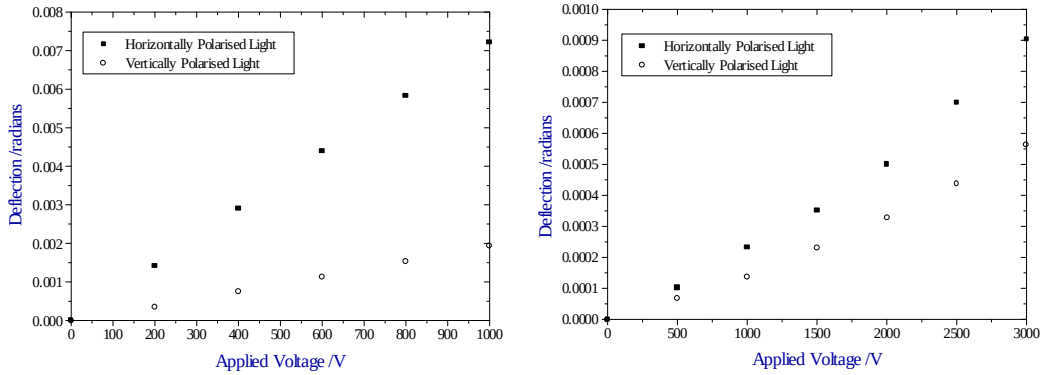

Figure 81 – Deflection of horizontally and vertically polarised light in a) 1mm aperture quadrupole deflector and b) 0.5mm prism Q-switch.

The figure above shows how the performance changes when the polarisation of the light passing through the deflector is changed. The deflection from the quadrupole deflector was approximately 3.7 times greater in one plane than the other, independent of aperture size. This arises from the induced refractive index gradient in one plane being less than other because of the field orientation and differing electro-optic coefficients along each axis. The deflection from the prism Q-switch remained greater for one polarisation, though only 60% greater than the other. These characteristics were used to align the Q-switch to give maximising performance. The poor deflection characteristics of the quadrupole in the second plane could limit its applicability to isotropic and weakly anisotropic gain materials where the laser may reach threshold in the plane of the weaker deflection.

The deflection angle for the quadrupole devices showed excellent linear dependency on the applied voltage (R^2=0.994). In contrast, the deflection from the prism Q-switch indicated a quadratic dependence (R^2=0.9994). Further work could address the origin of this dependence, which is not considered here. The nature of these relationships could be exploited potentially to yield a prismatic Q-switch with superior performance.

From Figure 80 and Figure 70 the smaller aperture quadrupole deflectors can be operated at voltages below 1kV and still provide sufficient deflection to prevent lasing. It is worth noting that distortion of the beam decreases with the smaller and shorter deflectors, and is therefore believed not to contribute to the Q-switching

process in the case of the 1mm deflector, in contrast to the prism deflectors.

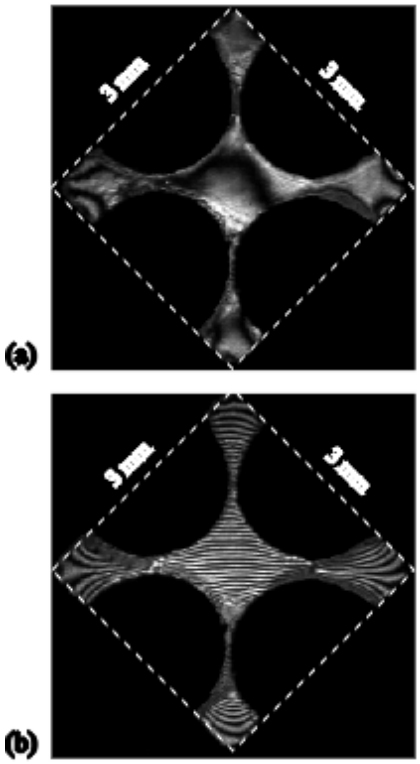

Figure 82 – Interferograms of induced refractive index gradient in 1mm aperture QPD: a) no applied voltage and b) 950V applied between opposite electrodes.

The second method used to examine the effect of an applied voltage was interferometry between the front and back surfaces of the deflector. Typical results from a 1mm-aperture deflector using a HeNe-based Fizeau interferometer are shown above. Friel [256] showed these interferograms predicted the same beam deflection as observed from the far-field beam deflection measurements above. He also showed that residual effects associated with the piezo-optic effect increased the switching time experienced, from that of the transistor switch used. Further interferometric work also revealed signs of damage after prolonged use of the Q-switch.

With the 1mm aperture quadrupole deflector present in a 13mm cavity, and a dc voltage applied to it, it was found that a voltage of 400V, giving deflection of ~2.4mrad, was required to prevent lasing. This result complements the results from the earlier work examining the effect of mirror misalignment and provides an indication of the deflection required from improved devices.

In conclusion, it has been shown that the beam deflecting properties of the

quadrupole deflector were significantly better than the prism deflector, although both showed their potential for use as the basis of an electro-optic Q-switch.

4.3 Passive Q-Switching of Microchip Lasers

4.3.1 Introduction

The use of a saturable absorber to passively Q-switch a microchip laser, can maintain the advantages offered by a monolithic microchip laser geometry. It offers a compact, rugged source of potentially sub-nanosecond pulses with no high voltage electrical requirements, in contrast to active Q-switching.

The relatively uncontrollable nature of passive Q-switching, with the small range of suitable materials, has historically restricted its use with large frame lasers in deference to active Q-switching. There has however been a revival of interest in passive Q-switching in the last decade with the development of smaller DPSSLs and solid-state saturable absorbers, allowing the aforementioned advantages to be realised. Previously, saturable absorbers often took the form of complicated dye-jets, which would be prohibitive in a microchip or small solid-state laser system; or colour-centre crystals, which were unstable and often required operation at low temperatures or in the dark. In comparison to dyes, such as Rhodamine 6G, or to colour centre crystals, such as LiF:F_2^-, doped crystals are more photochemically and thermally stable with higher damage thresholds. There has also been a renewed interest in dye-impregnated solids, though degradation and stability are still issues. For this work, we are particularly interested in doped crystals to match the microchip style and wide range of operating conditions.

4.3.1.1 Historical Review of Passive Q-Switching

The first passively Q-switched microchip laser was reported in 1994 [257]. A device consisting of a 0.5mm long piece of 1.8% Nd:YAG and a 0.25mm long piece of Cr^{4+}:YAG was constructed, with a small signal absorption coefficient of 5.7cm^{-1} at 1064nm. The ratio between the ground-state and excited-state absorption cross-sections, a figure of merit for saturable absorbers, was reported as ~6 for Cr:YAG. This composite microchip laser was end-pumped by a butt coupled 1.2W fibre-coupled diode and produced 11μJ pulses of 337ps duration, giving peak powers in

excess of 28kW at a repetition rate of 6kHz. The output coupler was directly coated onto the Cr:YAG and had 94% reflectivity. The large, unfocussed pump spot size used, gave the relatively high threshold of 0.8W. Therefore, the laser was not operated much above threshold when pumped with the 1.2W laser diode.

The stability was reported to be better than 0.5%, and a conversion efficiency in excess of 70% was recorded for single-pass second harmonic generation of these pulses in a 5mm long piece of KTP. Single-pass doubling of the green output using a 5mm long BBO crystal with 44% efficiency produced 0.7μJ pulses at 266nm [258]. Similarly, by mixing the 1064nm and 532nm radiation, 0.3μJ at 355nm was produced, and 0.01μJ pulses at 213nm by mixing the fundamental and 266nm radiation.

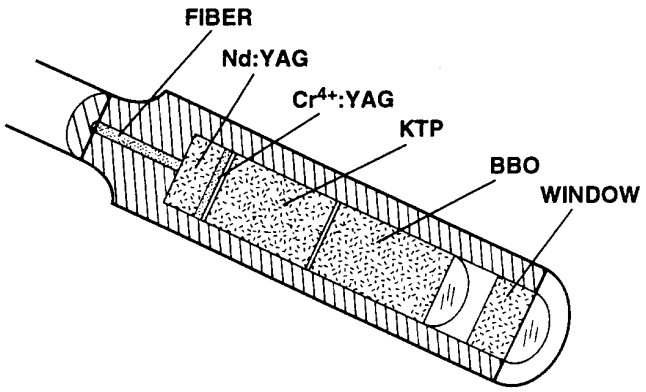

Figure 83 - Passively Q-Switched Frequency Quadrupled System (after [258])

Subsequently Zayhowski used modified forms of these passively Q-switched devices to pump a periodically poled lithium niobate crystal (PPLN) to produce an optical parametric amplifier (OPA) [259]. He subsequently repeated the use of KTP in an optical parametric oscillator (OPO), pumped by the frequency doubled output of the passively Q-switched microchip laser described earlier [260].

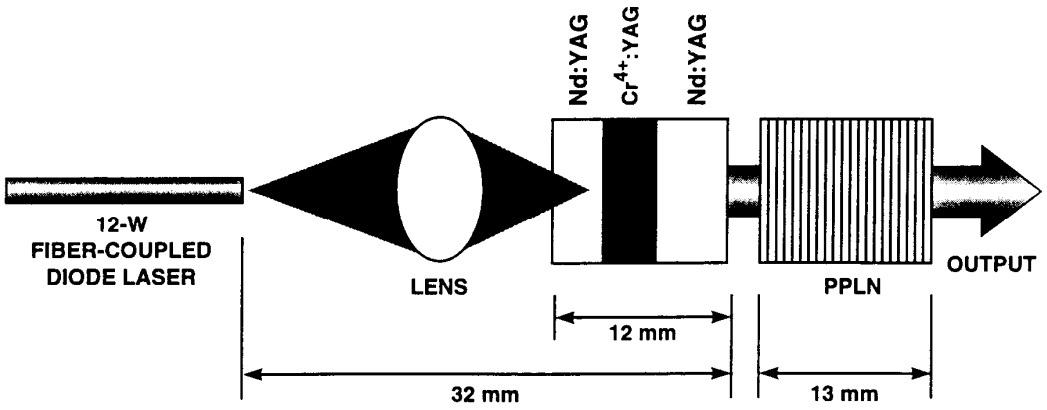

Figure 84 - Microchip Pumped PPLN OPA (after [259])

The PPLN optical parametric amplifier was pumped by a coupled-cavity passively Q-switched microchip, comprising a 3mm piece of 1.1% Nd^{3+} Nd:YAG bonded to a 3mm piece of Cr:YAG (absorption coefficient $1.5cm^{-1}$) and then the output coupler was bonded to this and consisted of a 6mm piece of Nd:YAG coated for 50% reflection at the fundamental. When pumped by a fibre-coupled 12W-diode laser it produced 157μJ pulses at 1064nm in a single transverse and longitudinal mode of 800ps duration at a repetition rate below 2kHz. Eight separate 2cm long PPLN OPA's with grating periods 28-31μm were pumped by this Q-switched laser to give quasi-phase matched operation of the range 1.4-4.3μm. The resulting signal and idler comprised 25% of the incident average power, with a pulse width of <500ps and signal pulses of up to 26μJ and of tens of nanometres bandwidth. The output of the OPA was however no longer a single transverse mode for these results.

A frequency doubled version of the pump laser, used a 5mm piece of KTP to produce 56μJ pulses at 532nm with 600ps duration. These pulses were used to pump a doubly resonant OPO based on a 5mm piece of KTP, which operated around degeneracy and 2.2 times above threshold. The signal and idler pulses produced were of a single transverse and axial mode, though not consistently the same axial mode on each shot. There was a 10% variation in pulse energies. The device could be operated with up to 500GHz separating the signal and idler wavelengths near 1064nm.

Zayhowski has also demonstrated the passive Q-switched operation of the 946nm transition of Nd:YAG using Cr:YAG, producing 0.1μJ pulses with a pulse width of ~10ns, which is attractive for measuring water vapour content in the atmosphere [261]. The three level nature and low stimulated emission cross-section of this

transition however limits its potential as a good source of passively Q-switched pulses at this wavelength.

The passive Q-switching of a large frame Nd:YVO_4 laser using Cr:YAG was first demonstrated earlier this year [262]. Stable laser pulses as short as 28ns with 20μJ energy were obtained using a 10W diode bar. Multiple pulse outputs with different divergences were observed at higher pump powers and attributed to spatial hole burning.

4.3.1.2 Comparison of Saturable Absorbers

In many respects Cr:YAG is not the optimum saturable absorber. Two of the most important parameters in defining a saturable absorber are its discrimination factor and its recovery time. The discrimination factor is defined as the ratio of the ground state absorption cross-section to that of the excited state. As can be seen from Table 13, this ratio is indeed much greater for other Cr^{4+} doped materials, which provide a much greater change in the Q of the cavity. The recovery time is important in determining the pulse duration and the saturation intensity required to bleach the absorber. For materials with very fast recovery times, high saturation intensities are required which in turn yield very high intensity, short pulses shaped by the rapid change in the absorption cross-section.

Parameters	**Cr:YAG**	**Cr:YSGG**	**Cr:LuAG**	**V:YAG**	
Refractive Index	1.82	1.933	1.836	1.82	
Saturated Transmission T_{max} @1064nm (%)	90.7	90.6	95.6	99.6 @1064nm	98.8 @1342nm
Small Signal Transmission T_0 @ 1064nm (%)	49.6	32.8	32.8	95.5 @1064nm	92.2 @1342nm
Ground State Absorption Cross-Section s_{gs} ($x10^{-18}$ cm^2)	3.2	4.55	1.1	30 @1064nm	72 @1342nm
Excited State Absorption Cross-Section s_{es} ($x10^{-18}$ cm^2)	0.45	0.4	0.043	1.4 @1064nm	7.4 @1342nm

Contrast Ratio σ_{gs}/σ_{es}	7.2	11.3	24.9	21.4	9.73
Saturation Intensity e_s (J/cm^2)	0.068	0.045	0.018		

Table 13 – Properties of Cr^{4+} and V^{3+} doped garnets as nonlinear absorbers.

With this in mind, it is perhaps surprising that to date only three other Cr^{4+} materials have been used as passive Q-switches: Cr:YSGG has been successfully used as a saturable absorber for a ruby laser [263], and Cr:YSO for a Cr:LiCAF laser [264]. Cr:LuAG has also been demonstrated to have superior operating characteristics to Cr:YAG, with significantly lower ESA [265].

Co-doping is also possible and has lead to a monolithic, self Q-switched laser in Cr,Nd:YAG [266,267,268]. In [267], pulses as short as 290ps with energies of 8μJ were obtained from a 1mm long crystal pumped by a quasi-CW laser diode with 350μJ pulses. In [268], the authors considered the effect of 'gain-guiding' on the transverse mode of a monolithic device and found that transient modal patterns exist which are considerably different from the eigen-mode calculated from the waveguide profile.

The main alternative to doped crystals for passively Q-switched microchip lasers in the production of ultra-short pulses, has been led by Keller's group at ETH in Zurich. The main limitations of Cr:YAG as a saturable absorber are derived from its relatively poor distinction ratio between absorption in its unsaturated and saturated states and in the recovery time of the bleached material (~300ns). To realise much shorter pulses, alternative saturable absorbers are required, and one approach is to use semiconductor saturable absorbing mirror (SESAMs), which have a recovery time of ~24ps, though a modulation depth of only 10-15%. Their composition can be altered however over a wide wavelength range to provide operation over most of the infrared spectrum and their relatively short length (~0.2mm) does not significantly lengthen the round trip time of a cavity.

The saturable absorber consists of 10-20 quantum wells, in an anti-resonant configuration between a high reflecting, buried bottom mirror and a partially transmitting (10-20%) top dichroic. When the transmitted light through this top dichroic exceeds the satuation intensity for the device, the carriers generation by the

absorption of the light in the quantum wells is sufficient to change the refractive index of the absorber to bring the Fabry-Perot cavity back on resonance and allow a short Q-switched pulse to be produced before the carriers recombine.

This technique has been successfully used in a number of different laser types. A 0.22mm piece of Nd:LSB was used with an InGaAs/AlGaAs MQW SESAM and a 10% output coupler to produce 180ps pulses, of 0.1mJ energy at a repetition rate of 110kHz [269]. The device could be operated up to 7MHz due to the relatively low saturation intensity required to bleach the SESAM, and this effected the stability of the device which was typically 5%. Subsequent improvement of the system, using a 0.2mm long, 3% doped Nd:YVO_4 crystal as the gain material, and higher quality SESAMs has yielded 56ps [270] and 28ps [271] from this system. At higher pump powers these devices operated in an elliptical multi-transverse mode with a jitter of less than 1% and peak powers up to 5kW for a 2W pumping laser diode.

SESAMs have also been successfully used to passively Q-switch a Nd:YVO_4 microchip laser operating at 1342nm [272], and an Er:glass laser operating at 1550nm [271]. The 1342nm laser used InGaAsP as the basis of its MQW, yielding 120nJ pulses of duration 230ps at a repetition rate of 53kHz. However the use of SESAMs have been limited to low power lasers because of their low damage threshold.

Other novel materials have been used as saturable absorbers. Later in this chapter we will look at the use of V:YAG as a saturable absorber at both 1064nm and 1342nm. Silicon has been used as a passive Q-switch for Nd:YAG at 1064nm based on the change in refractive index induced by lattice heating and free-carrier production [273]. Pulses of several millijoules and widths of down to 18ns were obtained. This use of the higher nonlinear refractive index n_2 to produce passively Q-switched operation has also been exploited in several liquids [274].

Before looking at the operation of doped crystals as saturable absorbers, we shall first look at modelling techniques for passively Q-switched systems.

4.3.2 Analytical Modelling of Passive Q-Switching

4.3.2.1 Introduction

Many of the ideas discussed in the first half of the chapter for the modelling of active Q-switching can be carried forward into the modelling of passive Q-switching, with

some allowance made for the presence of the saturable absorber.

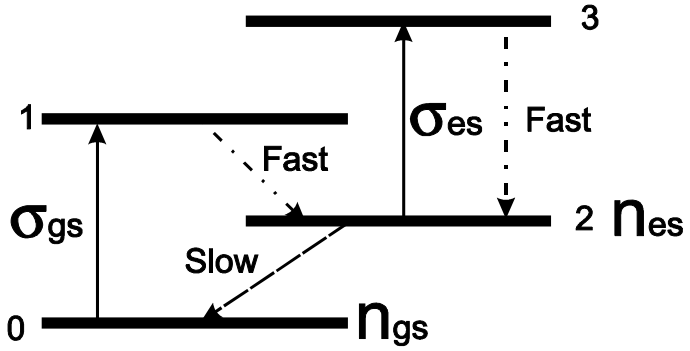

Figure 85 - Energy Level Scheme for a 4-Level Saturable Absorber

A saturable absorber is designed to have a high ground-state absorption (σ_{gs}) at the lasing wavelength. This prevents laser oscillation until the population inversion gives a gain exceeding the loss provided by the output coupler and saturable absorber. A schematic of a typical four-level saturable absorber is shown in Figure 85.

The recovery time from level-2 to the ground state can vary from tens of picoseconds to several hundred nanoseconds. This relaxation time determines the saturation intensity required to 'bleach' the absorber so that the absorption cross-section of the passive Q-switch tends towards the smaller value of the excited state (σ_{es}). The contrast between the absorption cross-section in the ground and excited states is important in determining the extraction efficiency of the system as the excited state absorption is essentially nonuseful loss to the laser system. Therefore the important parameters for a saturable absorber are the recovery time, and absorption cross-sections of the excited and ground states.

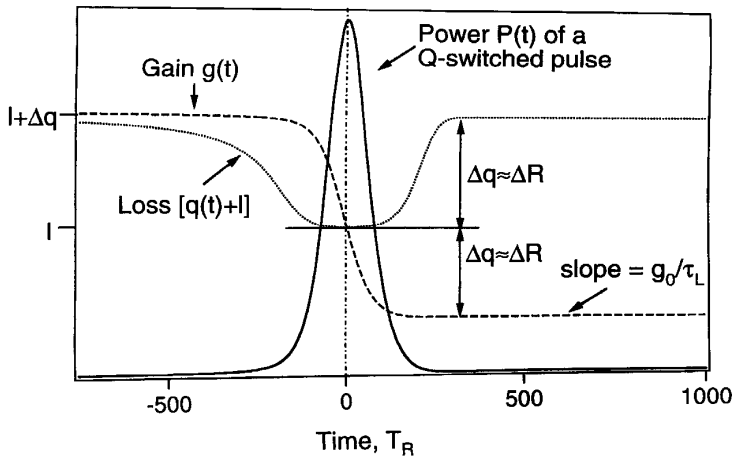

Figure 86 – Simulation of the Q-Switching Dynamics of a Passively Q-Switched Laser (after [270])

There are two important considerations in the rate equations. The recovery time from the excited state to the ground state can be long in comparison to the Q-switch pulse produced. This is particularly true for Cr:YAG which has relaxation time of ~300ns [279]. However in the case of doped semiconductors, where the recovery time is 10-100ps [271], it can be comparable to the pulse width. The other important consideration is the appreciable residual absorption attributed to excited state absorption. The dynamics of a passively Q-switched laser are shown in Figure 86 to illustrate the relationship between the variables of the laser system.

4.3.2.2 General Modelling of Passive Q-Switching

As described previously, numerical solutions have been used to describe the operation of rapidly Q-switched lasers for twenty-five years because of the problem of solving the coupled laser rate equations in a useful analytical form. Szabo and Stein were the first to derive the relevant rate equations for passive Q-switching and presented numerical results of their model [275]. They showed that where the cross-section of the saturable absorber is much greater than that of the gain material and the change in the Q of the cavity can be considered to be instantaneous producing a pulse width of:

$$t_p = \frac{S_p \tau_r}{\sigma_{gs} N l_s}\left[\frac{\delta(1+\delta)\eta}{\delta - \ln(1+\delta)}\right]$$

Equation 93

Where S_p is the pulse-shape factor (typically 0.86 for Q-switched laser pulses [276]), η is the energy extraction efficiency, σ_{gs} is the ground state absorption cross-section of the passive Q-switch, l_s is the saturable absorber length, and δ is the ratio of saturable to unsaturable losses. For Nd:YAG devices this relationship hold true, however the stimulated emission cross-section of Nd:YVO_4 ($1.6 \times 10^{18} cm^2$) is comparable to the absorption cross-section of Cr:YAG ($\sim 2 \times 10^{18} cm^2$) and is therefore more similar to slow Q-switching.

The use of a gain crystal with a large stimulated emission cross section is not advantageous in passive Q-switching. If it is larger than the absorption cross-section of the absorber, then the stored energy in the cavity may not be high enough to bleach the absorber, giving quasi CW operation. It can be shown that for efficient passive Q-

switching to occur then [262]:

$$\frac{\alpha_a l_s \sigma_{gs} A_g}{\alpha_g l \sigma A_a} > \frac{\gamma}{1-\frac{\sigma_{es}}{\sigma_{gs}}}$$

Equation 94

where σ is the stimulated emission cross-section of the laser material, l is the length of the laser gain material, σ_{es} is the excited state absorption cross-section, α is the absorption coefficient and A is the effective beam area with subscript g indicating gain crystal and subscript a indicating absorber. The inversion reduction factor, γ, is equal to one for an ideal four-level laser, and to two for a three level system. In the case of Nd:YVO_4, intracavity focusing of some description is required to ensure this inequality holds.

The saturation intensity of a thin absorber is defined as:

$$I_s = \frac{h\nu}{\sigma_{gs}\tau_s}$$

Equation 95

where τ_s is the effective lifetime of the excited state. For doped crystals, this is several hundred nanoseconds, giving a saturation intensity of several hundred kilowatts per square centimetre. In comparison in a semiconductor, the lifetime is normally determined by recombination that occurs in less than a nanosecond, giving a saturation intensity of up to several gigawatts per square centimetre. This is at the edge of the intensities available in a DPSSL. The decrease in absorption coefficient is related to the incident light by:

$$\varsigma = \frac{\varsigma_0}{1-\frac{I}{I_s}}$$

Equation 96

Where ζ_0 is the absorption coefficient at zero intensity. Similarly the time response of a saturable absorber to a step function in light intensity of amplitude I is [250]:

$$\tau_{RT} = \frac{\tau_s}{1+\frac{I}{I_s}}$$

Equation 97

Therefore, if we are interested in an absorber which can be appreciably bleached and with a quick response time, then we are looking for a material with a large cross-section and short lived excited state. These are the reasons why dyes are so attractive as they typically have cross-sections of $10^{-15} \rightarrow 10^{-17} cm^2$ with recovery times less than a nanosecond.

4.3.2.3 Theoretical Optimisation of Passively Q-Switched Lasers

More recently Degnan extended his theory of optimally coupled Q-switched lasers, described earlier in this chapter, to take account of saturable absorbers [277]. Xiao and Bass [278] extended and simplified Degnan's model to include ESA, which is appropriate for a four-level Cr^{4+} material used as a saturable absorber. A similar extension to Degnan's model has been proposed more recently by Zhang et al. to incorporate ESA in much the same way [279].

To describe a four-level system, the following coupled rate equations can be used:

$$\frac{d\phi}{dt} = \frac{\phi}{t_r}\left[2\sigma N l - 2\sigma_{gs} N_{gs} l_s - 2\sigma_{es} N_{es} l_s - \left(\left(\ln\frac{1}{R}\right) + \varepsilon\right)\right]$$

Equation 98

$$\frac{dN}{dt} = -\gamma\sigma c\phi N$$

Equation 99

$$\frac{dN_{gs}}{dt} = -\sigma_{gs} c\phi N_{gs}$$

Equation 100

$$\frac{dN_{es}}{dt} = \sigma_{gs} c\phi N_{gs}$$

Equation 101

$$N_{gs} + N_{es} = N_0$$

Equation 102

where ϕ is the intracavity photon density, N is the population inversion density of the laser material, and N_{gs}, N_{es} and N_o are the absorber ground, excited state and total

population densities respectively, R is the reflectivity of the output coupler, ε is the nonsaturable intracavity round-trip dissipative optical loss, l′ is the cavity optical length and $t_r = \frac{2l'}{c}$ is the cavity round-trip time where c is the speed of light.

By dividing Equation 99 by Equation 100 and integrating, we obtain:

$$N_{gs} = N_0 \left(\frac{N}{N_i} \right)^{\alpha'}$$

Equation 103

where N_i is the initial population inversion density in the gain medium and α′ is a constant defined by:

$$\alpha' = \frac{\sigma_{gs}}{\sigma\gamma}$$

Equation 104

Combining Equation 98-Equation 104 we get a relation between the initial and final population densities in the gain medium, N_i and N_f:

$$N_i - N_f - \frac{\left(\ln\left(\frac{1}{R} \right) + L' \right)}{2\sigma.l} \ln\left(\frac{N_i}{N_f} \right) - \frac{l_s.\gamma}{l.\gamma'_s} N_0 \left(1 - \left(\frac{N_f}{N_i} \right)^{\alpha'} \right) = 0$$

Equation 105

where $L' = \varepsilon + 2\sigma_{es}.N_0.l_s$, $\gamma'_s = \frac{FOM}{FOM - 1}$ and $FOM = \frac{\sigma_{gs}}{\sigma_{es}}$. FOM is a figure of merit, which can be used to compare the potential of different materials for use as passive Q-switches.

The upper state population just before the onset of oscillation, N_i, is given by equating the gain to loss in the cavity:

$$N_i = \frac{\left(\ln\left(\frac{1}{R} \right) + \varepsilon + 2\sigma_{gs} N_0 l_s \right)}{2\sigma.l}$$

Equation 106

The population inversion density N_t at the point of maximum power, can be calculated from:

$$N_t = \frac{\ln\left(\frac{1}{R}\right) + L'}{2\sigma.l}$$

Equation 107

So N_i, N_f and N_t can be calculated which enables the energy, peak power and duration of the Q-switched pulse to be calculated from Equation 80, Equation 88 and Equation 89.

The optimisation of this model can be carried out using a similar procedure to that discussed for active Q-switching.

Using the following dimensionless parameters:

$$z' = \frac{2\sigma N_i l}{L'}$$
$$z_s' = \frac{2\sigma_{gs} N_0 l_s}{L'\gamma_s'}$$
$$x' = \frac{-\ln(R)}{L'}$$
$$p = \ln\left(\frac{N_i}{N_f}\right)$$

Equation 108

the laser output energy can be rewritten as:

$$E = \left(\frac{h\nu AL'}{2\sigma\gamma}\right) p(z' - z_s' - 1)$$

Equation 109

Xiao and Bass extended Degnan's use of Lagrange multipliers to include ESA by redefining the dimensionless parameters by maintained the form to utilise the same solutions. It can be shown that the optimum value of the ground-state absorption cross-section can be expressed as a function of α' and p such that:

$$\sigma_{gs}^{opt} = \alpha' z(\alpha', p) \frac{(1 - e^{-p} - p)}{(1 - e^{-\alpha' p} - \alpha' p)} \frac{L'\gamma_s'}{2N_0 l_s}$$

Equation 110

where:

$$z(\alpha', p) = \frac{(1 - e^{-\alpha' p} - \alpha' p)^2}{(1 - e^{-\alpha' p} - \alpha' p e^{-p})(1 - e^{-\alpha' p} - \alpha' p) - \alpha'(1 - e^{-p} - p)(1 - e^{-\alpha' p} - \alpha' p e^{-\alpha' p})}$$

Equation 111

The optimum output coupling can be similarly expressed:

$$R_{opt} = z(\alpha', p) - \frac{2L'\gamma_s'\sigma_{gs}^{opt}}{2N_0 l_s} - 1$$

Equation 112

The passive Q-switches used for this work are based on Cr:YAG. If we use the equations above to model the expected behaviour for the crystal with 85% small signal transmission, we can see how the system may be optimised. The optimum output coupling and energy extraction are shown in Figure 87. As can be seen, the optimum output coupling for the range of pump powers available is approximately that of the single pass, small signal absorption of the passive Q-switch. The pulse energy can rise to several microjoules for optimal output coupling, however the crystals used for the experimental work had a fixed output coupling of 3%. The extraction efficiency approaches 40% for an optimally coupled system.

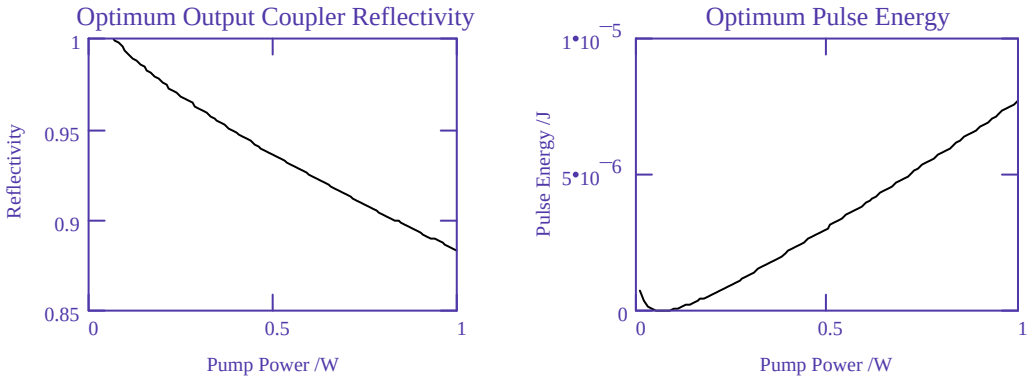

Figure 87 – Optimum output coupling and energy extraction

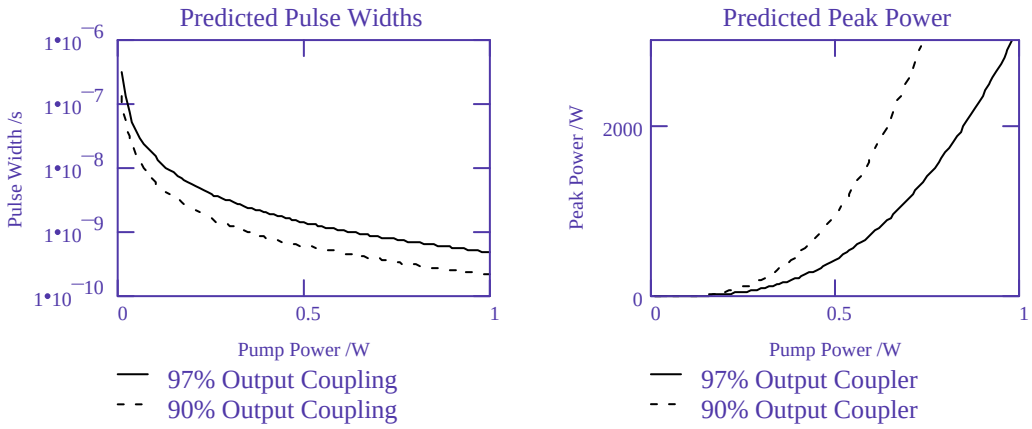

Figure 88 –Predicted pulse widths and peak powers of optimised 85%T Cr:YAG with 0.5mm long 3% doped Nd:YVO_4 crystal.

From using the equations, we can see that for our system we would expect pulses of slightly less than 1ns duration with a peak power of 3kW. If a more optimal output coupling was used, we can see that we would expect pulses down to 200ps with a corresponding increase in the peak power. These figures are consistent with the Q-switched operation observed by Zayhowski for Nd:YAG and Cr:YAG microchip lasers.

We will now proceed to look at the experimental operation of a range of passively Q-switched lasers. In the first sub-section the use of Cr:YAG to Q-switch the 1064nm transition in Nd:YVO_4 is described followed by the use of V:YAG for the 1342nm and 1064nm transitions.

4.3.3 Cr:YAG Passive Q-Switches

Three pieces of Cr:YAG were used to examine the passive Q-switching properties of Cr:YAG. Crystals of length 0.7 mm, 1.5 mm and 2 mm were used, giving nominal transmissions of 90%, and 85% and 80% respectively for small signals at 1064nm. These crystals were coated AR/97%R at 1064nm. In addition an extra crystal with 90% transmission was available and coated AR/AR at 1064nm.

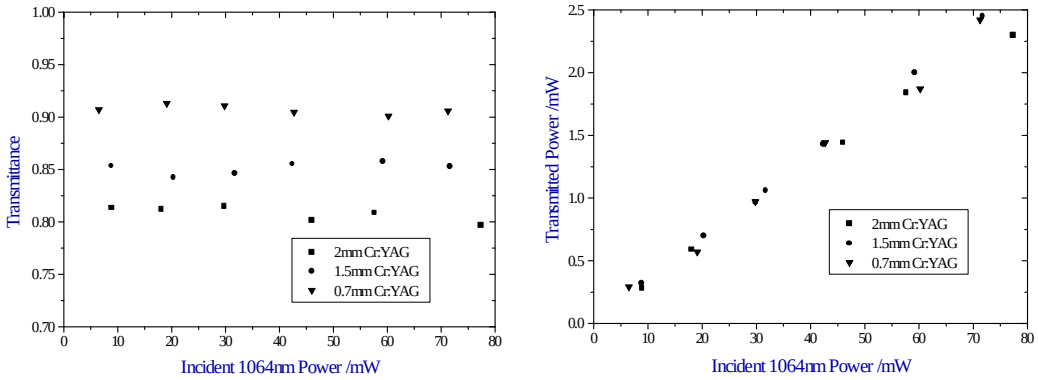

Figure 89 – Cr:YAG passive Q-switch properties – small signal transmission of a) crystals and b) output coupler on crystal for 0.7mm (90%T), 1.5mm (85%T) and 2mm long (80%T) Cr:YAG crystals.

The small signal transmission of these crystals and the reflectivity of the dielectric coatings were measured to confirm the specifications and the results shown in Figure 89. The crystals were of an unknown doping concentration, however an estimate was made for the modelling of these devices to match the observed absorption coefficient. The choice of output coupling was limited by the availability from the manufacturers of the Cr:YAG crystals, though it is hoped with future refinement a more suitable choice of output coupling would maximise the performance of these devices.

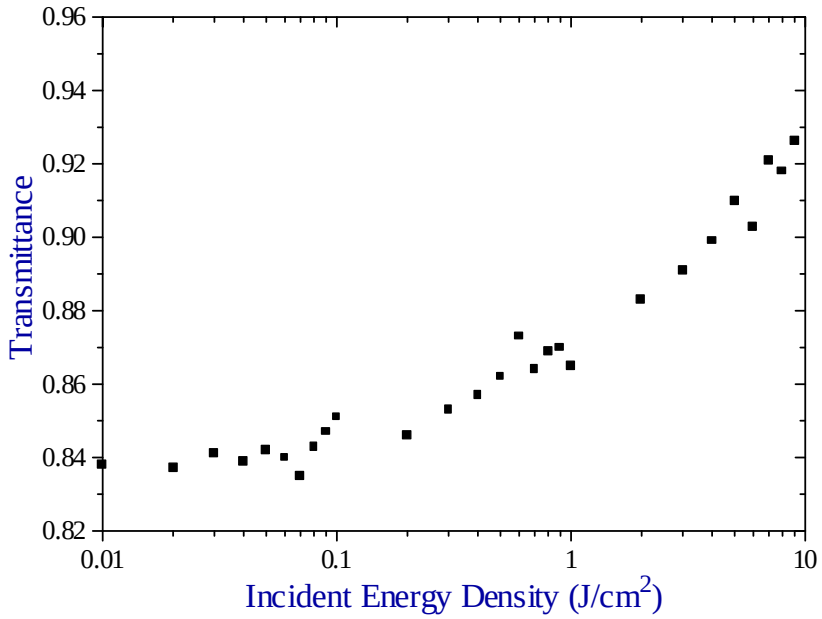

Figure 90 – Measurement of the Saturation Intensity of Cr:YAG at 1064nm.

The intensity dependent transmission of the 1.5mm long piece of Cr:YAG coated AR/AR at 1064nm was measured using a passively Q-switched laser producing 2ns pulses. By the use of a 100mm focal length lens and neutral density filters, different

energy densities were used to measure the transmittance of the sample, this nominally had an 85% small signal transmission. The results of this experiment are shown in Figure 90. These results compare favourably with the work of Moncorge et al. and Munin et al. [265,280]. Unfortunately, the intensity was not available to probe the residual excited state absorption in the excited state, though it is believed to be around 3-4%. The damage threshold of Cr^{4+} doped crystals is typically one to two orders of magnitude greater than that required to reach the 'bleached' state and therefore they are an attractive substitute to impregnated dyes. The saturation intensity of Cr:YAG is relatively low and easily achievable in a microchip geometry, in comparison to semiconductor materials, because of its long relaxation time.

4.3.3.1 Pump Spot Optimisation

There is a requirement to consider the optimal pump spot size because of the trade off between lasing threshold and passively Q-switched performance. With small pump spot sizes, threshold is reached at low intensities, giving low peak powers and long pulse durations. If the pump spot is too large, threshold will not be achieved. Using a diode pump source, consideration also needs to be given to the asymmetry, abosorption and divergence of the pump beam, which effects the beam for long and very short focal lengths.

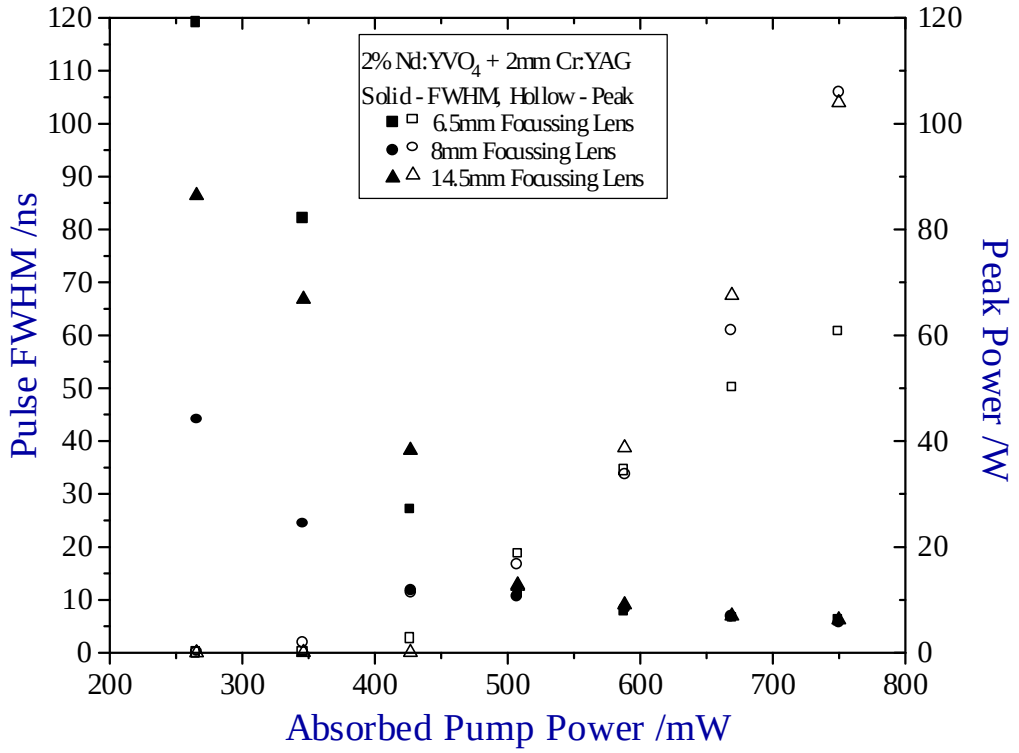

Figure 91 – FWHM and peak powers of a 2% doped 3x3x0.5mm Nd:YVO_4 and 2mm Cr:YAG sandwich for different pump spot sizes.

The effect of pump spot size was examined by using different focal length lenses to pump a 5x5x2mm Cr:YAG, 3x3x0.5mm 2% doped Nd:YVO_4 sandwich. From Figure 91, it can be seen that the 8mm lens provides the best performance from these devices. It is worth noting that the threshold for each focal length is similar. One possible explanation for this behaviour comes from the distribution of the gain and residual pump light contributing to the saturation of the Cr:YAG. The thermal lensing is also a contributing factor in defining the cavity, which favours the optimally coupled 8mm lens to pump the microchip laser.

The symmetry requirement on pump mode quality was illustrated using a 25.6mm focal length lens, which produced a highly asymmetric output. With diode pump shaping this dependency could be decreased, to give better Q-switched performance using longer focal length lenses. This is further illustrated by Zayhowski's work where he successfully pumped a similar device with a close to circular 400μm pump spot size from butt-coupling the device to the end of a fibre-coupled diode to give sub-nanosecond pulses.

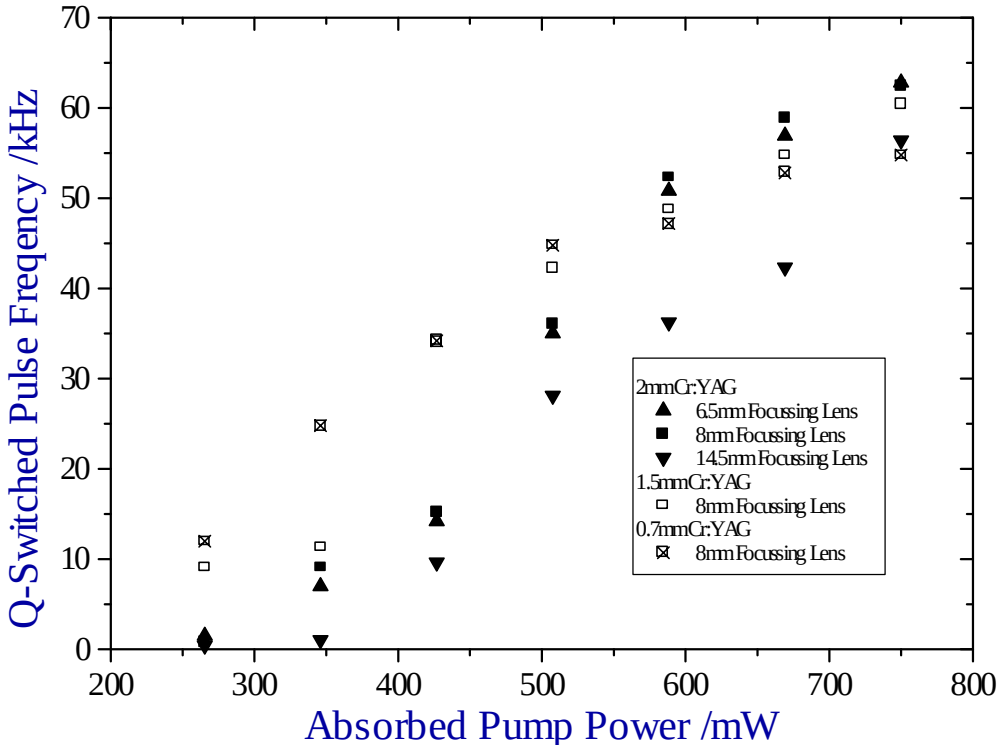

Figure 92 – Passively Q-switched pulse frequency for different pump spot sizes and lengths of Cr:YAG. The laser was composed of a 0.5mm long 2% Nd:YVO_4

crystal and Cr:YAG crystal in intimate contact, pumped by 1.2W laser diode.

The frequency of the pulses produced for the different pumping conditions is shown in Figure 92. As expected, the pulse frequency around threshold corresponds to a value between one to two times the upper state lifetime (90μs). This frequency increases with pump power, giving repetition rates of up to approximately 65kHz. This increase is nearly twice that expected from a simple analysis of threshold and pumping rate, indicating the effect of thermal lensing on determining efficiency and saturation.

Therefore, the optimal coupling is determined by a compromise between long focal length lenses, which give the best Q-switched performance, and shorter focal length lenses, which offer a more symmetric pumped volume and give enhanced cavity definition. In our case, the best performance was achieved with an 8mm focal length lens and this was used for the subsequent work. Further optimisation is required to realise the full potential of these devices through the shaping of the pump beam and optimisation to work at a particular pump power.

4.3.3.2 Cr:YAG With 80% Transmission

To examine the passive Q-switched operation of the Cr:YAG saturable absorbers, a sandwich was formed between the saturable absorber and a 5x5x0.5mm Nd:YVO_4 crystal doped with 3% Nd^{3+}. This sandwich was pumped by a 1.2W laser diode through an 8mm collimating lens and an 8mm-focussing lens.

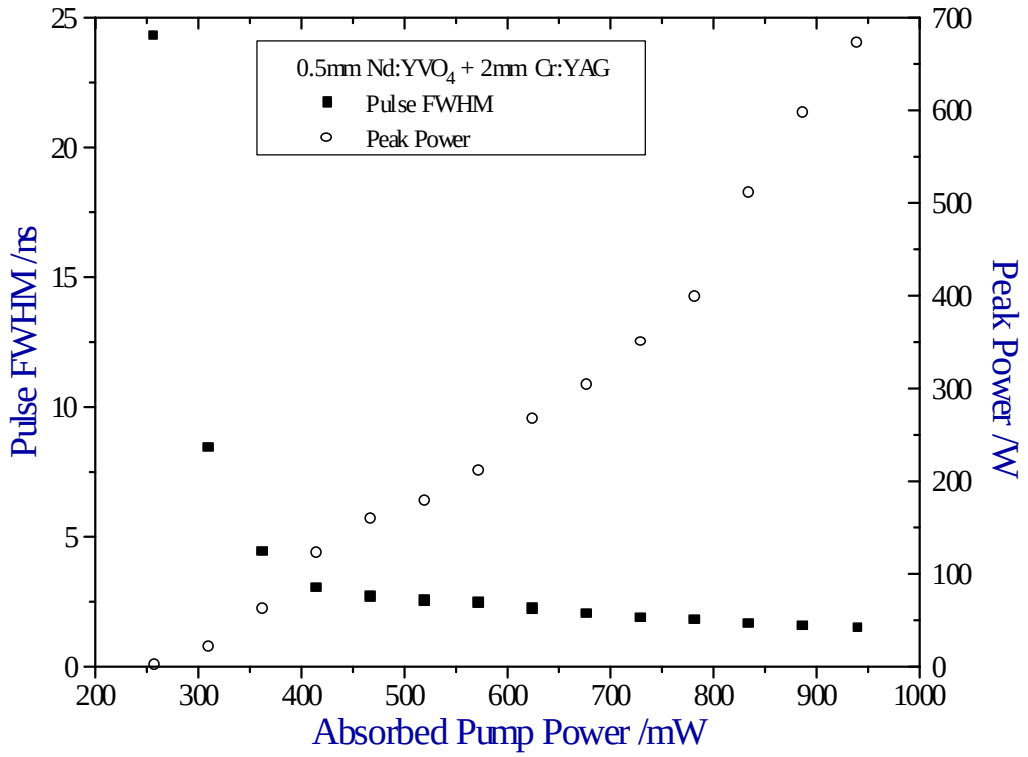

Figure 93 – FWHM and Peak Power for 80%T Cr:YAG Passive Q-Switch.

Of the devices studied, this was the most stable device, with an instrument limited pulse-to-pulse jitter of less than 0.5% (100ns), intensity stability of 2% peak-to-peak and a FWHM stability of less than 2%. This was achieved however at the expense of peak power and pulse duration as can be seen in Figure 93. Pulse widths of down to 1.48ns were measured at repetition rates up to 31kHz. The threshold for the device was 245mW with a slope efficiency of 4%, indicating the relative inefficiency of this form of passive Q-switching compared to CW operation.

4.3.3.3 Cr:YAG With 85% Transmission

Of the three saturable absorbers examined in a microchip geometry, the sample with 85% small signal transmission gave the best performance. Peak powers of over 930W were achieved with pulse widths down to 1.38ns. The improved performance of the 3% Nd:YVO_4 over the 2% doped material used for the earlier experiments be seen by the lower threshold in Figure 94. This enhancement is due to better coatings on the crystal with better mode definition offered by the more highly doped material.

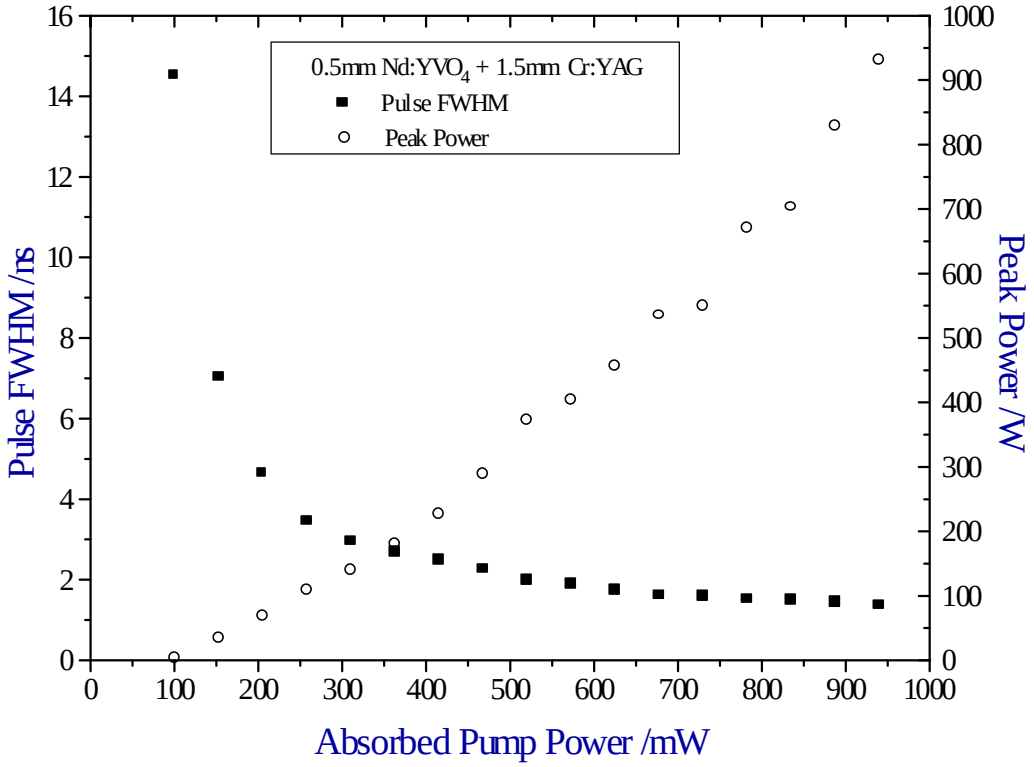

Figure 94 – FWHM and Peak Power for 85%T Cr:YAG Passive Q-Switch.

The slope efficiency of the device was again limited to around 4%, with pulse repetitions up to 53kHz. There was a decrease in stability of these devices over the 80% transmitting Cr:YAG. The peak-to-peak instability was measured to be 6% with a fluctuation in the FWHM of the pulses of around 4%.

For both of these devices there was no evidence of after pulsing and they operated in a near TEM_{00} mode, and with up to two longitudinal modes. Single frequency operation was not readily obtainable for pump powers more than twice threshold, which could limit potential applications for this technology. However with more highly doped Cr:YAG this constraint could be removed through the use of a shorter cavity and higher output coupling.

In comparison to a commercially manufactured passively Q-switched Cr:YAG, Nd:YAG combination, these devices gave similar performance, at a higher repetition rate and with greater stability, allowing for the shorter pulse lengths (0.8ns) of the commercial device.

4.3.3.4 Cr:YAG with 90% Transmission

Initial work with the 90% transmitting crystal and a piece of 2% doped material gave similar performance to that described in the next section for 1% doped material and

did not give satisfactory performance as a passive Q-switch. With more highly doped Nd:YVO_4 satisfactory performance was observed as is illustrated in Figure 95.

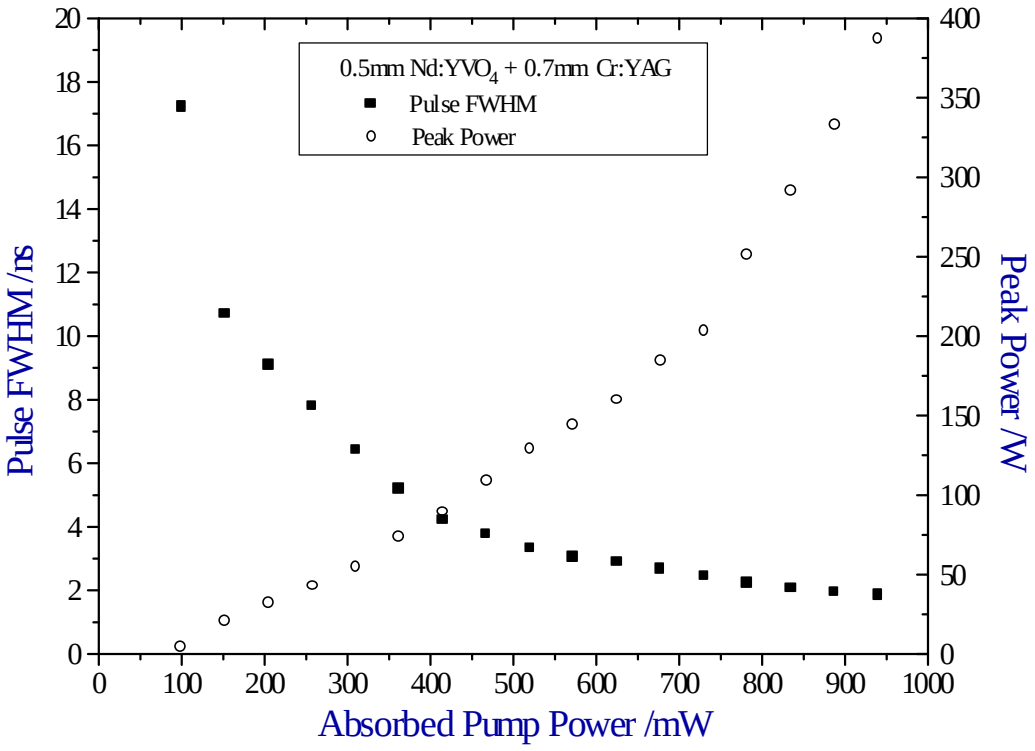

Figure 95 – FWHM and Peak Power for 90%T Cr:YAG Passive Q-Switch.

As expected this device exhibited the lowest threshold with the highest pulse repetition rates. Pulse repetition rates were measured to be as high as 67kHz with a low slope efficiency of approximately 3%. The relatively low change in transmission, from 90% to 97.5%, is not as significant as the other crystals examined, making these devices the least stable. Changes in the peak-to-peak intensity were measured to be up to 20%, with a similar figure for pulse duration. In some regions of operation, there was no well-defined pulse-to-pulse timing, similar to operation described in the next section. However in general, the devices operated with up to 10% timing jitter, suggesting there is not sufficient absorption to bleach the saturable absorber sufficiently to stabilise the pulse timing.

Of the three sandwich devices examined, the 85% transmission Cr:YAG device gave the best overall performance. This value matches the value used by many other groups working on passive Q-switching in Cr:YAG. As a rule of thumb, the optimal small-signal transmission of a saturable absorber is close to the optimal output coupling for the gain crystal in monolithic form. Lower transmission crystals increase the residual

losses and higher transmission crystals do not provide good discrimination.

4.3.3.5 Cr:YAG With 1% Doped Nd:YVO_4

As mentioned earlier, in the theoretical description of passive Q-switching, it is necessary to have some form of intracavity focussing to ensure good Q-switched behaviour when the gain cross section is equal to or greater than the absorption cross-section. When the 3% doped Nd:YVO_4 crystal was replaced by a larger 1% doped crystal, giving weaker thermal transverse mode definition, the importance of this relation was observed.

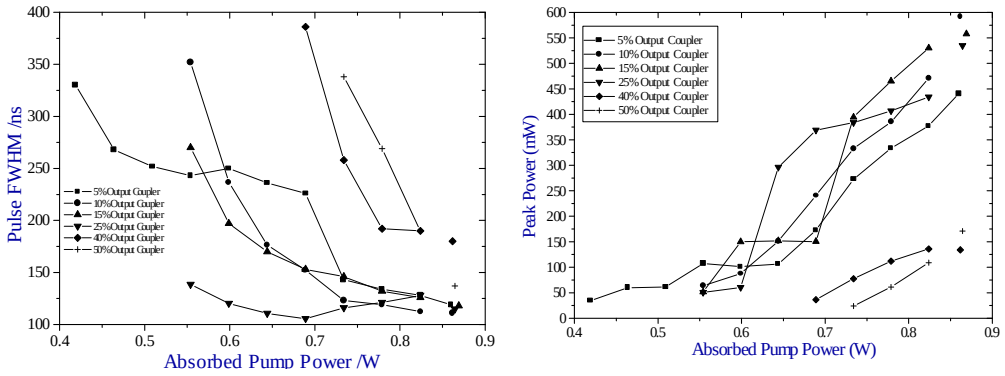

Figure 96 – Passive Q-Switched Behaviour with Different Output Coupling

A semi-monolithic laser, consisting of a 3x3x1mm, 1% doped Nd:YVO_4 crystal, with a 0.7mm, 90% transmittance Cr:YAG crystal, coated AR/AR@1064nm and a discrete output coupler was assembled, with an overall cavity length of 3mm, in order to determine the optimum output coupling. The results are shown in Figure 96. The laser operated quasi-CW with a series of high frequency (100-1000kHz) Q-switched pulses super-imposed. This behaviour is attributed to both the absorption cross-section being lower than the gain cross-section, and the approximately equivalent beam areas in both crystals. For the pulses that were observed, we discovered that the optimum output coupling for the system, given the relatively poor performance, was around the expected value of 10-15%.

This laser also operated on a peculiar pulse structure. For certain windows of operation two or three stable pulse shapes were produced with different intensities and pulse durations, though with no strongly distinguishable change in pulse-to-pulse separation. This was similar to the performance of the commercially produced passively Q-switched Nd:YAG laser and is attributed to the longitudinal mode interactions of the laser, each of the modes have different threshold conditions. There

was a good correlation between the number of modes measured using an optical spectrum analyser and the number of stable pulse shapes observed. However, a similar analysis to that performed on the self Q-switching effect described in Chapter Three, would help to resolve this effect more thoroughly and indicate possible solutions to give a more stable output.

The output coupler of the previous system was replaced by a 1.5mm KTP crystal coated with a HR@1064nm on one side and uncoated on the other to form a triple sandwich. The resulting green pulses were up to 120W peak power with pulse durations down to 10ns. The fundamental 1064nm pulses were measured to be approximately 40% longer than the green, with peak powers of up to 22W.

Although this efficient conversion is attractive, extra-cavity single pass doubling is more desirable for a number of reasons. The extra-cavity intensity is sufficient to give efficiencies above 50% without resonant enhancement, leaving the ability to optimise the fundamental system independently. The shorter cavity length and single pass nature give shorter pulses in a single direction. The instability of intracavity doubling was also evident from this work, however no suitable KTP crystals were available to demonstrate good single pass conversion.

In conclusion, we have demonstrated the use of Cr:YAG as a saturable absorber to passively Q-switch Nd:YVO_4 microchip lasers operating at 1064nm. Pulses as short as 1.38ns were obtained with a peak power approaching one kilowatt and at repetition rates of up to 65kHz. These pulse energies are comparable to those of the most efficient Nd:YAG/Cr:YAG passively Q-switched laser reported to date. With optimisation of the output coupling, pulses substantially below one nanosecond and peak powers of several kilowatts should be obtainable from the system described, providing a highly attractive, compact source of short, high intensity pulses at 1064nm.

4.3.4 V:YAG Passive Q-Switches

Most of the solid state passive Q-switches which have been developed have operated using the 1064nm transition of Nd^{3+} and therefore have been based on the saturable absorption of Cr^{4+} ions. The operation of Cr^{4+} devices ranges from approximately 900-1100nm, depending on the host properties. Part of the work for this thesis was to identify a new saturable absorber, which could operate at longer wavelengths, in particular with the 1342m transition of Nd^{3+}.

Working in conjunction with Malyarevich and Mikhailov from the International Laser Centre in Minsk, we identified V:YAG as a potentially attractive material. The nonlinear absorption characteristics have been investigated by a number of Belarussian groups, although not at the longer wavelengths of interest here [281,282,283]. Work is ongoing to identify the extent of the saturable absorption characteristics of V^{3+} at these longer wavelengths and will be the subject of a future publication.

4.3.4.1 Spectroscopy of V^{3+}:YAG

A 3mm long cylinder of V^{3+} doped YAG crystal was prepared with a doping concentration of $2x10^{20}$ atoms/cm^3. The absorption spectrum of the sample was measured in 900-1600nm region, as shown in Figure 97.

Two absorption peaks were observed at 1140nm and 1320nm, and attributed to the $^3A_2 \rightarrow {}^1E(^1D)$ and $^3A_2 \rightarrow {}^3T_2(^3F)$ transitions respectively of the tetrahedrally co-ordinated V^{3+} ion [284]. The energy level scheme associated with these absorption bands is illustrated in Figure 99. The fast decay of the $^1E(^1D)$ level to $^3T_2(^3F)$ has previously been measured to be 0.13ns [284]. To complete our knowledge of the system we measured the lifetime of the longer-lived decay $^3T_2(^3F) \rightarrow {}^3A_2$ using a pump-probe technique. Laser pulses at 1080nm with 15ps pulse duration were used for pump and probe. The lifetime of the $^3T_2(^3F)$ level was found to be 22±6ns (inset in Figure 97).

The saturable absorption of the V:YAG sample was measured using a Q-switched Nd^{3+}:YAG laser at 1064nm (pulse duration of 12ns) and Nd^{3+}:$YAlO_3$ at 1342nm (70ns). The pulse intensity was varied with a set of glass filters and the energy transmission of the sample was measured using two photodetectors. All the

measurements reported here were carried out at room temperature.

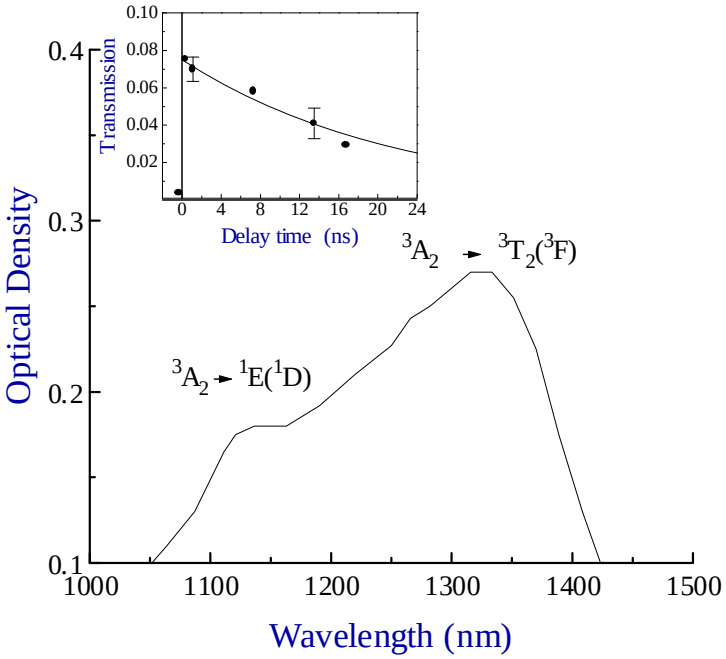

Figure 97 - Linear absorption spectrum of V^{3+}:YAG in the near infrared. The absorption peaks at 1320nm and 1140nm are attributed to the $^3A_2 \rightarrow {}^3T_2$ (3F) and $^3A_2 \rightarrow {}^1E$ (1D) transitions respectively. Inset shows pump-probe differential transmission for 15ps pulses at 1080nm.

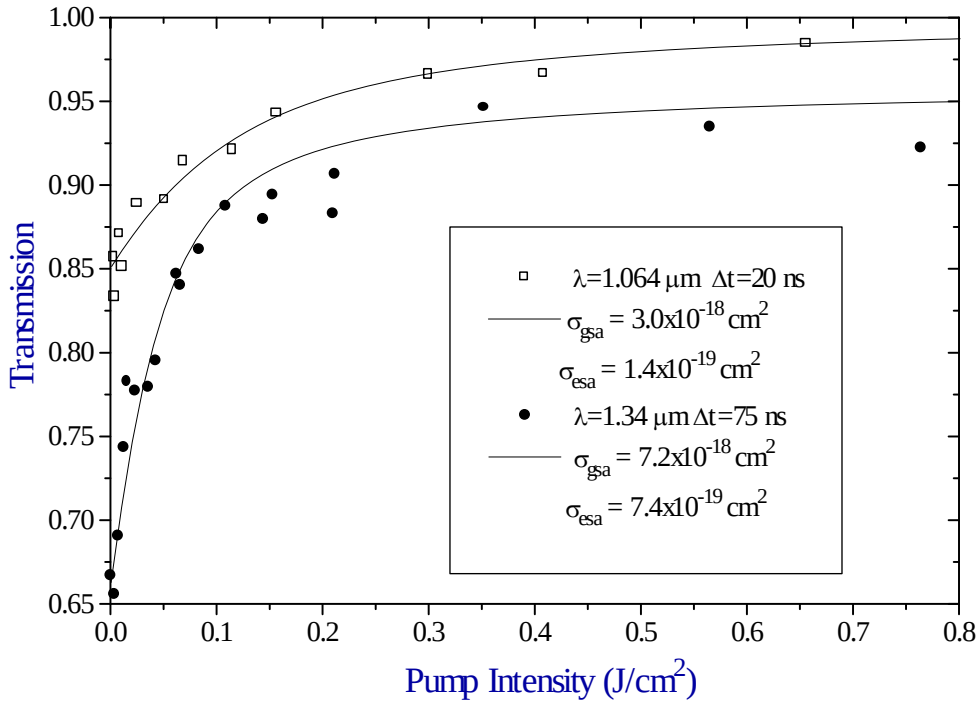

Figure 98 - Transmission of V:YAG as a function of incident pump intensity at a) 1064nm and b) 1342nm. The pulse durations are a) 12ns and b) 70ns. Solid

lines are the result of computer simulation for best fit to experimental data using a rate-equation model [285].

Rate-equation model calculations were made numerically fitted to the experimental data. This model took account of the finite lifetime of the $^3T_2(^3F)$ level (22ns) and the duration of the laser pulses at both pump wavelengths (12 and 70ns) [285]. The best fits are shown with solid lines in Figure 98. The ground and excited state absorption cross-sections were calculated to be $\sigma_{gsa} = 7.2\pm2.6\text{x}10^{-18}$ cm^2 and $\sigma_{esa} = 7.4\pm2.8\text{x}10^{-19}$ cm^2 at 1342nm, and $\sigma_{gsa} = 3.0\pm1.2\text{x}10^{-18}$ cm^2 and $\sigma_{esa} = 1.4\pm0.6\text{x}10^{-19}$ cm^2 at 1064nm. In comparison, Cr:YAG has ground and excited state absorption cross-sections of $\sigma_{gsa} = 3.2\text{x}10^{-18}$ cm^2 and $\sigma_{esa} = 4.5\text{x}10^{-19}$ cm^2 at 1064nm [285], indicating that V:YAG provides lower residual absorption at 1064nm, because of its lower excited-state/ground-state absorption ratio [278]. ($\sigma_{esa}/\sigma_{gsa}$ = 0.05 for V:YAG and 0.14 for Cr:YAG).

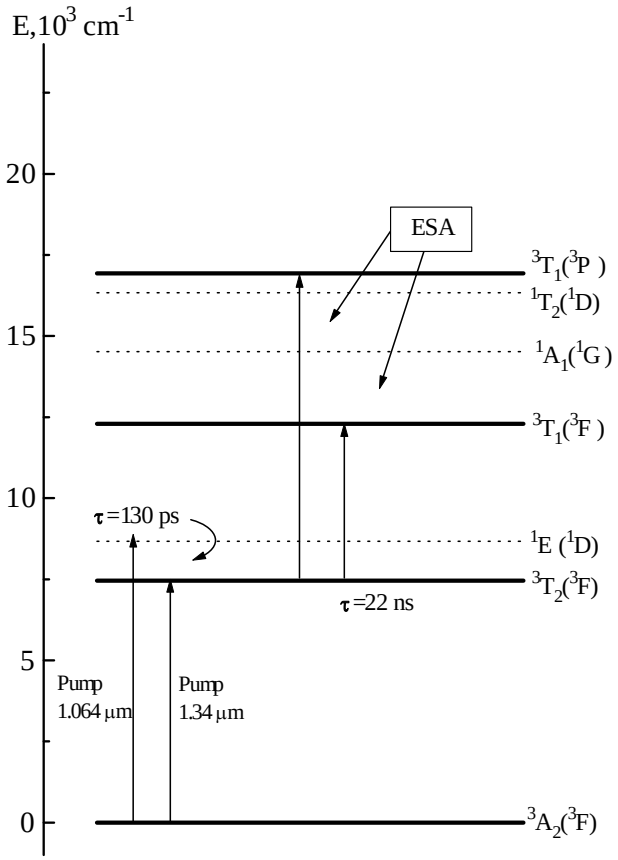

Figure 99 - Energy levels of V^{3+} associated with infrared saturable absorption.

For photons at 1064nm, ground-state absorption in V:YAG occurs due to the spin-allowed $^3A_2 \rightarrow {}^3T_2(^3F)$ and spin-forbidden $^3A_2 \rightarrow {}^1E(^1D)$ transitions. Generally it is known that spin-forbidden transitions have less oscillator strength. However, in V:YAG, the energy gap between the $^3A_2$ and $^1E(^1D)$ states, determined from a linear absorption spectrum at 77K, is ~9000 cm^{-1} (~1100nm) [284] and at room temperature this agrees closely with the pump photon energy of ~9400 cm^{-1} (1064nm). Therefore the $^1E(^1D)$ level is populated after excitation by the 1064nm photons. This was confirmed in [284] by the presence of ESA from this level.

The lifetime of the $^1E(^1D)$ level (0.13ns) is significantly less than the duration of the excitation pulses used for the pump/probe experiments showing saturable absorption (12ns). We believe that the spin-allowed excited state transitions from the $^1E(^1D)$ level to higher singlet levels and from the longer-lived (22ns) $^3T_2(^3F)$ level, to higher triplet levels make contributions to the excited state absorption at this wavelength. Due to the longer lifetime of the $^3T_2(^3F)$ level, it primarily determines the characteristics of the saturable absorption of V:YAG at 1064nm.

The energy of 1342nm photons provide a good match to the $^3A_2 \rightarrow {}^3T_2(^3F)$ transition (Figure 1). From the positions of the $^3T_2$, $^3T_1(^3F)$, and $^3T_1(^3P)$ energy levels obtained from the 80K linear absorption spectra [284], the excited state absorption at 1342nm can be tentatively assigned to the spin-allowed $^3T_2 \rightarrow {}^3T_1(^3F)$ transition.

4.3.4.2 Q-Switched Performance

The passive Q-switching of V:YAG was examined in a microchip geometry, using Nd:YVO_4 as the gain material operating at 1064nm and 1342nm. The small signal transmission of this 20x3mm thick V:YAG crystal was 95.5% and 92.2% at 1064nm and 1342nm respectively. There was less than 1% reflectivity from the broadband AR coatings applied to the polished faces, which were polished with a wedge of 4mrad between them.

The 1342nm laser consisted of a 1% doped 3x3x0.5mm piece of Nd:YVO_4 coated HR/AR at 1342nm, the V:YAG crystal, a discrete output coupler, and air gaps of 0.5mm, giving a total cavity length of 4mm. The output couplers used were flat with 1%, 2% and 5% transmission at 1320nm. A similar cavity, with a 3% doped

3x3x0.5mm crystal of Nd:YVO_4 coated HR/AR at 1064nm was used at 1064nm. Plane output couplers of up to 60% transmission were available at this wavelength.

A 2W SDL2372 laser diode was used to pump these arrangements through an 8mm collimating lens and an 8mm focussing lens. No attempt was made to shape the diode beam to optimise coupling or to double pass the pump light through the gain crystals.

The 1064nm laser was operated with a range of output couplers and with pump powers of up to 1.5W. In all cases pulses were seen superimposed on a CW background level. The pulses were at a repetition rate of up to 1MHz, with pulse durations down to 22ns and peak powers of up to 20W. This poor performance arises because of the relatively small change in transmission of the V:YAG, on saturation of absorption, from 95.5% to 99.8%. This change does not provide sufficient modulation to the quality of the cavity to prevent CW lasing of the 1064nm transition. It is believed that the use of higher V^{3+} doping concentrations and consequently larger absorption would be more effective for this laser and in addition provide a shorter cavity length. Alternatively, gain materials with lower gain coefficients would offer superior Q-switched performance in this geometry. Indeed, results better than those reported using Cr:YAG at 1064nm should in principle be attainable.

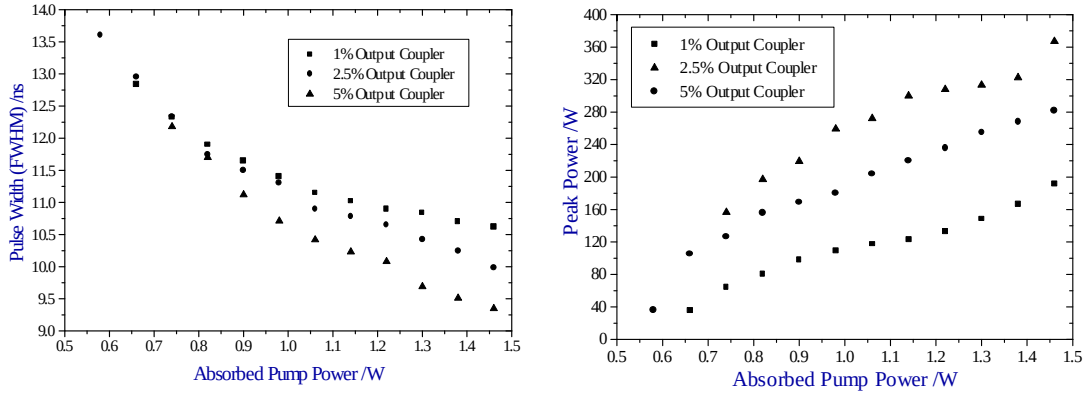

Figure 100 - Passive Q-switched performance of 20x3mm V:YAG crystal and 0.5mm long Nd:YVO_4 crystal AR/HR @ 1342nm. Output coupling was achieved using a discrete output coupler.

The stimulated emission cross-section of the 1342nm Nd^{3+} ion transition is several times lower than for 1064nm, although it can offer comparable CW performance to the 1064nm transition [286]. If the larger absorption cross-section of V:YAG at 1342nm is also taken into account, then more successful Q-switching may be expected at 1342nm, compared to 1064nm. Using the same geometry as the 1064nm

experiment, up to 1.8W of pump power was incident on the Nd:YVO_4 crystal, giving a maximum of 1.5W of absorbed power in a focused spot size of approximately120x80μm. Without the V:YAG present in the cavity, 420mW of CW light was produced at 1342nm, with a slope efficiency of 32%.

The threshold for Q-switched operation was 0.55W with the V:YAG in the cavity. Of the output couplers examined, the 2.5% transmissive output coupler provided the best performance, with a pulse repetition rate approximately the inverse of the Nd:YVO_4 upper-state lifetime of 110μs. The measured peak powers and pulse widths (FWHM) for the 1342nm with a 2.5% output coupler are shown in Figure 100. Pulses as short as 9.3ns with peak powers in excess of 350W were obtained at a repetition rate of 8.4kHz.

The output from this laser was frequency doubled in a single pass using a piece of 3x3x2mm LBO cut for type II NCPM at 1342nm. Although these short crystals were not optimised for this application, having been designed for intracavity work [286], 5.4ns pulses were generated at 671nm with peak powers of 25W.

4.3.4.3 Conclusions

In conclusion, we have demonstrated the use of V:YAG as a new saturable absorber for miniature diode-pumped solid state lasers, extending the range of available doped crystalline passive Q-switches further into the infrared. The saturable absorption at 1064nm and 1342nm has been investigated in detail to determine the suitability of V:YAG as a passive Q-switch. The passive Q-switched performance of a V:YAG crystal was then examined at these wavelengths in a Nd:YVO_4 microchip laser. Pulses of less than 10ns duration with peak powers of 350W were produced at 1342nm, with a demonstration of the potential for similar operation at 1064nm.

With further refinement of the growth of these crystals, V:YAG provides an attractive alternative to Cr:YAG at 1064nm and is the material of choice for high power passive Q-switching at 1342nm.

4.4 Conclusions

In this chapter, we have explored the active and passive Q-switching of microchip lasers. A novel form of active Q-switch, based on the deflection of the optical path in the cavity has been demonstrated and a new solid-state saturable absorber has been identified which has been used successfully at near-infrared wavelengths. The properties of these different Q-switching techniques are summarised in the table below with the inclusion of the self Q-switching system described in Chapter Three of this thesis.

Property	**Self Q-Switching**	**Passive Q-Switching**		**Active Q-Switching**	
Active Material	-	20x3mm V:YAG	5x5x1.5mm Cr:YAG	0.5mm Prism – $LiNbO_3$	1mm Quadrupole – $LiTaO_3$
Gain Crystal	5x5x0.25mm 3%	3x3x0.5 mm 1%	3x3x1mm 3%	3x3x1m m 1%	3x3x1mm 1%
Wavelength /nm	1064 (1342)	1342 (1064)	1064	1064	1064 (1342)
Cavity Length /mm	0.25	4	2	40	13 (13)
Output Coupling	5%	3%	3%	75-90%	40-95% (95-99%)
Pulse Energy /μJ	0.05	3.32	1.3	1.86	13.9 (4.94)
Pulse FWHM /ns	1.85	9.3	1.38	5.8	1.08 (9.5)
Peak Power /W	28	358	935	320	11600 (520)
Repitition Rate /kHz	~10	5-20	5-70	0.5-50	0.5-50 (0.5-50)

Table 14 – Comparison of Q-Switching Techniques

Passive Q-switching has been demonstrated at both the 1064nm and 1342nm transitions of Nd:YVO_4. Cr:YAG was successfully used to generate pulses up to 1kW and pulse widths down to 1.38ns at 1064nm, while V:YAG was used to generate 9.3ns pulses with a peak power of 358W at 1342nm.

Further investigations are required to discover the wavelength range over which V:YAG exhibits saturable absorption, although initial work has shown it can be used at 1064nm. This new material, in combination with the more familiar Cr:YAG, now covers most of the near infra-red spectrum, and with future work hopefully other transition metal ions can be identified to provide passive Q-switching further into the infrared.

At 1064nm there is a need to develop new saturable absorbers to overcome some of the limitations of Cr:YAG. Polymers and semiconductor materials are two of the most exciting prospects offering the potential of high performance capabilities in sub-millimetre sized crystals.

We believe the active Q-switching work reported here is the first example of a deflective Q-switch being employed. This initial work has shown the promise of these devices and their scalability. Two differing techniques have been illustrated, each with its own merits and disadvantages. Pulses down to 1.08ns have been achieved with peak powers close to 12kW from the quadrupole deflectors, and 5.8ns pulses of 320W peak power from the prism deflectors. Operation at both 1064nm and 1342nm has been demonstrated, illustrating the potential advantages and versatility of this design.

Further work to examine the effect of a more complicated shaped electrode, to provide multiple prisms should show the performance of the prism devices to be comparable to that of the quadrupole deflectors. Other materials may enhance the electro-optic properties or include other non-linear phenomenon into cavity.

Investigation of the damage mechanisms and scalability of the quadrupole deflectors would help in the commercialisation of this technique to fill the gap in the market where traditional Q-switching techniques are considered too ‘lossy’, bulky or complicated.

References:

[244] A.J.C. Vieira, P.R. Herczfeld and V.M. Contarino, OSA Tech. Digest CLEO'97, Paper CTuP44 (1997)

[245] J.J. Zayhowski, Lincoln Lab Journal, 3:3, 442 (1990)

[246] J.J. Zayhowski and C. Dill, OSA Tech. Digest CLEO'92, Paper CM17 (1992)

[247] J.J. Zayhowski and C. Dill, Opt. Lett., **17:7**, 1201 (1992)

[248] J.J. Zayhowski and C. Dill, Opt. Lett., **20**, 716 (1995)

[249] H. Plaessmann, K.S. Yamada, C.E. Rich and W.M. Grossman, Appl. Opt., **32:33**, 6616 (1993)

[250] W. Koechner, "Solid-State Laser Engineering" (3rd Ed.), Springer-Verlag (1992)

[251] W.G. Wagner and B.A. Lengyel, Appl. Phys., **34**, 2040 (1963)

[252] J.E. Midwinter, J. Appl. Phys., **16**, 1125 (1965)

[253] J.J. Degnan, IEEE J. Quantum Electron., **25:2**, 214 (1989)

[254] M. Gottlieb, C.L.M. Ireland and J.M. Ley, "Electro-Optic and Acousto-Optic Scanning and Deflection", Marcel Dekker Inc (1983)

[255] H. Plaessmann, K.S. Yamada, C.E. Rich and W.N. Grossman, Appl. Opt., **32**, 6616 (1993)

[256] G.J. Friel, R.S. Conroy, A.J. Kemp, B.D. Sinclair and J.M. Ley, "Q-switching of a diode-pumped Nd:YVO4 laser using a quadrupole electro-optic deflector", submitted for publication in Applied Physics Letters (1998)

[257] J.J. Zayhowski and C. Dill, Opt. Lett., **19:18**, 1427 (1994)

[258] J.J. Zayhowski, Opt. Lett., **21**, 1229 (1996)

[259] J.J. Zayhowski, Opt. Lett., **22:3**, 169 (1997)

[260] J.J. Zayhowski, IEEE Photon. Tech. Lett., **9:7**, 925 (1997)

[261] J.J. Zayhowski, OSA Tech. Digest CLEO'97, Paper CWF1 (1997)

[262] Y. Bai, N. Wu, J. Zhang, J. Li, S. Li, J. Xu and P Deng, Appl. Opt., **36:12**, 2468 (1997)

[263] W. Chen, K. Sparosu and R. Stultz, Opt. Comm., **104**, 71 (1994)

[264] Y.K. Kuo, M.F. Huang and M. Birnbaum, J. Quantum Electron., **31**, 657 (1995)

[265] R. Moncorge, H. Manaa, F. Deghoul, Y. Guyot, Y. Kalisky, S.A. Pollack, E.V. Zharikov and M. Kokta, Opt. Comm., **132**, 279 (1996)

[266] S. Zhou, K.K. Lee and Y.C. Chen, Opt. Lett., **18**, 511 (1993)

[267] P. Wang, S-H. Zhou, K.K. Lee and Y.C. Chen, Opt. Comm., **114**, 439 (1995)

[268] G. Yao, S-H. Zhou, P. Wang, K.K. Lee and Y.C. Chen, Opt. Comm., **114**, 101

(1995)

[269] B. Braun, F.X. Kartner, U. Keller, J.P. Meyn and G. Huber, Opt. Lett., **21:6**, 405 (1996)

[270] B. Braun, F.X. Kartner, G. Zhang, M. Moser and U. Keller, Opt. Lett., **22:6**, 381 (1997)

[271] B. Braun, F.X. Kartner, G. Zhang, M. Moser and U. Keller, OSA Tech. Digest CLEO'97, Paper CThAA2 (1997)

[272] R. Fluck, B. Braun, E. Gini, H. Melchoir and U. Keller, Opt. Lett., **22:13**, 991 (1997)

[273] R. Hua, L. Qian, T. Zhi, X. Deng, Opt. Comm., **143**, 47 (1997)

[274] M.C. Marconi, O.E. Martinez and F.P. Diodati, Opt. Comm., **63**, 221 (1987)

[275] A. Szabo and R.A. Stein, J. Appl. Phys., **37**, 4953 (1965)

[276] J.J. Zayhowski and P.L. Kelley, J. Quantum Electron., **27**, 2220 (1991)

[277] J.J. Degnan, IEEE J. Quantum Electron., **31:11**, 1890 (1995)

[278] G. Xiao and M. Bass, IEEE J. Quantum Electron., **33:1**, 41 (1997)

[279] X. Zhang, S. Zhao, Q. Wang, Q. Zhang, L. Sun and S. Zhang, IEEE J. Quantum Electron., **33:12**, 2286 (1997)

[280] E. Munin, A.B. Villaverde, X.X. Zhang, and M. Bass, Appl. Phys. Lett., **63:13**, 1739 (1993)

[281] N.N. Ilichev, A.V. Kiryanov, P.P. Pashinin, V.A. Sandulenko, A.V. Sandulenko and S.M. Shpuga, Kvan. Elek., **22:12**, 1192 (1995)

[282] K.V. Yumashev, N.V. Kuleshov, A.M. Malyarevich, P.V. Prokoshin, V.G. Shcherbitsky, N.N. Posnov, V.P. Mikhailov and V.A. Sandulenko, J. Appl. Phys., **80:8**, 4782 (1996)

[283] V.P. Mikhailov, N.V. Kuleshov, N.I. Zhavoronkov, P.V. Prokoshin, K.V. Yumashev and V.A. Sandulenko, Opt. Materials, **2**, 267 (1993)

[284] K.V. Yumashev, N.V. Kuleshov, A.M. Malyarevich, P.V. Pzokoshin, V.G. Shcherbitsky, N.N. Posnov and V.A. Sandulenko, J. Appl. Phys., **80:8**, 4782 (1996)

[285] W. Rudolph and H. Weber, Opt. Comm., **34**, 491 (1980)

[286] R.S. Conroy, A.J. Kemp, G.J. Friel, B.D. Sinclair, Opt. Lett., **22:23**, 1781 (1997)

Chapter 5 - CW INTRACAVITY FREQUENCY DOUBLING OF Nd^{3+} TRANSITIONS

5.1 Introduction

In the last chapter we extended the concept of a microchip laser to a composite microchip cavity, by introducing a Q-switching element. This extended the range of operation for microchip lasers from the simple CW output of the monolithic devices described in Chapter Two, to the generation of short, high peak power pulses. This chapter describes how this range can be expanded to include other wavelengths, by replacing the Q-switch element with a nonlinear crystal to give frequency conversion.

In particular, we are interested in the process of frequency doubling. The three main Nd^{3+} transitions at 0.9, 1.06 and 1.3μm can be frequency doubled to the blue, green and red parts of the visible spectrum respectively. For miniature CW lasers, the most efficient up-conversion technique is generally intracavity frequency doubling of the fundamental laser wavelength. This can be achieved using a simple sandwich of the gain material and nonlinear material, coated appropriately. Here we report the operation of a red, green and blue microchip laser based on such a design.

Previously, if a visible laser was required large, inefficient gas lasers were used. Laser diodes can now operate in the red spectral region and are a common replacement for HeNe lasers. The progress of laser diodes to shorter wavelengths will eventually replace the shorter wavelength green and blue solid-state and gas lasers currently used in many applications. However there will always be a niche market for DPSSLs.

Many of the attractions of the monolithic microchip lasers, such as the possibility of single transverse and longitudinal mode operation, are maintained in composite devices. Therefore frequency doubled, solid-state lasers provide an attractive alternative to gas lasers, and provide competition in the marketplace after visible laser diodes become widely available.

This chapter will begin with a review of the theory of frequency conversion, and intracavity frequency doubling in particular. Possible schemes to provide doubling of the three main Nd^{3+} transitions will then be discussed, followed by the results of three

of these schemes to produce red, green and blue light from a microchip laser.

5.2 Frequency Conversion

The first half of this chapter will look at the concept of frequency conversion, and in particular intracavity frequency doubling. The basic theory will be considered, with reference to material properties, to determine suitable schemes for the frequency doubling of the 0.9, 1.06 and 1.3μm transitions in Nd^{3+} doped microchip lasers. Modelling of these schemes is then presented in the next section as a prelude to the experimental investigations in second half of this chapter.

5.2.1 Introduction to Frequency Conversion

The first experimental observation of frequency conversion using the nonlinearity of a material was made in 1961 when ultraviolet light, at twice the frequency of a ruby laser, was observed after propagation through a quartz crystal [287].

Before the invention of the laser, it was already known that ions in a lattice structure experienced an anharmonic potential in the local field of the lattice. An applied electric field, E, will induce a polarisation, P, in a suitable crystal, such that:

$$P = \varepsilon_0(\chi^{(1)}E + \chi^{(2)}E^2 + \chi^{(3)}E^3 + ...)$$

Equation 113

Where $\chi^{(1)}$ is the linear susceptibility and $\chi^{(2)}$ is the second-order nonlinear susceptibility and so on. Most processes are normally dominated by the linear first term because of the very small magnitude of the nonlinear susceptibilities ($\chi^{(1)}:\chi^{(2)} = 1:10^{-8}$). However, the invention of the laser gave a means by which the high intensities required to realise such nonlinear effects could be easily generated.

Nonlinear phenomena have been observed in all phases of matter, from solids to plasmas. Frequency conversion of solid-state lasers from the ultraviolet to the mid-infrared is commonly done using crystals. However only non-centrosymmetric (ones without unit cell inversion symmetry) crystals give rise to $\chi^{(2)}$ effects. To generate very high order nonlinear susceptibilities plasmas are regularly exploited using terrawatt pulses to generate the 40^{th} harmonic and higher [288].

As well as these elastic processes, where energy is conserved, there are inelastic nonlinear processes, such as stimulated Raman scattering and stimulated Brillouin

scattering, which can be used to alter the frequency of a beam of laser radiation.

Raman scattering is generally used effect to generate additional spectral lines below (Stokes) and above (Anti-Stokes) the frequency of the fundamental beam. The frequency shifts are determined by the electronic system and material in which the scattering occurs, and can range from several to several hundred nanometres. This material-dependent shift is a useful spectroscopic tool for the identification of liquids and gases.

Brillouin scattering is mostly commonly used in the realisation of phase conjugation, a third order nonlinear effect that makes wavefront reversal possible. It has a relatively small frequency shift (<1GHz) as scattering occurs from phonons rather than electron energy levels. Such scattering is often realised in hydrocarbon liquids, such as benzene and methanol.

Returning to elastic processes, the most commonly exploited nonlinearity is $c^{(2)}$, the second order nonlinearity, which can give rise to processes include frequency mixing and the Pockels effect. The nonlinear susceptibility tensor for $c^{(2)}$ processes can be expressed as:

$$P_i(\omega_3) = \varepsilon_0 \chi^{(2)}_{ijk} E_j(\omega_1) E_k(\omega_2)$$

Equation 114

where $\omega_3 = \omega_2 \pm \omega_1$, and i=x,y,z, j=x,y,z, k=x,y,z. This gives the second rank tensor, $c^{(2)}$, which contains twenty seven components to describe a material's nonlinearity, though many of these can be approximated to zero, or equal to or opposite in sign to other tensor elements because of symmetry in the material structure (Kleinman's Conjecture).

From Equation 114 it can be seen that sum and difference frequency mixing of two different frequencies to give a third is possible, given a suitable material. A special case exists, second harmonic generation, where $\omega_3 = 2\omega_1 = \omega_1 + \omega_1$. This is often the preferred means of generating alternative wavelengths, primarily because only two frequencies are involved, though sum and difference frequency mixing are also used to generate particular wavelengths of interest. Second harmonic generation, or frequency doubling, was choosen as the frequency up-conversion technique for this work and we will now consider it in more detail.

5.2.2 Frequency Doubling

If Maxwell's equations are solved for a coupled fundamental and second harmonic wave propagating in a nonlinear material, then the power generated in the second-harmonic wave is given by [289]:

$$P_{2w} = P_w \tanh^2\left[lK^{\frac{1}{2}}\left(\frac{P_w}{A}\right)^{\frac{1}{2}} \frac{\sin(\frac{\Delta kl}{2})}{(\frac{\Delta kl}{2})}\right]$$

Equation 115

where l is the length of the nonlinear material, A is the area and P_w is the power of the fundamental. Δk is the phase mismatch between the two propagating beams given by:

$$\Delta k = \frac{4\pi}{\lambda_w}\left(n_w - n_{2w}\right)$$

Equation 116

and

$$K = 2\eta^3\omega_w^2 d_{eff}^2$$

Equation 117

where η is the plane-wave impedance, ω_w is the frequency of the fundamental wave, and $d_{eff} = \varepsilon_0 c^{(2)}$ is the effective nonlinear coefficient for the direction of propagation from the second order nonlinear tensor. If a small signal approximation is made in the case of a material where there is phase matching (ie. $\Delta k=0$) and assuming relatively low conversion efficiencies then Equation 115 becomes:

$$P_{2w} = l^2 K \frac{P_w^2}{A}$$

Equation 118

Therefore, to a first approximation, the conversion efficiency from the fundamental to the second harmonic is dependent on the square of the intensity of the fundamental, the effective nonlinearity of the material and the interaction length. These parameters will be important, along with practical considerations such as easily achieving a phase matching condition and material transparency, in determining suitable materials for use in a frequency doubled laser.

5.2.3 Phase Matching Schemes

To achieve efficient conversion it is necessary to 'phase match' or 'index match' the fundamental and second harmonic waves. That is to say, the phase velocities of the fundamental and second harmonic waves need to be matched, to make Equation 116 equal to 0. If the waves are not phase matched, then a sinusoidal variation in the second harmonic intensity arises from Equation 115, as back-conversion of the second harmonic takes place as the waves move into anti-phase. The effect of phase matching is more clearly illustrated in Figure 101.

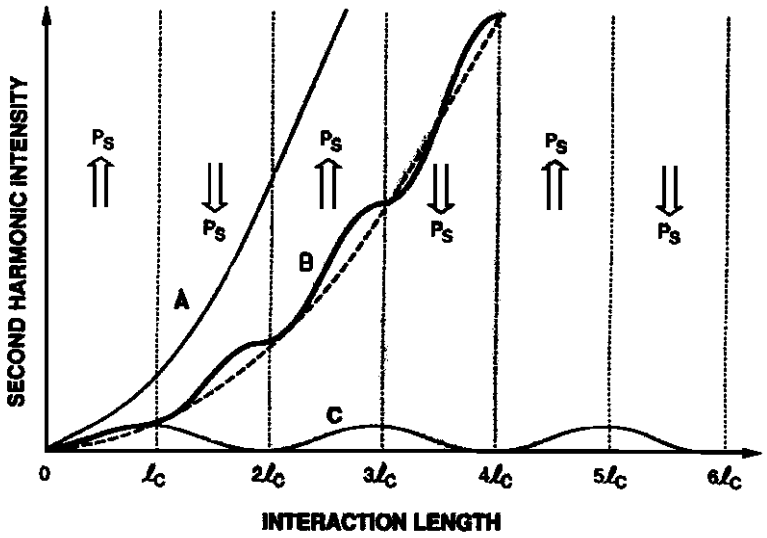

Figure 101 – Comparison of second harmonic conversion efficiency of (A) phase matched, (B) quasi-phase matched and (C) unphase matched systems [after 290]

Achieving phase matching can be a major problem. The refractive index of a material generally decreases with wavelength according to the Sellmeier equations, making phase matched schemes in isotropic materials impossible. However the birefringence of anisotropic crystals was quickly identified as a method to phase match the two wavelengths and has led to a wide variety of frequency conversion schemes.

An alternative technique, quasi phase matching, has been developed where the domain structure is reversed to avoid back-conversion of the second harmonic, though it has generally been impractical to implement until recently.

Both of these schemes are illustrated in Figure 101 along with the output from a non-phase-matched system. Birefringent and quasi phase matching will now be discussed in more detail to illustrate their relative merits and disadvantages.

5.2.3.1 Birefringent Phase Matching

The birefringence of biaxial or uniaxial crystals can be used to realise phase matching because of the different refractive indices along each crystal axis. If the fundamental frequency propagates through the crystal along a crystal axis of high refractive index, then its phase can be the same as the second harmonic propagating along an axis with lower refractive index. In this case the wavelength dependent refractive index of each axis can be used to achieve phase matching.

Two types of phase matching exist in uniaxial crystals:

1. **Type I** – fundamental propagates along extraordinary, (e) axis (positive crystal) or ordinary axis (o) (negative crystal), with the second harmonic generated in phase in the o axis (positive), or e axis (negative)
2. **Type II** – fundamental propagates along a combination of e and o axes, with the second harmonic generated along o axis (positive) or e axis (negative)

where a positive crystal is one where the refractive index of extraordinary axis is greater than that of the ordinary axis, and vice-versa for a negative crystal.

Phase matching schemes can also be realised by changing the propagation direction with respect to the crystal axes (critical phase matching). The special case where the phase matching angle is 90^o with respect to the optic axis is referred to as non-critical phase matching (NCPM) and is desirable. To achieve this special case, temperature tuning or an applied electric field can be used to vary the refractive indices experienced by the fundamental and second harmonic waves.

NCPM is desirable because the birefringence can lead to double refraction if the phase matching is accomplished at an angle other than along a crystal axis. For critical phase matching, the directions of Poynting vectors for the fundamental and second harmonic will have a small angular difference. For a negative type-I uniaxial crystal this 'walk off' angle is given as: [291]

$$\tan\psi = \frac{(n_1^0)^2}{2}\left(\frac{1}{(n_2^e)^2} - \frac{1}{(n_2^o)^2}\right)\sin 2\vartheta$$

Equation 119

where θ is the phase-matching angle with respect to the optic axis, n_1^0 is the refractive

index of the fundamental along the ordinary axis, n_2^e is the refractive index of the second harmonic along the fast e-axis and n_2^o is the refractive index of the second harmonic along the o-axis. For a weakly focused Gaussian beam, the distance over which the fundamental and second harmonic beams will separate, is given by:

$$l_a = w_0 \sqrt{\frac{\pi}{\psi}}$$

Equation 120

where w_0 is the minimum beam waist. Alternatively the walk off can be accounted for, to first order, by expressing the material constant to include the reduction due to walk off according to:

$$K_w = \frac{K}{\left(1 + \frac{l}{l_a}\right)}$$

Equation 121

where l is the length of the nonlinear crystal. Similar corrected equations can be derived for the angular and spectral acceptance bandwidths of a crystal as well as for other crystal types [289,291].

Thus a long crystal which is non-critically phase-matched but has a low d_{eff} can be as efficient as a much shorter crystal with a large d_{eff} in a critically phase matched geometry. The most desirable material for frequency doubling would be a suitably long nonlinear crystal with a high d_{eff} cut for non-critical phase matching. However other factors such as damage threshold, optical quality including absorption and scattering, thermal properties and acceptance bandwidths are additional important considerations.

The frequency doubled microchip lasers described in this chapter all use birefringent phase matching to give efficient conversion. Indeed, compared to quasi matching it is more efficient under ideal conditions as illustrated in Figure 101. However the scope of wavelengths that can be successfully phase matched by birefringent crystals with large nonlinear coefficients is limited. These shortcomings are part of the motivation behind the development of quasi phase matching.

5.2.3.2 Quasi Phase Matching

An alternative to using standard birefringent phase matching is to use quasi-phase matching (QPM). QPM was first suggested as a technique to compensate for refractive index dispersion in 1962 [292]. This technique is particularly attractive because it can be applied to isotropic materials and to anisotropic materials where interactions are not normally phase-matchable. The removal of this strict dependency has opened up a search for new, highly nonlinear materials, including organic materials and polymers, where large d_{eff} coefficients can now be easily accessed.

Figure 101 shows how QPM works. Curve A represents birefringent phase-matching, as outlined previous, and is dependent on the square of the interaction length. Curve C shows the periodic nature of conversion in a material without phase matching. However by modulating the sign of the nonlinear coefficient of a material at odd multiples of the coherence length l_c, $\left[l_c = \frac{\lambda}{2(n_{2w} - n_w)} \right]$, it is possible to achieve efficient coupling between the fundamental and second harmonic waves, although with a lower efficiency in comparison to equivalent birefringent phase-matching (curve B).

Several techniques have been developed for creating a periodic domain structure in materials. Poling of the material is possible at the growth stage and a number of groups have shown systems which rely on temperature changes or chemical changes to alter the domains [293,294].

A more reliable and common technique now is to grow a single domain crystal and pole it by depositing a metallic grating of the desired period on one side of the crystal and applying a pulsed high voltage between the grating and a floating electrode at the opposing crystal face. For example, in the case of $LiNbO_3$ an enhancement factor of $23N^2$ (where N is the number of domains) is possible by using d_{33} (which is normally not possible with birefringent phase matching) instead of d_{31} [295].

Periodically poled materials have only recently become commercially available and will revolutionise frequency conversion in the future, removing many of the problems associated with conventional birefringent phase matching. For the work in this chapter however we have used the more traditional birefringent materials and techniques because of the maturity of the technology behind their use and their

availability to operate at commonly used wavelengths.

5.3 Frequency Doubling

In the previous section we developed the idea of frequency conversion into frequency doubling and the conditions required for efficient doubling. We will now consider how efficient frequency doubling of a laser can be achieved using a nonlinear crystal.

There are a number of different schemes which can be used to frequency double the fundamental output of a laser, each with its own merits and disadvantages. The three most common techniques used are ‘single-pass doubling’, ‘resonant doubling’ and ‘intracavity doubling’. In this section a brief overview of the first two techniques will be given, with a more in-depth discussion of intracavity doubling, the technique used in the red, green and blue microchip lasers described in the second half of this chapter.

5.3.1 Single-Pass Frequency Doubling

Single-pass frequency doubling is where the fundamental wavelength of a laser is passed once through a nonlinear crystal outside the laser cavity. This technique is typically only used with short pulse, high peak power laser systems because of the high intensities required to give efficient conversion.

However it is the most attractive scheme for a number of reasons. There is no resonance cavity around the nonlinear crystal to cause alignment or resonance restrictions. The output is also produced in a single direction with the same geometric characteristics of the fundamental. Finally the laser and nonlinear crystal can be optimised independently for the most efficient operation in each case.

For example, using a Nd:YAG/Cr:YAG passively Q-switched microchip, it is possible to use a 5mm piece of KTP to frequency double the 18kW pulses at 1064nm to 532nm with 44% efficiency, and a further 5mm piece of BBO to double the 532nm, 8kW pulses to 266nm with 20% efficiency [296].

5.3.2 Resonance Cavity Frequency Doubling

For continuous wave lasers, the intensity of the output is not usually sufficient to

give efficient frequency doubling in a single pass scheme. However resonance of the fundamental in a cavity containing the nonlinear crystal can provide a higher circulating intensity, giving more efficient conversion.

This cavity can include the gain material, 'intracavity doubling', or a separate cavity containing only the nonlinear crystal, 'resonant doubling'. In the case of resonant doubling, as shown in Figure 102, the resonant frequency of the external cavity is locked to that of the fundamental laser by way of a feedback circuit.

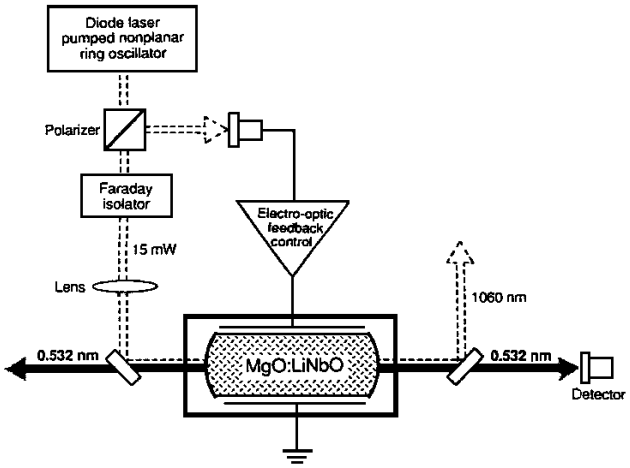

Figure 102 - Resonant Doubling in External Cavity (after [297])

This technique has the advantage of allowing the laser and nonlinear crystal to be optimised separately. However, for this scheme to work well, the locking of the two cavity frequencies must be well controlled and the fundamental laser has to be a single frequency. The complexity of the electronics involved would not be ideal for maintaining the compact, turn-key operation desirable from a frequency-doubled microchip, although it can give an efficient conversion to a single frequency output.

In the case of the experiment illustrated in Figure 102, the single frequency power from a MISER (Section 1.2.4.4) was doubled using MgO:$LiNbO_3$ in a resonant cavity. The frequency-doubled output again takes on the characteristics of the fundamental and gives a single transverse and longitudinal mode at 532nm. Potentially the output of the single frequency monolithic microchip lasers described in Chapter Two could also have been doubled in the same way.

MgO:$LiNbO_3$ is a common choice of nonlinear crystal in resonant cavities because its electro-optic properties can be used to alter the length, and hence resonant frequency of the cavity, as well as acting as the doubling crystal. KTP has been

successfully used as well [298,299]. Recently 1.1W of single frequency 532nm power was generated from a system similar to that shown in Figure 102, with a 89% conversion efficiency from 1064nm and a wall-plug efficiency of 9% [300].

5.3.3 Intracavity Frequency Doubling

Placing the nonlinear crystal inside the laser cavity removes the need for complex feedback electronics and potentially a much smaller and less complex laser can be constructed. These 'intracavity' frequency doubled lasers are the most attractive scheme for constructing a visible wavelength CW microchip laser, however their operation is also the most complex. This sub-section will explore these advantages and disadvantages and how the operation of such a laser can be modelled analytically.

5.3.3.1 Schemes for Intracavity Frequency Doubling

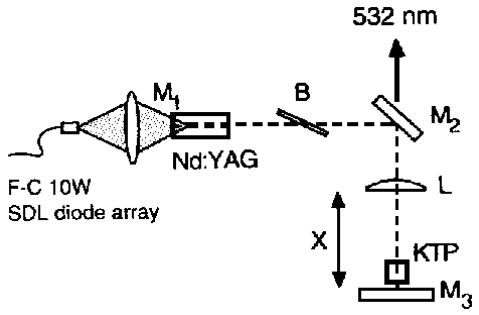

Figure 103 - Intracavity frequency doubling in a dog-leg cavity [after 301]

Figure 103 illustrates a typical large frame intracavity frequency doubled laser. A two-leg cavity geometry forms a high finesse cavity for the fundamental wavelength, 1064nm, between the mirrors M_1, M_2 and M_3. A Brewster-angled glass plate B is added to maintain the polarisation of the laser and correct for the polarisation rotation cause by the birefringent KTP at 45^o to the Nd:YAG crystal axes. The KTP crystal is placed in the focal region of the lens L near M_3 to maximise the 1064nm intensity in the crystal. M_3 is then coated to be highly reflecting at 532nm and M_2 to have minimal reflection, giving a green output in a single direction. This system produced more than 600mW in a linearly polarised, single longitudinal and transverse mode for 10W of pump power from a fibre coupled laser [301]. This and other DPSSLs have now been developed to give multi-watt outputs in the green, rivalling argon ion lasers, which are less efficient and bulky, with shorter operational lifetimes.

The nonlinear crystal can also be exploited as a Q-switch within the cavity to

provide intensity modulation as well as frequency conversion [302,303]. For 1W of pump power the device illustrated Figure 104 produced more than 100mW of 532nm power CW and pulses as short as 8ns with peak powers of 220W when Q-switched.

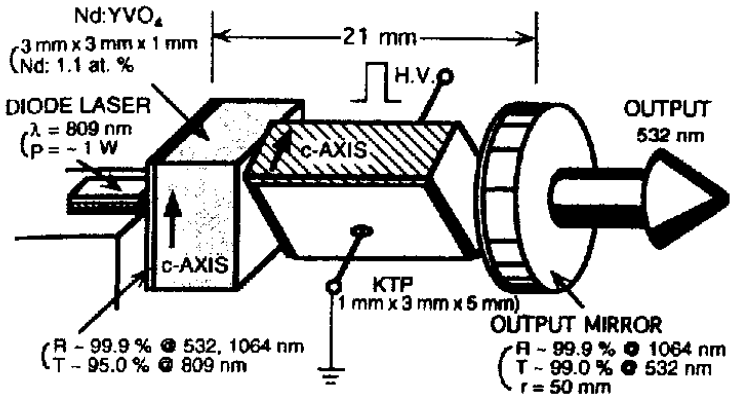

Figure 104 - Intracavity frequency doubling and Q-switching [after 303]

An alternative to having separate gain and nonlinear crystals, is to use a doped nonlinear crystal which can self-frequency double the lasing wavelength, allowing a monolithic device to be fabricated. Nd:YAB, $Nd,Sc_2O_3:LiNbO_3$ and $Nd:MgO:LiNbO_3$ have all been demonstrated as frequency doublers in a monolithic format or semi-monolithic with a discrete output coupler. $Nd:MgO:LiNbO_3$ was found to overcome the photorefractive damage associated with $LiNbO_3$ though lased in the wrong polarisation to exploit type I NCPM [304]. $Nd,Sc_2O_3:LiNbO_3$ overcomes this problem giving 11% conversion efficiency to 546nm from the pump wavelength [305]. 60mW of green power at 531nm has been realised from a Nd:YAB laser when pumped with an injection locked 1W diode representing a 20% optical conversion efficiency [306].

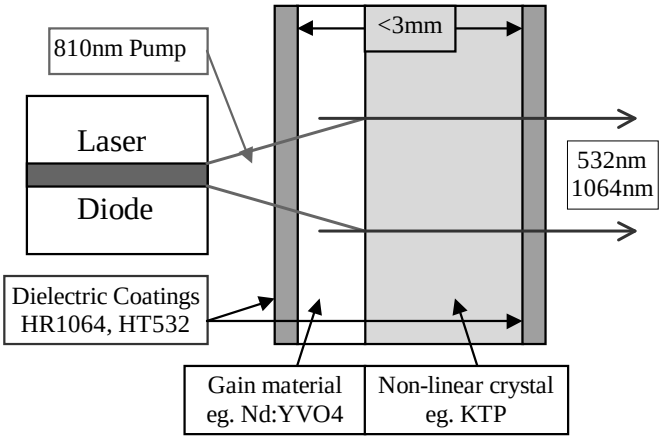

Figure 105 - Intracavity frequency doubled microchip laser

Figure 105 depicts the intracavity frequency-doubling scheme used in this chapter. The cavity is formed by placing a thin slice of gain material in intimate contact with a nonlinear material, either by means of direct contact or with index matching fluid, to minimise the reflectance and etaloning effect of the boundary between the materials. The two exterior faces of the device are then coated to be highly transmitting at the pump wavelength and the second harmonic, but highly reflecting at the fundamental wavelength. The doubled radiation is then emitted in both the forward and backward directions with no attempt to force it in one direction.

The 'sandwich' can then be pumped with an AlGaAs laser diode. The high reflecting surfaces produce an intense fundamental field within the device, of the order of $0.15 MWcm^{-2}$, which gives efficient second harmonic generation in the KTP crystal. The imperfections of not being able to produce a 100% reflective coating permits some of the fundamental to escape, producing an output composed of both fundamental and second harmonic wavelengths.

There are however a number of problems associated with this technique. Large amplitude fluctuations can occur because of the nonlinearity in the cavity and these will be discussed in more detail in a later sub-section. The second disadvantage is that the laser has to be optimised in conjunction with the nonlinear crystal. With careful planning however, both of these problems can be solved. To assist with this planning, a simple analytical model came be derived for the operation of these devices.

5.3.3.2 Theoretical Modelling of Intracavity Frequency Doubling

We will now consider the effect of including a nonlinear crystal within a laser cavity to generate the second harmonic. Intracavity frequency doubling is attractive for CW systems, to take advantage of the high intensity within the cavity.

Carrying forward the assumptions made in the preceding sections concerning the use of the small signal approximation, the intracavity frequency doubling of a microchip laser can be modelled by examining the loss and gain of such a laser. A number of other approximations are made to simplify the analysis. It is assumed that the laser gain is small such that $e^{2gl} \approx 1 + 2g_0 l$, that the output coupling is relatively small so that the intensity is approximately twice the circulating intensity $I \approx 2I_{cir}$, and that the beams propagating in the cavity are plane waves, with no variation in the beam intensity in the transverse plane. Although these assumptions are quite unreasonable

approximations, this analysis is beneficial as a first approximation and guidance for optimisation.

Following the approach of Smith [307], the steady-state intracavity intensity can be found by equating the round trip saturated gain to the linear and nonlinear losses:

$$\frac{2g_0 l}{1+\left(2I/I_0\right)} = \alpha - \ln(R_1 R_2) + 2KI$$

Equation 122

where $I_0 = \frac{h\upsilon}{\sigma_e \tau_f}$ is the saturation intensity and l is the length of the gain material, with α as the round trip linear loss factors, such as scattering and absorption, and R_1 and R_2 as the reflectivity of the mirrors forming the cavity. The nonlinear crystal provides an intensity dependent loss, 2KI, only half of which will be emitted in the forward direction. This is a potential disadvantage of intracavity frequency doubling, unless some attempt is made to couple the second harmonic out in only one direction.

The small signal gain, g_0, is defined as:

$$g_0 = \sigma_e \frac{\eta W_p}{\pi r_p^2 l} \tau_f$$

Equation 123

where σ_e is the emission cross section, η is the efficiency of the transition including the Stokes factor and quantum efficiency and W_p is the pumping rate in the laser mode volume, itself defined as $\pi r^2 l$. τ_f is the fluorescence lifetime of the lasing level. The nonlinear loss coefficient K is equal to:

$$K = \frac{2w_l^2 d_{eff}^2}{c^3 n^3 \varepsilon_0} l_{nlc}^2$$

Equation 124

where w_l is the frequency of the fundamental, n is the refractive index of the waves propagating in the nonlinear material and l_{nlc} is the crystal length.

If we group the linear losses together into a linear loss term L, and rearrange Equation 122 to determine the intracavity intensity I, solving the quadratic equation gives:

$$I=\begin{bmatrix} \frac{-1}{(8\cdot K)}\cdot\left(2\cdot L+2\cdot K\cdot I0+2\cdot\sqrt{L^2-2\cdot L\cdot K\cdot I0+K^2\cdot I0^2+8\cdot K\cdot g0\cdot I0}\right) \\ \frac{-1}{(8\cdot K)}\cdot\left(2\cdot L+2\cdot K\cdot I0-2\cdot\sqrt{L^2-2\cdot L\cdot K\cdot I0+K^2\cdot I0^2+8\cdot K\cdot g0\cdot I0}\right) \end{bmatrix}$$

Equation 125

The negative branch gives the real solutions for the intracavity intensity and these are modelled later for the laser systems described in the experimental half of this chapter using Mathcad. The second harmonic power can then be calculated using Equation 118. As can be seen from Equation 122 this power can be maximised by reducing the parasitic cavity losses to zero. In practice however, imperfect coatings will always limit the efficiency, especially for lasers where the nonlinear crystal has a low effective output coupling ($2KI \sim \alpha - \ln(R_1R_2)$). Additional intracavity elements will increase the parasitic losses, favouring the basic approach of a microchip design.

Smith showed that the optimum transmission of the output coupling from the nonlinear crystal for a intracavity doubled system is exactly the same as conventional mirror of an equivalent laser operating in the fundamental [307]:

$$T_{opt} = \sqrt{2g_0 lL} - L$$

Equation 126

and thus the maximum power available in the second harmonic can be expected to be the same as for the laser operating only in the fundamental when the optimum output coupling is used. Therefore knowing the optimal output coupling of the cavity without the nonlinear crystal, it is possible to choose the length of second harmonic crystal required, maximising the second harmonic power.

5.3.3.3 'Green Noise Problem'

There is however a drawback to intracavity frequency doubling. There are a number of possible mechanisms through which the output of an intracavity-doubled laser can be undesirably modulated. The most common mechanism and potentially the most serious in a microchip device is due to longitudinal mode coupling through the gain and nonlinear crystals and is often referred to as the 'green noise problem'.

The 'green noise problem' was first described by Baer for a CW intracavity frequency doubled Nd:YAG laser in 1986 [308]. His use of a laser diode to end-pump a short cavity aided his observations. This is because with a very long cavity, there

are many longitudinal modes present and although coupling does occur between individual modes, this does not drastically effect the overall output. In contrast very short cavities, with only one longitudinal mode, by their nature do not exhibit this type of noise. However in cavities where only a few (2-~10) longitudinal modes are present, fluctuations in the intensities of the modes caused by coupling effects can have a significantly effect on the overall output as observed by Baer. These fluctuations can be very significant, up to several times the normal CW intensity, and are therefore very undesirable.

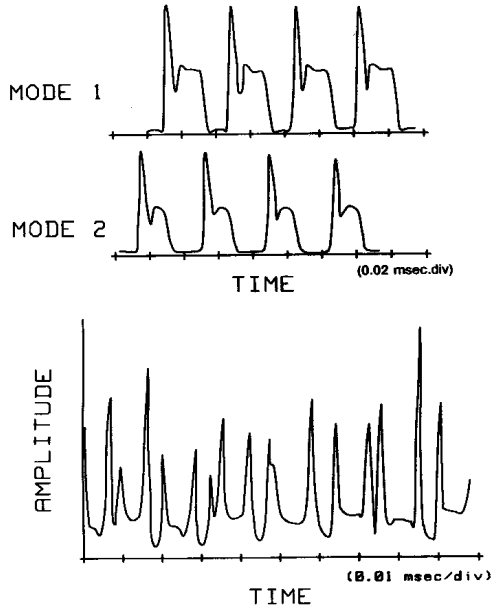

Figure 106 - 'Green Noise Problem' – coupling between longitudinal modes 1&2 through the nonlinear crystal can cause large amplitude fluctuations in the output of an intracavity frequency doubled laser [after 308]

The lower trace in Figure 106 shows a sample of the modulated output power from the laser used by Baer. The upper traces reflect the amplitude fluctuations observed in each of the two longitudinal modes present if considered independently. The coupling between the longitudinal modes arises because some nonlinear crystals, such as KTP, have large spectral acceptances. Oscillation occurs when there are two or more nonlinear output couplings present in combination with cross-saturation of the gain through spatial hole burning. Solving the time-dependent rate equations to include these processes produces theoretical results in agreement with experimental observations in Figure 106. Further work has shown this form of nonlinear mode coupling only occurs for longitudinal modes in particular polarisation states [309].

A number of methods have been developed to minimise the ‘green noise problem’: through increased rejection of undersirable cavity eigen-modes or by forcing a laser to operate on a single longitudinal mode. These including the use of an intracavity quarter-wave plate [309], a Brewster plate [310], accurate alignment of gain and nonlinear crystals [311], the use of the gain material as a polarising element [312], and the use of shorter highly doped gain crystals and shorter nonlinear crystals [313].

For isotropic gain materials polarisation instability can lead to large jumps in the output over periods range from seconds to minutes. Therefore if a highly anisotropic gain material cannot be used, often a waveplating configuration, to achieve polarisation discrimination, or brewster angled surfaces are included to minimise these effects.

Hopping, or tuning of the longitudinal mode structure can also cause instability in the output. This can be caused by drift in the pump intensity or wavelength, or environmental conditions changing. This is generally not a problem, though if the gain material has more than a single terminating level for the lasing transition, such as in Nd:YAG this can be problematic with more than one transition reaching threshold. Wavelength selective elements and stabilisation of the pumping laser and environmental conditions can help to minimise these forms of fluctuation.

Back reflection of second harmonic light into the cavity is a further form of instability identified by Anthon [314]. This reflection can come from both surfaces outside and inside the cavity and interferes with light being generated by the nonlinear process producing power fluctuations of several percent.

In summary there are a number of mechanisms that can contribute to the instability of an intracavity frequency-doubled laser, the most serious of which is mode-coupling for the devices investigated here. These can however be minimised through careful design and operation.

5.3.4 Conclusion

In this section we have explored three frequency-doubling schemes, of which intracavity frequency doubling provides the most attractive scheme for an efficient, visible CW microchip laser. A simple analytical model has been described which will be used in the next section to investigate the expected operation of our red, green and

blue microchip lasers. The origin of intensity noise in intracavity frequency doubled lasers has also been considered, with solutions to how it can be minimised.

In the next section we will consider the criteria for the selection of laser gain materials and nonlinear crystals used to construct our red, green and blue microchip lasers. The operation of these microchip lasers will then be described.

5.4 Intracavity Frequency Doubled Microchip Lasers

The materials used for this work were chosen carefully for their commercial availability and maturity with good lasing and frequency conversion properties, while maintaining a diode-pumped microchip geometry and environment. Table 15 outlines some of the major properties of the crystals used.

Transition	**946-> 473nm**	**1064->532nm**	**1342->671nm**
Laser Crystal	Nd:YAG [315]	Nd:YVO_4 [316]	Nd:YVO_4 [316]
Emission X-Section (cm^{-19})	0.51	15.6	5.88
Fluorescence Lifetime (μs)	255 (1%)	110 (1%) 57 (3%)	110 (1%) 57 (3%)
Refractive Index	1.82	2.17	2.17
Absorption Coefficient for 1% doping @ 810nm (mm^{-1})	0.85	4.07	4.07
Nonlinear Crystal	$KNbO_3$	KTP [289]	LBO [317]
Phase Matching Condition	Type I CPM	Type II CPM	Type II NCPM
Phase Matching Angle	41^o	24.3^o	90^o
Operating Temperature (^oC)	40-45	25	35-40
Mohs Hardness	4.5	5.5	5.3
Refractive Index	2.2	1.75	1.6
Absorption at Fundamental Wavelength (cm^{-1})	-	0.01	0.005
d (pm/V)	$d_{31} = 16.4$ $d_{32} = 20.5$	$d_{24} = 3.3$ $d_{15} = 2.6$	$d_{31} = 1.05$ $d_{32} = 0.98$
Acceptance Angle (mrad cm)	47	25	>70
Temperature Acceptance (^oC cm)	0.6	25	6.7
Spectral Acceptance (nm cm)	0.23	0.56	0.75

Walk Off Angle	1.02^o	0.26^o	0^o
Damage Threshold ($GWcm^{-2}$)	0.35	0.5	2.5

Table 15 - Properties of Crystals for Frequency Doubling Nd^{3+} Transitions

The gain materials used, Nd:YAG and Nd:YVO_4, are both commonly used in monolithic and composite microchip laser systems and have a proven track record as laser gain materials. Nd:YVO_4 offers a high stimulated emission cross section and high absorption coefficient, combined with a broad absorption band around 810nm, making it very amenable to diode pumping. Chapter two of this thesis outlined the excellent lasing properties of Nd:YVO_4 at 1064nm and 1342nm including high efficiencies and low thresholds with a strongly polarised output.

The nonlinear crystals, potassium niobate ($KNbO_3$), potassium titanyl phosphate (KTP) and lithium triborate (LBO) again are commonly used materials, which have been well characterised for frequency doubling. We will now consider the choice of these materials for our red, green and blue microchip lasers, with comment on possible alternatives. The modelling of our chosen materials, using the equations derived in the previous section, will also be considered to give an indication of expected operation.

5.4.1.1 Green Microchip Laser – Nd:YVO_4 & KTP

For a diode-pumped, frequency-doubled, green microchip laser, Nd:YVO_4 represents an almost ideal gain material. The broad and strong absorption band at 810nm allows efficient diode pumping of sub-millimetre sized crystals. The intense, well-polarised emission gives excellent operation at 1064nm for monolithic microchip lasers, as described in Chapter Two. Although Nd:YAG has been successfully used in higher power frequency doubled lasers, an intracavity polarising element is required to give polarised operation and stop mode hopping. In addition, larger crystals and more careful pump control are required because Nd:YAG has a narrower and weaker absorption band at 810nm, when compared with Nd:YVO_4.

Potassium titanyl phosphate (KTP) is an attractive and commonly used nonlinear material for frequency doubling the 1064nm transition of Nd^{3+} doped materials. Indeed, up to 80% conversion efficiency from 1064nm to 532nm has been reported using KTP in an externally resonant cavity [318].

The wide spectral and thermal acceptance windows make KTP particularly suitable

in a microchip environment because active temperature or frequency control is not required. In addition, the useful nonlinear coefficient (d_{eff} = 3.2pm/V) can give efficient doubling for relatively short crystals (<5mm). Mechanically, it is attractive because it can be easily polished and has stable ferroelectric domains making fabrication and coating relatively easy (in contrast to $KNbO_3$).

Critical phase matching of KTP is possible over the range 0.99-1.08μm in the x-y plane and over the range 1.1-3.4μm for material cut in the x-z plane. Normally for the doubling of 1064nm radiation, KTP is cut at 24^o to the optical axis in the x-z plane to give type II critical birefringent phase matching at room temperature along the x-y plane. Doping can also allow type II non-critical phase matching at room temperature. In addition to frequency doubling, KTP cut in the x-z plane has been used successfully used in OPO systems to provide tuning into the mid-infrared [319].

There are two main limitations to the use of KTP, especially in higher power systems. The first is the effect of grey-tracking which arises because of the alteration of the crystalline structure from absorption of the laser radiation. These regions cannot then be used for efficient doubling. Improved growing techniques and post-growth annealing has reduced this effect, though the problem still limits the scalability of KTP-based systems. The other major drawback of KTP is the relatively large walk-off angle between the Poynting vectors of the fundamental and second harmonic. This walk-off angle (0.26^o) effectively limits the length over which second harmonic generation can take place to approximately 15mm. In our case neither of these limitations effect the operation of our laser because of the relatively low powers and short crystals used.

For high power systems, the main alternative to using KTP is lithium triborate (LBO). Although it has a much lower nonlinear coefficient (d_{eff} =1.16), with heating to around 130^{o}C it is possible to NCPM LBO in a type II geometry for frequency doubling of 1064nm. Therefore longer crystals can be used without loss in efficiency. In addition there are no problems with grey-tracking and LBO has a large damage threshold. Several commercial systems now employ LBO as the nonlinear material to produce several watts of CW green power with conversion efficiencies greater than 40%.

A second alternative to KTP is lithium niobate ($LiNbO_3$), a commonly used

nonlinear material, in particular for acousto-optical and electro-optical devices. The use of $LiNbO_3$ has been limited by photorefractive damage when exposed to green or shorter wavelength light and therefore it is generally doped with MgO to prevent this problem. It is also possible to dope it sufficiently to achieve type I NCPM at room temperature for frequency doubling of 1064nm, though generally it is achieved around 100°C (5% MgO) to help prevent photorefractive damage. It has a large d_{eff}=4.7pm/V making it attractive, however a relatively low damage threshold and large thermo-optical coefficients, leading to strong and asymmetric thermal lensing, have limited its wide-spread use. The electro-optic properties of $LiNbO_3$ makes external resonant cavities possible using feedback to the crystal to maintain resonance. In this way conversion efficiencies of more than 65% have been achieved [297].

However the low nonlinear coefficient of LBO and the damage problems of $LiNbO_3$, with the preference for high temperature operation of both of these materials, make them unsuitable as a nonlinear material in a green microchip laser. Therefore it was decided to use a combination of Nd:YVO_4 and KTP for our green microchip lasers.

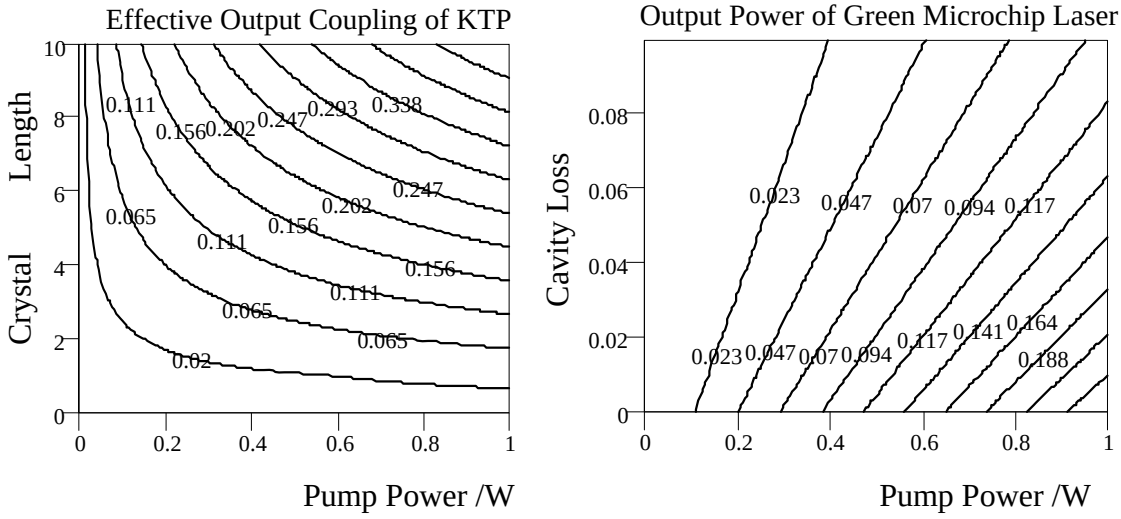

Figure 107 - Optimisation of green microchip laser. The a) effective output coupling (fraction) of the KTP (increasing pump power [watts] along x-axis, crystal length [mm] along y-axis) and b) output power (watts) of green microchip laser in a single direction plotted as function of increasing pump power (watts along x-axis) and fractional cavity loss (along y-axis).

Figure 107 shows the operating characteristics of a green device, based on the equations derived in the previous section. The optimal output coupling for a monolithic Nd:YVO_4 microchip laser at 1064nm is approximately 15%, and therefore

from Figure 107a) a 3-4mm long crystal of KTP would maximise output. However, to maintain a smaller geometry and reduce any extra parasitic losses, a 2mm long crystal was used.

The expected output power in a single direction of this 2mm long KTP crystal, in combination with a 0.5mm long 3% doped Nd:YVO_4 crystal is shown in Figure 107b). This combination is relatively insensitive to increasing parasitic loss (y-axis) and is expected to give good conversion efficiencies, with up to 250mW of green light produced in the forward direction for 1W of pump power.

5.4.1.2 Blue Microchip Laser – Nd:YAG & $KNbO_3$

One major drawback of Nd:YVO_4 however is that it has very poor lasing performance for the 916nm transition, because the terminating level for the transition is very close to the ground state ($439cm^{-1}$) giving a significant thermal population. Instead, Nd:YAG was chosen as the gain material in our blue microchip lasers.

Nd:YAG has a higher terminating level ($848cm^{-1}$) than Nd:YVO_4 and most other Nd^{3+} doped materials, leading to fewer problems with reabsorption at the fundamental wavelength and a lower thermal population in the terminating level. The better thermal properties and lower absorption coefficient of Nd:YAG around 810nm also equate to a lower temperature rise in the pumped region, making cooling less critical. Combined with the strongest emission characteristics of any Nd^{3+} doped materials, Nd:YAG is by far the most efficient material working on this transition, with efficiencies in excess of 50% and thresholds of less than 50mW [320].

There are however a number of problems with Nd:YAG as the gain material in a frequency doubled microchip laser, as mentioned earlier. The absorption band at 810nm is weaker and narrower than for Nd:YVO_4, requiring careful control of the pumping laser diode wavelength and longer crystal lengths. In addition, the output of a Nd:YAG laser is typically not polarised, because of its isotropic crystal structure. In a microchip laser, no polarisation control is possible and so unpolarised emission can be a significant disadvantage giving lower than expected conversion efficiencies because the laser can lase in a non-phase-matched polarisation.

Two of the materials described in Chapter Two could provide an alternative to Nd:YAG and address these problems. Nd:YOS has good diode-pumping characteristics and gives a polarised output around 912nm with the advantage of

ground-state depletion reducing the population in the terminating laser level. However for a microchip laser, the low doping concentrations available and the low stimulated emission cross-section would create a new set of problems to be addressed. Nd:SFAP has better pumping and absorption characteristics with a polarised output at 945nm and a stimulated emission cross section half that of Nd:YAG. Unfortunately it has much worse thermal characteristics, which would give large temperatures in the pumped region, giving a significant thermal populations in the terminating level. Therefore Nd:YAG was chosen as the gain material.

Potassium niobate ($KNbO_3$) is a very attractive nonlinear material because of its large nonlinear coefficient (d_{eff} = 17pm/V) which can give low threshold operation, from short crystals. It is a biaxial crystal, classified as an orthorhombic crystal with a mm2 point-group symmetry, and has a transparency range from 0.4-5μm with birefringent phase matching for second harmonic generation possible over much of this range [321]. For 946nm, type I critical birefringent phase matching can be achieved around room temperature at an angle of ~40-50^o to the a-axis, with the second harmonic generated along the c axis. If the crystal is heated to approximately 180^{o}C, then type I NCPM phase matching is possible along the same axes [322]. However depoling of $KNbO_3$ into multiple ferroeletric domains is common under slight stress and/or temperature cycling, and limits the conditions under which it can be used [323]. Care also has to be taken because there is a phase change around 223^{o}C.

The optical properties of $KNbO_3$ would also give both critical and non-critical phase matching at 1064nm and critical phase matching at 1342nm. However the difficulties in using this material, and the availability of other nonlinear materials, albeit with lower nonlinear coefficients, lead us to only consider it for use in the blue microchip lasers.

The good nonlinear coefficient is offset by the poor mechanical and thermal properties of $KNbO_3$, which make it difficult to fabricate, polish and operate. In addition, the relative large walk off angle (1.02^o), and the rather small angular, spectral and temperature acceptance ranges require careful environmental and system control and the use of short crystals. These properties do however allow a wide range of phase matching conditions to be met, and $KNbO_3$ is one of the few birefringent materials to give phase-matching for 946nm and efficient blue generation

[324,325,326,327].

Although KTP has been used to sum frequency mix the 1064nm output of a Nd^{3+} laser and the 810nm pump radiation to give 459nm [328], birefringent phase matching of the 946nm line is not possible using the same crystal axis. It can be cut for type I CPM with a phase matching angle of 53^o to x-y plane, but with an effective nonlinear coefficient of only 0.72pm/V. Similarly, light at 447nm has been generated using $LiIO_3$ by tripling the output of a 1341nm Nd:YAP laser [329], although again no birefringent phase matching is possible for doubling 946nm. Early work did use KDP as a frequency doubling material [330], however its hygroscopic nature and low nonlinear coefficient would not be suitable in a microchip geometry. Three possible geometries in LBO would give type I or type II critical phase-matching and type I NCPM of 946nm radiation, though these have not been explored yet. BBO is also an alternative for doubling 946nm with type I or type II CPM at phase matching angles of 25^o and 35^o respectively with a larger nonlinear coefficient (d_{eff} =2.2pm/V).

The most likely replacements of $KNbO_3$ as a frequency doubling materials for 946nm are periodically poled materials. Periodically poled lithium niobate (PPLN) has already been successfully demonstrated to give 50mW of CW blue light from a Nd:YAG laser, with single pass conversion efficiencies of 4.6% [331].

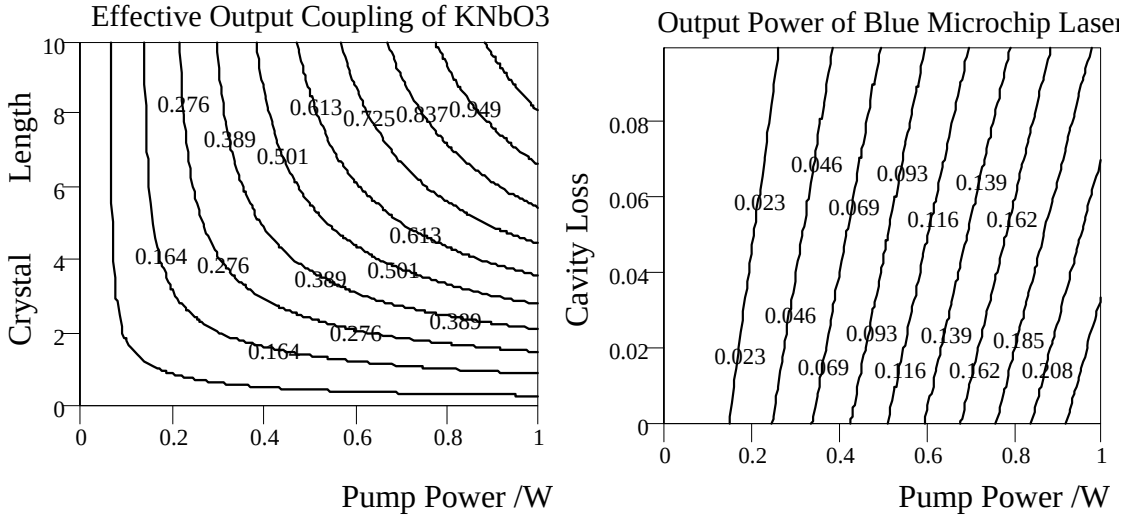

Figure 108 - Optimisation of blue microchip laser. The a) effective output coupling (fraction) of the $KNbO_3$ (increasing pump power [watts] along x-axis, crystal length [mm] along y-axis) and b) output power (watts) of blue microchip laser in a single direction plotted as function of increasing pump power (watts along x-axis) and fractional cavity loss (along y-axis).

Figure 108a) shows how the effective output coupling of a $KNbO_3$ crystal in a blue microchip laser varies with pump power (x–axis) and length (y-axis). The optimal output coupling of a 946nm laser is typically around 5% and therefore a crystal of ~1mm is sufficient to give optimal performance. Figure 108b) shows the expected output power in a single direction for a blue microchip laser composed of a 1mm long piece of Nd:YAG and 1.5mm long piece of $KNbO_3$ with increasing pump power (x-axis) and cavity losses (y-axis). Therefore similar performance to the green laser is expected, assuming the blue device is a four-level system with good absorption characteristics and coatings and a polarised output. However a narrow operating window can be expected because of the characteristics of $KNbO_3$.

5.4.1.3 Red Microchip Laser – Nd:YVO_4 & LBO

The third and final frequency doubled microchip laser was designed to double the 1.3μm Nd^{3+} transition to give a red output. As for the green device, neodymium doped yttrium vanadate was chosen as the gain material because of the excellent operating characteristics of the 1342nm monolithic microchip lasers described in Chapter Two.

Although monolithic Nd:YAG microchip lasers have been demonstrated at 1320nm [332], the cross-section of the 1320nm transition in Nd:YAG is approximately $1/6^{th}$ that of the 1342nm transition in Nd:YVO_4 and the output is unpolarised. Combined with its poorer absorption properties, Nd:YAG is a less suitable gain material. Of the other materials examined in Chapter Two, Nd:SFAP potentially could offer performance to rival that of Nd:YVO_4 at 1.3μm. Previous work has shown slope efficiencies of 46% from Nd:SFAP at 1328nm with a strongly polarised output, though with a lower emission cross-section and at lower doping concentrations than Nd:YVO_4 [333]. Therefore Nd:YVO_4 was chosen as the gain material for our red laser.

Lithium triborate (LBO) is a moderately nonlinear material (d_{eff} = 1.02pm/V) with very low angular sensitivity and broad transparency range (0.16-2.6μm). It is a negative biaxial crystal, of orthorhombic structure and mm2 point group symmetry. The triborate structure gives a crystal almost free of inclusions, with good mechanical properties and a very high damage threshold.

Along the x-axis type I non-critical phase-matching is possible in LBO over the

range 900-1700nm with temperature tuning from -50^{o}C-300^{o}C. For the doubling of 1342nm the temperature required for type I NCPM is -5^{o}C. Such a device would need to be hermetically sealed and carefully environmentally controlled, negating some of the advantages of a microchip laser. Along the z-axis however type II NCPM is possible over the range 1100-1500nm with temperature tuning from -50^{o}C-50^{o}C. At 1342nm this corresponds to a temperature of 37^{o}C allowing a practical device to be constructed using a thermoelectric cooler to heat the laser sufficiently above room temperature.

There are two disadvantages with using LBO in a microchip geometry. The greatly varying thermal expansion coefficients in each optical plane (x=10.8 y=-8.8 z=3.4 x10^{-5} K^{-1}) makes LBO difficult to coat directly other than with simple anti-reflection coatings. Combined with the large and negative thermo-optical coefficients, the thermal expansion can lead to significant thermal distortion in the cavity if there is an appreciable thermal gradient in the crystal. Both of these prevent LBO being used coupled directly to the gain crystal with a high reflecting coating on one face to form the microchip laser, as for the green and blue devices.

The second disadvantage arises from the relatively low nonlinear coefficient providing low coupling into the second harmonic. Therefore for efficient operation, in cavities with large parasitic losses, a long crystal would be required.

An alternative to LBO is to use KTP, which can be cut for type II CPM doubling of 1.3μm radiation. The large phase matching angle of 60^{o} leads to a walk-off angle of 2.5^{o}, though it has a larger d_{eff} =2.8pm/V. A second alternative, and one not considered previous to this work, is to use MgO:$LiNbO_3$ which can be cut for CPM at 1342nm with at an angle of 56^{o} accessing a nonlinearity of d_{eff} =5.7pm/V. Walk-off is lower than for KTP and efficiency would not be compromised in a 2mm long crystal. A final alternative would be BBO, which could be cut for either type I or type II critical phase matching. However LBO was chosen because of its previous use for doubling 1.3μm, and the type II NCPM geometry.

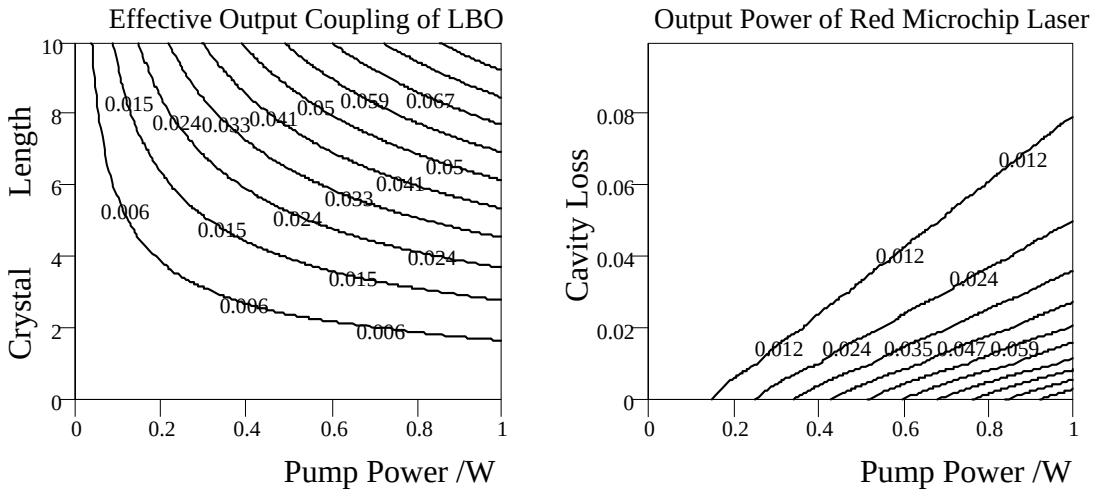

Figure 109 - Optimisation of red microchip laser. The a) effective output coupling (fraction) of the LBO (increasing pump power [watts] along x-axis, crystal length [mm] along y-axis) and b) output power (watts) of green microchip laser in a single direction plotted as function of increasing pump power (watts along x-axis) and fractional cavity loss (along y-axis).

Figure 109a) shows how the effective output coupling of a LBP crystal in a red microchip laser varies with pump power (x-axis) and length (y-axis). The optimal output coupling for a 1342nm Nd:YVO_4 monolithic laser is ~10%, requiring a crystal of ~15mm, impractical for a microchip laser. Figure 109b) shows the predicted performance of our red device composed of a 2mm long LBO crystal and 0.5mm 1% doped Nd:YVO_4 crystal and a high reflecting mirror with increasing pump power (x axis) and cavity losses (y-axis). As can be seen the output power is approximately half that of the blue and green devices with a rapid fall off with increasing cavity loss. Therefore the red device is expected to have the lowest output powers of our visible microchip lasers and care is required to minimise the parasitic cavity losses.

In this section the selection of gain and nonlinear crystals for red, green and blue microchip lasers have been considered. For the green microchip laser a combination of Nd:YVO_4 and KTP was chosen, offering potentially the most efficient operation of the three frequency-doubled devices because of the good operating characteristics of both materials. The wide bandwidth of KTP does not place any limitations on the operating conditions of these lasers, and the only major concern is from the possibility of ‘green noise’.

In the case of the blue microchip laser, a sandwich of Nd:YAG and $KNbO_3$ was chosen. Potentially the operation of this laser can match that of the green laser,

however the performance is likely to be limited by one of a number of factors. The Nd:YAG is a naturally unpolarised material, therefore efficient operation will be limited to areas where the crystal is stressed in the correct orientation to give a polarised output which can be efficiently doubled. The difficulty in diode-pumping a short Nd:YAG crystal and the quality of the coatings will also limit the performance. The operating environment has also to be tightly controlled because of the small acceptance parameters of the nonlinear crystal and its sensitivity to thermal effects.

The red microchip laser design chosen was a combination of Nd:YVO_4 and LBO. This laser is not expected to operate as well as the first two because of the low nonlinear coefficient of LBO and the short crystal length chosen. The sensitivity to parasitic cavity losses is also of concern, partly because of the additional intracavity surfaces, and hence losses, due to not being able to apply a high reflecting coating to the LBO crystal. However its operating environment is expected to be less constrictive than for the blue device.

We will now consider the experimental operation of these three visible microchip laser schemes. The most developed of these systems, the green laser will be considered first, followed by the blue laser and finally the red laser.

5.5 Intracavity Doubling of 1064nm Transition in Nd:YVO_4

5.5.1 Introduction and Motivation

The 1064nm is the strongest transition of the Nd^{3+} ion from the $^4S_{3/2}$ metastable level and was the first observed to lase. A discussion of the historical development and the use of this transition in solid state lasers, and in particular monolithic microchip lasers, was given in Chapter One and Chapter Two of this thesis.

Frequency doubling of the 1μm transition is the most commonly reported frequency conversion, using many different and novel techniques and materials. The first and subsequent frequency-doubled microchip lasers, other than the ones reported by our group and discussed in the following sections, have been based on this transition.

The first intracavity frequency-doubled microchip laser was reported in 1990 using a close-coupled cube of LNP, 0.5mm long, and a 0.5mm long KTP crystal, giving 2.5mW at 523nm and 526nm for 200mW of pump power [334,335]. The following

year the first Nd:YVO_4 and KTP combination was reported by Sasaki et al. giving 221mW of 1064nm and 16mW of 532nm for 1W of diode pump power [336]. Our group in St.Andrews reported 50mW of green power from the same material combination using a 0.5W laser diode in 1993 [337], and subsequently 220mW using a 1.2W laser diode, representing a conversion efficiency approaching 40% [319]. Recently Huber's group in Hamburg have reported 1.2W of multi-transverse mode green power from a Nd:LSB/KTP system similar in size to a microchip, pumped by a 10W pigtail fibre diode, giving 26% conversion efficiency from the pump power [338].

Many commercially produced miniature green lasers are now available with improved performance with output powers up to 100mW. Such devices have been investigated for use in digital video disc technology [339], though there is an expectation that blue diodes will be the basis of the next generation of optical storage devices because of their lower unit cost.

In this section the operating characteristics of the fourth generation of green microchip devices is discussed. Each successive iteration of device has given improved operation, as can be seen from a comparison of the results given here with work on the first and second generations devices reported by MacKinnon [340].

5.5.2 CW Lasing Performance

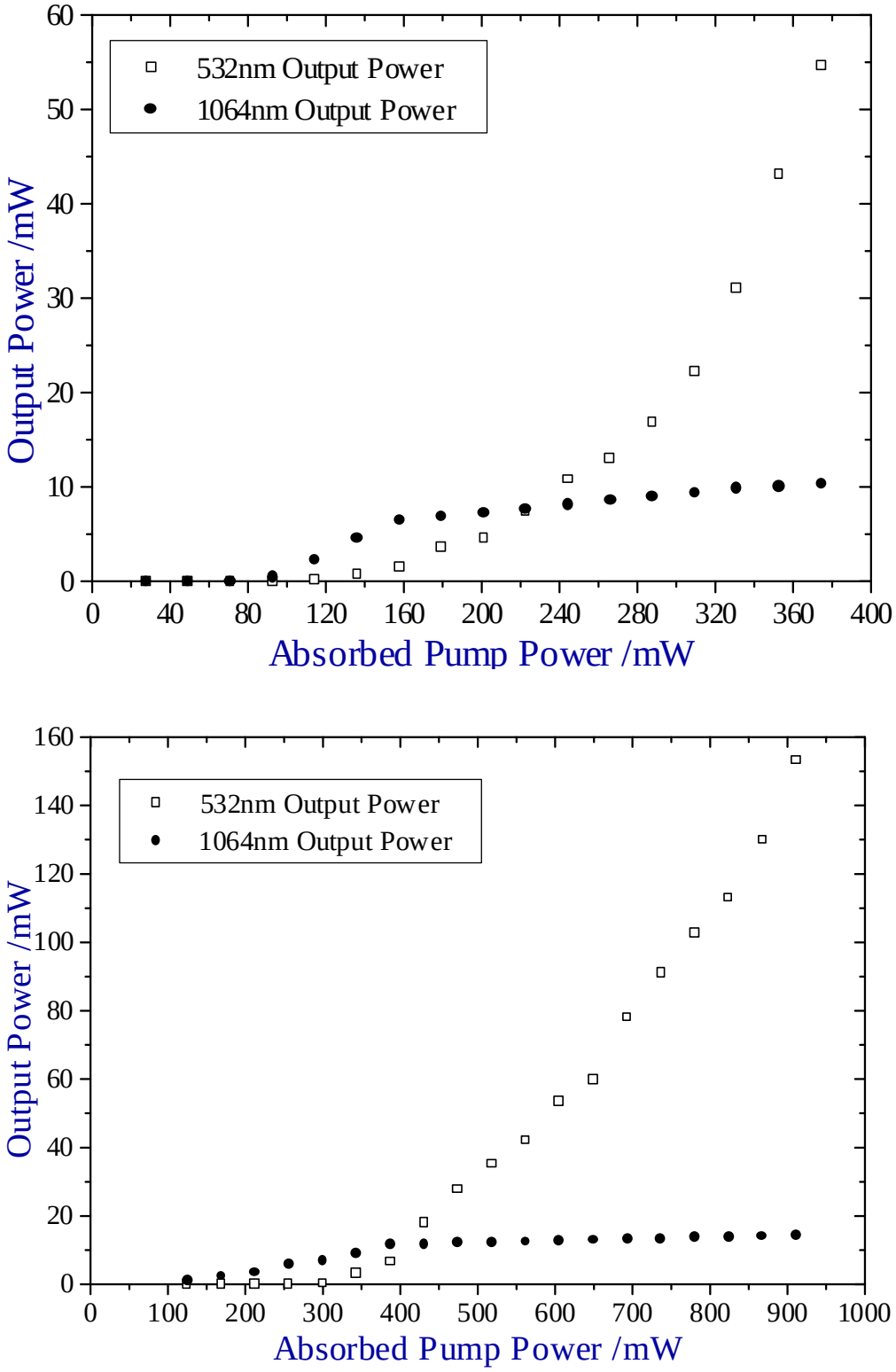

Figure 110 - Green and infrared power from green microchip laser, composed of a 0.5mm long 3% doped Nd:YVO_4 and 2mm long KTP, pumped by a) 0.5W b) 1.2W laser diode, through an 8mm collimating lens and 8mm focussing lens.

These green lasers, as with the earlier devices, were constructed from a 0.5mm long

piece of Nd:YVO_4 doped with 3% Nd^{3+} in intimate contact with a 2mm long piece of KTP cut for critical phase matching of 1064nm radiation at room temperature. The output from a 0.5W or a 1.2W laser diode was imaged into these microchip lasers using an 8mm collimating lens and 8mm focussing lens to provide a pump source. The green microchip lasers absorbed 97.4% of the incident diode pump light with 0.8% reflected. The measured absorption coefficient of $7.3mm^{-1}$ for these lasers was slightly lower than expected, indicating the doping concentration of the Nd:YVO_4 may have been less than the 3% quoted by the manufacturers.

The main factor enhancing the performance of this generation of green laser over previous generations was the improved dielectric coatings. The coatings were measured to have a reflectance of 99.97% at 1064nm, in comparison with 99.92% for the earlier devices. This equates to a higher maximum fundamental field intensity within the microchip laser (25W to 33W), giving more efficient doubling.

In addition, the improved parallelism, crystal quality and contacting method contributed to the superior performance of this generation of green laser. There was no evidence of wedging of the crystals when the chipsets were examined in a HeNe-based interferometer, indicating a parallelism better than 0.002^o. The contacting method is believed to give less than 1% residual reflection between the interface of the Nd:YVO_4 and KTP crystals.

The lasing performance of one of these green microchip lasers, pumped by a 0.5W and a 1.2W laser diode is shown in Figure 110. Up to 57mW of green power was measured for 0.5W of laser diode pump power and 154mW for 1.2W. No attempt was made to force the green output out in only one direction. An equivalent amount of power was assumed to be generated in the direction of the laser diode, though could not be measured due to geometry considerations. Overall, this equates to a conversion efficiency of up to 32% from diode pump power to green power. This operation was in good agreement with that predicted from the theoretical modelling in Figure 107.

Both the 1064nm and 532nm outputs had an ellipticity of <1:1.2 and were of near-TEM_{00} quality in the far-field with a minimum beam radius inside the cavity of 30μm for 1W of incident pump power. The ellipticity was observed to increase with increasing pump power because of the uniaxial nature of the crystal and the unequal thermal coefficients in the two directions perpendicular to the axis of the device. The

strong thermal lensing within the device help to produce such a small beam waist and hence high intensity to give high levels of second harmonic power. A more in-depth discussion of thermal lensing was given in Chapter Three of this thesis.

The improved coatings resulted in a lower 1064nm-output power, which was limited to approximately 10mW. Higher green powers were measured, up to 178mW of green power for 1.2W diode pumping, although these outputs were not stable and decayed after several seconds, indicating thermal dependence for the operating efficiency.

5.5.3 Longitudinal Mode Structure

Up to 8mW of single frequency green output was measured from this green microchip laser. Above this, the laser operated on two or more longitudinal modes at 1064nm, typically separated by 0.46nm/121GHz. However with careful adjustment, the second longitudinal mode could have an intensity at least 13dB lower than the intensity of longitudinal mode closest to the gain centre. This equates to more than 95% of the total green power in a single longitudinal mode. This property was used later to provide a successful pump source for a doubly resonant OPO, described later.

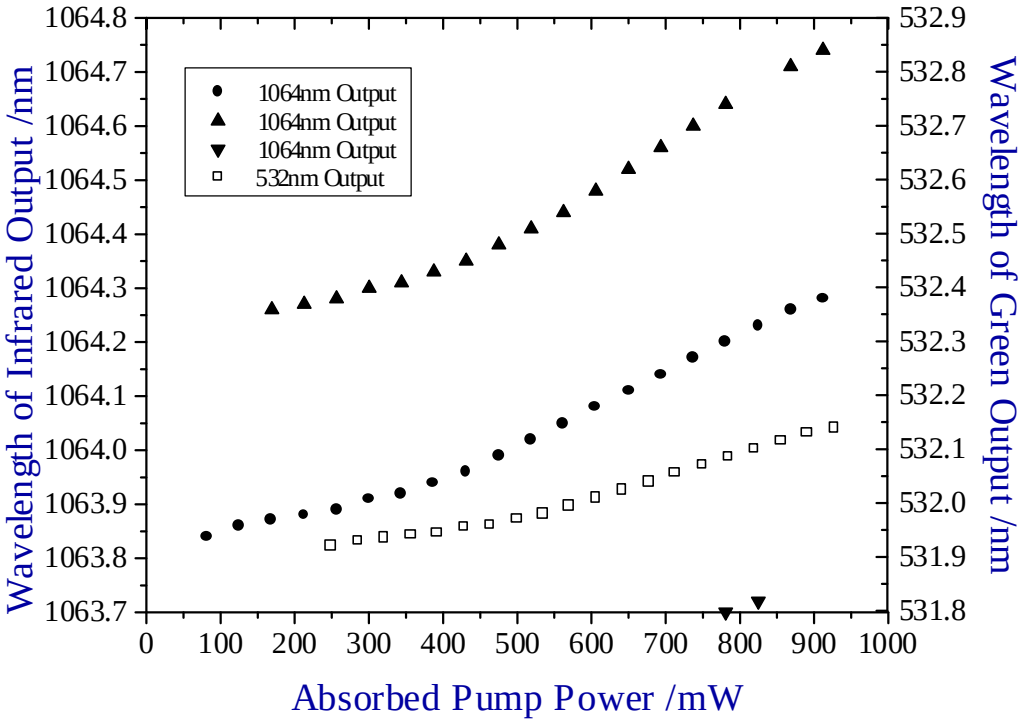

Figure 111 - Wavelength tuning of green device, composed of 0.5mm long 3% doped Nd:YVO_4 and 2mm long KTP, pumped by 1.2W laser diode.

The typical spacing of the longitudinal modes was much greater than the free

spectral range of the cavity (~30GHz) suggesting that adjacent longitudinal modes experience significantly different losses or gain. The nature of the cavity eigen-modes for an intracavity frequency doubled microchip laser, using a type II phase-matching scheme is under current investigation within our group to address the complicated longitudinal modes structures which were observed.

For 900mW of absorbed pump power, the device tuned smoothly over 0.5nm/132GHz as shown in Figure 111. In the region around 800mW of absorbed power the complementary longitudinal mode on the shorter wavelength side of the gain bandwidth could be seen to lase. In this operating window 'green noise' was observed. Below 750mW and above 850mW the device did not exhibit any form on intensity fluctuations within the bandwidth (1GHz) of the photodiode used.

5.5.4 'Green Noise'

The radio frequency spectrum of the green device operating at full pump power is shown in Figure 112. There is no evidence of any noise, including relaxation oscillations, out to 20MHz and indeed up to the frequency response of the photodiode (1GHz). This leads to a short term intensity instability of less than 1% peak-to-peak.

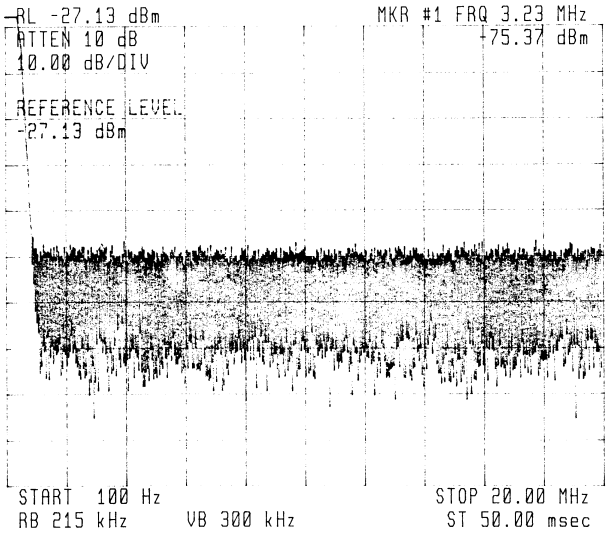

Figure 112 - Green microchip laser with no observable noise

Within the 'green noise' operating window the device had a strong modulation at a well defined frequency of 1.4MHz as shown in Figure 113. This modulation was 35% peak-to-peak of the average CW power. The higher harmonics of this modulation are also evident in the frequency spectrum.

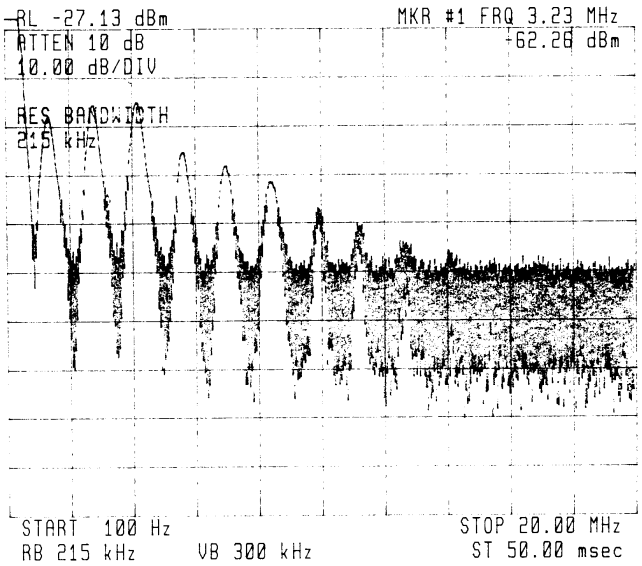

Figure 113 - Green microchip laser with periodic noise

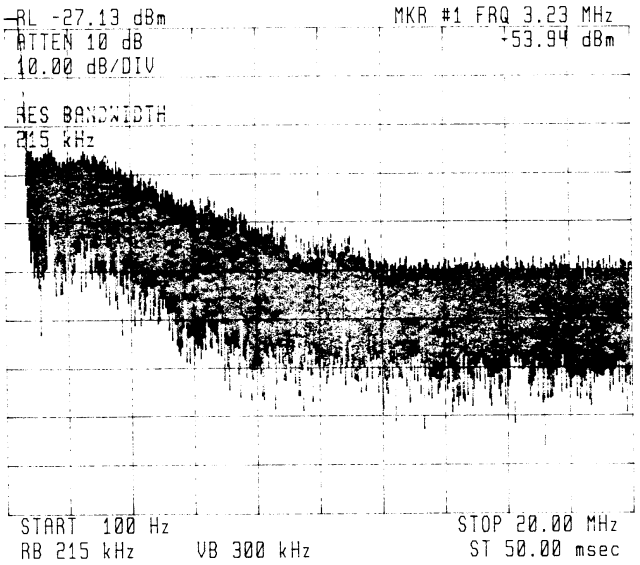

Figure 114 - Green microchip laser with aperiodic noise

In addition to periodic noise, regions of random noise could be identified, producing a RF spectrum as illustrated in Figure 114. These chaotic fluctuations can arise directly from the presence of a large number of nonlinear output couplings. The primary difference between periodic and aperiodic noise spectrums appears to be the different number of modes present and their effective nonlinear output couplings.

The large operating ranges in which no green noise occurs were attributed to the relatively low nonlinear output coupling of the KTP in these devices and the

dominance of one longitudinal mode. However, a more thorough analysis of the cavity eigen-polarisation modes is required to give theoretical verification or contradiction to these attributions.

5.5.5 Long Term Intensity Stability

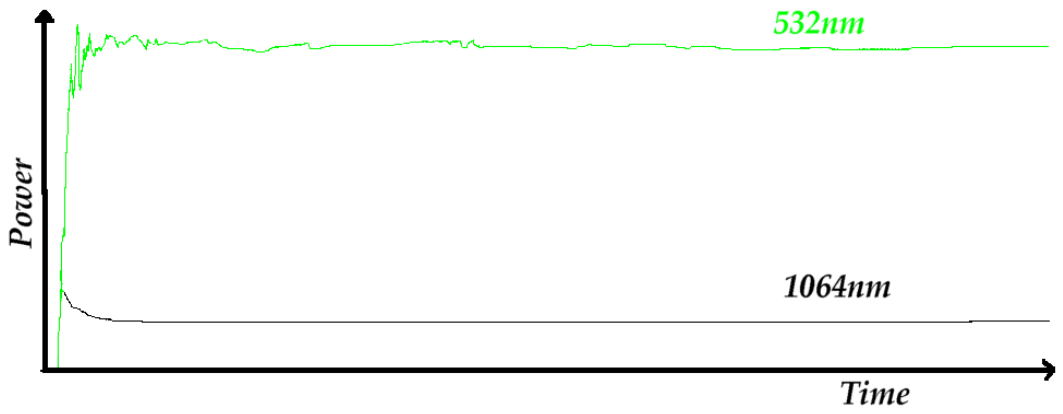

Figure 115 - Long term intensity stability of green microchip laser

The longer-term intensity stability of the green microchip laser was excellent with less than a 1% fluctuation peak-to-peak in the green output power over a minute. Figure 115 shows the output powers of the infrared and green from the over a time period of five minutes from switch on. As can be seen see the device settles to it CW level within 20 seconds from switch on, after an initial spiking period. This spiking period is believed to be due to neither crystal having reached thermal equilibrium. The spiking arises because the strength of the thermal lens is constantly changing after switch-on until equilibrium is reached, providing rapid mode tuning and consequently changing the efficiencies and overlaps for each longitudinal mode. The decay of the spiking gives an indication of the time for thermal equilibrium to be reached, in this case approximately one minute.

Overall, the frequency and intensity stability of these green microchip lasers was superior to previous generations and act as a good benchmark for the other frequency doubled microchip lasers.

5.5.6 Optical Bistability in Green Microchip Lasers

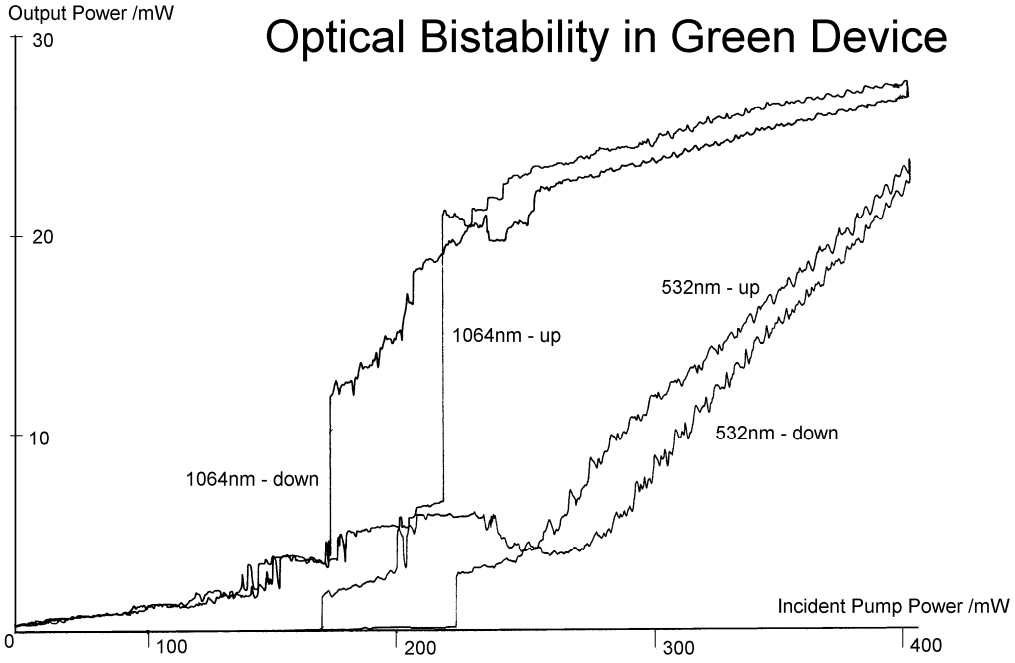

Figure 116 - Optical bistability in green microchip laser

A peculiar phenomenon was observed under certain operating conditions. A form of optical bistability, where two stable output power levels could be achieved for the same pump power, was found to occur. The pump power was slowly modulated with a triangular wave at a frequency of 0.001Hz and the power measured using a photodiode based power meter on a x-y plotter as illustrated in Figure 116. This effect is thought to be thermal in nature with a weaker thermal lens being maintained while the power is slowly turned down because it is more efficient for the laser to operate in this regime. With increasing pump power however the thermal lens has not been formed sufficiently well to provide such a comparably stable cavity. I hope future work will clarify the nature of this effect and its implications for frequency-doubled laser design.

5.5.7 Microchip Pumped OPO

In recent years, there has been much interest in the development of miniature, CW optical parametric oscillators (OPO's) as sources of tunable coherent radiation. CW OPO's traditionally require high intensity pump sources, operating on a single transverse and longitudinal mode. Such pump lasers are usually several hundred millimetres in length and incorporate intracavity elements to ensure single mode

operation. Recently passively Q-switched microchip lasers have been reported as the pump source for a pulsed doubly resonant OPO (DRO) [341]. Here we have used the CW output of our green microchip laser to pump a similar CW DRO based on KTP.

Despite the multi-longitudinal mode nature of the output, the majority of the power was in a single longitudinal mode, giving well-defined pump depletion for the locking of the OPO cavity. There was no active locking of the frequency of the laser to maintain the frequency spectrum of the output, other than through temperature control of the mount. Back reflections from the OPO, resulting in intensity and frequency instabilities in the pump laser, were suppressed using an optical isolator. The frequency stability of the green laser was measured to be ~50 MHz over several minutes with a short-term linewidth less than 300 kHz. The intensity stability of the pump laser was better than 3% peak-to-peak. These stability measurements are attributed to the small fluctuations in the diode pump power and changes in the environment surrounding the microchip. The frequency of the output of the microchip laser could be smoothly tuned by controlling the temperature of the thermoelectric mount.

Despite their first demonstration in the 1960's [342, 343] the use of CW OPOs has lagged behind that of pulsed devices. Until recently, threshold considerations have meant that most CW OPO's have been configured as doubly resonant oscillators (DRO's) where both the signal and idler fields are resonated in the cavity. Even when using the latest nonlinear materials, singly resonant oscillators (SRO's) still require pump powers of many watts for efficient operation [344], reducing to ~1W for pump enhanced systems [345]. Such pump powers are well outside the capabilities of a microchip laser. By contrast DRO's have been built with pump power thresholds of a few 10's mW [346] or lower [347,348].

Doubly resonant oscillators have the disadvantage in that they are over constrained by requiring simultaneous resonance of the signal and idler fields in a single cavity. This introduces complications in the tuning of these devices [349,350], resulting in the occurrence of mode and cluster hops [346,350] for changes in cavity length or pump frequency of a few nm or MHz respectively. Operation can only occur at discrete cavity lengths where the signal and idler frequencies satisfy the above constraints. However, once stabilised, the extremely stringent conditions for the simultaneous resonance of the signal and idler fields becomes a significant advantage.

The frequency selective property of the DRO ensures that the output is restricted to a single pair of signal and idler modes without the need for intracavity frequency selective components [351]. We can therefore demonstrate a device, which has the combination of good frequency selection while maintaining a very low pump power threshold. Smooth tuning of the output frequencies requires two parameters, pump frequency and cavity length, to be varied simultaneously.

The DRO was successfully stabilised by means of a cavity length servo system maintaining a constant output power and hence holding the OPO to a single signal and idler mode pair. Smooth tuning of the pump source while servo controlling the cavity length to maintain constant output power, resulted in the smooth tuning of the OPO output frequencies [352].

The experimental configuration of the OPO used in this work was similar to that reported in ref. [346] and was based on a 6mm long KTP crystal cut for near-degenerate, critical, type-II, phase matching. The mirrors used were highly-reflecting at both the signal and idler wavelengths, thus forming a doubly resonant oscillator, and their curvatures calculated to give a beam waist of only 40μm at the centre of the crystal. The resulting threshold of our OPO varied between 35mW and 120mW depending on the number of longitudinal modes oscillating within the pump laser. In all cases, however, the strong frequency selectivity of our DRO ensured that the output of the OPO was a single pair of signal and idler modes. With the OPO stabilised in this way, we obtained a combined signal and idler output power of 10mW, with an intensity modulation of ~8% at kilohertz frequencies. By temperature tuning the pump laser, while servo controlling the cavity length of the OPO, we achieved smooth tuning of the OPO output frequencies over 1.7 GHz. This was limited only by the tuning range of the pump laser. The doubly resonant nature of the DRO eliminates cavity length related frequency drifts [346] hence the linewidth of our OPO is expected to be that of the pump source (in this case better than 300 kHz).

5.5.8 Conclusion

In conclusion an efficient compact green source has been demonstrated which can produce in excess of 200mW of green power in a TEM_{00} output with the majority of power in a single longitudinal mode. Its ability to pump a DRO has been demonstrated.

5.6 Intracavity Doubling of 946nm Transition in Nd:YAG

5.6.1 Introduction and Motivation

There is a significant market demand for low-cost, compact, efficient blue lasers for many applications, including optical data storage, materials inspection, biomedical applications, reprographics and chemical analysis. Many of these applications make use of the smaller minimum spot sizes available through the use of a shorter wavelength and of the absorption edge of many materials in the blue spectral region.

Currently the most common low power blue lasers are air-cooled argon ion lasers, which produce tens of milliwatts on the ArII lines around 457nm. However these gas lasers are inefficient, bulky and have many difficulties with operation. Therefore there has been a determined effort to produce long-life blue laser diodes. This effort was discussed in more detail in Chapter One.

For some applications however there are constraints which prevent the use of laser diodes, such as the need for a single transverse or longitudinal mode, or short duration, high energy pulses. This has provided the motivation for intracavity frequency doubling of the 0.9μm transition in Nd^{3+} doped materials.

However this transition is weak in comparison to the 1.06μm and 1.3μm transitions and therefore many alternative approaches have been investigated to generate blue light from solid-state lasers. These include direct frequency doubling of the output of a laser diode in an external cavity [353], sum frequency mixing the output from a diode with 1064nm radiation [328], and the frequency tripling of the 1341nm transition [354].

As discussed in the previous section, Nd:YAG has the highest stimulated emission cross-section at 946nm of the commonly used Nd^{3+} materials with good thermal properties. Unfortunately it gives an unpolarised output, and therefore is not ideal as a gain material. Similarly, there are problems associated with the use of $KNbO_3$ as a nonlinear crystal for doubling into the blue because of its small acceptance windows and fragility, though again it potentially offers the best performance.

Therefore frequency doubling of the 946nm transition in Nd:YAG using $KNbO_3$ is a commonly used, though perhaps not ideal route to generating blue radiation. Our

group, primarily through the work of Dr David Matthews and Dr Neil MacKinnon, were the first to report the doubling of this transition in a microchip geometry, using the geometry illustrated in Figure 117 [355].

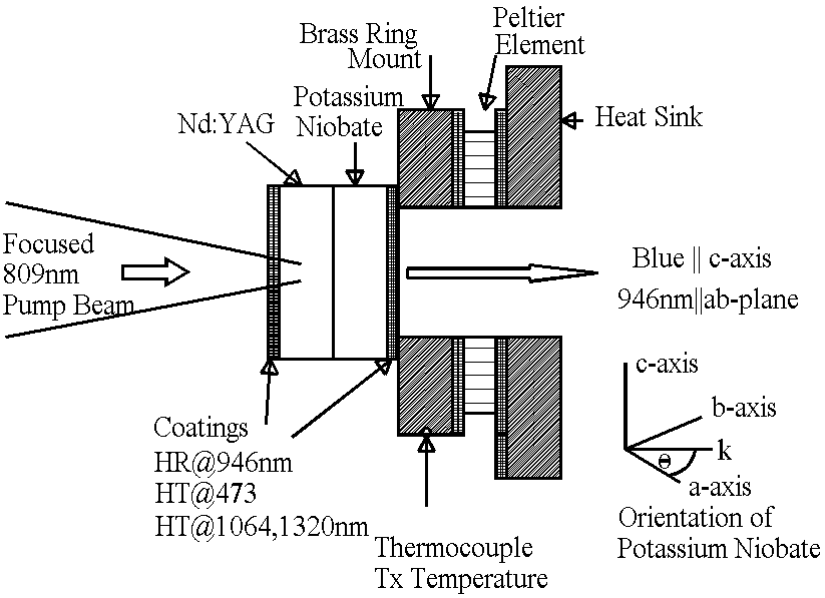

Figure 117 – Schematic of blue microchip laser design

The blue microchip laser was composed of a Nd:YAG and $KNbO_3$ crystal bonded together using the same technique as the green laser and coated appropriately to give a high finesse cavity at 946nm and transmit both the pump and second harmonic light. This 'sandwich' was then mounted on a peltier element to give the temperature tuning required to achieve efficient phase matching in $KNbO_3$.

Two generations of blue microchip lasers have been investigated using this design. Both of these will now be discussed to show the improvements that were gained through refinement of the manufacturing process for the second device.

5.6.2 First Blue Microchip Laser

5.6.2.1 Temperature Bandwidth of $KNbO_3$

In the first blue device examined, a 1mm thick piece of Nd:YAG, doped with 1.1% Nd^{3+}, was brought into intimate contact with a 1.5mm thick piece of $KNbO_3$ cut for type I critical phase matching at 45°C. The exposed ends of the device were then coated to be highly reflecting for the 946nm and anti-reflecting at 473nm, 810nm, 1064nm and 1320nm to minimise parasitic effects. A subsequent measurement however revealed that 28% of the pump light was reflected from these coatings. Of

the pump light transmitted by the coatings only 50% was absorbed by the Nd:YAG because of its relatively small absorption coefficient. The calculated 1% reflectivity of the YAG/$KNbO_3$ interface leads to only weak etalon effects and was not thought to significantly effect the operation of these devices.

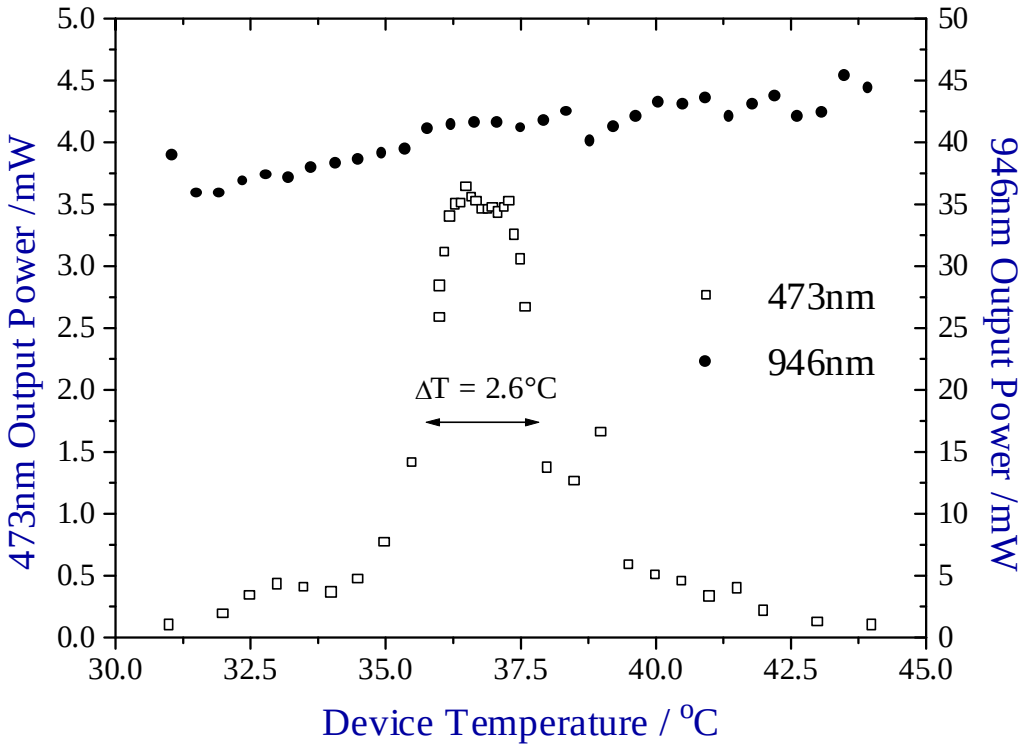

Figure 118 - Temperature bandwidth of first blue microchip laser, composed of a 1mm long Nd:YAG and 1.5mm long $KNbO_3$ crystal, pumped with 280mW from a Ti:sapphire through 25mm focussing lens.

Initial work was carried out using a CW Ti:sapphire laser as the pump source, tuned to the peak absorption of Nd:YAG at 808.5nm and focused to a spot size of 17+/-5μm inside the crystal set using a f=25mm lens. A thermoelectric cooler was used to temperature tune the device to 36.6°C which corresponded to the optimum blue output power of 3.6mW, as shown in Figure 118. The FWHM of this band was measured to be 2.6°C in relatively good agreement with the calculated figure of 2.9°C from Table 15. As the pump power was reduced, additional heating from a setpoint of 36.6°C at maximum pump power to 45°C at threshold was required to ensure that the $KNbO_3$ crystal remained phase-matched, indicating substantial heat transfer from the Nd:YAG to $KNbO_3$.

With temperature tuning, no significant change in the output power of the 946nm

fundamental beam was observed because of the relatively low coupling into the second harmonic beam, even within the phase-matching temperature bandwidth. The low thermal acceptance bandwidth of the $KNbO_3$ and the thermal transfer between the nonlinear crystal and the 'hot' gain material were expected to result in a degradation of the phase matching both along and across the beam. However, the width of the curve is not significantly different from that expected, showing good phase matching is achieved. The gradual 20% increase in the power of the 946nm was attributed to the changing absorption and reflection characteristics of the crystal and dielectric coatings with temperature. No attempt was made to investigate this further.

5.6.2.2 CW Lasing Performance - Ti:sapphire Pumping

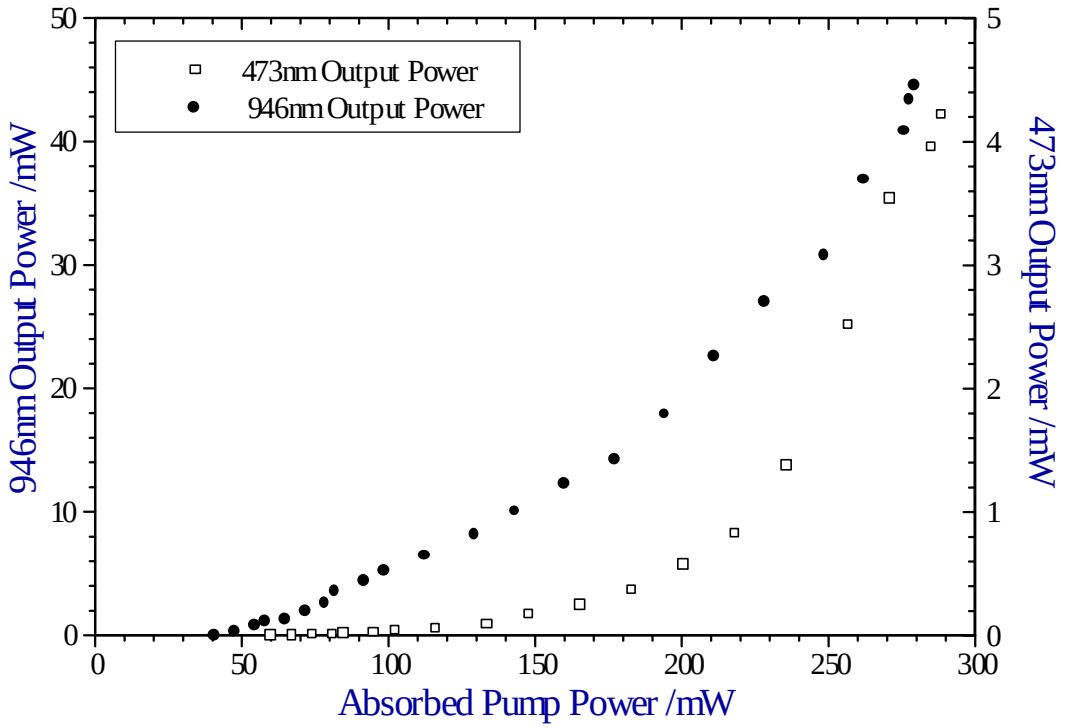

Figure 119 - Ti:sapphire pumping of first blue microchip laser

Figure 119 shows the output powers measured at 473nm and 946nm when the device was configured for maximum blue power. The maximum blue power measured was 4.3mW for 279mW of absorbed pump power. The threshold for lasing of the fundamental was 40mW of absorbed power, with 45mW of output power for 279mW of absorbed pump, representing a slope efficiency of 18.7%. Blue light was observable down to P_{abs} = 54mW. As the coating specifications were the same for both the output surfaces of the Nd:YAG and $KNbO_3$ we would expect the same output

generated in the direction of the pumping laser.

The relatively low frequency conversion efficiency was attributed to a number of factors. To maintain the peak conversion efficiency into the blue it was necessary to adjust the temperature of the composite device as the pump power changed because of the differing thermal load imposed on the chipset. The 1.02^{o} walk-off angle for the angle-cut CPM of this transition was calculated to have reduced the conversion efficiency to the blue by 23%. The poor quality of the $KNbO_3$, with some evidence of structural damage and depoling, also contributed to the poor frequency conversion efficiency observed.

The 946nm longitudinal modes were found to be strongly linearly polarised ($>1:10^3$) either perpendicular or parallel to the axes of the $KNbO_3$, depending on the pumped area of the crystal chosen. In some cases however the polarisation of all the longitudinal modes was not the same. Large fluctuations in the blue power were also found according to the choice of pumped region. This behaviour was attributed to micro stresses and strains introduced during the cutting, polishing and coating of the Nd:YAG crystal.

For these blue devices there is no waveplating effects within the cavity because the crystal axis of both crystals are used as the propagation planes because of the type I phase-matching geometry. This eliminates some of the complexities of the other two frequency-doubled microchip schemes. No jumping of the polarisation of the longitudinal modes was observed, which was attributed to the relatively low coupling into the second harmonic not significantly effecting the gain observed by two mutually orthogonal eigenmodes.

Both the 946nm and 473nm outputs had an ellipticity of <1:1.1 and were of near-TEM_{00} quality in the far-field with a blue minimum beam waist inside the cavity of 45μm. For the maximum pump power, 3 longitudinal modes were observed in both the blue and infrared outputs, with 2 modes at lower pump powers. The spacing of these modes was 0.25nm, greater than the calculated longitudinal mode separation of 0.1nm, suggesting spatial hole burning within the gain material preventing adjacent longitudinal modes lasing.

5.6.2.3 CW Lasing Performance – Diode Pumping

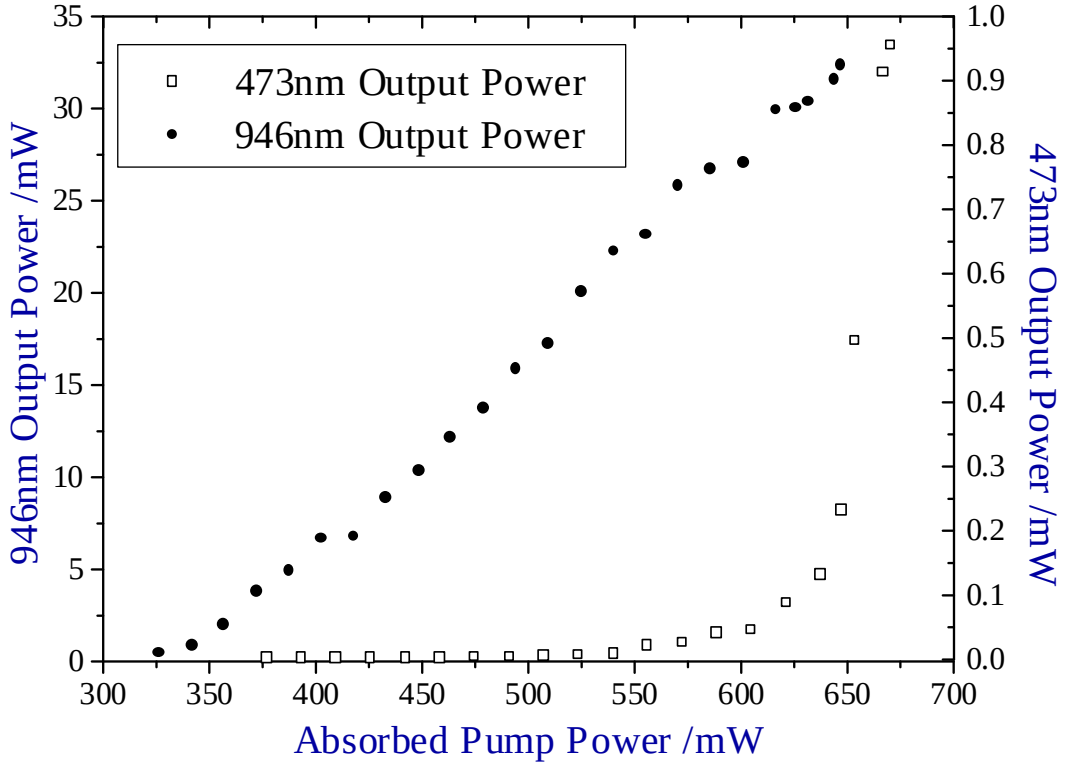

Figure 120 - Diode pumped performance of first blue microchip laser, composed of 1mm long Nd:YAG and 1.5mm $KNbO_3$, pumped by 2W laser diode through aspheric lens coupling.

When pumped with a 2W laser diode (200x1µm emitter) and an aspheric lens pair, a maximum blue output power of P_{blue}=0.954mW at the maximum absorbed pump power of P_{abs}=647mW was observed. This was accompanied by P_{946}=32mW of fundamental radiation, with the blue output first observable at P_{abs}=380mW. The 946nm fundamental output threshold occurred at P_{abs}=326mW resulting in a slope efficiency of 9.9%.

5.6.2.4 Conclusion

Following this work, a second blue microchip laser was constructed, benefiting from the experienced gained. The performance of the first blue laser was primarily inhibited by the quality of the coating and the $KNbO_3$ crystal, both of which were addressed in the preparation of the second laser.

5.6.3 Second Blue Microchip Laser

5.6.3.1 Temperature Bandwidth of $KNbO_3$

The second blue device examined was identical in design to the first apart from the $KNbO_3$, which was cut for temperature phase matching at 40°C and was of higher optical quality. The coating through which the device was pumped by the laser diode reflected 24% of the incident pump light, with 66% of the transmitted light absorbed in the Nd:YAG. The slightly lower operating temperature was chosen to reduce the threshold and increase the performance of the Nd:YAG because of the smaller thermal population in the ground level.

In fact, the optimal operating temperature of this device was slightly higher than that of the first device, as shown in Figure 121. The temperature bandwidth was also slightly smaller than expected. These effects were attributed to less thermal transfer from the Nd:YAG to $KNbO_3$ for this experiment because a 0.5W laser diode was used with a larger pump spot size than the Ti:sapphire pump used previously, and it is believed the actual temperature of the interaction region in the $KNbO_3$ of the second device was less than for the first blue microchip laser.

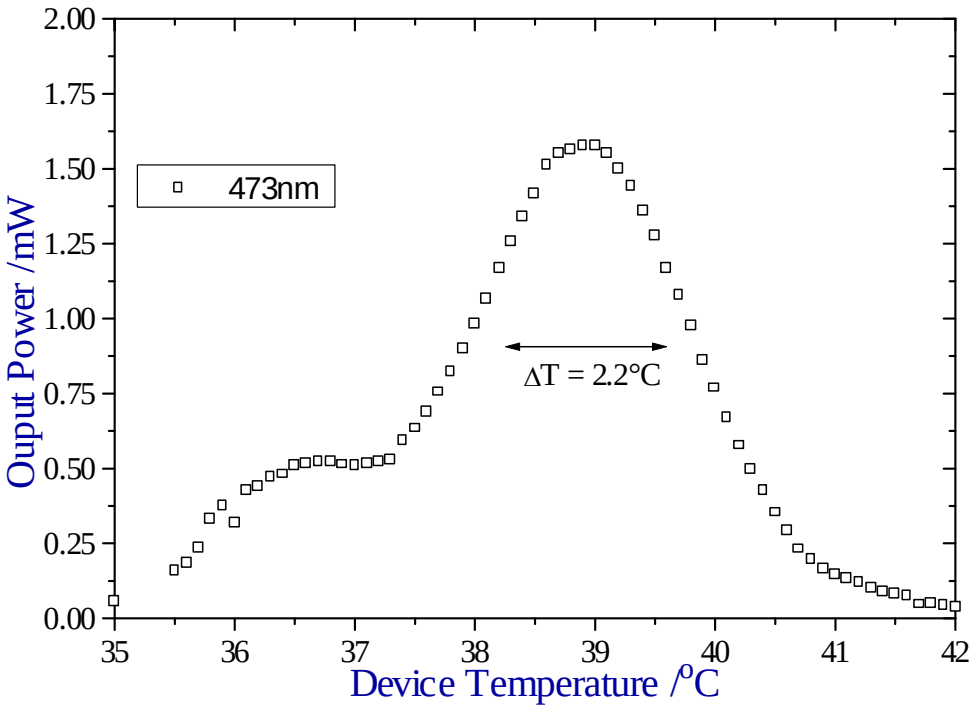

Figure 121 - Temperature bandwidth of blue device 2, composed of 1mm long Nd:YAG and 1.5mm $KNbO_3$ pumped by 0.5W laser diode through 8mm collimating lens and 6.5mm focussing lens.

These improved operating characteristics allowed this device to be pumped successfully by 0.5W and 1.2W high-brightness laser diodes through an 8mm collimating lens and 6.5mm focusing lens. The input/output characteristics under these pumping conditions are shown in Figure 122.

5.6.3.2 CW Lasing Performance – Diode Pumping

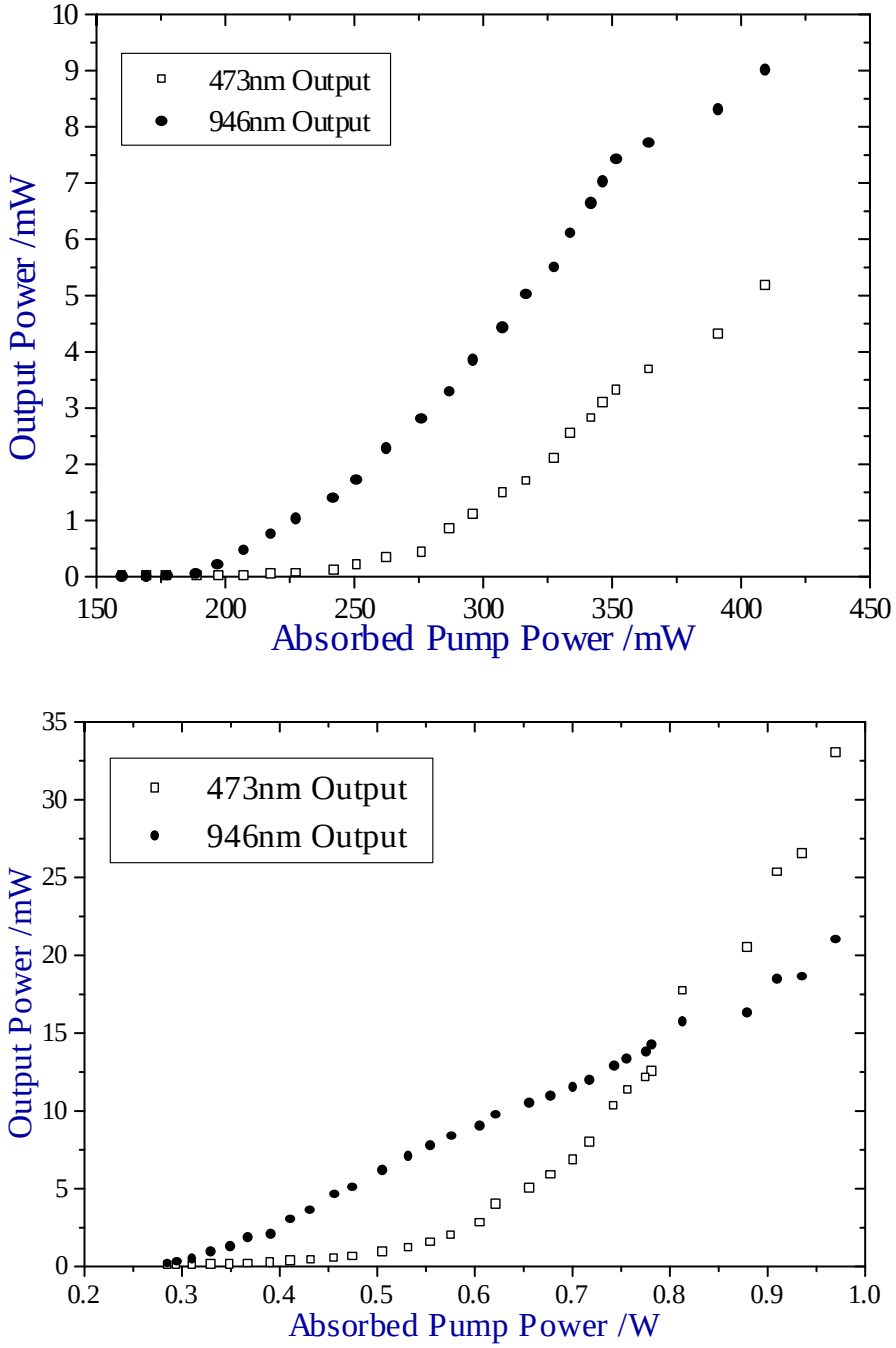

Figure 122 - Diode pumped performance of blue device 2, composed of 1mm long Nd:YAG and 1.5mm $KNbO_3$, pumped by a) 0.5W laser diode and b) 1.2W laser diode through 8mm collimating lens and 6.5mm focussing lens.

Maximum blue powers of 5.5mW and 33mW were obtained for 415mW and 970mW of absorbed power from a 0.5W and a 1.2W laser diode respectively. The blue and infrared outputs were both single transverse mode, however the laser operated on multiple longitudinal modes at all pump powers. The minimum beam waist of the fundamental lasing mode within the microchip device was measured to be 60μm at maximum pump power with the 1.2W laser diode.

The improved coatings can be seen to decrease the amount of emitted 946nm radiation and increase the 473nm power over the first blue device, through a higher circulating intracavity fundamental field. The other operating characteristics described for the first device were found to be common with this second device.

5.6.3.3 Variation in Output Power with Pump Spot Position

The output of the blue microchip laser varied significantly depending on the selection of the pumped region. A typical scan across the device is shown in Figure 123. The operation of the device can be seen to fluctuate significantly across the face, depending on pump position.

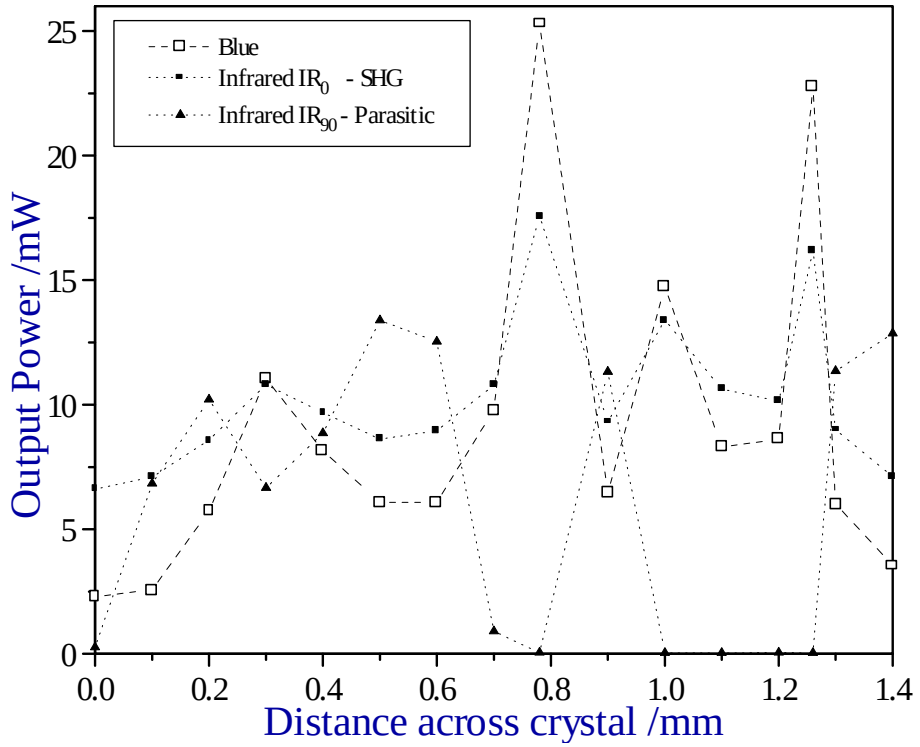

Figure 123 - Variation in polarisation of 946nm power across blue microchip laser

The component of the 946nm output aligned with the c-axis of the $KNbO_3$ (IR_0) is the component which is doubled into the blue and the relationship between this and the blue output power can be seen clearly.

The overall output power at 946nm was found however to be more closely related to the polarisation perpendicular to the c-axis of the $KNbO_3$. The ratio of the powers between the two polarisations was found to vary between 1:5 and 10:1 in favour of the c-axis depending on pumping site. This gave a variation in the generated blue power from a few microwatts to 33mW. Again it is apparent that some mechanism is inducing a spatially dependent polarisation, perhaps through some residual stress and strain left in the Nd:YAG from its processing.

5.6.3.4 'Blue Noise'

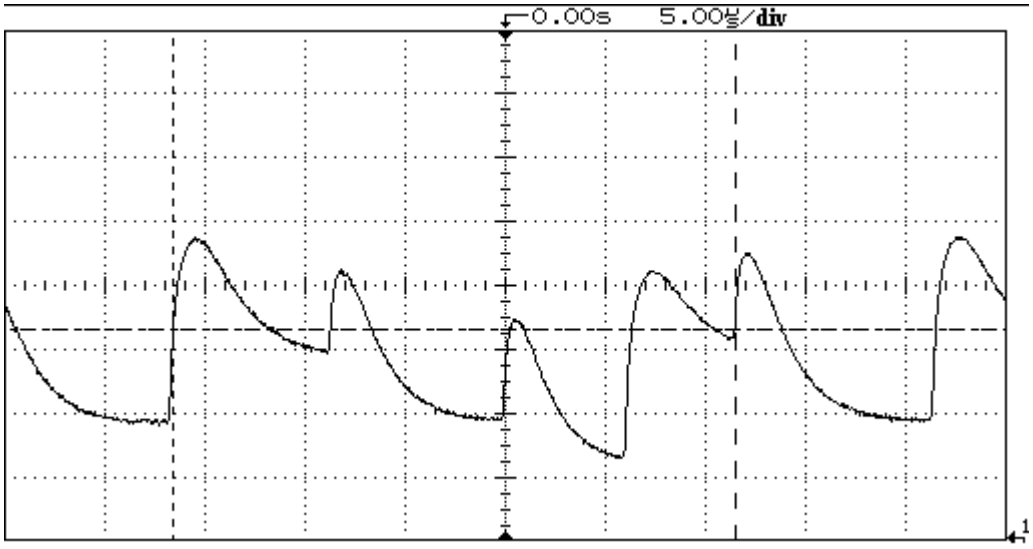

Figure 124 - Blue intensity noise in first blue microchip laser

In this device 'blue noise' was present in small operating regions producing intensity fluctuations, as shown in Figure 124, the depth and spectral content of which varied with crystal temperature. A radio frequency spectrum analysis indicated both distinct frequency and random noise are present dependent on the operating conditions. One such noise spectrum was characterised by 9% peak to peak fluctuation at around 2MHz. This was of higher frequency than the relaxation oscillations of the cavity (<1MHz) and was attributed to mode coupling between the longitudinal modes as discussed earlier, though does not fit with results given by the modelling of Baer [308].

5.6.3.5 Long Term Intensity Stability

The longer-term intensity stability of this device was examined using a photodiode. Temporal variation in the polarisation after switch on showed that the preferential polarisation is not formed in conjunction with cavity formation. That is to say the ratio of the two orthogonal infrared modes remains approximately the same. The main variation in this ratio is the depletion in the 946nm power in the polarisation due to the generation of the blue. This experiment did show a substantial drift in the blue output over time indicating the sensitivity to the relatively narrow phase-matching bandwidth.

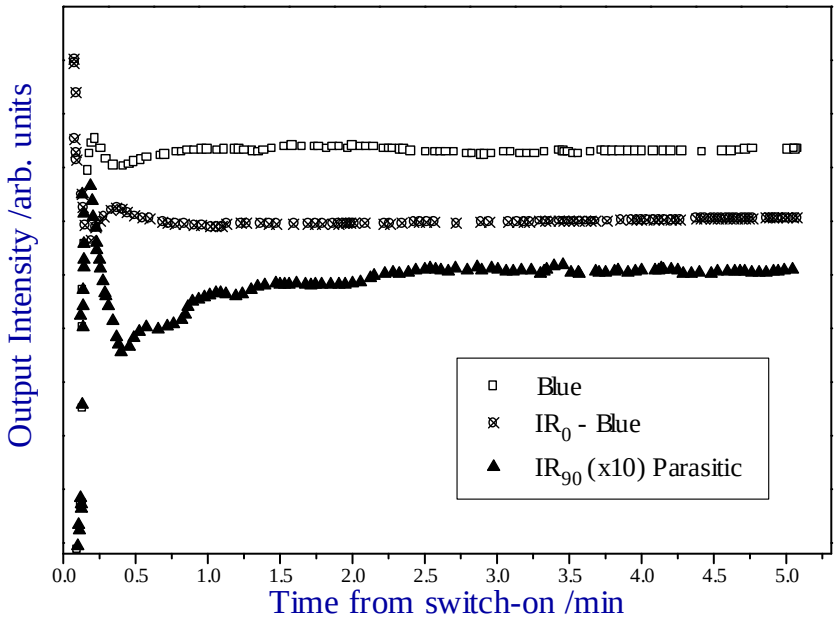

Figure 125 - Long term intensity stability of second blue microchip laser

5.6.4 Conclusion

In conclusion, we have demonstrated the first two generations of a blue microchip laser device giving up to 33mW of 473nm power. The main disadvantages with the system described are the narrow temperature bandwidth of the $KNbO_3$ and the isotropic nature of Nd:YAG. This later disadvantage could be overcome using a material such as Nd:SFAP which has been shown to be an efficient host operating at 945nm [356], or Nd:$YAlO_3$ which has been used to produce 15mW at 465nm [357]. The former disadvantage can be addressed through the use of periodically poled materials, such as PPLN, though even this material has thermal problems due to its

large thermo-optical coefficients and narrow temperature bandwidth (~2^{o}C) [331,358].

5.7 Intracavity Doubling of 1342nm Transition in Nd:YVO_4

5.7.1 Introduction and Motivation

Although the 1.3μm transition of Nd^{3+} has been investigated in several materials showing performance close to that of the 1064nm transition, it is the least frequently doubled Nd^{3+} transition. This has latterly been due to the development of laser diodes in the red spectral region, which can provide efficient generation of such radiation. Currently the CW powers available from red frequency doubled solid-state lasers still exceed those from red laser diodes, though this will inevitably change.

There are however, a number of applications where a solid-state red laser may have advantages over these competing laser diodes. The excellent spectral and transverse quality of the output, combined with the potential for pulsed operation with high peak powers give a solid state device the edge in medical applications such as the activation of photosensitive drugs in the blood stream. The output can also potentially be used to pump transition metal doped lasers, such as Cr:LiSAF, which are sensitive to waste heat and have low stimulated emission cross-sections. The gaussian beam of a DPSSL can have a higher brightness than the multimode output of a laser diode and can be focused to a smaller spot within the doped material, so enhancing performance.

A diode-pumped, frequency-doubled ring laser based on Nd:YAG and type I NCPM LBO generating 1319 and 659.5nm radiation was reported in 1994 [359]. A subsequent improvement using Nd:YLF as the gain material and using LBO cut for type I critical phase matching to avoid sub-zero phase-matching temperatures, gave 300mW at 659nm, which was used to pump a mode-locked Cr:LiSAF laser [360].

Work in St.Andrews with a similar motivation looked at the Q-switched doubling of a diode pumped Nd:YLF rod and compared the use of type I and type II LBO with KTP for the doubling of the 1321nm output [361]. Up to 40% conversion efficiency was achieved with type II NCPM LBO and the output was successfully used to pump a tunable, gain-switched Cr:LiSAF laser. The identification of type II NCPM in LBO above room temperature has aided the doubling of the 1.3μm transition. Most

recently, the same material combination as reported here has been used to generate several hundred milliwatts of CW red power at 671nm [362].

5.7.2 CW Lasing Performance

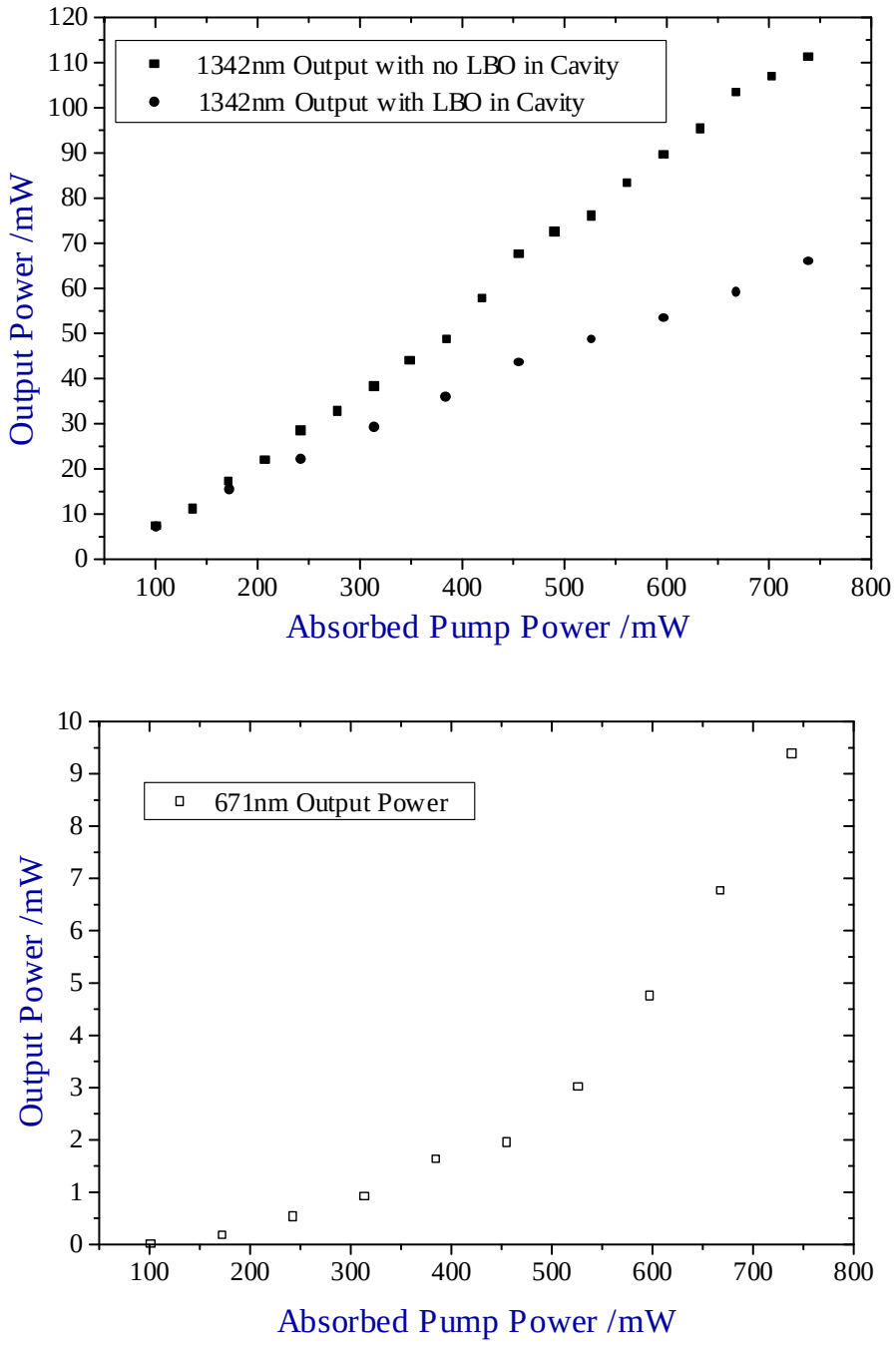

Figure 126 - Red and infrared output from red microchip laser. Top figure compares infrared output power with and without the LBO crystal in the cavity.

Our red microchip laser was constructed from a 0.5mm long piece of 1% doped Nd:YVO_4, a 2mm piece of LBO cut for type II NCPM and a discrete high reflecting

mirror. As mentioned earlier, the unusual expansion and contraction properties of LBO limited coatings on the nonlinear crystal to thin anti-reflection coatings. Measurement revealed these coatings to have a 0.3% reflectance at 1342nm, with the LBO crystal having an overall single pass transmission of 98.9% at 1342nm. The Nd:YVO_4 was coated to be highly reflecting at 1342nm and highly transmitting at 810nm on the pumped surface and antireflection coated on the other. The high reflection coating was measured to be 99.1% reflecting at 1342nm and 1.2% at 810nm, with the AR coating reflecting 0.2% of incident 1342nm light. The discrete high reflecting output coupler was used to form the other feedback mirror to the cavity and it was measured to have 99.5% reflectance at 1342nm. At 671nm the highly reflecting coating were found to have approximately 38% reflectance.

These poor coatings, as with the first generation of blue and green devices, limited the performance of this device, as did to the extra intracavity surfaces required because of the difficulty in applying a high reflecting coating to the LBO. With refinement of the coatings and materials it should be possible to enhance these figures and show similar performance to the green device.

Using a 1.2W laser diode (100x1μm stripe) to pump this device through an 8mm collimating lens and an 8mm-focusing lens, the 1342nm and 671nm performances were examined. The 1% doping concentration of the Nd:YVO_4 absorbed 78% of the incident pump light. For 740mW of absorbed pump power 9.6mW of 671nm power was emitted from the front facet of the red microchip laser. Red power was observed right down to threshold of the fundamental, though limited to the microwatt regime at lower pump power levels. This is in good agreement with the expected behaviour calculated from analytical model and illustrated in Figure 109.

Figure 126a) shows the relatively high threshold and large amount of 1342nm power emitted from the device with and without the LBO crystal in the cavity because of the lossy coatings. The marked effect of including the LBO in the cavity can be seen by a 41% decrease in the output, from a slope efficiency of 22% to 12%.

This decrease is attributed to the complicated eigen-polarisation states the type II crystal introduces into the cavity and the smaller effects of weak etaloning between the intracavity surfaces. A quantitative theoretical and practical investigation of eigen-modes of the cavity is not given in this thesis, though work in currently on-

going within our group to further understand the polarisation states of frequency doubled microchip lasers. With the 0.5% output coupling of the high reflecting front surface, the 1342nm power indicated a circulating field of 14W within the cavity at maximum pump power, significantly lower than for the green device (33W).

The output was measured to have a Gaussian intensity profile in the far-field and indicated a minimum beam radius inside the cavity of 34μm for 750mW of absorbed power. Thus, the circulating intensity of the red device is approximately 31% that of the green device, indicating why there is such a dramatic difference in performance between the two devices. The ellipticity was observed to be better than 1:1.2 for the full range of incident pump powers for the 0.5W and 1.2W pumping laser diodes.

5.7.3 Temperature Bandwidth of LBO

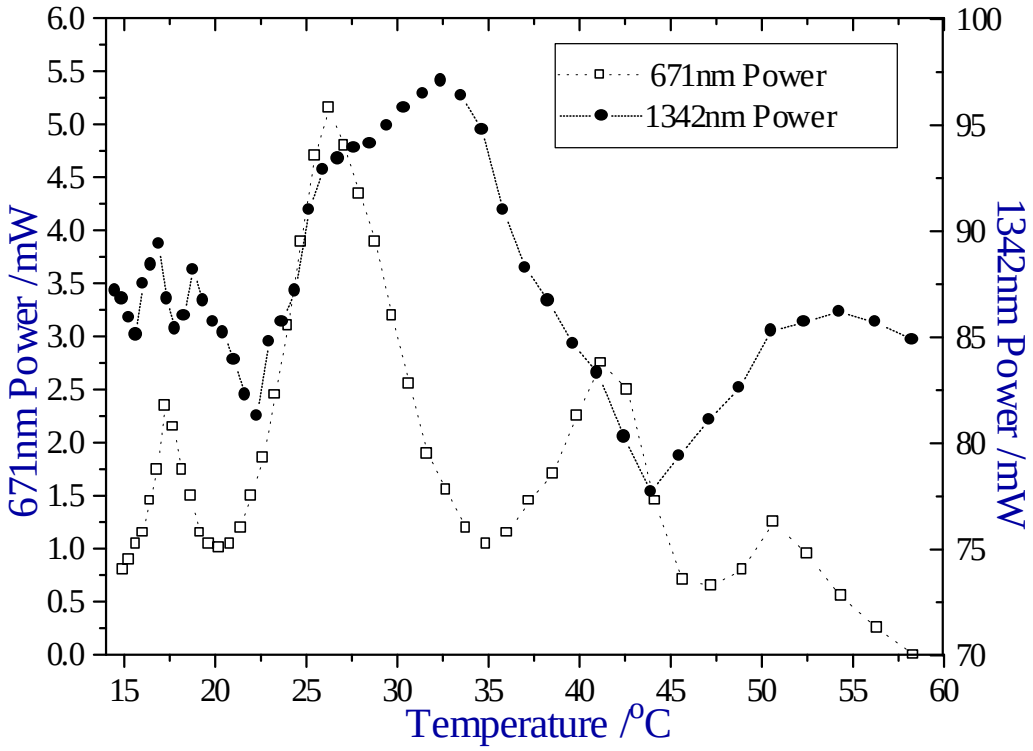

Figure 127 - Temperature bandwidth of red microchip laser, composed of 0.5mm long 1% doped Nd:YVO_4, 2mm long LBO crystal and a high reflector at 1342nm, pumped by 2W laser diode through a 8mm collimating lens and 6.5mm focussing lens

The red output exhibited a complicated temperature bandwidth when the device was temperature tuned with the temperature bandwidth centred at 27°C. The FWHM temperature bandwidth of the red, if the wings are included, is 26°C in reasonable

agreement with the expected bandwidth of 29^{o}C. The FWHM of the central peak alone is 8^{o}C, much lower than expected.

The effect is attributed to the strongly temperature dependent refractive indices of LBO which introduce a temperature sensitive waveplate into the cavity. This waveplate can act in conjunction with the waveplating nature of the Nd:YVO_4 to form a polarisation rotation for the circulating 1342nm field. If the rotation is 0^{o} or 180^{o} then optimal performance would be expected, but detuning from either of these cases would decrease the fundamental field intensity and affect the second harmonic efficiency. A similar sinusoidal variation in the output power was observed by Sasaki for a green device similar to the one described earlier [336]. In that case the temperature bandwidth of KTP was very large, so as the background effect of the phase-matching condition was not significant, in contrast to the red device where the sinusoidal modulation has overlaid the normal phase-matched bandwidth. As mentioned previously a more complete understanding of this effect is being carried out.

The 1342nm output can be seen to fluctuate 23% peak-to-peak over the same temperature range with a period roughly twice that of the second harmonic in agreement with the observations of Sasaki.

5.7.4 Temperature Tuning and Longitudinal Mode Structure

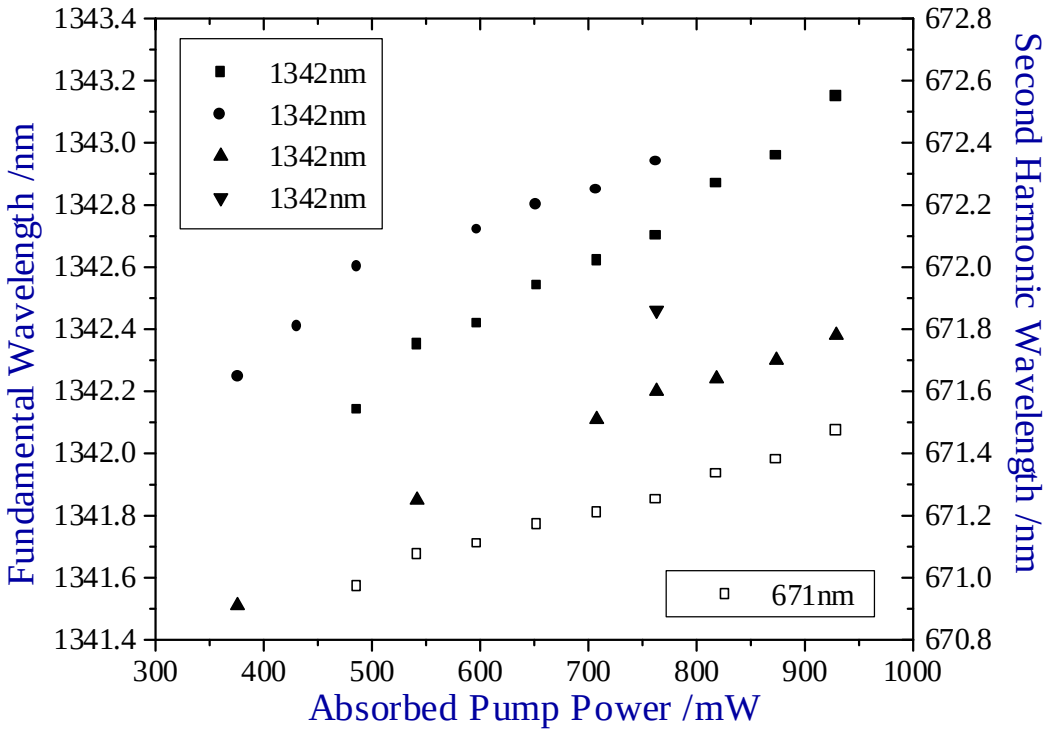

Figure 128 - Temperature tuning of composite red device. Four longitudinal modes were evident at 1342nm, although only a single line was generated at the second harmonic.

For 0.5W of absorbed power the central longitudinal mode of the device tuned 1nm as can be seen in Figure 128. The device operated on up to 4 longitudinal modes in the infrared separated by 0.26nm/43GHz, twice the free spectral range of the cavity. The typical longitudinal mode structure of two longitudinal modes is shown in Figure 129.

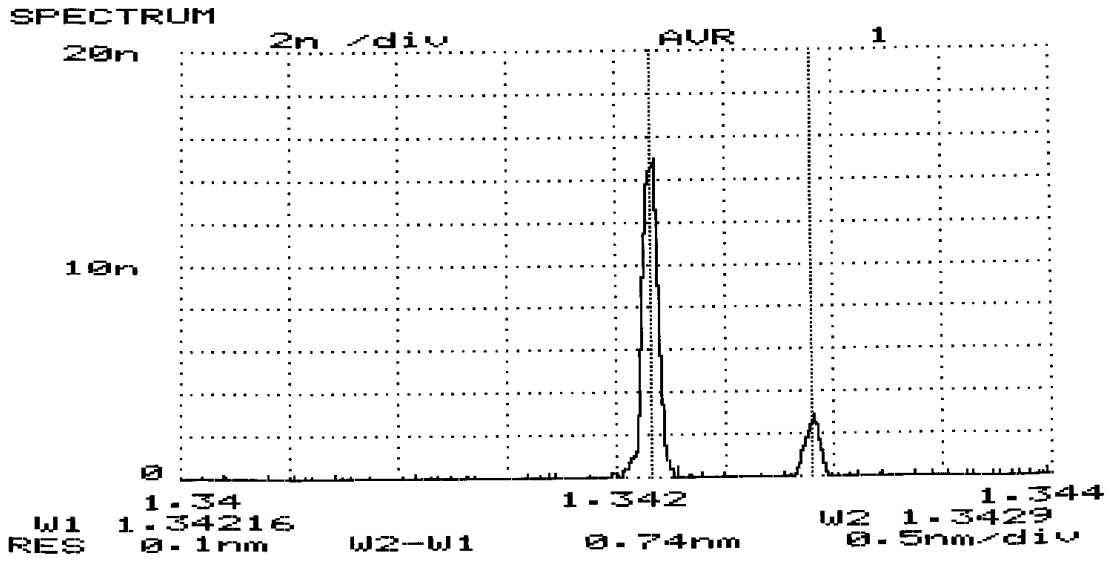

Figure 129 - Longitudinal mode structure of the red microchip laser at fundamental wavelength

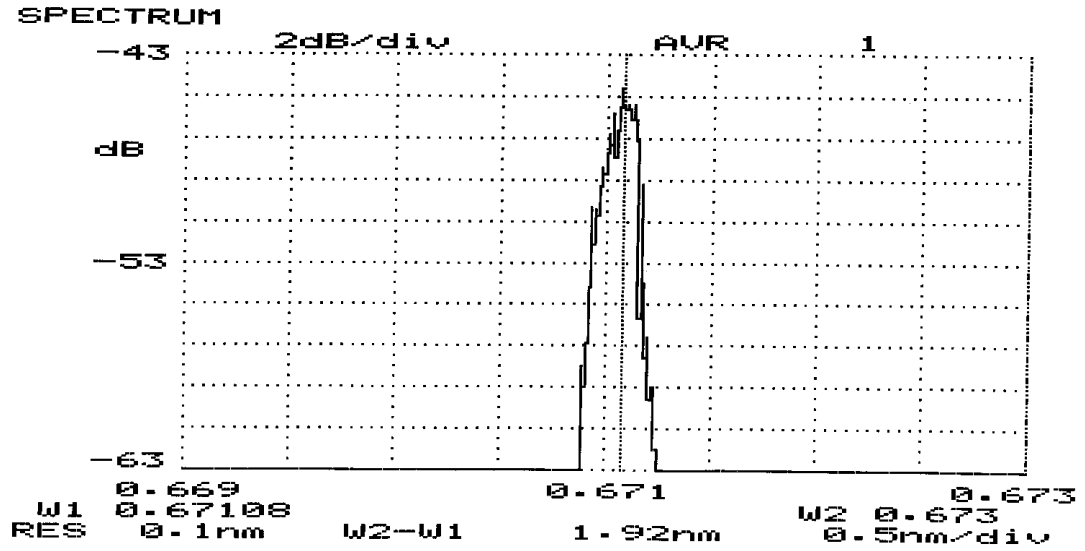

Figure 130 - Single longitudinal mode operation of the red microchip laser at 671nm.

The axial mode closest to the centre of the gain profile, which tunes from 1342.1 - 1343.2nm in Figure 128, was found to be at least six times the intensity of any of the adjacent lasing modes and was the main source of the generated red radiation. The competition between the modes and the complicated pattern produced suggests there is a strong pump power dependence on the phase shifts experienced by axial modes in one round trip of the cavity. No attempt was made to measure the polarisation of the fundamental output to resolve how these phase-shifts altered with pump power.

At maximum pump power, although two axial modes were oscillating in the fundamental, only one axial mode was found at the second harmonic as illustrated in Figure 130. This was attributed to both the lower intensity of this second axial mode combined with inefficient doubling of this second mode in the LBO because of non-optimal phase-matched conditions and a more complicated eigen-mode.

5.7.5 'Red Noise'

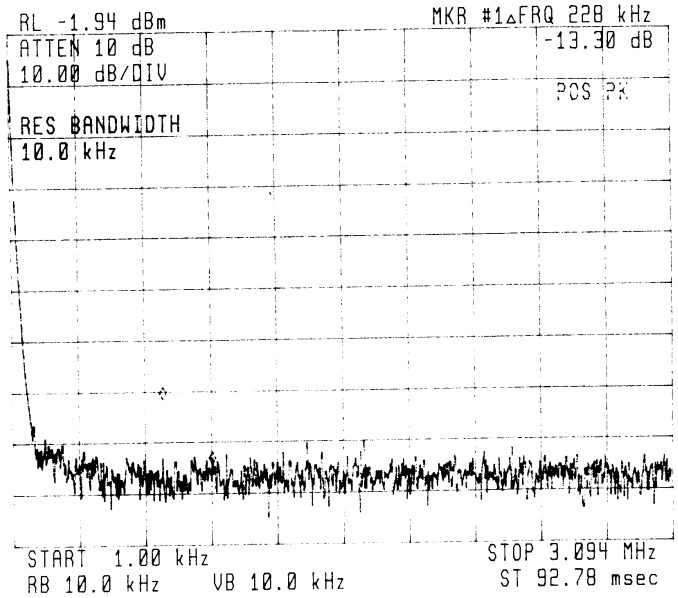

Figure 131 – Radio frequency spectrum of a 'quiet' red microchip laser

A typical radio frequency (RF) spectrum of the red laser is Figure 131, with a measured short-term intensity stability of less than 1% peak-to-peak. This mode of operation occurred over the majority of the operating range of the device. However within the region of 500-600mW of absorbed pump power in Figure 132, 'red noise' was observed associated with longitudinal mode jumping. Only periodic noise was observed in contrast to the green device and at a much lower fundamental frequency of 27kHz as shown in Figure 132.

The frequency of the noise characteristics of the red, green and blue microchip lasers is contrary to that expected by the Baer model [308]. Baer postulated that as the nonlinear coupling decreased, the mode-coupling oscillation frequency would increase until the relaxation oscillation frequency. From the large output coupling of the $KNbO_3$, to the lower KTP and the lowest for LBO, we observed a decrease in noise frequency. This suggests that the mechanisms for generating coupled

longitudinal mode ‘noise’ in microchip lasers may be more complicated than those considered by Baer for larger intracavity frequency doubled lasers. For example, Baer assumed equal mode intensities and did not account for the cross-saturation of the gain varying in different crystals. The current work on the cavity eigen polarisation modes will address this problem in more detail.

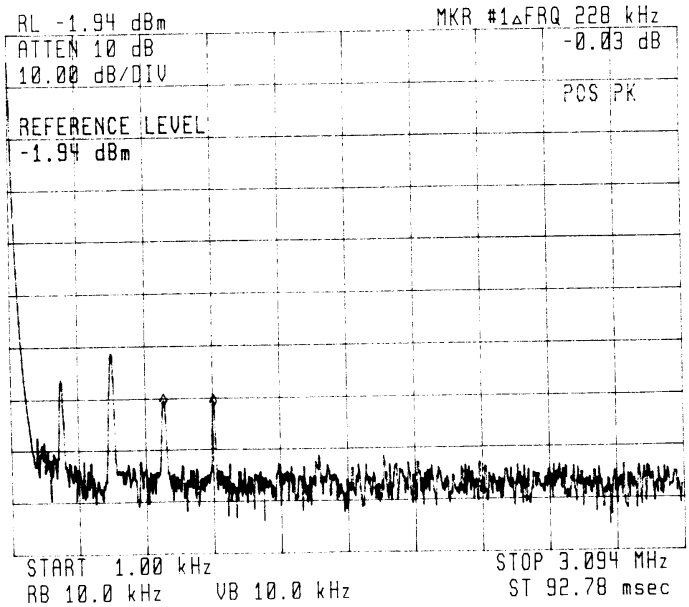

Figure 132 – Radio frequency spectrum with periodic 'red noise' from red microchip laser.

Overall, the noise characteristics of the red microchip laser were similar to those of the green microchip laser. Small operating regions are characterised by significant periodic perturbations to the CW level attributed to the coupling of longitudinal modes through the nonlinear crystal and the cross-saturation of the gain material. However, most of the operating range was characterised by a stable output at both the fundamental and second harmonic with fluctuations of ~1% peak-to-peak, largely attributed to the small fluctuations in the laser diode pump power.

5.7.6 Long Term Intensity Stability

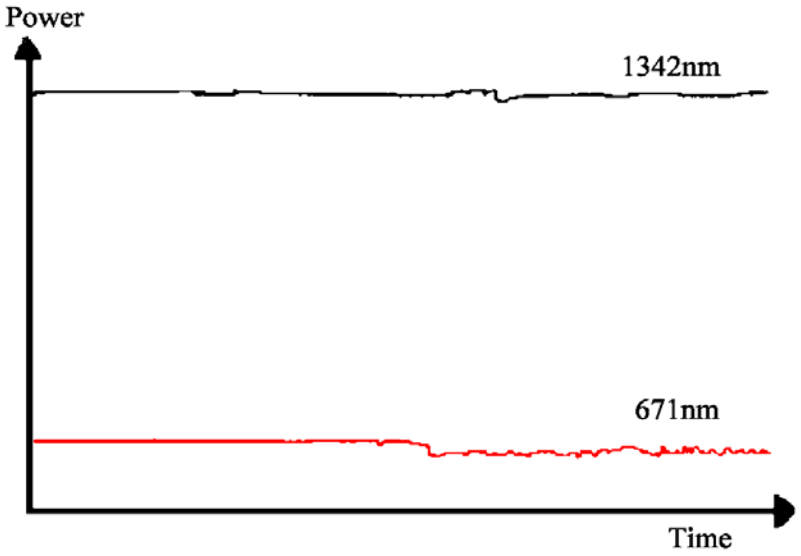

Figure 133 - Long Term Intensity Stability of Red Device

The longer-term stability of the red power was found to be dependent on the temperature stability of the thermoelectric cooler used to heat the device to 27°C. Figure 133 shows how the intensity of both the fundamental and second harmonic varied over five minutes.

There was a 5% fluctuation in the infrared output and 10% in the red output over this period, indicating the sensitivity of this device to environmental variables.

5.7.7 Conclusion

In conclusion, we have demonstrated the first generation of red microchip lasers. The performance of this device was limited by the poor coatings and low nonlinear coefficient of the LBO which could not be coated with a highly reflecting coating. However 10mW of 671nm power was generated in a single longitudinal and transverse mode which was sufficient to pump a monolithic Cr:LiSAF microchip to just above threshold. With refinement of optical coatings and perhaps the use of $LiNbO_3$ as the doubling material, higher red powers should be possible.

5.8 Conclusions and Future Work

In this chapter, the frequency doubling of the three main transitions of Nd^{3+} has been described, to give red, green and blue radiation from a microchip geometry. The operating characteristics of these lasers are summarised in Table 16.

Transition	**946→473nm**	**1064→532nm**	**1342→671nm**
Gain Material	0.5mm (1.1%) Nd:YAG	0.5mm (3%) Nd:YVO_4	0.5mm (1%) Nd:YVO_4
Nonlinear Material	1.5mm $KNbO_3$	2mm KTP	2mm LBO
Cavity Coating Characteristics	24%R @ 810nm, >95%R @ 946nm	0.8%R @ 810nm, 99.97%R @ 1064nm	1.2%R @ 810nm, 99.1%R @ 1342nm
Pump Absorption at 810nm	66%	97%	78%
Max 2nd Harmonic Power /mW	33	220	9.6
Max SLM 2nd Harmonic Power	<1	8	9.6
Conversion Efficiency (Pump → 2nd Harmonic)	3.5% / 7%	19% / 38%	1.4% / 2.8%
Residual Fundamental Power /mW	18	10	66
Temperature Bandwidth	2.2°C @ 39°C	-	8°C @27°C

Table 16 - Operating Characteristics of Doubled Microchips

The blue and green devices have been made commercially available and will continue to be refined and enhanced. There is little commercial incentive to develop the red devices because of the competing red diodes which can offer greater output powers, albeit with poor spatial and spectral mode characteristics.

The ongoing work in St.Andrews to improve and characterise the operation of green lasers has been described, highlighting the improvements that can be made by refinement of optical coatings and material quality. The efficiency of the green generation is now comparable to that of the infrared power from a monolithic device.

Future work on these devices is required to understand the effect of the birefringence of both the Nd:YVO_4 and KTP and the effect this has on the operation of the device. The remaining significant goal is to produce a device that inherently operates on a single axial mode, either through the use of a shorter cavity, or through a form of intracavity wavelength selectivity. The shorter cavity could be realised through the use of periodically poled material with a higher nonlinear coefficient to offset the shorter crystal length, and a gain material with a higher doping concentration. The wavelength selectivity is more difficult to address in a truly microchip geometry. Further refinement of the coatings should make it possible to successfully extract all the green power in a single direction without loss in efficiency or polarisation.

The first two generations of blue device have been described, highlighting some of the problems faced in generating blue radiation using an isotropic gain material. Some of the problems could be overcome by using a gain material with a polarised output, such as Nd:YAlO or Nd:SFAP. The 0.9μm transition is the weakest transition in Nd^{3+} and suffers from a ground state population causing reabsorption, so a phase-matching condition at room temperature or lower would be more suitable. Again periodically poled material would remove some of the disadvantages of $KNbO_3$ especially relating to it extreme fragility. Further work looking at alternative materials is required if a more efficient, stable system is desired.

Finally the first generation of red device was described, highlighting the importance of loss on the cavity, especially when using a material with a low nonlinear coefficient. The 1342nm transition hold a lot of promise which has not been realised. The use of an alternative nonlinear material with a higher nonlinear coefficient and better coatings would undoubtedly significantly enhance the performance of these devices.

References:

[287] P.A. Franken, A.E. Hill, C.W. Peters, G. Weinreich, Phys. Rev. Lett., **7**, 118 (1961)

[288] A. Lhuillier, I.O.P. Conference Series, 444 (1996)

[289] W. Koechner, "Solid State Engineering" (3rd Ed.), Springer-Verlag, 511 (1992)

[290] R.L. Byer, Laser Focus World, **25:3**, 77 (1989)

[291] G.D. Boyd, A. Ashkin, J.M. Dziedzic and D.A. Kleinman, Phys. Rev., **137**, 1305 (1965)

[292] J.A. Armstrong, Phys. Rev., **127**, 1918 (1962)

[293] Y.S. Luh, J. Crystal Growth, **78**, 135 (1986)

[294] E. Lim, M. Fejer, R.L. Byer, OSA Tech. Digest CLEO'89, Paper CTh1 (1989)

[295] D. Feng, Appl. Phys. Lett., **37**, 607 (1980)

[296] J.J. Zayhowski, Laser Focus World, 32:4, 81 (1996)

[297] R.L. Byer, Science, **239**, 742 (1988)

[298] Z.Y. Ou, S.F. Pereira, E.S. Polzik and H.J. Kimble, Opt. Lett., **16**, 1493 (1988)

[299] R. Paschotta, K. Fielder, P. Kurz, R. Henking, S. Schiller and J. Mlynek, Opt. Lett., **19**, 1325 (1994)

[300] K. Schneider, S. Schiller, J. Mlynek, M. Bode, I. Freitag, Opt. Lett., **21:24**, 1999 (1996)

[301] A. Agnesi, S. Dell'Acqua, G.C. Reali, P.G. Gobbi and D. Ragazzi, Appl. Opt., **36:3**, 597 (1997)

[302] T. Taira and T. Kobayashi, Appl. Opt., **34:21**, 4298 (1995)

[303] T. Taira and T. Kobayashi, IEEE J. Quantum Electron., **30:3**, 800 (1994)

[304] T.Y. Fan, A. Cordova-Plaza, M.J.F. Digonnet, R.L. Byer and H.J.Shaw, J. Opt. Soc. Am. B, **3:1**, 140 (1986)

[305] J.K. Yamamoto, A. Sugimoto and K. Yamagishi, Opt. Lett., **19:17**, 1311 (1994)

[306] J. Bartschke, R. Knappe, C. Becher, B. Beier, K.J. Boller and R. Wallenstein, OSA Tech. Digest CLEO'94, Paper ATuD2-1 (1994)

[307] R.G. Smith, IEEE J. Quantum Electron., **6:4**, 215 (1970)

[308] T. Baer, J. Opt. Soc. Am. B, **3:9**, 1175 (1986)

[309] M. Oka and S. Kubota, Opt. Lett., **13:10**, 805 (1988)

[310] H. Nagai, M. Kume, I. Ohta, H. Shimizu and M. Kazumura, IEEE J. Quantum Electron., **28:4**, 1164 (1992)

[311] G.E. James, E.M. Harrell, C. Bracikowski, K. Wiesenfeld and R. Roy, Opt. Lett., **15:20**, 1141 (1990)

[312] K. Suzuki, K. Shimomura, A. Eda and K. Muro, Opt. Lett., **19:20**, 1624 (1994)

[313] W.L. Zhou, T. Sasaki and S. Nakai, Japanese J. Appl. Phys., **33**, L779-782 (1994)

[314] D.W. Anthon, D.L. Sipes, T.J. Pier and M.R. Ressl, IEEE J. Quantum Electron., **28:4**, 1148 (1992)

[315] S. Singh, R.G. Smith and L.G. Van Uitert, Phys. Rev. B, **10:6**, 2566 (1974)

[316] A.W. Tucker, M. Birnbaum, C.L. Fincher, J.W. Erler, J. Appl. Phys., **48:12**, 4907 (1977)

[317] LBO Crystal Data, Fujian Castech Crystals Inc., (1995)

[318] V.G. Dmitriev, G.G. Gurzadyan and R. Nikogosyan, "Handbook of Nonlinear Optical Crystals" (1st Ed.), 103-105 (1993)

[319] G. Gibson, R.S. Conroy, A.J. Kemp, B.D. Sinclair, M.J. Padgett and M.H. Dunn, accepted for publication in Optics Letters (1998)

[320] I.D. Lindsay, M. Ebrahimzadeh and M.H. Dunn, accepted for publication in Applied Optics (1998)

[321] I. Biaggio, P. Kerkoc, L.S. Wu and P. Gunter, J. Opt. Soc. Am. B, **9:4**, 507 (1992)

[322] J. Hong, Chapter 7, PhD Thesis, University of St.Andrews Library (1992)

[323] G.J. Dixon, Proc. Soc. Photo-Opt. Inst. Eng., **16**, 1219 (1990)

[324] G.J. Dixon, Z.M. Zhang, R.S.F. Chang and N. Djeu, Opt. Lett., **13:2**, 137 (1988)

[325] W.P. Risk, R. Pon and W. Lenth, Appl. Phys. Lett., **54:17**, 1625 (1989)

[326] J. Hong, B.D. Sinclair, W. Sibbett and M.H. Dunn, Appl. Opt., **31:9**, 1318 (1992)

[327] F. Hanson, Opt. Lett., **20**, 148 (1995)

[328] J.C. Baumert, F.M. Schellenberg, W. Lenth, W.P. Risk and G.C. Bjorkland, Appl. Phys. Lett., **51**, 2192 (1987)

[329] W.X. Lin, H.Y. Shen, Y.P. Zhou, R.R. Zeng, G.F. Yu, C.H. Huang, Z.D. Zeng and W.J. Zhang, Opt. Comm., **82:3,4**, 333 (1991)

[330] R.W. Wallace and S.E. Harris, Appl. Phys. Lett., **15:4**, 111 (1969)

[331] V. Pruneri, R. Koch, P.G. Kazansky, W.A. Clarkson, P.J. Russell and D.C. Hanna, Opt. Lett., **20:23**, 2375 (1995)

[332] M.J.P. Dymott, A.I. Ferguson, Opt. Lett., **19:23**, 1988 (1994)

[333] X.X. Zhang, P. Hong, G.B. Loutts, J. Lefaucheur, M. Bass and B.H.T. Chai, Appl. Phys. Lett., **64:24**, 3205 (1994)

[334] G.J. Dixon, L.S. Lingvay and R.H. Jarman, SPIE Solid State Lasers, **1223**, 291 (1990)

[335] G.J. Dixon, S.G. Grubb, OSA Tech. Digest CLEO '90, Paper CPDP37-1 (1990)

[336] T. Sasaki, T. Kojima, A. Yokotani, O. Oguri and S. Nakai, Opt. Lett., **16:21**, 1665 (1991)

[337] N. MacKinnon and B.D. Sinclair, Opt. Comm., **105**, 183 (1994)

[338] V.G. Ostroumov, F. Heine, S. Huck, G. Huber, V.I. Mikhailov and I.A. Shcherbakov, Appl. Phys. B, **64**, 301 (1997)

[339] B.S. Choi, J.K. Chee, Y.M. Hwang, H.Y. Jang, Y.D. Kwon and S.H. Lee, Japanese J. Appl. Phys., **32**, 5453 (1993)

[340] N. MacKinnon, Chapter 5, PhD Thesis, University of St.Andrews Library (1994)

[341] J.J. Zayhowski, IEEE Photon. Tech. Lett., **9:7**, 925 (1997)

[342] R.G. Smith, J.E. Geusic, H.J. Levinstein, J.J. Rubin, S. Singh and V. Uitert, Appl. Phys. Lett., **12:9**, 308 (1968)

[343] R.L. Byer, M.K. Oshman, J.F. Young and S.E. Harris, Appl. Phys. Lett., **13:3**, 109 (1968)

[344] W.R. Bosenberg, A. Drobshoff, J.I. Alexander, L.E. Myers and R.L. Byer, Opt. Lett., **21:10**, 713 (1996)

[345] K. Schneider, P. Kramper, S. Schiller, J. Mlynek, Opt. Lett., **22:17**, 1293 (1997)

[346] A.J. Henderson, M.J. Padgett, F.G. Colville, J. Zhang and M.H. Dunn, Opt. Comm., **119**, 256 (1995)

[347] C.D. Nabors, R.C. Eckardt, W.J. Kozlovsky and R.L. Byer, Opt. Lett., **14:20**, 1134 (1989)

[348] L. Lichtenberg, P. Hansen and P. Buchhave, Opt. Lett., **22:14**, 1074 (1997)

[349] D. Lee and N.C. Wong, J. Opt. Soc. Am. B, **10:9**, 1659 (1993)

[350] R.C. Eckardt, C.D. Nabors, W.J. Kozlovsky and R.L. Byer, J. Opt. Soc. Am. B, **8:3**, 646 (1991)

[351] G.M. Gibson, M.H. Dunn, M.J. Padgett, "Application of a continuously tunable, cw optical parametric oscillator for high-resolution spectroscopy," to be published in Opt. Lett. (1998).

[352] A.J. Henderson, M.J. Padgett, J. Zhang, W. Sibbett and M.H. Dunn, Opt. Lett. **20:9**, 1029 (1995)

[353] G.J. Dixon, C.E. Tanner and C.E. Wiemann, Opt. Lett., **14**, 731 (1989)

[354] W.X. Lin, H.Y. Shen, Y.P. Zhou, R.R. Zeng, G.F. Yu, Z.D. Huang and W.J. Zhang, Opt. Comm., **82:3**, 333 (1991)

[355] D.G. Matthews, R.S. Conroy, B.D. Sinclair and N. MacKinnon, Opt. Lett., **21:3**, 198 (1996)

[356] X.X. Zhang, P. Hong and B.H.T. Chai, OSA Trends in Optics and Photonics, **1**, 428 (1996)

[357 J.H. Zarrabi, P. Gavrilovic and S. Singh, Appl. Phys. Lett., **67:17**, 2439 (1995)

[358] Y. Lu, L. Mao, S. Cheng, N. Ming and Y. Lu, Appl. Phys. Lett., **59:5**, 516 (1991)

[359] G.J. Hall and A.I. Ferguson, Opt. Lett., **19:8**, 557 (1994)

[360] J.R. Lincoln and A.I. Ferguson, Opt. Lett., **19:16**, 1213 (1994)

[361] G.R. Morrison, M. Ebrahimzadeh, C.F. Rae and M.H. Dunn, Opt. Comm., **118**, 55 (1995)

[362] B.D. Sinclair, Private Communication (1998)

Chapter 6 - CONCLUSIONS AND FUTURE WORK

6.1 Introduction

This thesis records the significant progress that have been made in the understanding, development and application of microchip lasers over the past four years in St.Andrews. Much of the work reported here was ground-breaking at the time of writing and reflected the youthfulness of the field and the expertise and diversity of the group over the last four years.

The choice of the four topical chapters of this thesis to summarise this work highlights the areas in which I feel we have made key contributions to the field of microchip lasers. However there was also a substantial quantity of work carried out but not reported in this thesis either because time did not permit a sensible investigation to be carried out, or the work did not fall into any of these four key areas. Some of this work has been mentioned in passing at relevant points of the thesis, and much of the rest is touched on in this chapter. I hope some of these ideas will contribute towards spawning further microchip laser related research.

The introductory chapter of this thesis reviewed the progress of diode-pumped solid-state lasers since their inception. The most exciting developments in this area over the next few years will undoubtedly be driven by the availability of higher brightness and shorter wavelength diode lasers. These new pump sources will rejuvenate interest in many gain materials not currently in vogue and drive the field to investigate new physics and applications. Indeed, blue GaN based laser diodes now have lifetimes exceeding 10,000 hours and will potentially be commercially available within the next five years.

The aim of the chapter was to indicate the historical developments that led to the development of microchip lasers and the context in which the work in this thesis was carried out. This broad overview also included indications of areas where miniature laser research may go not within the remit of the remaining chapters, for example in the development of vibronic laser materials and in spin-coating deposition techniques.

6.2 Gain Materials for Microchip Lasers

In chapter two the operation of a range of Nd^{3+} doped gain crystals with short absorption depths was characterised. These crystals, Nd:YVO_4, Nd:YOS, Nd:SFAP and Nd:SVAP, were prepared in the form of monolithic microchip lasers for pumping by a laser diode around 810nm and lasing at around 1064nm. In addition, monolithic Nd:YVO_4 microchip lasers operating at 1342nm were characterised. This characterisation took the form of both CW operations, examining thresholds and slope efficiency, and pulsed operation, investigating gain-switching.

These gain materials, with the exception of Nd:SVAP, showed exceptionally good operating characteristics. This operation took the form of low thresholds (<100mW) and high slope efficiencies (>40%). Indeed, their operation equalled, and in some cases exceeded that reported elsewhere for the same gain materials, showing the potential of monolithic microchip lasers as low-medium power laser sources. The most significant and attractive feature of operation of these monolithic microchip lasers, was however the significant single transverse and longitudinal mode powers (~100mW), making these devices unique by their simplicity. Nd:YVO_4 showed exceptional good lasing properties and was therefore concentrated on in the rest of this thesis.

Further investigations using the other crystals could concentrate on a number of key areas. With its long upper-state lifetime, Nd:YOS has potential to make a good gain crystal in Q-switched laser systems. It also provides an attractive option for doubling into the blue because it exhibits ground state depletion. Nd:SFAP is a promising all-round gain material, well-suited for microchip work. The lower stimulated emission cross-section and longer upper state lifetime would offer advantages over Nd:YVO_4 for Q-switching, and efficient lasing has been reported for all three main Nd^{3+} transitions (945nm, 1059nm and 1320nm).

Beyond Nd^{3+} doped materials, there is a desire for lasers of many different wavelengths to meet many different applications, which can be addressed by the use of other active ions. An important goal in this direction would be the development of a widely tuneable microchip-style laser. The use of an electro-optic crystal as part of a coupled cavity with a transition metal doped gain crystal could provide such a system.

6.3 Modelling of Microchip Lasers

The third chapter of this thesis examined the guiding mechanisms of the transverse mode within miniature monolithic gain crystals, in particular Nd:YVO_4. The understanding of guiding effects is critical in determining the operating envelope of these lasers and methods in which their operation can be improved.

Several different modelling techniques were explored with comments on their applicability. Numerical solutions were found to give the best representation of heat flow, especially in anisotropic crystals, though were limited by the processing time required. Analytical solutions provided good guidelines for the operating characteristics of the devices, and are powerful tools for deriving relational dependencies. These theoretical results were compared with measurements of optical path distortion and beam characteristics to show how a cavity is defined primarily by thermal characteristics for a CW pumped system.

This work brought together for the first time a wide range of theoretical and experimental techniques to determine the nature of the transverse mode guiding, significantly contributing to the understanding of the mechanisms involved. However, time did not permit a full solution to be developed and several issues remain to be characterised. The impact of other cooling systems, such as face cooling, were not considered experimentally and could open new paths for the stabilisation of these lasers, and in particular composite lasers, which are particularly sensitive to temperature fluctuations. I also feel improvements in the interferometry to resolve smaller changes, and work involving other gain materials would help to clarify and support these initial investigations and provide a more complete solution.

Our observation of self Q-switching, and consequently the first theoretical description of a mechanism by which self Q-switched pulses can be generated, led to a more in-depth investigation of the relative contributions from thermal guiding to gain guiding. The effect of high gain at low average powers was shown to have a significant effect on the operation of the laser through dispersion. A basic theoretical model extending the previous thermal modelling was derived, and goes part way to explaining discrepancies observed between the interferometric and far-field measurements made. Further work should again clarify this, and provide a more rounded solution.

6.4 Frequency Converted Microchip Lasers

An attractive feature of Nd^{3+} ions is that the three transitions excited by diode pumping, can be frequency doubled to produce red, green and blue light. Chapter four of this thesis built on previous work in St.Andrews, by examining the further refinement of green microchip lasers and the first demonstration of the doubling of the 1.3μm and 0.9μm to give red and blue microchip lasers respectively.

The further refinement of the green laser, has produced a frequency doubled laser with a pump-green efficiency (~40%) approaching that of the fundamental output from monolithic microchip laser. This is one of the highest conversion efficiencies ever reported for a CW frequency doubled laser, and indicates how refinement of coatings and contacting to minimise losses can significantly enhance operation. However issues regarding the stability and cavity dynamics need to be addressed and I hope further work will provide useful solutions, for example in the use of cavity effects to produce a single longitudinal mode, eliminating the presence of green noise.

The demonstration of the first red and blue microchip lasers showed how this technology could be extended to other wavelengths. Although successful and novel in their own right, the first generation of each laser has shown weaknesses, which I believe, can be addressed with further refinement. For the blue laser, an anisotropic gain material with a high terminating level and large cross-section would be ideal, though there are no obvious candidates. Another possible route would be to frequency double the output of a Cr^{3+} laser. For the red laser the use of an alternative frequency-doubling crystal, such as $LiNbO_3$ would substantially enhance performance. In all cases, periodically poled inorganic and organic materials may ultimately prove to be the best choice of nonlinear material.

Self-frequency doubling in materials such as Er,Yb:$LiNbO_3$, and a microchip OPOs are two related areas where I feel significant progress can be made. Compact, transition-independent systems could offer an ideal low power source of tuneable radiation. The first step would be to demonstrate a CW intracavity OPO based on a microchip laser, perhaps in its simplest form, a Y-shaped cavity formed by the coated, angled intracavity surface of the gain crystal, with two arms to resonant the fundamental and signal wavelengths or a linked linear dual cavity system.

6.5 Q-Switched Microchip Lasers

The fifth chapter highlighted a second form of composite microchip lasers, Q-switched microchip lasers. By introducing a time dependent modulation to the losses of a cavity it is possible to 'Q-switch' the laser to produce short, high intensity pulses. This is generally done either actively, using an electro-optic crystal, or passively, using a saturable absorber.

An entirely new scheme of active Q-switching was described in this chapter. Two systems were described, a quadrupole deflector, and an active electro-optic prism, each offering a single element, low loss, low cost, compact Q-switch with relatively low electrical requirements. The prism Q-switch, despite having relatively poor deflection properties, still produced pulses down to 5.8ns and peak powers of 350W. The quadrupole deflector showed significantly more deflection, producing pulses down to 1.08ns and peak powers in excess of 12kW. The flexibility of the concept behind these Q-switches does not limit their application to microchip lasers and it is hoped they will be employed in larger systems, giving similarly high performance. The main issues to be addressed with this work remain on the technical side, concerning the choice of electro-optic crystal to reduce optical damage, and the electrical switching system.

The second half of the chapter compared the passive Q-switching of the 1064nm transition in Nd:YVO_4 using Cr:YAG and the 1342nm transition using V:YAG. Although Cr:YAG is a relatively common saturable absorber, our joint work with the ILC in Minsk using V:YAG was the first demonstration of a bulk saturable absorber at 1.3μm. The Cr:YAG system produced pulses down to 1.38ns and one kilowatt peak power, comparable to commercially available systems, and the V:YAG pulses less than 10ns and peak powers of 350W, giving comparable pulse energies to the Cr:YAG system, with the prospect of significant improvement with further material refinement. I hope this work will be built-upon, developing further international links to investigate other novel saturable absorbers for wavelength regions not currently covered.

Other future work on semiconductor structures and new gain materials could offer new possibilities in shorter, higher peak power pulses from microchip lasers. A particularly interesting and novel scheme would to employ spin-coated polymers as

Q-switches, giving a low cost, highly compact alternative to expensive, exotic crystals.

6.6 Summary

To summarise, this thesis records a wide range of exciting and novel developments made in the previous four years at St.Andrews. In particular, the lasing and guiding characteristics of monolithic, short absorption depth materials were investigated and the frequency doubled and Q-switched operation of these gain materials was demonstrated. I hope the microchip laser work in St.Andrews will continue to be as exciting and successful in the next four years.

Appendix A – Publications and Presentations

- Malyarevich, Denisov, Yumashev, Mikhailov, Conroy, Sinclair, "V:YAG – A New Passive Q-Switch for Diode-Pumped Solid-State Lasers", Submitted for publication in Applied Physics B – Lasers and Optics
- Conroy, Lake, Kemp, Friel, Sinclair, "Self Q-Switched Nd:YVO_4 Microchip Lasers", Paper CThBB3, CLEO'98 Tech Digest, May 1998
- Conroy, Sinclair, Malyarevich, Denisov, Yumashev, Mikhailov, "V:YAG as Passive Q-Switch at 1342nm and 1064nm", Paper CtuM72, CLEO'98 Tech Digest, May 1998
- Gibson, Conroy, Kemp, Sinclair, Padgett, Dunn, "Microchip Pumped CW Doubly Resonant OPO", Paper , CLEO'98 Tech Digest, May 1998
- Gibson, Conroy, Kemp, Sinclair, Padgett, Dunn, "Microchip Pumped CW Doubly Resonant OPO", Accepted for publication in Optics Letters
- Conroy, Lake, Friel, Kemp, Sinclair, "Self Q-switched Nd:YVO_4 Microchip Lasers", Accepted for publication in Optics Letters
- Conroy, Kemp, Friel, Sinclair, "Microchip Nd:Vanadate Lasers at 1342nm and 671nm", Opt Lett, 22:23, 1781 (1997)
- Conroy, Kemp, Friel, MacKinnon, Matthews, Sinclair, "Red, Green and Blue Intracavity Doubled Microchip Lasers", 13th UK Quantum Electronics Conference, Sept 1997
- Conroy, Marks, Friel, Kemp, Sinclair, "Passively Q-Switching of Nd:YVO_4 Microchip Lasers", 13th UK Quantum Electronics Conference, Sept 1997
- Ley, Conroy, Kemp, Friel, Sinclair, "Novel Q-Switching of a Microchip Laser Using a Quadrapole Deflector", 13th UK Quantum Electronics Conference, Sept 1997
- Kemp, Conroy, Friel, Sinclair, "Polarisation Eigenmodes of a Nd:YVO_4 / KTP Intracavity Frequency-Doubled Microchip Laser", 13th UK Quantum Electronics Conference, Sept 1997
- Conroy, Kemp, MacKinnon, Sinclair, "Comparison of 671/1342nm Generation with 532/1064nm in Nd:YVO_4 Microchip Lasers", Paper CFO6, CLEO'97 Tech Digest, May 1997
- Conroy, Marks, Friel, Kemp, Sinclair, "Passively Q-Switched Nd:YVO_4 Microchip Lasers", Scottish LEOS Chapter Meeting, St.Andrews University, March 1997

- Conroy, Kemp, Marks, MacKinnon, Sinclair, "Thermal Transverse Mode Definition in Short Absorption Depth Lasers", Advances in Solid State Lasers (Half Day Meeting of Quantum Electronics Group of the I.O.P.), London, Nov 1996
- Conroy, MacKinnon, Sinclair, "ND:YVO_4 Microchip Lasers Operating at 1342nm", Scottish LEOS Chapter Meeting, Heriot Watt University, Sept 1996
- Conroy, Matthews, MacKinnon, Sinclair, "Microchip Lasers", Talk 8 & Poster 11, Highlights of British Physics Research and R&D", Royal Society, London, Sept 1996
- Conroy, MacKinnon, Matthews, Sinclair, "Diode-Pumped Nd:YVO_4 Microchip Lasers Operating at 1342/671nm", Paper CFH1, CLEO Europe'96 Tech Digest, Sept 1996
- Matthews, Boon, Conroy, Sinclair, "A Comparative Study of Diode Pumped Microchip Laser Materials: Nd-doped YVO_4, YOS, SFAP and SVAP", J Mod Opt 43:5, 1079-1087 (1996)
- Matthews, MacKinnon, Conroy, Sinclair, "Blue Microchip Laser Fabricated From Nd:YAG and $KNbO_3$", Opt Lett, 21:3, 198-200 (1996)
- Conroy, Kemp, Matthews, Sinclair, "Gain-Guiding and Thermal Distortion in Diode-Pumped Nd:YVO_4 microchip Lasers", Paper CTuP4, CLEO'96 Tech Digest, May 1996
- Matthews, MacKinnon, Conroy, Sinclair, "Diode Pumping of a Blue (473nm) Nd:YAG/$KNbO_3$ Microchip Laser", Paper CTuP3, CLEO'96 Tech Digest, May 1996
- Matthews, MacKinnon, Conroy, Sinclair, "A Diode-Array Pumped Continuous Wave Blue Microchip Laser", Advances in Solid State Lasers 1996
- Conroy, MacKinnon, Matthews, Sinclair, "Intensity -Modulated Microchip Lasers", 12th UK Quantum Electronics Conference, Paper P2-7, Sept 1995
- Conroy, MacKinnon, Matthews, Sinclair, "Thermal Distortion in Laser-Diode Pumped Nd:YVO_4 Microchip Lasers", 12th UK Quantum Electronics Conference, Paper P3-3, Sept 1995
- Matthews, Boon, Conroy, Sinclair, "A Comparative Study of Diode Pumped Microchip Laser Materials: Nd-doped YVO_4, YOS, SFAP and SVAP", 12th UK Quantum Electronics Conference, Paper P1-5, Sept 1995
- Conroy, Matthews, MacKinnon, Sinclair, "Microchip Lasers", SUSSP 1995, St.Andrews, August 1995

- Conroy, MacKinnon, Sinclair, “Gain Switched Nd:YVO_4 Microchip Lasers”, Paper CTuP2, CLEO’95 Tech Digest, June 1995

Appendix B – Table of Diagrams & Figures

Figures:

Tables:

Appendix B - Table of Diagrams & Figures